MIXED-VALENCE BIMETALLIC DITHIOLATES OF IRON, COBALT, AND NICKEL AND THEIR RELEVANCE TO THE HYDROGENASES

BY

GEOFFREY MORGAN CHAMBERS

DISSERTATION

Submitted in partial fulfillment of the requirements
for the degree of Doctor of Philosophy in Chemistry
in the Graduate College of the
University of Illinois at Urbana-Champaign, 2016

Urbana, Illinois

Doctoral Committee:

Professor Thomas B. Rauchfuss, Chair
Professor Gregory S. Girolami
Assistant Professor Alison R. Fout
Assistant Professor Josh Vura-Weis

Abstract

The world's energy economy is driven by petroleum, but this resource is limited and its consumption drives global climate change. As a result, it is crucial for the ongoing prosperity of humans to find an alternative means of energy production and storage. One alternative is hydrogen. Nature utilizes metalloproteins called hydrogenases (H_2ases) to efficiently interconvert protons and electrons with dihydrogen. Though this is one of the simplest possible reactions, it is of utmost importance for countless microorganisms. The performance of these enzymes exceeds that of the leading artificial catalyst used by humans: platinum. Though platinum based catalysts are currently the best, the scarcity of this metal makes widespread utilization unfeasible. Nature, by necessity, must utilize earth abundant metals. Indeed, the premier enzymes that facilitate this reaction utilize the abundant metals nickel and iron.

The active sites the [NiFe]- and [FeFe]-H_2ases possess bimetallic cores bridged by thiolates. The iron centers are ligated by species that are peculiar in biological systems: carbon monoxide and cyanide. Due to the effectiveness of H_2ases as H_2 oxidation proton reduction catalysts, there is a strong drive to synthesize small molecule models of these active sites. Chapter 1 introduces hydrogen in the context of energy storage and microbiology and continues on to describe the details of the hydrogenases. The second half of this chapter discuses model compounds of the hydrogenases and various strategies, challenges, and successes in this area.

Though more is known about the [NiFe]-H_2ase, model compounds to date have largely failed to replicate any of the extensive mixed-valent states of this active site. This thesis advances this area specifically through the synthesis and examination of mixed-valent bimetallic dithiolate complexes. Chapter 2 focuses on the NiRu dithiolate compound (dppe)Ni(pdt)Ru(*p*-cymene) (dppe = 1,2-bis(diphenylphosphino)ethane; pdt = 1,3-propanedithiolate, *p*-cymene = *p*-isopropyltoluene). The protonation and oxidation chemistry of this system are described. The principal finding this work is that the mixed-valent cation $[(dppe)Ni(pdt)Ru(p\text{-cymene})]^+$ both structurally and spectroscopically mimics the [NiFe]-H_2ase active site in the Ni-L state and is the first such reported example. A disadvantage of these compounds is that they contain the platinum-group metal ruthenium. All other chapters in this thesis utilize only first row transition metals.

Chapter 3 discusses the synthesis and properties of the cyclopentadienyl NiFe compound $[CpNi(pdt)Fe(dppe)CO]BF_4$ (Cp = cyclopentadienide). These cyclopentadienyl complexes are the first reported examples of model compounds to accurately replicate the

redox inactive iron center of [NiFe]-H_2ase. Additionally, this system is shown to stabilize nickel in the first, second, and third oxidation states.

Treatment of the Ni(II)Fe(II) compound [CpNi(pdt)Fe(dppe)CO]BF_4 affords the neutral, mixed-valent compound CpNi(pdt)Fe(dppe)CO, which has been extensively characterized through numerous spectroscopic techniques and DFT calculations to be a *bona fide* Ni(I)Fe(II) complex. When this compound is treated with acid, the Ni(II)Fe(II) cation $[CpNi(pdt)Fe(dppe)CO]^+$ is regenerated with the concomitant production of 0.5 equiv. of H_2 making this system a proton reduction catalyst. The catalytic cycle was analyzed using DFT. The mixed-valence hydride [CpNi(pdt)(μ-H)Fe(dppe)CO]BF_4 is not observed directly but is unambiguously Ni(III)Fe(II), akin to the mixed-valent Ni-C state of [NiFe]-H_2ase, by DFT analysis.

Chapter 4 describes the synthesis and characterization of mixed-valent di- and tri-nickel cyclopentadienyl dithiolates. The reaction between nickelocene and monothiols has long been known to yield dimers of the form $[CpNi(SR)]_2$ with loss of CpH. The reaction of nickelocene with *di*thiols is investigated in chapter 4 and is found to be quite complex: dinickel, trinickel, and pentanickel species are formed. In contrast to the known monothiolate dimers, the dithiolate compounds feature a pyramidalized Ni_2S_2 core by virtue of the dithiolate linker. This distortion of the Ni_2S_2 core forces the two nickel centers together. As a consequence, the dinickel compounds $Cp_2Ni_2(pdt)$ and $Cp_2Ni_2(edt)$ (edt = 1,2-ethanedithiolate) have a thermally accessible triplet state, a feature which has been proposed in some DFT analyses of the [NiFe]-H_2ase active site. Another consequence of the close proximity of these metal centers is a facile one electron oxidation to generate $Ni(2.5)_2$ compounds. This chapter includes DFT analysis of the monothiolate dimer $Cp_2Ni_2(SEt)_2$ in which the Ni_2S_2 core is distorted computationally. This study shows the drastic effects of bending the Ni_2S_2 core.

Chapter 5 investigates the properties of the mixed-valent cation $[Cp_2Co_2(pdt)]^+$ and the mixed-valent bridging hydride complexes $Cp_2Co_2(xdt)H$ (xdt = edt, pdt). The CpCo fragment is isoelectronic with the $Fe(CO)_3$ fragment that frequently appears in model complexes. The cation $[Cp_2Co_2(pdt)]^+$ generates the bridging hydroxide cation$[Cp_2Co_2(pdt)OH]^+$ upon treatment with aqueous THF. Similarly, the bridging thiolates compounds are generated upon treatment of $[Cp_2Co_2(pdt)]^+$ with thiols. Both the mixed-valent bridging hydride compounds and the mixed-valent cation are discrete Co(III)Co(II) species, in contrast to the $Ni(2.5)_2$ species in the analogous nickel systems.

Table of Contents

Abbreviations Used

adt/adt^{2-}	2-aza-1,3-propanedithiolate	$(SCH_2NHCH_2S)^{2-}$
BAr_4^{F-}	tetrakis(3,5-bis(trifluoromethyl)phenyl)borate	$[B(C_6H_3(CF_3)_3)_4]^-$
bda	benzilideneacetone	
bdt	1,2-benzenedithiol	
Bu	*n*-butyl	
Cp	cyclopentadienide	$[C_5H_5]^-$
Cp’	methylcyclopentadienide	$[C_5H_4Me]^-$
Cp*	pentamethylcyclopentadienide	$[C_5Me_5]^-$
CV	cyclic voltammogram or cyclic voltammetry	
Cy	cyclohexyl	C_6H_{11}
dcpe	1,2-bis(dicyclohexylphosphino)ethane	
dppe	1,2-bis(diphenylphosphino)ethane	
dppv	*cis*-1,2-bis(diphenylphosphino)ethene	
edt/edt^{2-}	1,2-ethanedithiolate	$C_2H_4S_2^{2-}$
Et	ethyl	CH_3CH_2-
Fc$^{0/+}$	ferrocene/ferrocenium redox couple	
H_2ase	hydrogenase	
Me	methyl	CH_3-
Me_2pdt	2,2-dimethyl-1,3-propanedithiol	$(SCH_2CMe_2CH_2S)^{2-}$
Nbdt/Nbdt^{2-}	1,2-norbornanedithiolate	
odt/odt^{2-}	2-oxo-1,3-propanedithiolate	$(SCH_2OCH_2S)^{2-}$
TEMPO	2,2,6,6-tetramethylpiperidine-N-oxide	
tdt	3,4-toluenedithiol	
pdt/pdt^{2-}	1,3-propanedithiolate	$^-S(CH_2)_3S^-$
PCET	proton coupled electron transfer	
Ph	phenyl	C_6H_5-
xdt	generic dithiol	

Chapter 1:

Overview of Hydrogen, Hydrogenases, and Model Complexes.

1.1 Energy Usage and Production in the United States

Energy production and demand is a growing concern for the United States and the rest of the world. Currently, an overwhelming majority of the energy produced in the United States is derived from non-renewable resources; in 2014, the United States generated 98.3 x 10^{15} BTUs of energy of which only about 10% was derived from renewable sources (Figure 1.1).[1]

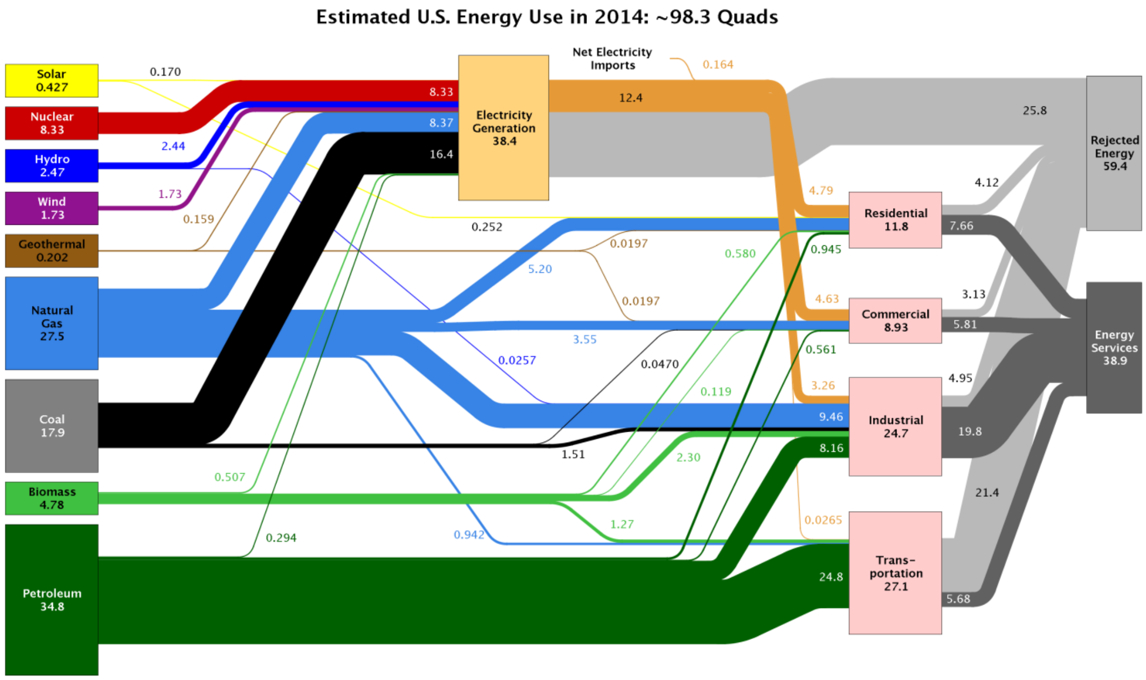

Figure 1.1. Diagram of energy consumption in the United States for the year of 2014. Source: Lawrence Livermore National Laboratory and the Department of Energy.

An obvious practical concern for non-renewables is that their supply is limited. At the current rate of consumption, proven petroleum reserves are expected to last about 50 years.[2] In addition, non-renewable resources such as coal, natural gas, and petroleum are the principal sources of human-based CO_2 emissions, a primary contributor to global climate change.[3,4] To alleviate the burden on the environment, an increasing the amount of energy must come from carbon neutral sources.

For over one hundred years, biomass and hydroelectric power generation have been dominate sources of renewable energy in the United States.[5] In the past twenty years, the contribution from wind generated electricity has increased drastically, accounting for 5% of renewable energy production in 1990 to 15% in 2012. Solar energy has made similar gains (Table 1.1).[5]

Table 1.1. Net Electricity Generation (All Sectors) in the United States

Year	Hydroelectric (10^{12} BTU)	Solar PV (10^{12} BTU)	Wind (10^{12} BTU)
2005	2.703	0.063	0.178
2009	2.669	0.098	0.721
2014	2.469	0.427	1.734

Transportation accounts for nearly 30% of the United States' energy expenditure (Figure 1.1).[5] Nearly all of this energy is derived from burning fossil fuels in internal combustion engines (ICEs). Typical efficiencies for ICEs are in the range of 20 to 25%. In contrast, oil- and coal- powered power plants have typically have efficiencies around 33% while gas-powered power plants have efficiencies as high as 65%.[6] Transportation constituents a significant portion of human energy expenditure and shifting the burden of energy production in this area from individual vehicles to large scale facilities by the use of electric vehicles would help preserve resources and reduce greenhouse gas emissions. Solely pursuing this route would only delay the effects of climate change, and a comprehensive plan should include multiple approaches including increased usage of renewable energy sources.

1.2 Renewable Energy, Energy Storage, and Hydrogen

Although hydroelectric energy remains the chief source of renewable energy in the United States, solar and wind energy production have increased drastically in the last decade (Table 1.1).[5] Solar and wind energy production however are inherently intermittent, generating phases of surplus and deficit electrical power. As a result, energy storage becomes more important as a means to alleviate shortages during a deficit.

Many means of energy storage have been proposed such as flywheels, compressed air, and water pumps, but this section will only discuss batteries and chemical fuels. Batteries and chemical fuels both have advantages and disadvantages.

Batteries have desirable weight *power* density, but their weight *energy* densities are typically an order of magnitude lower than chemical fuels (Figure 1.2).[7] An appealing property of batteries however is their high recharge energy efficiency which is typically 80-90% (only 100 kWh is needed to recharge an 80-90 kWh battery).[8] Typical electrical power transmission losses are 6.5%, as estimated by the US Energy Information Administration. Consequently, the total energy lost during recharge by consumers is minimal. Recharge efficiency is an important factor when considering energy storage media and the analogous parameter for chemical fuels would be the electrical energy to fuel conversion efficiency.

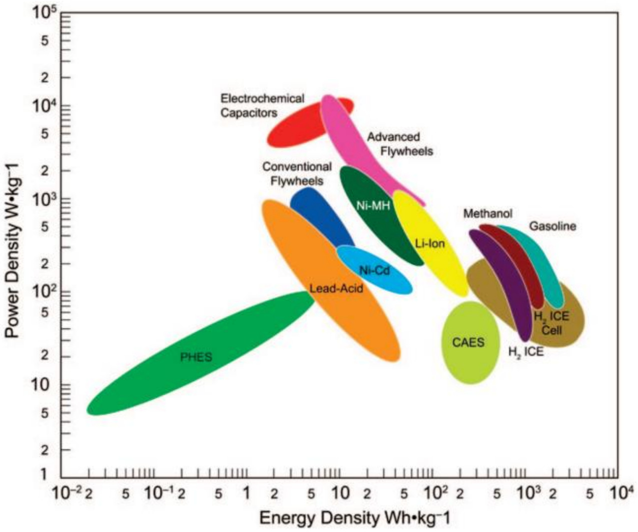

Figure 1.2. Weight power density vs weight energy density graph showing typical energy storage media.[7]

Chemical fuels such as gasoline, methanol, and hydrogen, have similar weight power densities but far greater weight energy densities than batteries (i.e. batteries possess less energy per unit weight than chemical fuels). The efficient conversion of electrical energy to commonly used chemical fuels such as gasoline, methanol, or ethanol, is not currently possible at any reasonable efficiency. Hydrogen is a chemical fuel which is significantly less difficult to synthesize from electrical energy.

The vast majority of industrial hydrogen production is through the energy intensive coal gasification, steam reforming, and water-gas shift processes (eq. 1-3). Steam reforming of methane is currently the cheapest way of producing hydrogen and nearly half of the world's hydrogen is produced this way.[9] Generating hydrogen through these traditional processes, which utilize non-renewable resources, is essentially self-defeating when the goals are energy efficiency and reduction in greenhouse gas emissions.

$$C + H_2O \xrightarrow{1100\text{-}1300\ ^\circ C} CO + H_2 \qquad (1)$$

$$CH_4 + H_2O \xrightarrow{700\text{-}925\ ^\circ C} CO + 3\ H_2 \qquad (2)$$

$$CO + H_2O \xrightarrow{400\ ^\circ C} CO_2 + H_2 \qquad (3)$$

Using hydrogen to store energy generated from renewable sources such as solar of wind would entail electrochemical generation of hydrogen, typically through the electrolysis of water (Scheme 1.1). The best heterogeneous catalysts for this process in both the forward and reverse directions are those based on platinum.[10] Although perhaps feasible for H_2 production or consumption at electrical power plants, the low-abundance and high cost of platinum prohibits its extensive use as a catalyst in fuel cell vehicles.

Scheme 1.1. Electrochemical Oxidation of Water

$$
\begin{array}{lrcll}
 & 2\,H^+ + 2\,e^- & \rightleftharpoons & H_2 & \\
 & H_2O & \rightleftharpoons & 0.5\,O_2 + 2\,H^+ + 2\,e^- & \\
\hline
\textbf{Overall:} & H_2O & \rightleftharpoons & H_2 + 0.5\,O_2 & E = -1.23\text{ V}
\end{array}
$$

Fuel cells offer superior fuel-to-energy conversion efficiencies compared to internal combustion engines. For hydrogen, with today's hydrogen fuel cell technologies, typical operating efficiencies exceed 45%,[11] with a theoretical maximum of 83%. Even with these desirable qualities, significant challenges remain in hydrogen storage and in cheap, efficient catalysts for hydrogen-to-energy conversion.

The energy and power density by weight of hydrogen are comparable to other chemical fuels but the densities by volume are much less impressive. The low power and energy densities by volume arise from the fact that hydrogen is a gas above 33K and liquid hydrogen has a density of only 0.07 g/mL. To achieve acceptable energy capacities, pressurized gaseous hydrogen or liquefied hydrogen would be required, but these forms of storage present safety hazards.

Both compressed and liquefied hydrogen have lower energy densities by volume than liquid fossil fuels by a factor of 5-10. Additionally, the increased energy density by volume obtained by compression or liquefaction comes at a cost; liquefaction of hydrogen is non-trivial and can consume up to 30-40% energy equivalent of the fuel itself.[9] The low energy volume density of hydrogen presents a significant challenge in its widespread adoption as an energy storage medium. Though not a focus of this thesis, work in the area of hydrogen storage is ongoing with and possible materials with applications in this area include metal-organic frameworks and molecular hydride complexes.[12-14]

The success of hydrogen as a fuel is dependent on the discovery or design of earth-abundant catalysts for the electrochemical generation and consumption. In this pursuit, heterogeneous catalysts, such as the platinum based catalysts in H_2 production and H_2

oxidation, are more difficult to characterize and probe and make rational design challenging. Homogeneous catalytic systems provide greater opportunity to understand reaction mechanisms through the use of several spectroscopic techniques which would guide rational design of efficient catalysts.

1.3 Hydrogen in the Biosphere

The electrolysis of hydrogen entails the disassembly of the dihydrogen molecule into protons and electrons. Protons and electrons are the simplest constituents of chemical reactions. The transfer and control of these species is of crucial importance in numerous biological processes and nature has developed numerous methods of controlling these substrates. On the cellular scale, protons are used as a terminal electron acceptor while dihydrogen is used as a source of energy, depending on the specific needs and environment an organism. Nature's mastery of these processes provides rich insights into the design of catalysis for H_2 oxidation and proton reduction.

In the microbial world, many metabolic processes continuously produce hydrogen. These processes typically take place in anaerobic environments such as several inches into topsoil or still water (Figure 1.3) and example metabolic processes include fermentation and methanogenesis. Most, but not all, of the generated hydrogen does not have a chance to make it into the atmosphere due to its value as an energy commodity. The hydrogen that does escape the biosphere does not accumulate over long periods of time in the Earth's atmosphere because the dihydrogen molecule is not massive enough to be permanently retained by the Earth's gravity. As a consequence, hydrogen gas only accounts for 1 ppm of Earth's atmosphere, even though hydrogen constitutes the majority of ordinary matter in the universe.

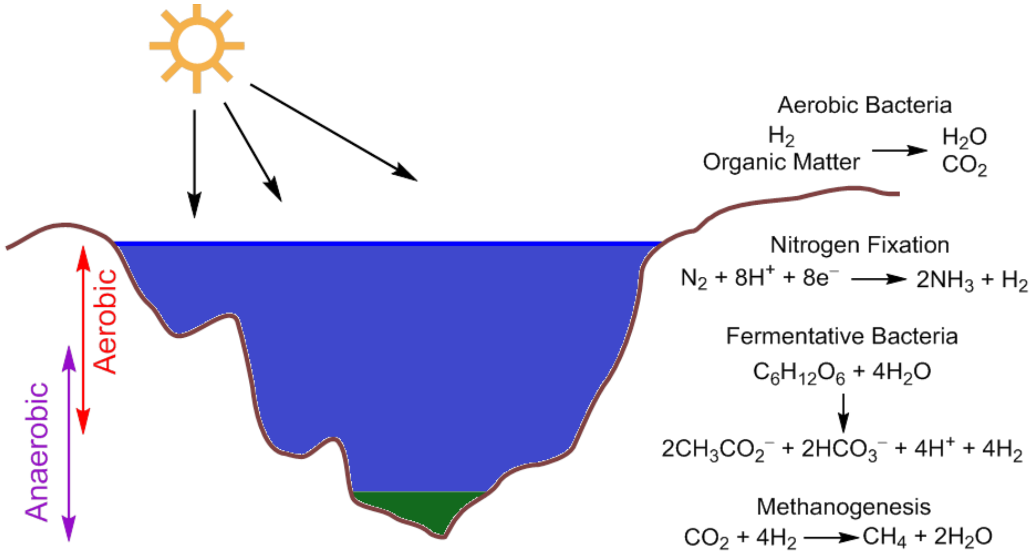

Figure 1.3. Depiction of a generic still water environment in which a variety of exergonic metabolic processes take place. The environment is increasingly anoxic with depth. Reactions on the right are ordered such that the top reactions are more prevalent in aerobic organisms and the reactions on the bottom are more prevalent in anaerobic organisms.

In some cases, the generation of hydrogen from substrate by a solitary organism may be endergonic. Organisms in this situation exist in symbiotic relationships with partners that make the reaction more favorable. One example is the case of *Synthrophus aciditrophicus*, which oxidizes benzoate to acetate in the presence of water to generate H_2 (Scheme 1.2).[15] This process is not thermodynamically favorable for the organism by itself, but by pairing with a sulfate-reducing partner, the overall process now becomes exergonic, benefitting both organisms. In this example, hydrogen generated in one organism is consumed by another; the transfer of energy via the hydrogen molecule in this process is facilitated by enzymes called hydrogenases.

Scheme 1.2. Benzoate Oxidation by *S. aciditrophicus* with and without a Sulfate-reducing Partner

Without partner: $\text{benzoate}^- + 7\ H_2O \longrightarrow 3\ \text{acetate}^- + HCO_3^- + 3H^+ + 3H_2 \quad \Delta G^o = +70.6\ \text{kJ/mol}$

With partner: $4\ \text{benzoate}^- + 7\ SO_4^{2-} + 16\ H_2O \longrightarrow 12\ \text{acetate}^- + 4HCO_3^- + 3HS^- + 9H^+ \quad \Delta G^o = -43.3\ \text{kJ/mol}$

1.4 The Hydrogenases

Hydrogenases (H_2ases) are the enzymes that mediate the oxidation of hydrogen or the reduction of protons (eq. 4). These air-sensitive enzymes are found in anaerobic microorganisms and have drawn substantial attention due to their remarkable efficiencies, utilization of earth abundant metals, and uncommon ligands, carbon monoxide and cyanide.

$$H_2 \xrightleftharpoons{\text{Hydrogenase}} H^+ + 2\,e^- \qquad (4)$$

Though these enzymes catalyze one reaction, the enzyme can have multiple purposes. The main functions of hydrogenases is to provide an avenue to extract energy from molecular hydrogen or remove reducing equivalents; the specific direction of operation is determined by the exact location of the protein within the cell.[16] H_2ases also play a role in the regulation of proton gradients in some organisms as a consequence of protons being substrates or products.[17]

The H_2ases are divided into two main types: [FeFe]-H_2ase, and [NiFe]-H_2ase classifications that originate from the transition metals found in the active sites.[18] These proteins are expressed in a large variety of archaea, bacteria, and some eukarya. The H_2ases differ in weight between species, but the active sites and surrounding residues are highly conserved. A third class with a single iron in the active site, called [Fe]-H_2ase, is often grouped with the other two, but this family does not directly catalyze eq. 4. Instead, [Fe]-H_2ase catalyzes the hydrogenation of methenyl-H_4MPT$^+$ (eq. 5).[19]

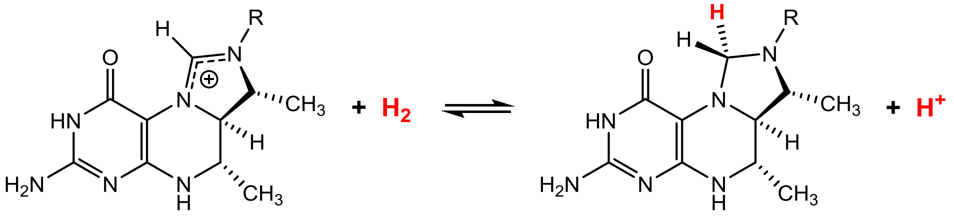

(5)

methenyl-H_4MPT$^+$ methylene-H_4MPT

The H_2ases have been studied using protein film electrochemistry (PFE), a technique where purified proteins are physisorbed onto an electrode surface, allowing controlled electron flow at sustained potentials. PFE has allowed quantification of turnover frequencies (Table 1.2)[20] and overpotentials of the H_2ases under catalytic conditions. PFE experiments have allowed analysis of the H_2ases at different pH's and the responses various substrates or potential poisons.[21,22]

Table 1.2. Selected rates for H_2 oxidation and proton reduction in different H_2ases.

System	**Type**	**H_2 Oxidation Rate (mol H_2/(mol·s)**	**H^+ Reduction Rate (mol H_2/(mol·s)**
Desulfovibrio desulfuricans	[FeFe]	53,500	7,300
Megasphaera elsdenii	[FeFe]	8,700	6,800
Delsufovibrio gigas	[NiFe]	4,500	1,300
Desulfomicrobium baculatum	[NiFeSe]	5,000	5,800
Platinum	N/A	15	15

The PFE experiments on the H_2ases allow a comparison to platinum, the abiological standard. H_2ases, being proteins, are quite large (typically ≥ 50 kD) compared to platinum atoms; however, the per mole efficiencies of platinum are dwarfed by even the slowest hydrogenases (Table 1.2).[23]

The active sites of both the [NiFe]- and [FeFe]-H_2ase feature low spin iron centers with carbon monoxide and cyanide ligands (Figure 1.4). The cyanide ligands are hydrogen bonded to the protein scaffold, simultaneously holding these ligands in place and attenuating any latent basicity of the nitrogen lone-pair. The carbon monoxide ligands reside in hydrophobic pockets. Though strikingly similar, these two enzymes are not genetically related and are examples of convergent evolution.

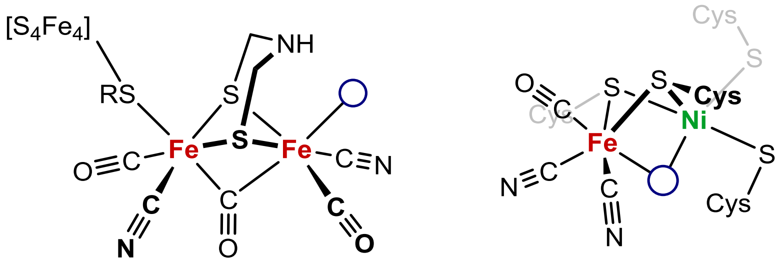

Figure 1.4. Active sites of [FeFe]-H_2ase (left) and [NiFe]-H_2ase (right). The empty circles indicate vacant binding sites.

Most H_2ases utilize chains of Fe_4S_4 clusters to mediate electron transfer from outside to the protein to the active site. Some small molecular weight [NiFe]-H_2ases are known without these clusters. These iron-sulfur clusters serve not only as conductors for electron transfer, but also as a means of electron storage.

A family of membrane bound [NiFe]-H_2ases are active under aerobic conditions (Figure 1.5). This oxygen tolerance is most likely facilitated by the ability of the enzyme to quickly deliver electrons to oxygen-bound species, reducing oxygen before any permanent damage caused by reactive oxygen species can take place.[21] This oxygen reduction process is mediated by an unusual Fe_4S_3 cofactor which is ligated by six, instead of four, cysteine residues, and is called the 6C cluster. In contrast, the [FeFe]-H_2ases are irreversibly destroyed by oxygen.

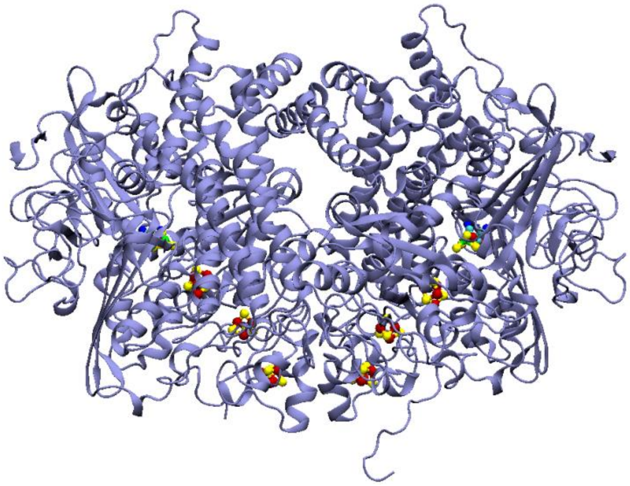

Figure 1.5. Cartoon depiction of the oxygen-tolerant [NiFe]-H_2ase from *Hydrogenovibrio marinus* (pdb: 3AYX). Iron-Sulfur clusters and the NiFe cofactors have been emphasized.

The active site of [FeFe]-H_2ase features a coordinatively saturated octahedral iron center (called the proximal iron) connected to a square-pyramidal iron center (called the distal iron) via an azadithiolate linker (Figure 1.4, left). The distal iron is bridged to an Fe_4S_4 cluster by a cysteinate residue. This assembly is known as the H-Cluster. This azadithiolate cofactor in the H-cluster is believed to serve as a proton relay to the distal iron. Compared to [NiFe]-H_2ase, spectroscopic characterization of the states of [FeFe]-H_2ase, particularly catalytically active states, is less comprehensive. Though the work presented in this thesis focuses primarily on models [NiFe]-H_2ase, model systems for both enzymes utilize similar chemical principles, making comparisons of value.

The active site of [NiFe]-H_2ase contains a nickel center ligated by four cysteinate residues, two of which bridge to an iron center bound to two cyanides and one carbon monoxide (Figure 1.4, right). There is an additional binding site between the two metals that is occupied by hydride, water, hydroxide, or carbon monoxide ligands or is vacant, depending on the state of the active site.

The states of [NiFe]-H_2ases have been extensively characterized and many distinct states are known (Figure 1.6). It is noteworthy that the iron center in [NiFe]-H_2ase is redox inactive and is always low-spin Fe(II), while the nickel center primarily alternates between Ni(II) and Ni(III).

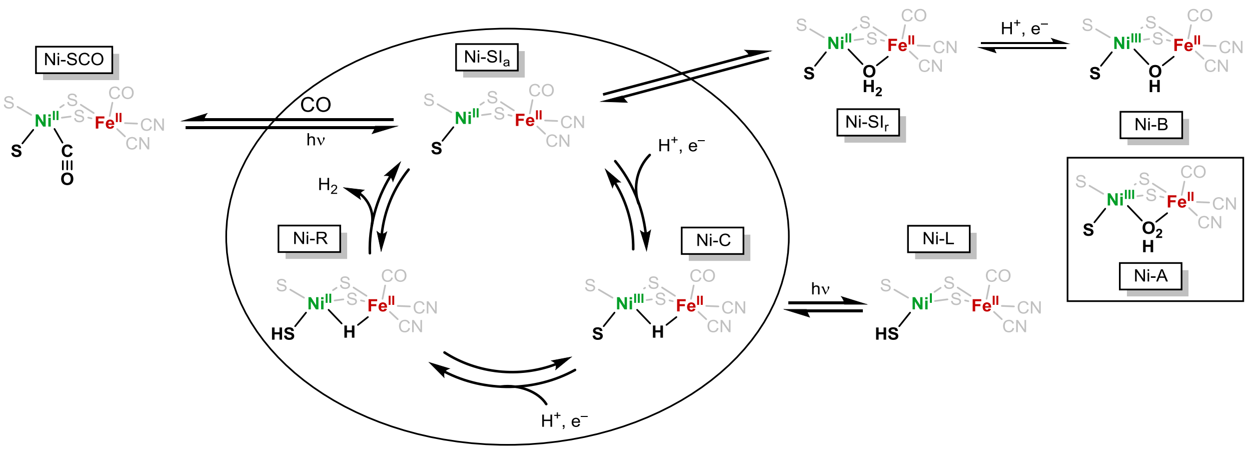

Figure 1.6. Known states of the [NiFe]-H_2ase. The proposed catalytic cycle and active states are present within the circle. The Ni-L state is observed upon low temperature light irradiation of the Ni-C state. The Ni-A, Ni-B, Ni-SI_r, and Ni-SCO states are inactive states. A terminal cysteinate is proposed to be protonated in the Ni-R and Ni-L states.

The first states to be discovered were denoted as Ni-A, B, and C and states. The SI (silent) label is used to denote EPR silent states. The inactive, oxidized states Ni-A and Ni-B differ primarily in their activation time under reducing conditions, with the former having activation times on the order of an hour while the latter activates within minutes, as probed by PFE. The nature of the third bridging ligand between the metal centers is not definitively known for the Ni-A state, but has been proposed to be a hydroperoxo species. Some crystallographic analyses however indicate that a monatomic ligand is present in the site for the Ni-A State.[18] The third bridging ligand in the Ni-B state is well-established through crystallographic and spectroscopic characterization to be a hydroxide. Reduction of the Ni-B state produces the Ni-SI_r (silent – ready) state which retains a third bridging ligand that is proposed to be water. Further reduction, centered at an iron-sulfur cluster, prompts ligand dissociation and produces the Ni-SI_a (silent – active) state, which is catalytically active.

The most commonly proposed catalytic cycle for [NiFe]-H_2ase includes the Ni-C, Ni-SI_a, and Ni-R states. The catalytic cycle in the proton reduction direction proceeds with two proton coupled electron transfer (PCET) steps followed by dihydrogen release, closing the cycle

(Figure 1.6, inside circle). It has also recently been proposed that another state, the Ni-L state, may be implicated in catalysis.

Upon light irradiation at low temperatures, the Ni(III) bridging hydride state, Ni-C, undergoes proton transfer to a nearby base, generating a formally Ni(I)Fe(II) core, called Ni-L. This transformation was probed by electron nuclear double resonance (ENDOR) spectroscopy.[24] Originally, the Ni-L species was considered somewhat anomalous and not relevant for catalysis, but it has since been demonstrated that this state can be produced without light irradiation.[25] Recent studies show that the Ni-L/Ni-C relationship is pH dependent.[26] In the absence of light, the Ni-L state is more stable at high pH while the Ni-C state is more stable at low pH. The non-transient observation of the Ni-L state supports the possibility of its relevance in the catalytic cycle.

The proton transfer associated with the Ni-L/Ni-C transformation is frequently proposed to be facilitated by a terminally bound cysteinate on nickel. A recent high resolution X-ray structure of [NiFe]-H_2ase in the Ni-R state was published in which the bridging hydride ligand and other protons were resolved.[27] Some debate remains whether the depicted proton on the cysteinate is genuine.[28]

An arginine residue, which provides a canopy below the third bridging site, is an alternative proposed site for this proton transfer based on site-directed mutagenesis studies.[29] The appeal for this residue acting as a base for catalysis is that it does not compromise the primary nickel coordination sphere and would implicate that the [NiFe]-H_2ase operates with similar principles to the [FeFe]-H_2ase through the use of outer-coordination sphere bases. Because of the facile conversion of Ni-C to Ni-L, it is proposed that this Ni(I)Fe(II) state could be an intermediate between the Ni-SI_a and Ni-C states in the catalytic cycle (Figure 1.7).

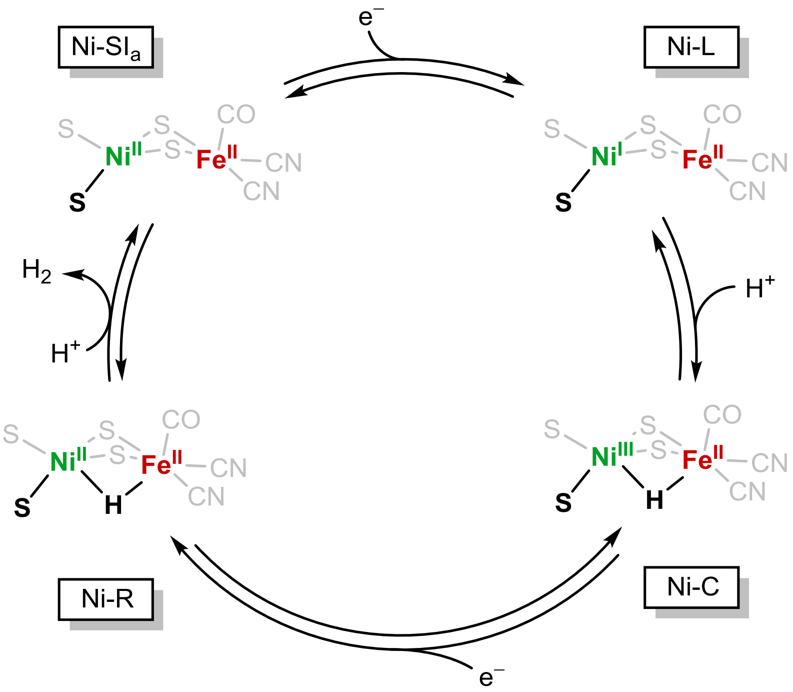

Figure 1.7. Proposed catalytic cycle for [NiFe]-H_2ase with discrete proton and electron transfer steps and the inclusion of Ni-L. Terminal cysteinate protonation is not invoked.

Two distinct carbon monoxide inhibited states are known, Ni-SCO and Ni-CO. The EPR-silent state can be generated from by treating the Ni-SI$_a$ of the enzyme with CO while the EPR-active state is derived from the treatment of the Ni-L state with CO. The carbon monoxide binds to the nickel center, not the iron center, in both cases. The metal preference may suggest that nickel is also the site of hydrogen binding, though this is speculative. The Ni-SCO state has been crystallographically characterized and reveals a highly bent Ni-C-O angle (161°≤φ≤136°).[30] The carbon monoxide binding process is reversible with dissociation achieved either upon light irradiation at low temperatures or thermally.

It is worth noting that the Ni-SCO and the Ni-L states are formally Ni(II) and Ni(I) species. Molecular carbonyl complexes of Ni are rare in the divalent state, compared to the mono- and zero-valent states. The primary reasoning being that higher valent nickel is unable to effectively backbond to the carbonyl ligand, making the M-CO bond labile. Generally, higher valent nickel carbonyl complexes are stabilized by the presence of highly basic ligands such as the nickel carbonyl carborane complex [*nido*-7,9-$C_2B_9H_{11}$]Ni(CO)$_2$.[31] This demonstrates that the nickel center in the active site retains significant electron density in the divalent state.

1.5 Model Complexes of the Hydrogenases

Model complexes of an enzyme active site serve two principal purposes: providing support for unknown or speculative mechanisms within the enzymatic system and to replicate the reactivity of the enzyme. The second purpose is particularly relevant for chemical reactions with potential large scale applications, such as proton reduction or hydrogen evolution. H_2ases are quite efficient catalysts, but due to the difficulties of obtaining enzymes in significant amounts and the possible complications of enzyme stability outside their natural environment, direct use of H_2ases as catalysts is not feasible. Model compounds provide the possibility of being highly active, light-weight catalysts that are more easily prepared in large scales.

Models for the [FeFe]-H_2ase are by far the most advanced towards these two goals. The active site has several distinguishing features: cyanide and carbon monoxide cofactors, an azadithiolate ligand, a bridging carbonyl ligand, and an Fe_4S_4 cluster bridged to the diiron core by a cysteinate residue. All of these features have been replicated at least to some degree in model complexes.[18] A notable example is the azadithiolate complex $Fe_2(adt)(dppv)_2(CO)_2$, which is a potent proton reduction catalyst.[32] When treated with strong acids, this compound forms a doubly protonated species in which a short 1.89 Å ammonium-H and iron-H contact is formed (Figure 1.8). DFT calculations show that this crystallographically determined distance is elongated by the presence of the two tetrafluoroborate counterions and the contact shortens to 1.40 Å in the optimized structure in the absence of counterion effects.[33] Hydrogen release is achieved upon one electron reduction.

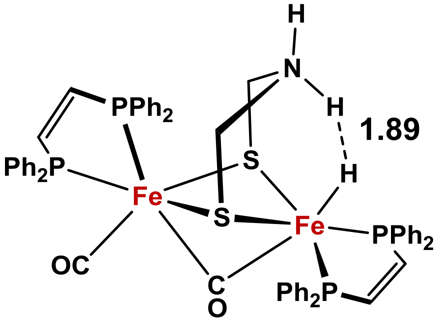

Figure 1.8. Depiction of the doubly protonated model system $[Fe_2(adtH)H(dppv)_2(CO)_2]^{2+}$

Due to the typical low resolutions obtained from protein X-ray crystallography, the identity for the central atom of the dithiolate bridge in the [FeFe]-H_2ase active site had long been unknown and speculated to be either carbon, nitrogen, or oxygen (Figure 1.4, left). Model complexes of [FeFe]-H_2ase have been extraordinarily valuable in elucidating the identity of this atom.

Pioneering work performed by the combined efforts of the Fontecave, Lubitz, and Happe groups where the artificially synthesized FeFe model compounds $Fe(xdt)(CO)_4(CN)_2$ (xdt = odt[34], pdt[35], adt[36]) were inserted into apo-protein established unambiguously that this atom is nitrogen.[37,38] Only the model compound with the central atom being nitrogen (adt) retained catalytic activity. Surprisingly, the additional carbon monoxide ligands in the models dissociate spontaneously in this process.

Models for the [NiFe]-H_2ases are overall less advanced in terms of both structural and functional modeling. The tetrathiolate motif is thought to play a pivotal role in the stabilization of the high-valent Ni(III) intermediates. Incorporation of this tetrathiolate ligation into model compounds is an ongoing challenge. This aspect has been particularly difficult due to the lability of tetrathiolato nickel complexes and the propensity of nickel thiolate complexes to form oligomers and polymers.[39]

Some stable, monomeric tetrathiolate complexes are known and a notable example is bis(norbornanedithiolate) which additionally exhibits a reversible Ni^{II}/Ni^{III} couple.[40] In the case of ethanedithiolate (edt^{2-}), the mononickel anion $Ni(edt)_2^{2-}$ exists in equilibrium with the dinickel dianion $Ni_2(edt)_3^{2-}$ (eq. 6).[41] Tetrathiolate complexes of nickel using arylthiols are also known, but these ligands are established to be non-innocent.[42] Using 1,2-benzenethithiolate, stable [NiFe] compounds with NiS_4 centers were synthesized (Figure 1.9, right).

$$2\ Ni(edt)_2^{2-} \rightleftharpoons Ni_2(edt)_3^{2-} + edt^{2-} \qquad (6)$$

Due to the instability of many tetrathiolato nickel complexes, some approaches compromise by substituting some S^- donors with amines and thioethers. Typical examples are the [NiFe]-model compounds which use tetradentate ligands such as the ones depicted in Figure 1.9, left.[43,44] Many of these tetradentate ligands lock the nickel center into square planar geometry. This restriction limits the stability or accessibility of monovalent nickel, which usually adopts tetrahedral or distorted tetrahedral geometries and stabile Ni(I) complexes utilizing this ligand type are not known.

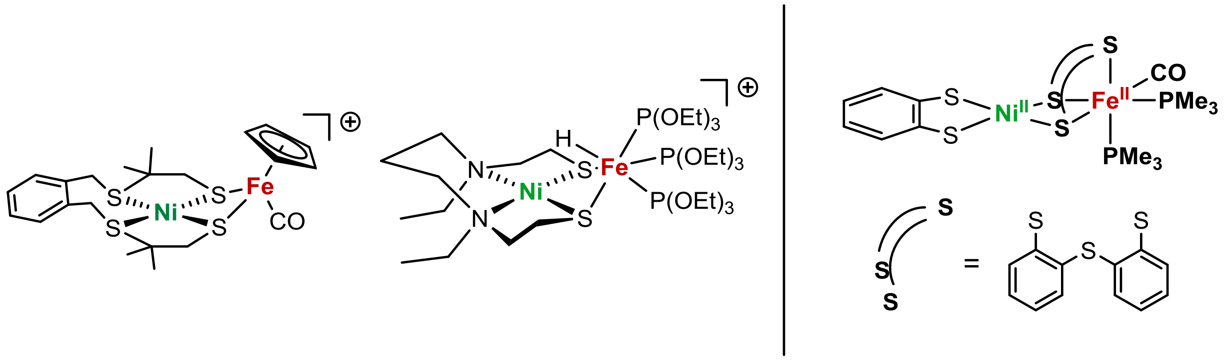

Figure 1.9. [NiFe]-H_2ase model complexes featuring tetradentate ligands with sulfur and amine donors (left). Model complex featuring a NiS_4 center.

One of the curious features of the [NiFe]-H_2ase is the coordination geometry at nickel which can be described as a see-saw (Figure 1.4, right). Replicating this distorted geometry has been not been a primary focus in [NiFe]-H_2ase modeling. Nearly all four-coordinate NiFe model complexes feature either square planar or tetrahedral nickel centers. Generally, catalytically competent model complexes of [NiFe]-H_2ase either fluctuate between these two geometries or constrain the nickel center to be square-planar in reduced states.[44-46] The intermediate geometry observed in the active site could be viewed as a compromise between these two states and the rigidity of the protein scaffold eliminates high reorganization energies.

Both [FeFe]- and [NiFe]-H_2ase are bidirectional and operate faster in the hydrogen oxidation direction than in the proton reduction direction. Several model complexes exhibit electrocatalytic activity for the hydrogen evolution reaction (HER). Dihydrogen activation and oxidation have remained a challenge in this area, with only few notable examples of NiFe or NiRu models, one of which is the (triethylphosphite)iron based system shown in Figure 1.9, left.[47-49]

As stated earlier, the [NiFe]-H_2ases have much more extensively characterized states than the [FeFe]-H_2ases. One of the key features of many of these states is the stabilization of the high valent Ni(III) oxidation state. Stabilizing this oxidation state is difficult in model systems and virtually all reported catalytic compounds operate at one overall oxidation state lower than that of the enzyme (i.e. Ni(I)Fe(I) at the lowest to Ni(II)Fe(II) at the highest). Not only are these oxidation states non-biomimetic, but the redox fidelity of iron is compromised.

1.6 Bioinspired Catalysis – Evolution of the Dubois Catalyst

The hydrogenases, and many other enzymes, utilize organic bases in the outer coordination sphere to facilitate facile proton transfers to and from the metal center. This feature likely evolved because protonation of metal centers is much slower than protonation at nitrogen and oxygen.[50] Pendant bases provide a site for rapid protonation and once protonated, greatly enhance the kinetics of metal protonation through a drastic increase in the local concentration of protons, a strategy utilized ubiquitously in biological processes.[51]

Work done by Dubois and coworkers has incorporated the concept of pendant base assisted proton reduction catalysis and hydrogen evolution catalysis quite remarkably while simultaneously demonstrating that the enzymatic systems are quite optimized.

Early work from the Dubois group focused on bis(diphosphino) nickel and platinum complexes such as $[M(dmpe)_2](BF_4)]_2$, $[M(dmpp)_2](BF_4)]_2$, etc. (M = Ni, Pt. dmpe = 1,2-bis(dimethylphosphino)ethane, dmpp = 1,3-bis(dimethylphosphino)propane) (Figure 1.10).[52] These complexes stoichiometrically activate dihydrogen in the presence of base.[53] Overall, these first generation systems are not particularly noteworthy catalysts; the electrocatalytic rate achieved by these systems for the HER was not determined and the rate for H_2 oxidation was on the order of 10^{-2} s^{-1}.

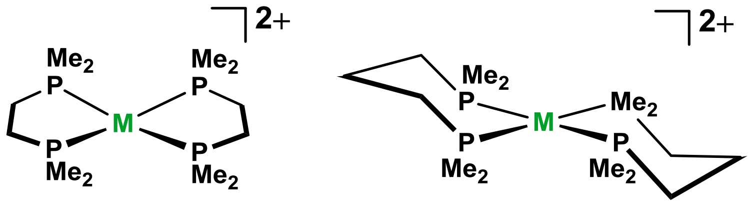

M = Ni, Pt

Figure 1.10. Bis(diphosphine) nickel and platinum cations capable of base-assisted H_2 heterolysis.

Newer designs featured the diphosphine $(Et_2PCH_2)_2NMe$ ($5P_2^{Et}N^{Me}$) which incorporates amine bases in order to achieve more effective electrocatalytic activity towards the HER and H_2 oxidation, (Figure 1.11, left).[54] This substitution was not as impressive as anticipated and was found to catalyze H_2 oxidation at a similar rate as the ethylphosphine derivative which lacked a pendant base; the HER turnover frequency was not determined. The bioinspired pendant base modification was not without benefits and reduced the electrocatalytic overpotential by 0.6 V. To explain the low turnover frequencies, it was reasoned that the six-membered chelate ring must be in the thermodynamically unfavorable boat conformation in order to effectively transfer protons to and from the metal center, (Figure 1.11, right). This type of complication does not arise in the hydrogenases due to the rigid protein scaffold.

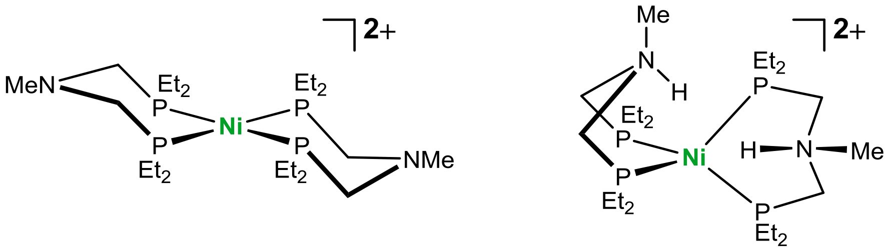

Figure 1.11. HER/H_2-oxidation catalyst Ni($P^{Et2}N^{Me}$) (left). Protonated amine Ni(0) complex with bis-boat conformation of P_2N ligands (right).

Consequently, the phosphine-amine ligand was further modified by incorporation of an additional amine base, which forces one amine on a particular side to adopt the boat conformation (Figure 1.12). This ligand is symmetrical and the eight-membered ring system is abbreviated as $8P_2^{R}N_2^{R'}$ (R=Ph, R'=Ph, Bn) where R and R' denote the substituents at phosphorus and nitrogen respectively. This bis(phosphine)bis(amine) system improved electrocatalytic performance for H_2 oxidation which was increased ten-fold compared to the $5P_2^{Et}N^{Me}$ system. Additionally, $Ni(8P_2^{R}N_2^{R'})_2^{2+}$ was found to be a competent proton reduction catalyst operating at acid independent rates of 740 s^{-1} with an overpotential of 0.35 V in MeCN with 1.2M H_2O and using protonated DMF ([(DMF)H]OTf , p*K*aMeCN=6.1)) as the acid source.

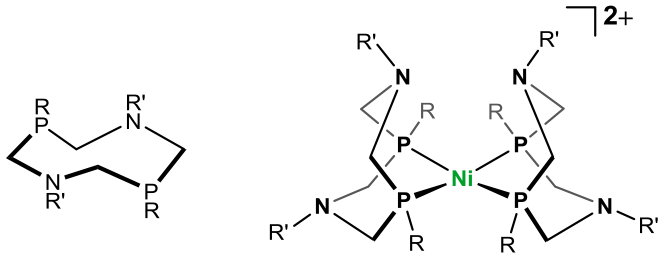

$8P_2^{R}N_2^{R'}$ $Ni(8P_2^{R}N_2^{R'})_2^{2+}$

Figure 1.12. (Left) $8P_2^{R}N_2^{R'}$ ligand. (Right) HER/H_2-oxidation catalyst $Ni(8P_2^{R}N_2^{R'})_2^{2+}$.

Theoretical and experimental investigation led to the proposal that proton reduction catalysis is hindered by the formation of stable, catalytically inert intermediates shown in Figure 1.13.[55] These intermediates are distinguished by protonated amines which hydrogen bond intramolecularly to the other amine on the same chelate, forming a pinched structure. This cooperative binding structure is similar to the protonated form of the base 1,8-bis(dimethylamino)naphthalene (proton sponge).

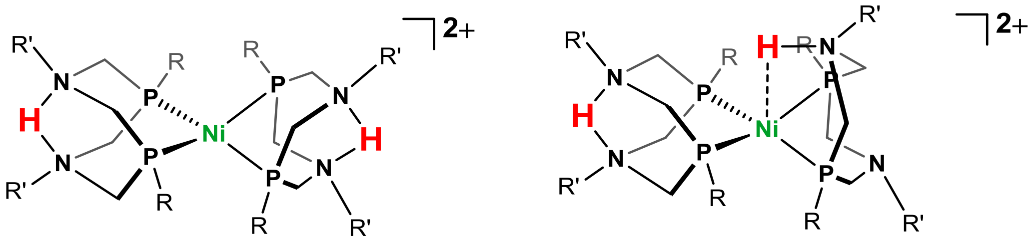

Figure 1.13. Two catalytically inert forms of the double protonated of the HER/H_2-oxidation catalyst $Ni(8P_2{}^{R}N_2{}^{R'})_2{}^{2+}$.

The most obvious way to prevent the formation of the inactive species depicted in Figure 1.13 is to eliminate an amine, but the new ligand would still need to favor formation of the boat conformation of the base containing chelate ring. The solution to this dilemma was the 7-membered ring system $7P_2{}^{Ph}N^{Ph}$, which contains only a single amine while simultaneously maintaining steric influence to favor the boat conformation for the chelate ring possessing the amine (Figure 1.14). The corresponding nickel cation $Ni(7P_2{}^{Ph}N^{Ph})_2{}^{2+}$ was found to operate at 10-fold faster rates for H_2 oxidation and 100-fold faster rates in proton reduction electrocatalysis compared to $Ni(8P_2{}^{Ph}N_2{}^{Ph})_2{}^{2+}$ under identical conditions (Table 1.3). This drastic increase in turnover frequency comes at the cost of greater overpotential, however.

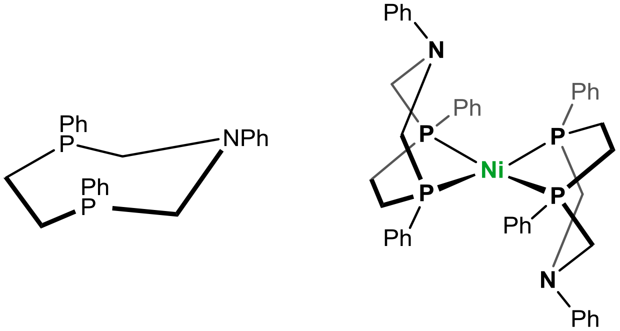

Figure 1.14. (Left) $7P_2{}^{Ph}N^{Ph}$ ligand. (Right) HER/H_2-oxidation catalyst $Ni(7P_2{}^{Ph}N^{Ph})_2{}^{2+}$.

Table 1.3. H_2 Oxidation and Proton Reduction Electrocatalytic Rates for $Ni(P_2)$ and $Ni(P_2N_2)$ Systems

System	H_2 Oxidation Rate (mol H_2/(mol·s))	H^+ Reduction Rate mol H_2/(mol·s)	Overpotential for HER (V)
P_2	<0.2	n.d.	n.d.
$5P_2{}^{Et}N^{Me}$	<0.2	n.d.	n.d.
$8P_2{}^{Ph}N_2{}^{Ph}$	1	720	0.35
$7P_2{}^{Ph}N^{Ph}$	10	106,000	0.68

n.d. = not determined.

Another catalytically inert state may arise from amine inversion. Amine bases naturally have a low barrier for inversion and the orientation of the substituent R can be either favorable or unfavorable for catalysis. *Endo* protonation is conducive to catalysis while *exo* protonation is nonproductive (Figure 1.15). In the event of *exo* protonation, catalysis can only proceed after deprotonation and subsequent inversion. Effective strategies to prevent or eliminate *exo* protonation have not yet been reported.

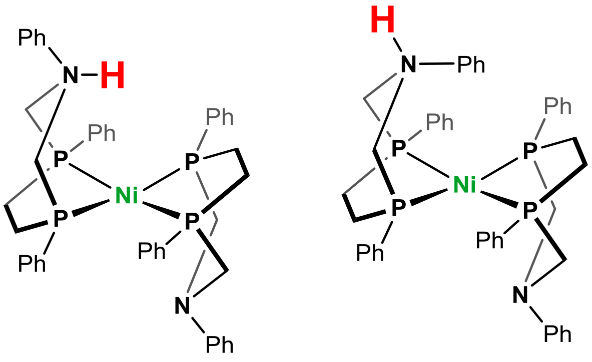

endo protonation *exo protonation*

Figure 1.15. Doubly protonated nickel complex Ni($7P_2^{Ph}N^{Ph}$)$_2^{2+}$ depicted *endo* protonation (left) and *exo* protonation (right).

In order to decrease the overpotential of Ni($7P_2^{R}N^{R'}$), Helm and coworkers investigated a similar diphosphine with a wider bite angle.[56] Increasing the P-Ni-P bite angle has been shown to shift Ni(II)/Ni(I) couples to more positive potentials;[54] therefore it was reasoned that modifying the P_2N system in this way would lower the electrocatalytic overpotential.

Indeed, the nickel complex of $8P_2^{R}N^{R'}$ with an 8-membered ring instead of a 7-membered ring has a lower overpotential than the $7P_2^{R}N^{R'}$ complex by 100 mV. Though the overpotential was lowered, the rates for proton reduction were an order of magnitude slower than that of Ni($7P_2^{R}N^{R'}$)$_2$ under identical conditions. The decreased rates are attributed to an increased proportion of *exo* protonated isomers, depicted in the proposed catalytic cycle (Figure 1.16).

The Dubois system demonstrates the important role of pendant bases for the HER and H_2 oxidation reactions, however, the system is complex and positioning of this base is crucial. Many synthetic modifications have been made to increase the probability that the pendant-base is in a position conducive for catalysis. One aspect of the Dubois system that has not received much attention is the geometry change involved in the $Ni^{0/2+}$ couple. The reorganization involved in this redox couple is nontrivial.

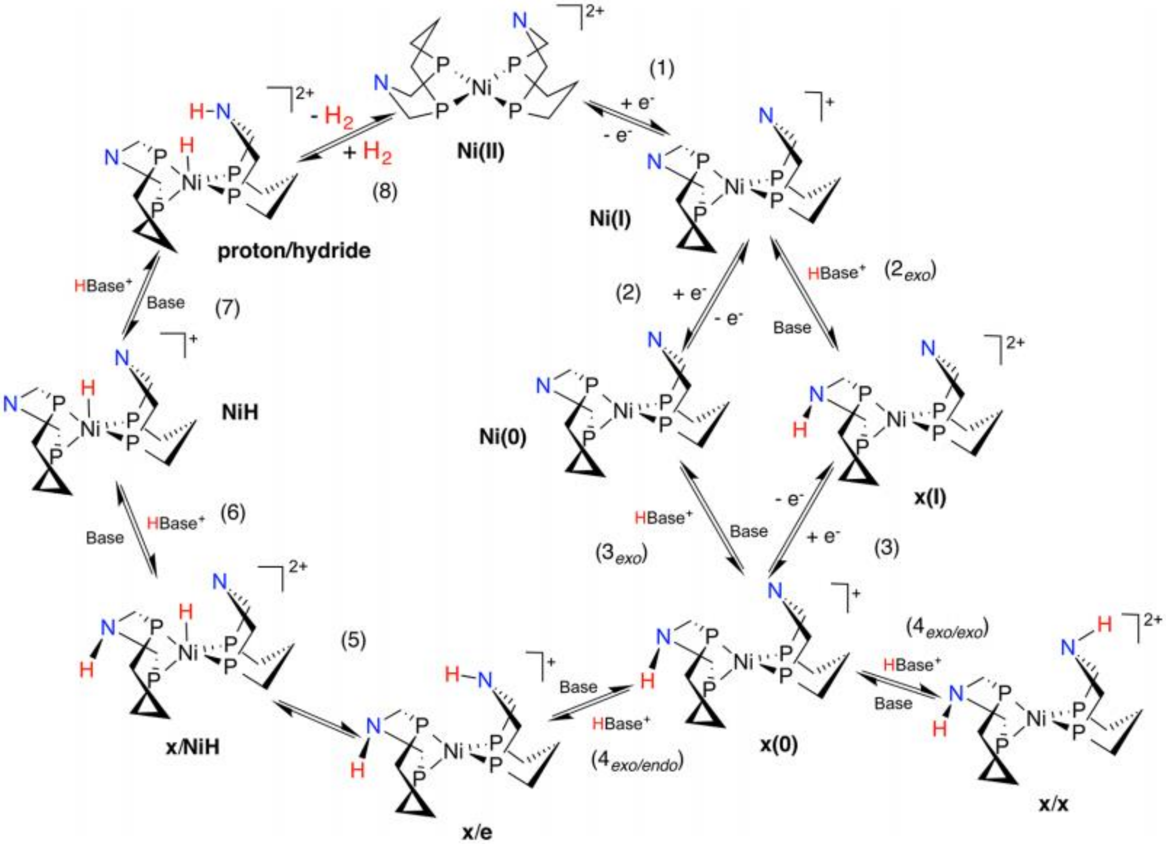

Figure 1.16. Proposed catalytic cycle for $Ni(8P_2^RN^{R'})_2$ with aryl substituents omitted for clarity.

1.7 Design Considerations for [NiFe]-Model Complexes

In contrast to [NiFe]-models, model complexes of the [FeFe]-H_2ase mimic the H-cluster sufficiently to allow reconstitution of the apo-protein.[38] Structural [NiFe]-models are less advanced. Structural models for the [NiFe]-H_2ase must ideally simulate the strong donor cyanide and the tetrathiolate motif at nickel. Incorporation of the tetrathiolate motif has been particularly challenging due to high tendency of thiolates to bridge multiple centers; many syntheses produce multi-metallic cluster byproducts (Figure 1.17).[57] The syntheses of heterometallic complexes often have the additional disadvantage of producing homometallic products (e.g., [FeFe] and [NiNi]), decreasing the yields of the desired heterobimetallic product.

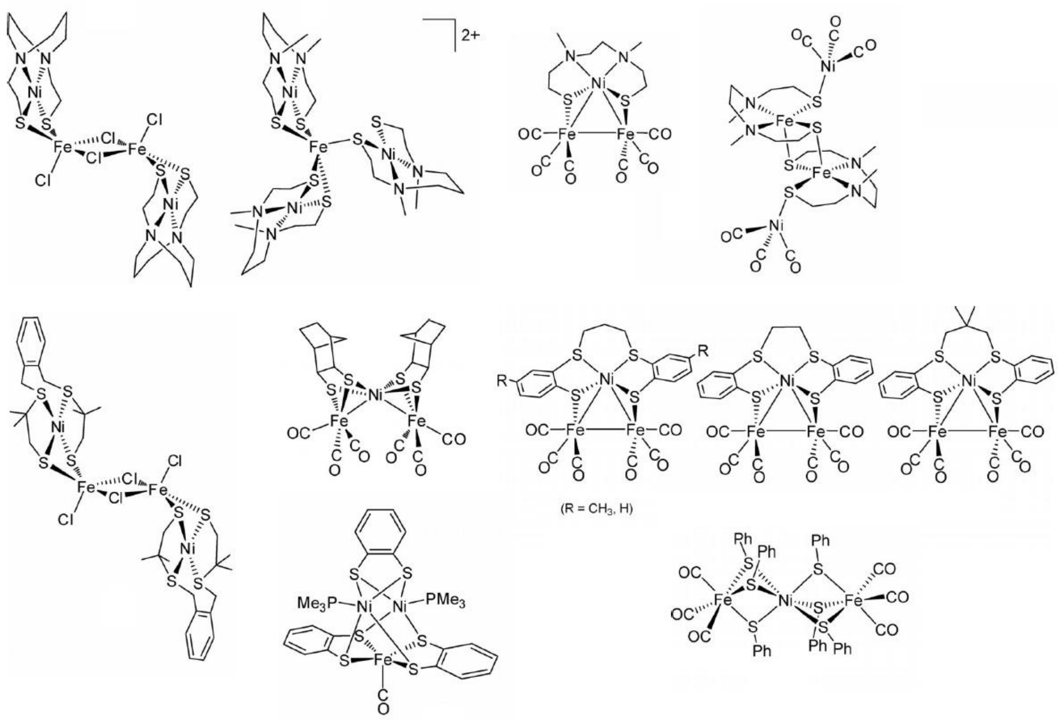

Figure 1.17. Examples of unintended multinuclear NiFe complexes bridged by thiolate ligands.

Incorporating cyanide ligands into both [FeFe]- and [NiFe]-model systems is also challenging. This difficulty arises from the tendency of cyanide to serve as a bridging ligand to other metal centers in an M-CN-M fashion and as a base in acid-base reactions.[58] A rare example of cyanide containing [NiFe] model complexes that is stable towards acid-base chemistry was recently synthesized by Rauchfuss and coworkers. The basicity of the nitrogen lone-pair was quenched by the formation of adducts with Lewis acidic boranes (Scheme 1.3).[48]

Scheme 1.3. Acid-base Stable Cyanide Containing [NiFe]-H_2ase Model Complex

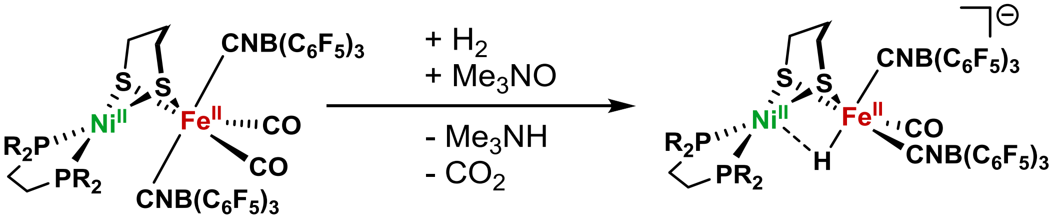

Some model systems use phosphines as a cyanide surrogate. This substitution is in part due to the synthetic limitations and added difficulty associated with metal-cyano complexes. Phosphine ligands are generally neutral donors, in contrast to the anionic cyanide ligand, but the basicities of these two species is comparable as assayed by infrared spectroscopy;

$M(CO)_nCN$ and $M(CO)L$ complexes have similar v_{CO} values.[59] Despite the similar basicities, the charge difference has a significant effect on the acid-base- and electro-chemistry. In the general case, the protonation of a neutral or anionic species is more facile than the protonation of cationic species. Similarly, the oxidation of neutral or anionic species tends to occur at more negative potentials than the oxidation of a cation. These effects implicate that ligand charge has drastic implications for electrocatalytic efficiency.

1.8 Synthesis of [NiFe]-H_2ase Model Complexes

The synthetic strategies of [NiFe]-model complexes can be put into one of two categories: a nickel(thiolate) nucleophile attacks an iron center (eq. 6, 7) or an iron(thiolate) attacks a nickel center (eq. 8, 9). The specific route chosen depends largely on the stability of the desired precursors. For example, stable $(CO)_4Fe(SR)_2$ complexes are not known; therefore if a complex with only carbonyl and thiolate ligands at iron is desired, the nickel(thiolate) route would likely need to be pursued. This section will discuss simple, mononuclear precursors, though in some syntheses, multinuclear precursors were used.[57]

$$L_2Ni(SR)_2 + FeX_2L'_4 \longrightarrow \begin{matrix} [L_2Ni(\mu\text{-}SR)_2FeL'_4]X_2 \\ [L_2Ni(\mu\text{-}SR)_2FeXL'_3]X \\ L_2Ni(\mu\text{-}SR)_2FeX_2L' \end{matrix} \tag{6}$$

$$L_2Ni(SR)_2 + FeL'_5 \longrightarrow L_2Ni(\mu\text{-}SR)_2FeL'_3 \tag{7}$$

$$L_4Fe(SR)_2 + NiX_2L'_2 \longrightarrow \begin{matrix} [L'_2Ni(\mu\text{-}SR)_2FeXL'_3]X \\ [L'_2Ni(\mu\text{-}SR)_2FeL'_3]X_2 \end{matrix} \tag{8}$$

$$L_2X_2Fe(SR)_2{}^{2-} + NiX'_2L'_2 \longrightarrow [L'_2Ni(\mu\text{-}SR)_2FeL_2X_2]^{2-} \tag{9}$$

For the iron(thiolate) based approach, various phosphino-iron and cyano-iron carbonyl precursors were prepared. For example, the phosphine derivatives iron(phosphino)(thiolate)(dicarbonyl) ($FeP_2S_2(CO)_2$) were prepared with various phosphines and thiols such as thiophenol, edt, pdt, 1,2-benzenedithiol, PMe_3, $P(OEt)_3$, dppe, dcpe, and others.[60,61] Some of these examples are depicted in Figure 1.18.

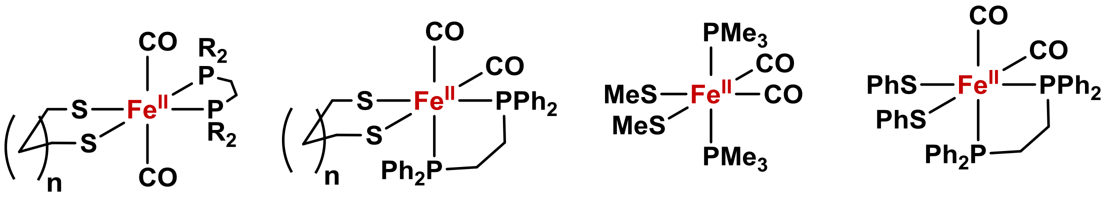

Figure 1.18. Examples ferrous(thiolate)(phosphino)(dicarbonyl) complexes that have been synthesized.

These ferrous $FeP_2S_2(CO)_2$ complexes can adopt a variety of isomers in which the various ligands are either *cis* or *trans*; the thiolate ligands are never observed to be *trans*. The $FeP_2S_2(CO)_2$ compounds are prepared by treating ferrous salts with the appropriate phosphine under an atmosphere of CO, followed by the addition of the deprotonated thiol (Scheme 1.4). The intermediate $FeS_2P_2X_2$ species, where X is a halide, has been isolated and characterized separately; Fe(diphosphine)$(CO)_2X_2$ exists exclusively as the *trans* CO isomer.[62] Yields vary greatly, ranging from less than 10% to 80% depending on the particular ligands.

Scheme 1.4. Synthesis of Ferrous(thiolate)(phosphino)(dicarbonyl) Complexes

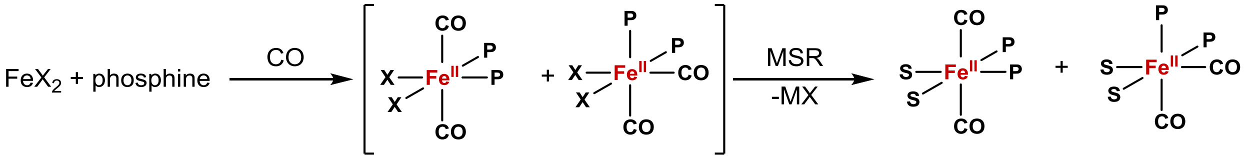

Heterobimetallic complexes are obtained from iron(thiolate) precursors by treatment with the appropriate electrophilic metal source. For nickel, these are typically nickel(diphosphine)dihalides.[63] Halogens can be removed from the resulting NiFe halide compound by reduction (Scheme 1.5).[64]

Scheme 1.5. Synthesis of NiFe Model Systems from Iron Thiolates

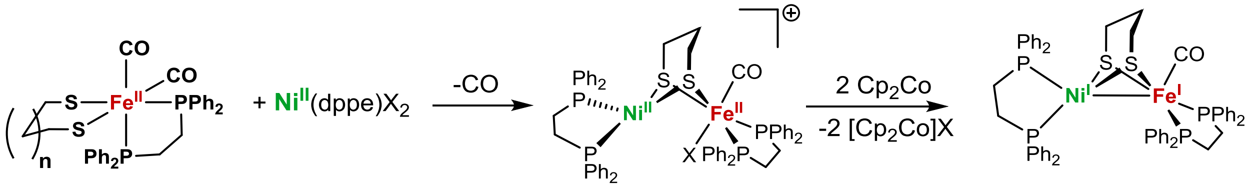

The $FeP_2S_2(CO)_2$ compounds are versatile precursors and have been used to synthesize other heterobimetallic systems such as FeCo, FeMo, and FeMn (Figure 1.19).[61,65] For these complexes, $CpCoI_2CO$, $Mo(CO)_3(MeCN)_3$, and (acenaphthene)$Mn(CO)_3$ served as the electrophilic metal complex.

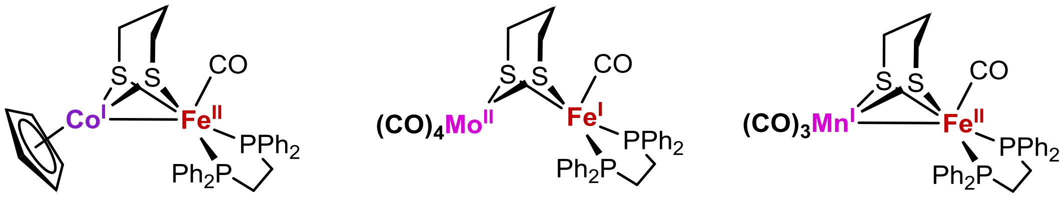

Figure 1.19. FeCo, FeMo, and FeMn complexes derived from Fe(pdt)(dppe)$(CO)_2$.

Ferrous(thiolate) cyanide nucleophiles are generally dianions, and compounds with monothiols and phosphines were synthesized (Figure 1.20).[57] The cyano complexes are prepared in a similar fashion to the phosphine derivatives when the thiol is 1,2-benzenedithiolate (bdt) (Scheme 1.6).[66] The pdt derivative is prepared by a slightly different route in which the tricarbonyl bromide $Fe(CO)_3CN_2Br$ is treated with K_2pdt (Scheme 1.7).[67]

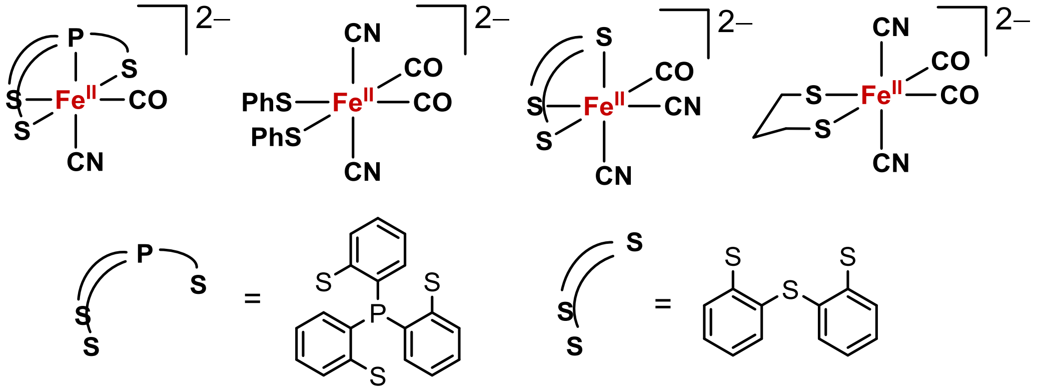

Figure 1.20. Examples of cyanide containing Fe(thiolate) precursors used in the synthesis of [NiFe]-model complexes.

Scheme 1.6. Synthesis of $[Bu_4N]_2[Fe(bdt)(CN)_2(CO)_2]$

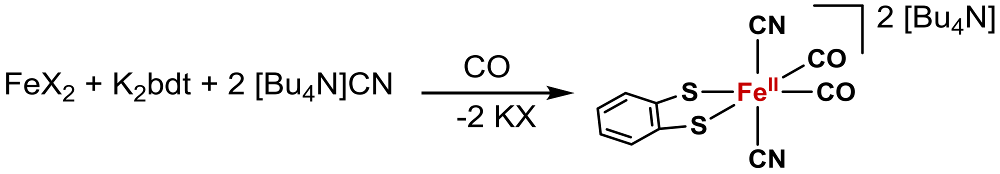

Scheme 1.7. Synthesis of K[Bu_4N][Fe(pdt)$(CN)_2(CO)_2$]

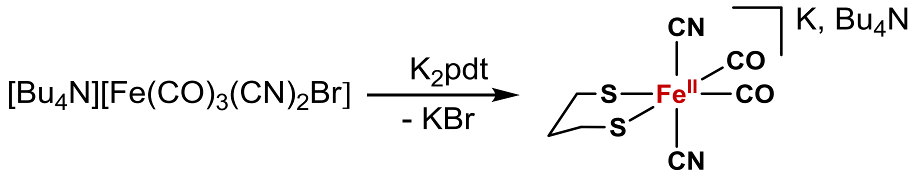

The cyano-iron anions are attached to nickel centers using Ni(dppe)X_2 or the dithiocarbamate complex Ni(PPh_3)Br(S_2CNEt_2) as the electrophilic nickel source (Figure 1.21).

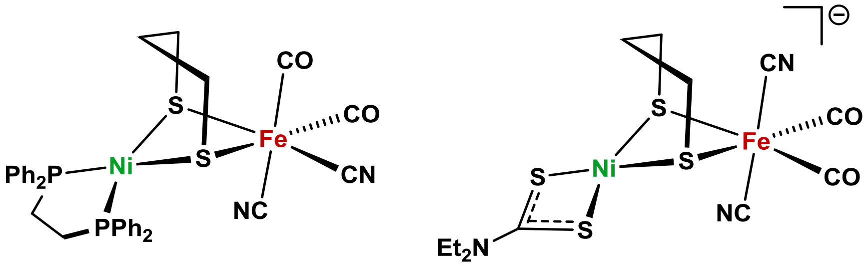

Figure 1.21. Cyanide containing models of [NiFe]-H_2ase derived from iron(thiolate)precursors

The nickel(thiolate) approach is overwhelmingly characterized by chelating phosphines and/or thiols. Many model systems have made use of nickel bearing tetradentate ligands containing thiolates (Figure 1.22). Complexes that are synthesized by this route thus far do not feature cyanide ligands.

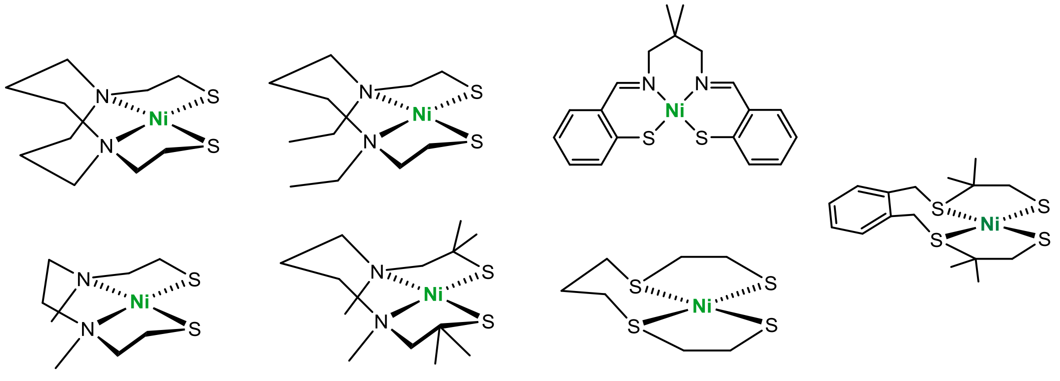

Figure 1.22. Tetradentate amino-thiolate, imino-thiolate, and thioether-thiolate nickel complexes used as precursors to model compounds.

Nickel(diphosphine)(dithiolate) complexes are also used as nucleophilic nickel sources. Numerous diphosphines and dithiolates were used such as dmpe, dppe, dcpe, dppv, pdt, edt, and bdt.[68]

Compared to the nickel electrophiles used in the syntheses of model compounds, the iron electrophiles utilized are quite varied. Both zero-valent and ferrous starting materials are used. Simple ferrous salts, such as halides, have a tendency to form multinuclear complexes and for this reason are generally avoided. The iron carbonyls, $Fe(CO)_5$, $Fe_2(CO)_9$, and $Fe_3(CO)_{12}$, are commonly used to install $(CO)_nFe$ fragments. Another possible iron carbonyl source is iron(bda)$(CO)_3$ (bda = benzylideneacetone). Iron(nitrosyl)-nickel complexes were synthesized using $Fe(CO)_2(NO)_2$ as the electrophilic iron precursor.[69] Cyclopentadienyliron [NiFe]-complexes were synthesized using $CpFe(CO)_2I$.[70] Pentamethylcyclopentadienyl derivatives can be synthesized using *in situ* generated "Cp*FeCl" by treatment of $FeCl_2(THF)_{1.5}$ with LiCp* at −40.[71]

1.9 Concluding Remarks

Mixed-valence metal clusters are present in both [NiFe]- and [FeFe]-H_2ases. Mixed-valence is not unique to hydrogenases, but is a phenomenon present in many metal clusters in biological systems.[72] Examples include iron-sulfur clusters and multi-metallic active sites such as those in laccase or the oxygen evolving complex in photosystem II. Additionally, the catalytic activity of bimetallic complexes has gained some interest.[73] As a result, mixed-valency has become a theme of increasing interest in respect to model complexes.[74,75]

In terms of evaluating model complexes, several factors are important such as: structural resemblance (e.g. the NiS_4 motif in [NiFe]-H_2ase or the azadithiolate cofactor in [FeFe]-H_2ase), the activity of the model complex, catalytic or otherwise, towards H_2 and/or acids, and the spectroscopic resemblance to the active site. Biophysical characterization of the hydrogenases is relatively rich and provides standards of comparison for IR and EPR spectroscopy.

The central theme of this thesis is mixed-valence metal clusters, particularly bimetallic complexes, in the context of the hydrogenases. Chapters 2 and 3 specifically address the syntheses of model complexes with mixed-valence states that are relevant to [NiFe]-H_2ase. Chapters 4 and 5 discuss mixed-valence homobimetallic systems of nickel and cobalt respectively.

1.10 References

(1) Lawrence Livermore National Laboratory; Energy, D. o. 2014.
(2) BP Statistical Review of World Energy June 2015. [Online Early Access]. Published Online: 2015. http://www.bp.com/content/dam/bp/pdf/energy-economics/statistical-review-2015/bp-statistical-review-of-world-energy-2015-full-report.pdf.
(3) Wigley, T. M. L.; Richels, R.; Edmonds, J. A. *Nature* **1996**, *379*, 240.
(4) Hoffert, M. I.; Caldeira, K.; Jain, A. K.; Haites, E. F.; Harvey, L. D. D.; Potter, S. D.; Schlesinger, M. E.; Schneider, S. H.; Watts, R. G.; Wigley, T. M. L.; Wuebbles, D. J. *Nature* **1998**, *395*, 881.
(5) Kaplan, S. *Renewable Energy*, U.S. Energy Information Administration, 2015.
(6) Bellman, D. *Electrical Generation Efficiency*, 2007.
(7) Cook, T. R.; Dogutan, D. K.; Reece, S. Y.; Surendranath, Y.; Teets, T. S.; Nocera, D. G. *Chem. Rev.* **2010**, *110*, 6474.
(8) Palacin, M. R. *Chem. Soc. Rev.* **2009**, *38*, 2565.
(9) Press, R. J.; Santhanam, K. S. V.; Miri, M. J.; Bailey, A. V.; G.A., T. *Introduction to Hydrogen Technology*; John Wiley and Sons Inc.: Hoboken, NJ, 2009.
(10) Debe, M. K. *Nature* **2012**, *486*, 43.
(11) Eberle, D. U.; von Helmolt, D. R. *Energy & Environmental Science* **2010**, *3*, 689.
(12) Jena, P. *The Journal of Physical Chemistry Letters* **2011**, *2*, 206.
(13) Suh, M. P.; Park, H. J.; Prasad, T. K.; Lim, D.-W. *Chem. Rev.* **2012**, *112*, 782.
(14) Orimo, S.-i.; Nakamori, Y.; Eliseo, J. R.; Züttel, A.; Jensen, C. M. *Chem. Rev.* **2007**, *107*, 4111.
(15) DeLong, E. F. *Science* **2007**, *317*, 327.
(16) Wu, L.-F.; Mandrand, M. A. *FEMS Microbiology Reviews* **1993**, *10*, 243.
(17) Vignais, P. M.; Billoud, B.; Meyer, J. *FEMS Microbiology Reviews* **2001**, *25*, 455.
(18) Lubitz, W.; Ogata, H.; Rüdiger, O.; Reijerse, E. *Chem. Rev.* **2014**, *114*, 4081.
(19) Thauer, R. K.; Kaster, A. K.; Goenrich, M.; Schick, M.; Hiromoto, T.; Shima, S. In *Annual Review of Biochemistry, Vol 79*; Kornberg, R. D., Raetz, C. R. H., Rothman, J. E., Thorner, J. W., Eds.; Annual Reviews: Palo Alto, 2010; Vol. 79, p 507.
(20) Ogata, H.; Kellers, P.; Lubitz, W. *J. Mol. Biol.* **2010**, *402*, 428.
(21) Wulff, P.; Day, C. C.; Sargent, F.; Armstrong, F. A. *Proceedings of the National Academy of Sciences* **2014**, *111*, 6606.
(22) Hexter, S. V.; Chung, M.-W.; Vincent, K. A.; Armstrong, F. A. *J. Am. Chem. Soc.* **2014**, *136*, 10470.
(23) Cracknell, J. A.; Vincent, K. A.; Armstrong, F. A. *Chem. Rev.* **2008**, *108*, 2439.
(24) Kampa, M.; Pandelia, M.-E.; Lubitz, W.; van Gastel, M.; Neese, F. *J. Am. Chem. Soc.* **2013**, *135*, 3915.
(25) Roessler, M. M.; Evans, R. M.; Davies, R. A.; Harmer, J.; Armstrong, F. A. *J. Am. Chem. Soc.* **2012**, *134*, 15581.
(26) Murphy, B. J.; Hidalgo, R.; Roessler, M. M.; Evans, R. M.; Ash, P. A.; Myers, W. K.; Vincent, K. A.; Armstrong, F. A. *J. Am. Chem. Soc.* **2015**, *137*, 8484.
(27) Ogata, H.; Nishikawa, K.; Lubitz, W. *Nature* **2015**, *520*, 571.
(28) Schilter, D. *Chembiochem* **2015**, *16*, 1712.
(29) Armstrong, F. A., The Chemical Principles of Biohydrogen.
(30) Pandelia, M.-E.; Ogata, H.; Currell, L. J.; Flores, M.; Lubitz, W. *Biochimica et Biophysica Acta (BBA) - Bioenergetics* **2010**, *1797*, 304.
(31) Hodson, B. E.; McGrath, T. D.; Stone, F. G. A. *Inorg. Chem.* **2004**, *43*, 3090.
(32) Carroll, M. E.; Barton, B. E.; Rauchfuss, T. B.; Carroll, P. J. *J. Am. Chem. Soc.* **2012**, *134*, 18843.

(33) Huynh, M. T.; Wang, W.; Rauchfuss, T. B.; Hammes-Schiffer, S. *Inorg. Chem.* **2014**, *53*, 10301.
(34) Song, L.-C.; Yang, Z.-Y.; Bian, H.-Z.; Hu, Q.-M. *Organometallics* **2004**, *23*, 3082.
(35) Schmidt, M.; Contakes, S. M.; Rauchfuss, T. B. *J. Am. Chem. Soc.* **1999**, *121*, 9736.
(36) Li, H.; Rauchfuss, T. B. *J. Am. Chem. Soc.* **2002**, *124*, 726.
(37) Esselborn, J.; Lambertz, C.; Adamska-Venkatesh, A.; Simmons, T.; Berggren, G.; Noth, J.; Siebel, J.; Hemschemeier, A.; Artero, V.; Reijerse, E.; Fontecave, M.; Lubitz, W.; Happe, T. *Nat Chem Biol* **2013**, *9*, 607.
(38) Berggren, G.; Adamska, A.; Lambertz, C.; Simmons, T. R.; Esselborn, J.; Atta, M.; Gambarelli, S.; Mouesca, J. M.; Reijerse, E.; Lubitz, W.; Happe, T.; Artero, V.; Fontecave, M. *Nature* **2013**, *499*, 66.
(39) Tremel, W.; Kriege, M.; Krebs, B.; Henkel, G. *Inorg. Chem.* **1988**, *27*, 3886.
(40) Fox, S.; Wang, Y.; Silver, A.; Millar, M. *J. Am. Chem. Soc.* **1990**, *112*, 3218.
(41) Snyder, B.; Rao, C.; Holm, R. *Australian Journal of Chemistry* **1986**, *39*, 963.
(42) Baker-Hawkes, M. J.; Billig, E.; Gray, H. B. *J. Am. Chem. Soc.* **1966**, *88*, 4870.
(43) Canaguier, S.; Field, M.; Oudart, Y.; Pecaut, J.; Fontecave, M.; Artero, V. *Chem. Commun.* **2010**, *46*, 5876.
(44) Ogo, S.; Ichikawa, K.; Kishima, T.; Matsumoto, T.; Nakai, H.; Kusaka, K.; Ohhara, T. *Science* **2013**, *339*, 682.
(45) Fontecave *Inorg. Chem.* **2006**, *45*, 4334.
(46) Canaguier, S.; Fontecave, M.; Artero, V. *Eur. J. Inorg. Chem.* **2011**, 1094.
(47) Matsumoto, T.; Ando, T.; Mori, Y.; Yatabe, T.; Nakai, H.; Ogo, S. *J. Organomet. Chem.* **2015**, *796*, 73.
(48) Manor, B. C.; Rauchfuss, T. B. *J. Am. Chem. Soc.* **2013**, *135*, 11895.
(49) Kim, K.; Kishima, T.; Matsumoto, T.; Nakai, H.; Ogo, S. *Organometallics* **2012**, *32*, 79.
(50) Kramarz, K. W.; Norton, J. R. In *Progress in Inorganic Chemistry*; John Wiley & Sons, Inc.: 2007, p 1.
(51) Oehler, S.; Müller-Hill, B. *J. Mol. Biol.* **2010**, *395*, 242.
(52) Berning, D. E.; Noll, B. C.; DuBois, D. L. *J. Am. Chem. Soc.* **1999**, *121*, 11432.
(53) Curtis, C. J.; Miedaner, A.; Ellis, W. W.; DuBois, D. L. *J. Am. Chem. Soc.* **2002**, *124*, 1918.
(54) Curtis, C. J.; Miedaner, A.; Ciancanelli, R.; Ellis, W. W.; Noll, B. C.; DuBois, M. R.; DuBois, D. L. *Inorg. Chem.* **2003**, *42*, 216.
(55) Kilgore, U. J.; Roberts, J. A. S.; Pool, D. H.; Appel, A. M.; Stewart, M. P.; DuBois, M. R.; Dougherty, W. G.; Kassel, W. S.; Bullock, R. M.; DuBois, D. L. *J. Am. Chem. Soc.* **2011**, *133*, 5861.
(56) Wiese, S.; Kilgore, U. J.; Ho, M.-H.; Raugei, S.; DuBois, D. L.; Bullock, R. M.; Helm, M. L. *ACS Catalysis* **2013**, *3*, 2527.
(57) Ohki, Y.; Tatsumi, K. *Eur. J. Inorg. Chem.* **2011**, 973.
(58) Schmidt, M. A.; Contakes, S. M.; Rauchfuss, T. B. *Abstr. Pap. Am. Chem. Soc.* **1999**, *218*, U774.
(59) van der Vlugt, J. I.; Rauchfuss, T. B.; Wilson, S. R. *Chem. Eur. J.* **2006**, *12*, 90.
(60) Takács, J.; Markó, L.; Párkányi, L. *J. Organomet. Chem.* **1989**, *361*, 109.
(61) Carroll, M. E.; Chen, J. Z.; Gray, D. E.; Lansing, J. C.; Rauchfuss, T. B.; Schilter, D.; Volkers, P. I.; Wilson, S. R. *Organometallics* **2014**, *33*, 858.
(62) Zhang, Z.-Z.; Zhang, J.-K.; Zhang, W.-D.; Xi, H.-P.; Cheng, H.; Wang, H.-G. *J. Organomet. Chem.* **1996**, *515*, 1.
(63) Barton, B. E.; Whaley, C. M.; Rauchfuss, T. B.; Gray, D. L. *J. Am. Chem. Soc.* **2009**, *131*, 6942.
(64) Ulloa, O., University of Illinois, Urbana-Champaign, 2015.

(65) Bouchard, S.; Clémancey, M.; Blondin, G.; Bruschi, M.; Charreteur, K.; De Gioia, L.; Le Roy, C.; Pétillon, F. Y.; Schollhammer, P.; Talarmin, J. *Inorg. Chem.* **2014**, *53*, 11345.

(66) Rauchfuss, T. B.; Contakes, S. M.; Hsu, S. C. N.; Reynolds, M. A.; Wilson, S. R. *J. Am. Chem. Soc.* **2001**, *123*, 6933.

(67) Liaw, W.-F.; Lee, J.-H.; Gau, H.-B.; Chen, C.-H.; Jung, S.-J.; Hung, C.-H.; Chen, W.-Y.; Hu, C.-H.; Lee, G.-H. *J. Am. Chem. Soc.* **2002**, *124*, 1680.

(68) Carroll, M. E.; Barton, B. E.; Gray, D. L.; Mack, A. E.; Rauchfuss, T. B. *Inorg. Chem.* **2011**, *50*, 9554.

(69) Liaw, W.-F.; Chiang, C.-Y.; Lee, G.-H.; Peng, S.-M.; Lai, C.-H.; Darensbourg, M. Y. *Inorg. Chem.* **2000**, *39*, 480.

(70) Zhu, W. F.; Marr, A. C.; Wang, Q.; Neese, F.; Spencer, D. J. E.; Blake, A. J.; Cooke, P. A.; Wilson, C.; Schroder, M. *Proc. Natl. Acad. Sci. U. S. A.* **2005**, *102*, 18280.

(71) Weber, K.; Erdem, Ö. F.; Bill, E.; Weyhermüller, T.; Lubitz, W. *Inorg. Chem.* **2014**, *53*, 6329.

(72) Wieghardt, K. *Mixed-Valence Systems: Applications in Chemistry, Physics, and Biology* Amsterdam, 1990.

(73) Cooper, B. G.; Napoline, J. W.; Thomas, C. M. *Catalysis Reviews* **2012**, *54*, 1.

(74) Wang, W.; Nilges, M. J.; Rauchfuss, T. B.; Stein, M. *J. Am. Chem. Soc.* **2013**, *135*, 3633.

(75) Schilter, D.; Nilges, M. J.; Chakrabarti, M.; Lindahl, P. A.; Rauchfuss, T. B.; Stein, M. *Inorg. Chem.* **2012**, *51*, 2338−2348.

Chapter 2:

Bimetallic NiRu models of [NiFe]-H_2ase in the Ni-L and Ni-R States†

2.1 Introduction: [NiFe]-H_2ase and the Schroeder Complex

Of the three hydrogenases, the [NiFe] enzyme has been the subject of particularly intense study since it was the first to be crystallographically characterized. Although there are numerous reports on structural models of this enzyme, mimicking the oxidation states, specifically the mixed-valence states, is difficult. The active site of [NiFe]-H_2ase, as described in chapter 1, features biologically unusual carbon monoxide and cyanide ligands (Figure 2.1, left).

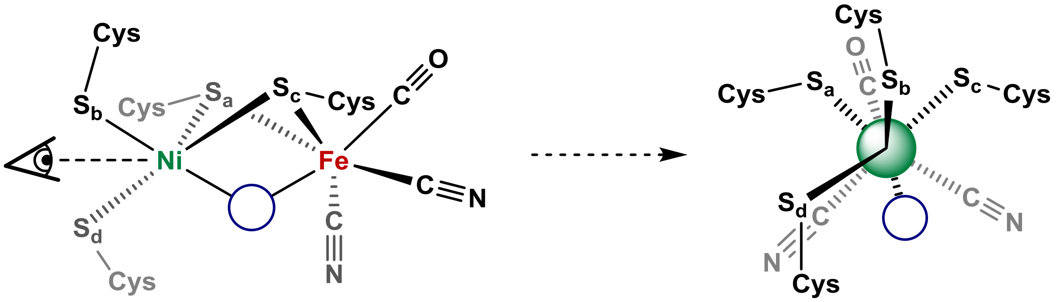

Figure 2.1. (left) The active site of [NiFe]-H_2ase. The blue circle indicates an additional binding site that bridges the two metals. (right) A Newmann projection of the active site looking at nickel down the Ni-Fe vector.

The iron site in [NiFe]-H_2ase is approximately octahedral while the nickel site is rather distorted and can be described as having a see-saw geometry (Figure 2.1, right). The iron center is redox inactive and remains low-spin iron(II) in all known states. The nickel shuttles between the first, second, and third oxidation states (Table 2.1). Organometallic complexes of nickel can differ quite drastically in coordination geometry depending on the oxidation state (e.g. four-coordinate tetrahedral Ni(I) vs four-coordinate square-planar Ni(II). Without a rigid framework, large reorganization energies would be required to shuttle between these oxidation states, but the protein scaffold enforces the geometry of the metal centers to be relatively invariant.[1] An ongoing challenge for [NiFe]-H_2ase modelling is limiting the geometric infidelity during redox processes, a problem addressed in chapter 3.

---

†Portions of this chapter are reproduced from the following publications with permission from the authors: Chambers, G. M.; Angamuthu, R.; Gray, D. L.; Rauchfuss, T. B. *Organometallics* **2013**, *32*, 6324. Chambers, G. M.; Mitra, J.; Rauchfuss, T. B.; Stein, M. *Inorg. Chem.* **2014**, *53*, 4243

Table 2.1. The of States [NiFe]-H_2ase

State	Ni Oxidation State	Bridging Site	Note
Ni-SI_r	II	water	
Ni-SI_a	II	vacant	
Ni-L	I	metal-metal bond	light induced
Ni-C	III	hydride	
Ni-R	II	hydride	S-protonated cysteinyl
Ni-SCO	II	carbon monoxide	Ni bound CO, inactive
Ni-B	III	OH^-	inactive
Ni-A	III	O_2H^-	inactive

Model complexes of [NiFe]-H_2ase have been shown to be redox and acid-base competent to some degree.[2] A particularly notable system is the NiFe complex (dppe)Ni(pdt)Fe$(CO)_3$ (**R1**) first reported by Schroeder et. al.[3] Rauchfuss and coworkers demonstrated that this Ni(I)Fe(I) system reacts with acids, forming stable bridging hydride complexes and the compound was shown to be a competent proton reduction catalyst.[4-6] The bridging hydride cation $[(dppe)Ni(\mu\text{-}H)(pdt)Fe(CO)_3]^+$ ([**R1**H]$^+$) (Scheme 2.1) was the first example of a model akin to the Ni-R state of [NiFe]-H_2ase, an intermediate in the proposed catalytic cycle.

Scheme 2.1. Chemistry of the Schroeder Complex **R1**

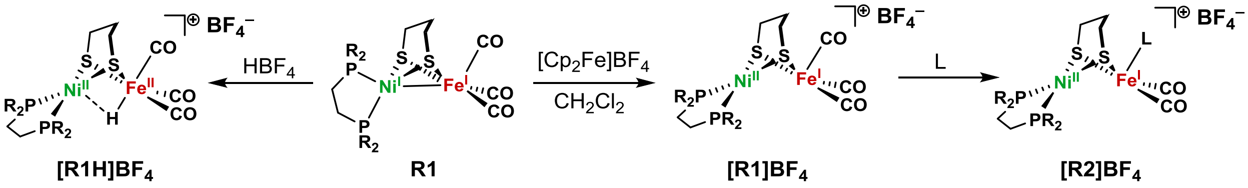

The Schroeder system is the first, and one of the few, model systems with stable, well-characterized mixed-valence states. Because of this, comparisons to the **R1** system are made throughout chapters 2 and 3. One-electron oxidation of the **R1** system forms mixed-valence Ni(II)Fe(I) complexes, the first example of a mixed-valence NiFe model.[7] However, the oxidation states of the metal centers in this cation are the reverse of the Ni(I)Fe(II) state observed for Ni-L. One rationalization for the observed oxidation at the nickel center rather iron in **R1** is the lack of strong donor ligands at iron to stabilize the divalent state, such as the cyanides in the protein. Substitution of a carbonyl ligand with various monophosphines proved ineffective towards biasing the cation to a ferrous state.[8] The principal challenge addressed in this chapter is stabilization of a Ni(I) mixed-valence species in the (diphosphine)nickel system, to generate the first well-characterized model complex of Ni-L with identical oxidation states observed in the enzyme.

2.2. Precedence for Ruthenium based Model Complexes

Bimetallic model systems of the [NiFe]-H_2ase using the second row metal ruthenium in place of iron have attracted attention in parallel with work on NiFe-based models.[9] These dithiolato complexes invariably feature Ru(II)-S_2Ni(II) cores with nickel centers bound by planar tetradentate bis(thioether)-dithiolate or diaminodithiolate ligands (Figure 2.2). Stable NiRu dithiolate complexes with oxidation states lower than II have not been characterized, and, interestingly, have been depicted to be square planar.[10]

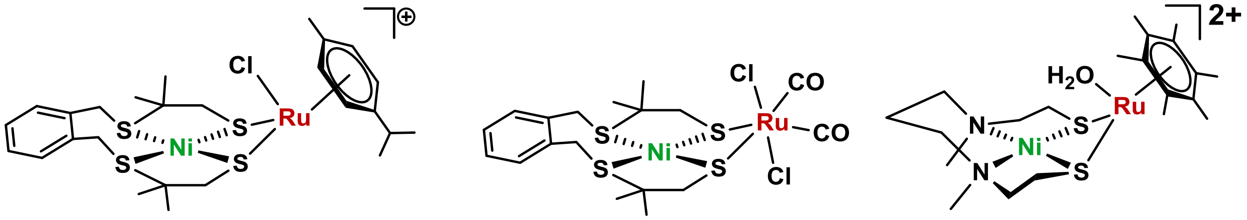

Figure 2.2. NiRu model complexes features a tetradendate S_4 or N_2S_2 ligand at nickel.

Although ruthenium-based models use a non-biomimetic metal, this substitution has been particularly fruitful in enabling H_2 activation, a capability that is rare amongst NiFe-based models, most notably in the dication [**R2**]$^{2+}$ (Scheme 2.2).[11] This Ni(II)Ru(II) system features a ruthenium-bound water, akin to the Ni-SI_r state of the NiFe active site. The water soluble dication [**R2**]$^{2+}$ reacts with hydrogen to afford the bridging hydride product [**R2**H]$^{+}$, which possesses an octahedral Ni(II) center with a nickel-bound water. The location of the hydride in the paramagnetic cation [**R2**H]$^{+}$ was determined using neutron diffraction. In addition to H_2 activation, the dication [**R2**]$^{2+}$ binds CO, forming the adduct [**R2**CO]$^{2+}$.[12] The carbon monoxide ligand binds at the ruthenium center in this model, whereas nickel is the CO binding metal center in the CO inhibited state of [NiFe]-H_2ase.

Scheme 2.2. (S_2N_2)NiRu(hmb) Model System and Reactivity

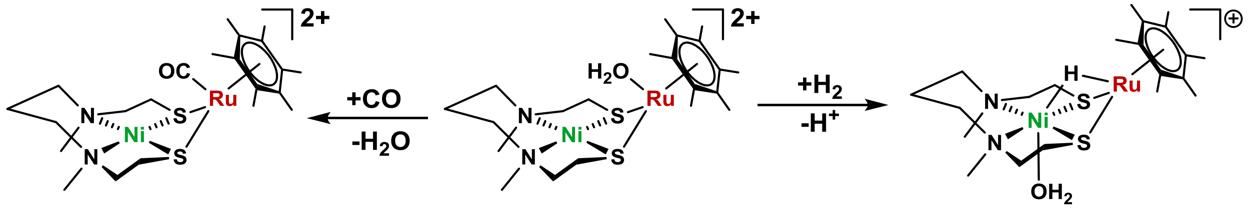

[**R2**CO]$^{2+}$ [**R2**]$^{2+}$ [**R2**H]$^{+}$

Ruthenium-based models have also been shown to form stable dioxygen adducts, which are not known for the first row congeners (Figure 2.3).[13,14] The pentamethylcyclopentadienyl analogue [**R3**]$^+$ also models the oxygen tolerant behavior of [NiFe]-H_2ase via reduction of bound oxygen to water, regenerating the starting aquo-complex.

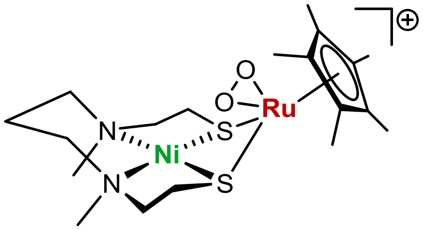

[**R3**]$^+$

Figure 2.3. Stable NiRu O_2-adduct [**R3**]$^+$.

This work primarily focuses on the ruthenium analogue of the Schroder complex **R1**. As mentioned in the previous section, oxidation of this complex yields an Fe(I)Ni(II) core. The main hypothesis tested in this chapter is that changing from [$(CO)_2$LFe(μ-pdt)Ni(dppe)]$^+$ to [(arene)Ru(μ-pdt)Ni(dppe)]$^+$ would relocalize the SOMO from Fe/Ru to Ni to generate the first stable model of the Ni-L state of [NiFe]-H_2ase.

2.3 Synthesis and Characterization of [(arene)Ru(Cl)(pdt)Ni(dxpe)]Cl

Solutions of Ni(pdt)(dppe) and [(*p*-cymene)$RuCl]_2$ in dichloromethane react to afford the salt [(cymene)Ru(Cl)(pdt)Ni(dppe)]Cl ([**1**Cl]Cl), which was purified by column chromatography (Scheme 2.3). This red, diamagnetic compound was shown to be C_s-symmetric according to ^1H and ^{31}P-NMR spectroscopy (see supporting information section). Other derivatives with 1,2-bis(dicyclohexylphosphino)ethane ([**2**Cl]Cl) and hexamethylbenzene ([**3**Cl]Cl) were also prepared from the appropriate precursors.

Scheme 2.3. Synthesis of NiRu Model Complexes.

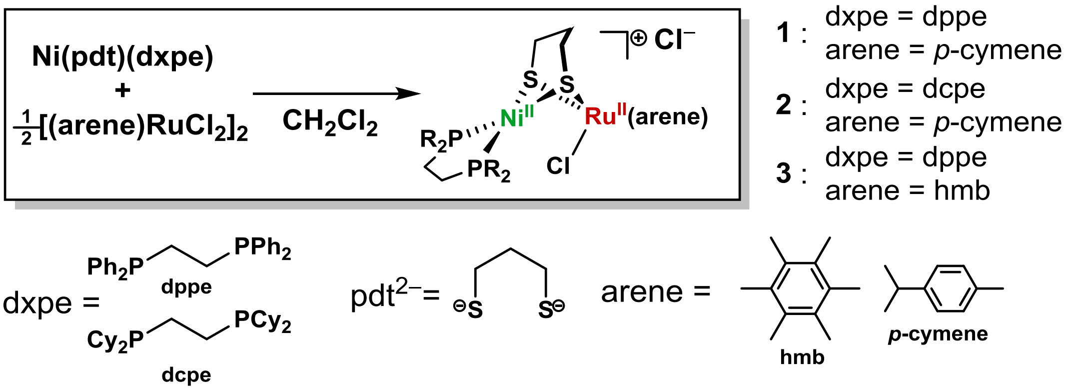

Crystallographic analysis of [**1**Cl]Cl revealed a distorted octahedral geometry at the Ru center, viewing cymene as a tridentate ligand. The Ni center remains square planar. The Ru−Cl distance is 2.426(3) Å, whereas the Ni−Cl distance is 2.818(5) Å, demonstrating the weak Lewis acidity of the square planar Ni(II) center (Figure 2.4).

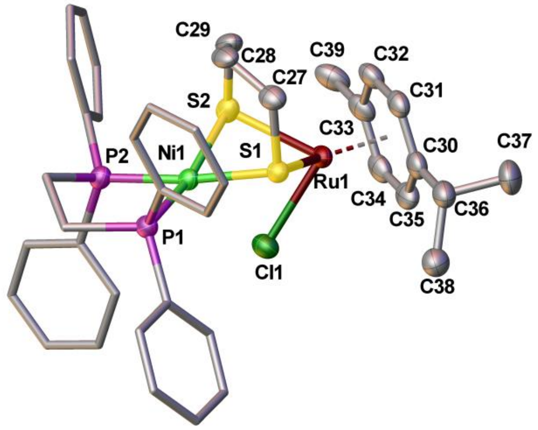

Figure 2.4. Structure of the non-hydrogen atoms of the cation [(arene)RuCl(pdt)Ni(diphos)]$^+$. Selected distances (Å) and angles (deg): Ru−Ni, 3.231(6); Ru−(cent), 1.687(6); Ru−Cl, 2.246(8); Ru−C$_{av}$, 2.184(6); Ru−S$_{av}$, 2.373(9); S1−Ru−S2, 77.5(1); Ni−S$_{av}$, 2.248(1); S1−Ni−S2, 82.6(1); Ni−Pav, 2.170(1); P1−Ni−P2, 86.12(1); Ni−Cl, 2.818(8).

Cyclic voltammetry of [**1**Cl]Cl in CH_2Cl_2 exhibited an event near −1.6 V (Figure 2.5). This couple is assigned to the 2e$^-$ conversion of [**1**Cl]Cl to **1**. The peak potential for the reduction (E_{pc}) is scan-rate dependent but remained irreversible over the range 1000 to 20 mV/s. The irreversible reduction is coupled to the appearance of a quasi-reversible 1e$^-$ event at −900 mV, assigned to the [**1**]$^{0/+}$ couple. The reversibility of this −900 mV event increases at higher scan rate, with i_{pa}/i_{pc} varying from 1.9 at 1000 mVs^{-1} to 3.5 at 250 mVs^{-1}. The scan rate-dependence of the reversibility is attributed to the effects of the competitive binding of chloride to electrogenerated [**1**]$^+$.

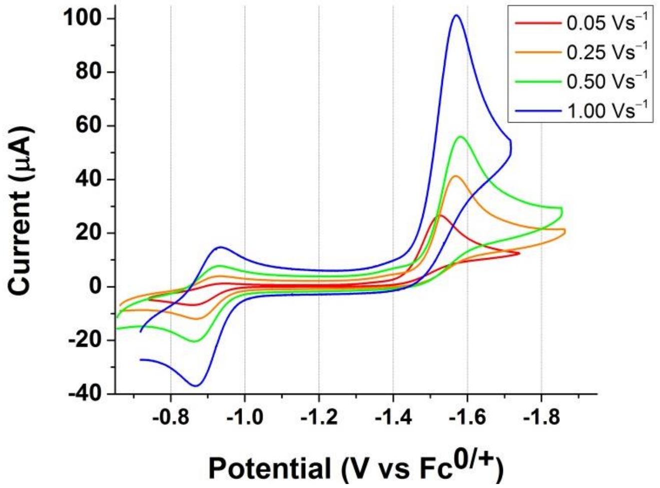

Figure 2.5. Cyclic voltammogram of [**1**Cl]Cl in CH_2Cl_2 at varying scan rates.

2.4 Reduced Model Complex

Zinc powder and zinc amalgam were used in initial attempts to reduce the dichloride complex, but conversions were poor, reaction times were long, reproducibility was poor, and multiple products were observed. An alternative, homogenous reductant, cobaltocene ($E_{½}$ = −1.33 V)[15], proved to be effective. Red solutions of [**1**Cl]Cl instantaneously became brown when treated with cobaltocene, followed by slow precipitation of yellow $[Cp_2Co]Cl$ over the course of minutes. After filtering, evaporation and recrystallization from CH_2Cl_2/pentane, the reduced, neutral complex **1** was obtained as black crystals in high yield (Scheme 2.4). The reduced complexes **2** and **3** were produced in a similar fashion.

Scheme 2.4. Reduction of NiRu Complex with Cobaltocene

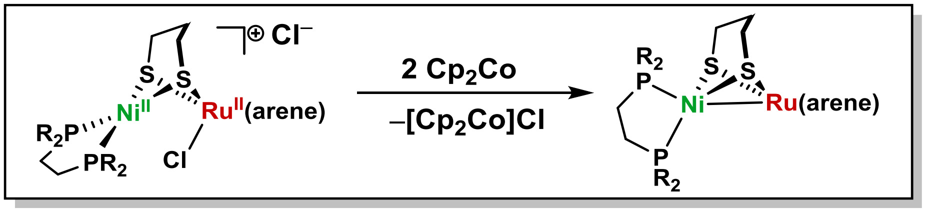

The reduced complex **1** was characterized crystallographically and notably features a tetrahedral nickel center with a short Ni-Ru contact of 2.5539(5) Å, indicative of metal-metal bonding (Figure 2.6). The angle between the NiP_2 and NiS_2 planes is 91.3° compared to the nearly coplanar arrangement in [**1**Cl]Cl. The reduced dcpe complex **2** was also crystallographically characterized and was structurally similar to **1**; the relevant distances and angles can be found in the supporting information section.

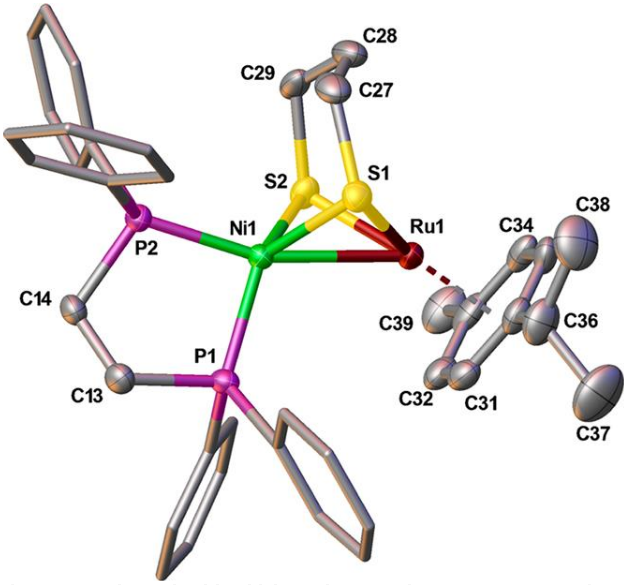

Figure 2.6. Structure of (cymene)Ru(pdt)Ni(dppe). Hydrogen atoms have been omitted for clarity. Selected distances (Å) and angles (deg): Ru−Ni, 2.5539(5); Ru−(cent), 1.710(5); Ru−C_{av}, 2.203(4); Ru−S_{av}, 2.333(7); S1−Ru−S2, 86.9(1); Ni−S_{av}, 2.342(8); S1−Ni−S2, 91.3(1); Ni−P2, 2.147(8); Ni−P1, 2.154(9); P1−Ni−P2 90.0(1).

The reduced complex **1** exhibits a reversible one electron oxidation at −1.015 V vs $Fc^{0/+}$ (Figure 2.7) assigned to the $\mathbf{1}^{0/+}$ couple and a quasi-reversible oxidation at −0.368 V assigned to the $\mathbf{1}^{+/2+}$ couple. The dcpe derivative **2** has similar features with the $\mathbf{2}^{0/+}$ couple shifted more negative relative to the $\mathbf{1}^{0/+}$ couple and is observed at −1.233 V. The $\mathbf{2}^{+/2+}$ couple is similarly shifted and is observed at −0.422 V. Both couples are affected by substitution of dcpe for dppe at nickel, suggesting that both couples are nickel centered. This would implicate that **1** and **2** are two-electron mixed valence compounds with a formal oxidation state of Ni(0)Ru(II). This assignment is further supported in later sections.

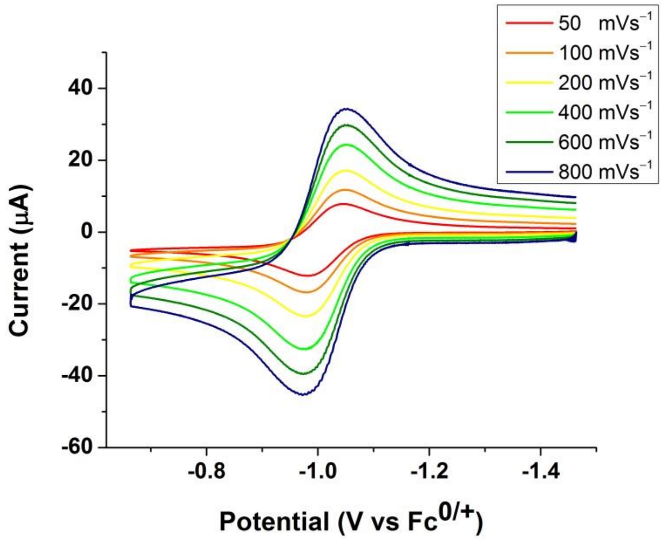

Figure 2.7. Cyclic voltammogram of **1** at various scan rates showing the reversibility of the **1**$^{0/+}$ couple. Conditions: ~1 mM in CH_2Cl_2, 100 mM $[NBu_4]PF_6$, glassy carbon electrode (d = 3 mm); Ag wire as pseudoreference with internal Fc standard at 0 V; Pt counter electrode.

2.5 Dynamic Isomerization Due to Ring Flipping of the Dithiolate Bridge ("Flippamers")

The NMR spectroscopy provided additional insights into the structure and dynamics of **1** and **2**. At room temperature, the ^{31}P NMR spectra of **1**-**3** consist of a distinct downfield doublet resonance and broad upfield resonance, suggesting the presence of dynamic behavior. Raising the temperature to 55°C, the broad resonance sharpens to the expected complimentary doublet. These two distinct doublet resonances indicate that the phosphorus centers are non-equivalent and do not rotate about the nickel center (Figure 2.8, right), a process that has been observed in the related Schroeder complex **R1**.[6]

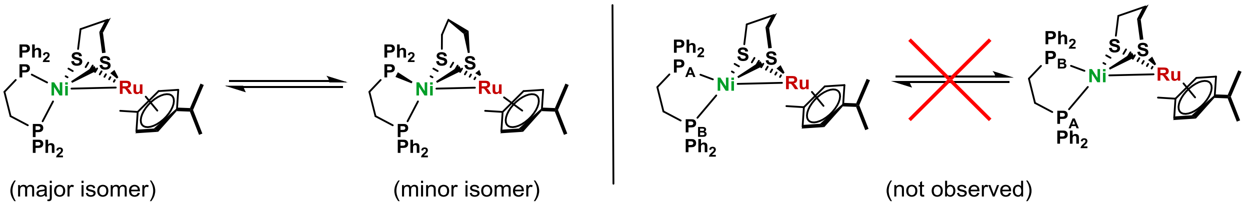

Figure 2.8. Conformations of the two flippers for **1** (left). Diphosphine rotation about nickel (right, not observed for **1**).

The low temperature $^{31}P\{^1H\}$ NMR spectra of **1** and **2** show two pairs of doublets at −80°C, ~ 6:1 ratio (Figure 2.9) in the case of **1** and ~2:1 ratio in the case of **2** (see supporting information section). These two species are conformers (sometimes called "flippamers") that differ with respect to the orientation of the propanedithiolate backbone (Figure 2.8, left).

Computer simulation of the NMR spectra are consistent with a $\Delta G^{\ddagger}$ of 11.46 ± 0.17 kcal/mol and $\Delta G^{\ddagger}$ of 10.95 ± 0.16 kcal/mol for **1** and **2** respectively (see supporting information section for derivation).

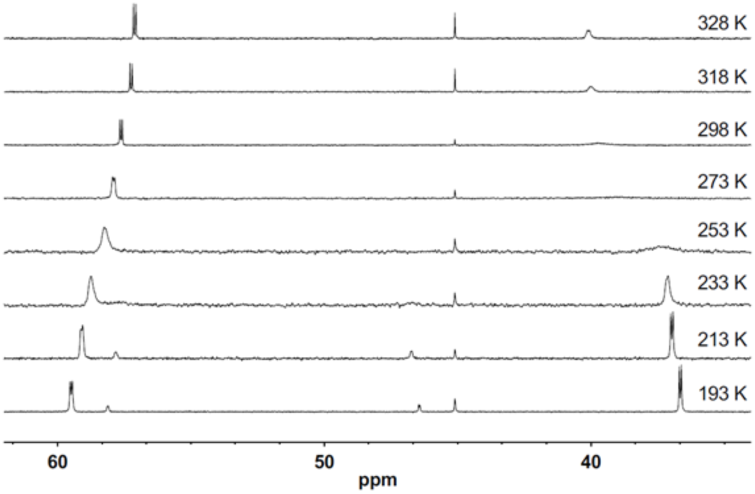

Figure 2.9. Variable NMR spectrum of **1** in THF-d_8. The resonance $\delta \approx 45$ ppm is an unknown impurity.

2.6 Protonation and pK_a Determination of NiRu Model Complexes

Compounds **1** and **2** protonate with $[H(OEt_2)_2]BAr_4^F$ to give the corresponding bridging hydride complexes [(cymene)Ru(μ-H)(μ-pdt)Ni(diphosphine)]BAr^F_4 ([**1**H]BAr_4^F and [**2**H]BAr_4^F, where BAr_4^F = tetrakis(3,5-bis(trifluoromethyl)phenyl)borate) (Scheme 2.5). These salts were isolated as red solids. The pK_a's of the bridging hydride complexes [**1**H]$^+$ and [**2**H]$^+$ were determined by acid-base titration. These experiments were conducted on PhCN solutions due to the poor solubility of **1** and **2** in MeCN and the acids used in these experiments were assumed to have similar acidities in MeCN and PhCN. The hydride [**1**H]$^+$ was found to have a pK_a^{PhCN} = 18.94 using the pyrrolidinium salt $[C_4H_8NH_2]BF_4$ (pK_a^{MeCN} = 19.56).[16] Compound **1** is quantitatively regenerated from [**1**H]$^+$ by DBU (1,8-diazabicyclo[5.4.0]undec-7-ene, pK_a^{MeCN} = 24.34).[16] Using the same approach, the pK_a^{PhCN} was determined for complex [**2**H]$^+$. The hydride complex [**2**H]$^+$ was found to have a pK_a^{PhCN} = 21.65 using benzoic acid (pK_a^{MeCN} = 21.51)[17]. The increased basicity observed upon substitution of dppe with dcpe is similar to that observed in the **R1** type systems, which change by ~2.5 pK_a units.[18]

Scheme 2.5. Protonation of **1** with $[(H(Et_2O)_2]BAr_4^F$

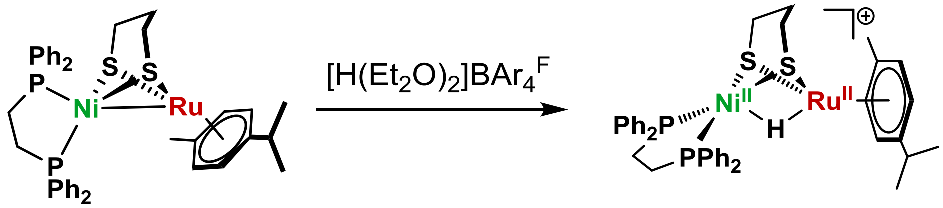

The structure of the hydride complex $[\mathbf{1}H]^+$ was deduced from NMR spectroscopy and also determined crystallography. The NMR data ($\delta_H = -5.62$, $J_{HP} = 3.9$ Hz) indicate that the two phosphorus centers are equivalent, consistent with a square planar Ni center. Crystallographic analysis of $[\mathbf{1}H]BAr^F{}_4$ confirmed that the Ni center is indeed square planar, consistent with this cation being described as a derivative of Ru(II)-Ni(II) (Figure 2.10). The Ru−H and Ni−H distances are 1.540(4) and 1.654(2) Å, respectively. Compared to typical nickel hydrides with distances c.a. 1.5 Å and below,[19-22] the Ni···H interaction is weak, a property also observed in **R1** models. The presence of a discernable $^2J_{HP}$ coupling in this system indicates that this interaction is present, as the corresponding alternative $^4J_{HP}$ would be almost negligible.

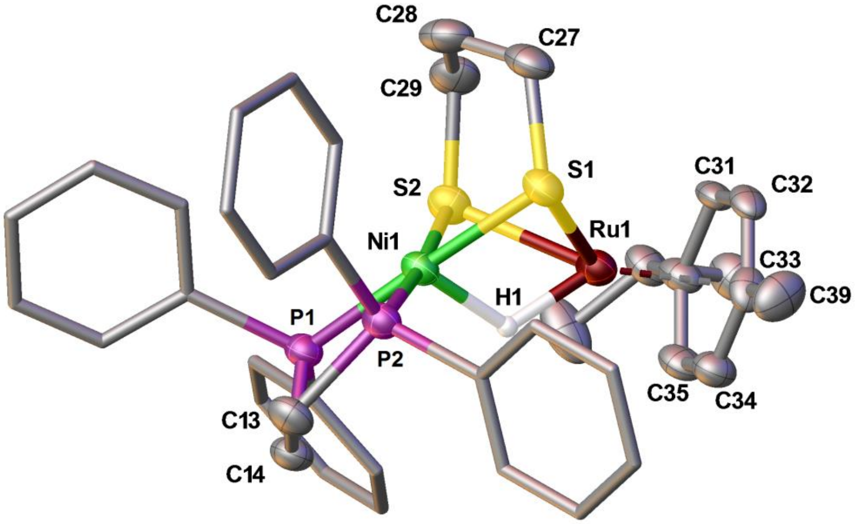

Figure 2.10. Structure of $[(\text{cymene})Ru(\mu\text{-}H)(\mu\text{-pdt})Ni(\text{dppe})]^+$ in $[\mathbf{1}H]BAr_4^F$. Hydrogen atoms, with the exception of the bridging hydride have been omitted for clarity. Selected distances (Å) and angles (deg): Ru1-Ni1, 2.553(7); Ru-centroid, 1.74(2); Ru-C_{avg}, 2.23(2); Ru-S_{avg}, 2.354(13); S1-Ru-S2, 81.39(17); Ni-S_{avg}, 2.224(12); S1-Ni-S2, 88.50(18); Ni-P_{avg}, 2.148(12); P1-Ni-P2, 87.30(18); Ru-H1, 1.54(2); Ni-H1, 1.65(2).

Cyclic voltammetric measurements show that [**1**H]$^{+}$ undergoes redox at the rather extreme potentials of +0.334 V and −1.761 V vs Fc$^{+/0}$ (Figure 2.11). The oxidation couple is reversible only at fast scan rates. At 15 mV^{-1}, the reversibility of the [**1**H]$^{+/2+}$ couple declines to i_{pc}/i_{pa} = 0.55. Doubling the concentration of [**1**H]$^{+}$ did not affect the reversibility, suggesting that [**1**H]$^{2+}$ degrades via a unimolecular pathway. A plausible pathway would involve dissociation of H^{+} from [**1**H]$^{2+}$. Consistent with this hypothesis, at slow scan rates, the voltammogram of [**1**H]$^{+}$ exhibits a new wave at E_{pc} = −0.366 V vs Fc$^{+/0}$ that corresponds to the [**1**]$^{2+/+}$ couple.

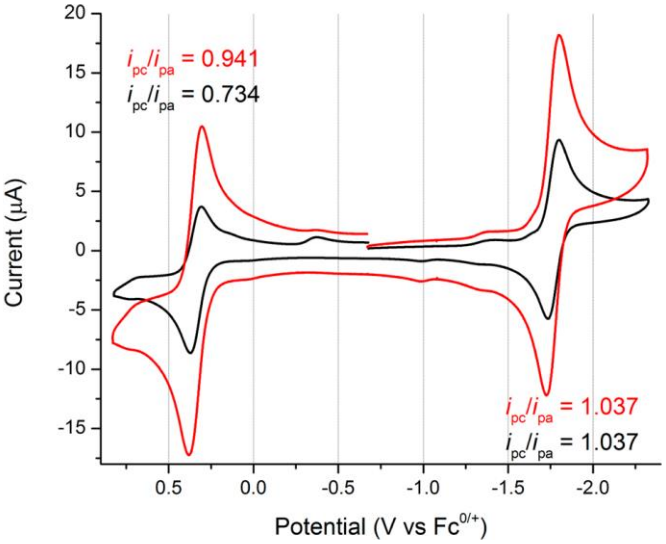

Figure 2.11. Cyclic voltammogram of [**1**H]BAr$_4^F$ at 50 (black) and 200 mVs^{-1} (red). Conditions: ~1 mM in PhCl, 40 mM [NBu$_4$]BAr$_4^F$, glassy carbon electrode (d = 3 mm); Ag wire as pseudoreference with internal Fc standard at 0 V; Pt counter electrode.

The dcpe hydride complex [**2**H]BAr$_4^F$ has an overall similar electrochemical profile. The quasi-eversible oxidation couple [**2**H]$^{+/2+}$ is unaffected by substitution and is observed at the same potential as the [**1**H]$^{+/2+}$ at +0.33 V vs Fc$^{0/+}$. The insensitivity suggests that the oxidation is primarily centered at the ruthenium center, forming a Ni^{II}Ru^{III} bridging hydride species, the opposite of the corresponding trivalent Ni-C state which is Ni^{III}Fe^{II}.

The reduction couple [**2**H]$^{+/0}$ is markedly shifted compared to [**1**H]$^{+/0}$, being −2.06 V and −1.76 V respectively. This 300 mV shift is a strong indication that the reduction is nickel centered, forming a Ni^{I}Ru^{II} bridging hydride species. For [**R1**H]$^{+}$, a decrease of −1.20 V to −1.46 V is observed upon substitution of dppe for dcpe. Overall the Ni-H-Ru(arene) system requires more forcing conditions to reduce than the corresponding Ni-H-Fe(CO)$_3$ system, a reflection of the increased basicity of the second row transition metal ruthenium compared to iron.

2.7 Oxidation of NiRu Model Complexes and DFT analysis

In section 2.4, it was shown that the reduced compounds **1** and **2** exhibited a reversible one-electron oxidation. On a preparative scale, a solution of **1** and **2** were treated with one equiv. of $FcBAr_4^F$ to afford red-violet solution. After removal of the cogenerated ferrocene by washing with pentane, the mixed-valence compounds [**1**]BAr_4^F and [**2**]BAr_4^F were isolated as dark red solids.

The X-band EPR spectrum of a toluene/PhCl solution of [**1**]BAr_4^F is rhombic, with *g*-values of 2.240, 2.053 and 2.025 (Figure 2.12). The spectrum exhibits hyperfine coupling to one $I = ½$ center corresponding to 139, 171, 147 MHz. This coupling is assigned to ^{31}P and suggests that [**1**]$^+$ is described as Ru(II)Ni(I) wherein the two phosphine centers contribute very differently to the SOMO. The EPR spectrum for [**2**]$^+$ exhibits similar with *g*-values with g = 2.271, 2.066, 2.027, but exhibits additional hyperfine coupling, suggesting a slightly different SOMO compared to [**1**]$^+$ (see supporting information section). EPR spectra of Ni(I) with $g_{\|} > g_{\perp} > 2.0$ are typical of a ground state with primarily d_{x2-y2} character.[23]

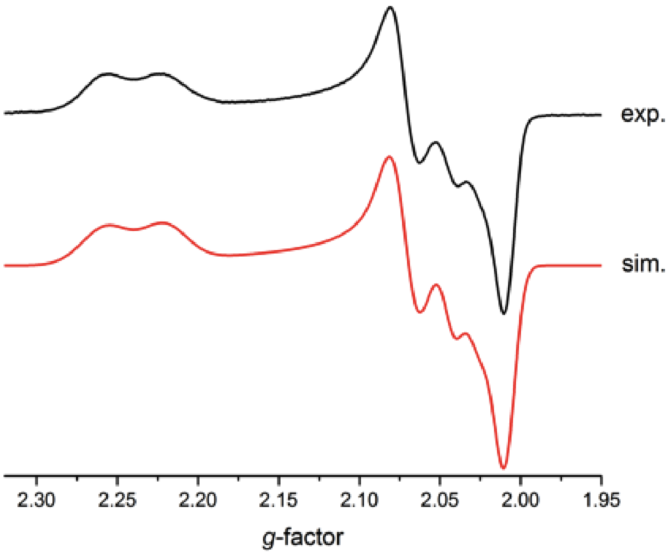

Figure 2.12. X-band EPR spectrum of a frozen PhCl/PhMe solution (110 K) of [(cymene)Ru(μ-pdt)Ni(dppe)]BAr_4^F ([**1**]BAr_4^F) and the simulated spectrum. Simulation parameters: $g_x = 2.025$, $g_y = 2.053$, and $g_z = 2.240$; $A_x(^{31}P) = 139.4$, $A_y(^{31}P) = 171.2$, and $A_z(^{31}P) = 147.4$ MHz.

Crystallographic analysis revealed that the structures of [**1**]BAr_4^F and its precursor **1** are very similar (Figure 2.13). The greatest change is the dihedral angle between the P_2Ni and S_2Ni planes being 71.78° and 84.91° in [**1**]BAr_4^F and **1**, respectively (Figure 2.14). The distorted geometry observed in [**1**]$^+$ is visually similar to the NiFe active site. Oxidation of the nickel center is indicated by lengthening of the Ni-P_{avg} distance by 0.089 Å. A similar effect is observed in [Ni(diphosphine)$_2$]$^{n+}$ complexes where the Ni-P distances elongate by 0.078 Å upon oxidation from Ni(0) to Ni(I),[24] reflecting the diminished role of π-backbonding in the Ni(I) state. The pertinent bond lengths and angles have are displayed in Table 2.2. The ruthenium-ligand distances are comparatively unchanged, indicating that the **1**$^{0/+}$ couple is nickel centered. The differences in the solid state further support the assignment of **1** as a two-electron mixed-valence Ni(0)Ru(II) complex, as proposed earlier in this chapter.

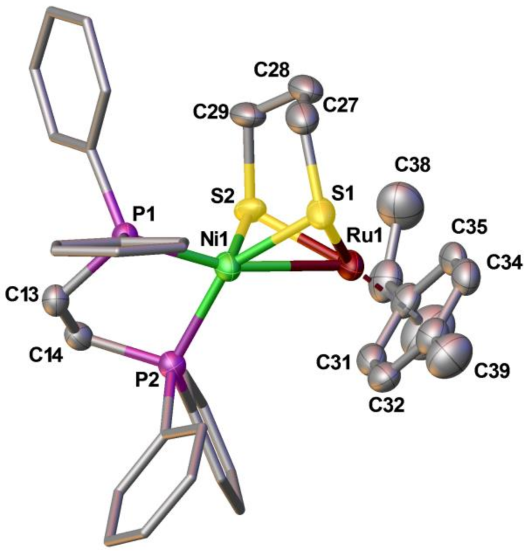

Figure 2.13. Structure of the non-hydrogen atoms of the cation [(cymene)Ru(pdt)Ni(dppe)]$^+$ in [**1**]BAr$_4^F$. Thermal ellipsoids are shown at the 50% level.

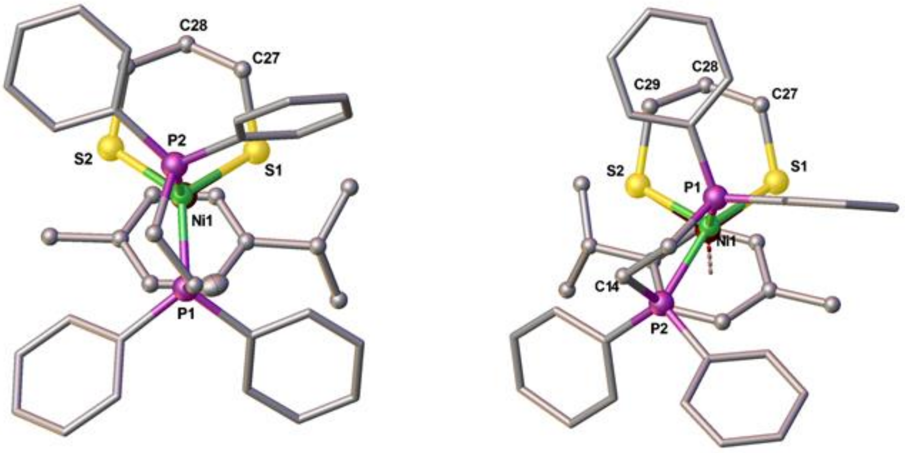

Figure 2.14. Structures of **1** (left) and of [**1**]$^+$ (right) viewed down the Ni-Ru bond axis.

Table 2.2 Selected Bond Distances (Å) and Angles (º) for [**1**]$^+$ and **1**.

Parameter	[**1**]$^+$	**1**
Ru-Ni	2.5321(8)	2.5539(5)
Ru-centroid	1.699(6)	1.710(5)
Ru-S	2.329(4), 2.324(4)	2.3326(7), 2.3336(7)
Ni-S	2.245(4) 2.275(4)	2.2442(8) 2.2443(9)
Ni-P$_{apical}$	2.242(2)	2.1465(8)
Ni-P$_{basal}$	2.236(2)	2.1542(9)
P-Ni-P	87.13(6)	90.00(3)
S-Ni-S	91.6(2)	91.29(3)
NiS_2/NiP_2 dihedral	71.8(2)	84.91(4)

DFT analysis was performed with the aim to assign oxidation states. Calculations reproduced the main structural features obtained in the crystallographic analysis of the neutral and oxidized complexes.

The HOMO of **1** is highly localized on Ni (48.3%) whereas Ru contributes about 13%. The HOMO is principally a Ni-P bonding orbital. The Ru-Ni bonding is manifested mainly in a lower energy bonding orbital (HOMO−2), which is significantly delocalized across the metal and ligand framework (Figure 2.15). A multipole derived atomic charge (MDC) analysis[25] revealed a positive charge of +0.50 on the Ru and a slight positive charge of +0.05 on the Ni atom in **1**, showing that there is a significant charge disparity between the metal centers.

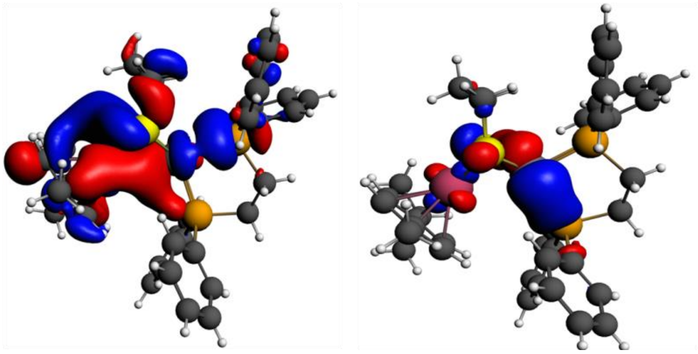

Figure 2.15. DFT-calculated isocontour plots (isovalue 0.04) of the bonding orbitals for **1**. Left: the doubly occupied orbital depicting Ru-Ni interaction (HOMO−2) is delocalized over the entire metal-ligand framework. Right: HOMO - electron density is principally centered on the Ni, S and one of the P atoms.

To benchmark the above description of **1**, the electronic structure of **R1** was reexamined. This Ni-Fe complex is described as Ni(I)Fe(I):[26] the MDC analysis revealed that the charges on Ni and Fe centers are very similar, in contrast to the case for **1**.

Of particular interest is the twist for the NiS_2P_2 site relative to the Ni-Ru bond axis. DFT analysis of [**1**]$^+$ gave a value of 74.25° for this angle whereas an angle of 69.54° is observed crystallographically. A scan of the dihedral angle along Ru-Ni-P-C vector for both **1** and [**1**]$^+$ revealed a relatively shallow potential energy surface at small twist angles (Figure 2.16). This scan shows that the energy difference for the observed difference in the twist angle is within the error for DFT analysis.

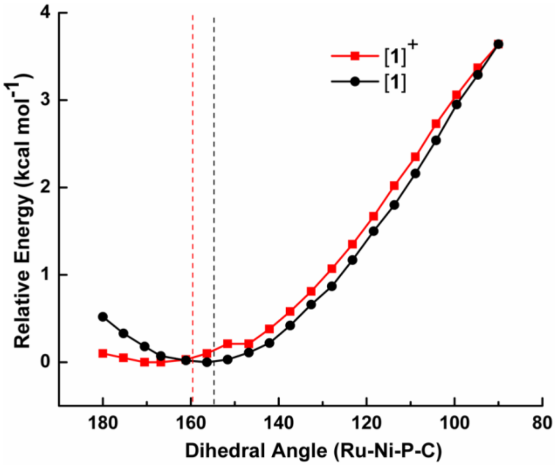

Figure 2.16. Variation in energy relative to the crystallographically obtained structures for both **1** and [**1**]$^+$ obtained from a scan of Ru-Ni-P-C dihedral angle. The vertical lines indicate the crystallographically obtained dihedral angles.

The calculated Ni-P bonds elongate from 2.12 in **1** to 2.18 Å in [**1**]$^+$ and the Ni-S bonds become unsymmetrical (from 2.26 each in **1** to 2.24 and 2.30 Å in [**1**]$^+$). The covalency of the Ni-P and Ni-S bonds is also manifested by analyzing the redistribution of charge upon oxidation. The MDC values at the metal ions are almost unchanged (+0.46 on Ru and -0.03 on Ni) in [**1**]$^+$ compared to (+0.50 on Ru and +0.05 on Ni) in **1**. The decreased positive charge calculated at the nickel center could be due to the decreased π-backbonding to phosphorus.

EPR analysis and calculations suggest that the oxidation is almost exclusively nickel-based. The unpaired electron spin is localized at the nickel center (0.54) and to a lesser extent at the ligand sulfur (0.21) and phosphorus atoms (0.09). The remaining ~15% spin is delocalized, but Ru atom only carries 0.08 e^-.

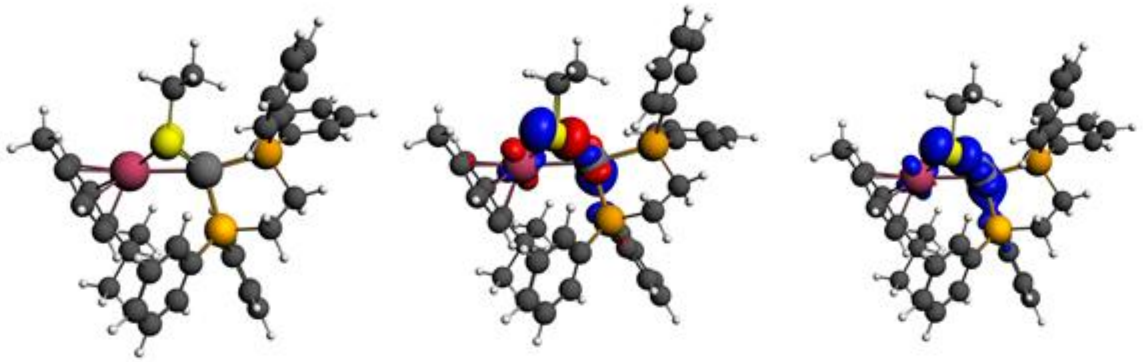

Figure 2.17. Optimized structure**,** highest-occupied molecular orbital (HOMO) from restricted open-shell and isocontour plot of the unpaired spin density distribution at 0.003 e^- from unrestricted open shell DFT calculations of complex [**1**]$^+$.

For [**1**]$^+$, density functional calculations (B3LYP/def2-TZVP) gave a rhombic *g*-tensor with $g_{x,y,z}$ = 2.01, 2.08, 2.25, which agree nicely with those recorded with X-band EPR spectroscopy ($g_{x,y,z}$ = 2.03, 2.05, 2.24). Only one of the two ^{31}P centers carries significant spin density, reflected by a large hyperfine interaction $A_{x,y,z}$ = (+102, +104, +140) MHz yielding an isotropic hyperfine interaction, A_{iso}, of +115 MHz. The hyperfine coupling of the second ^{31}P atom was smaller by almost an order of magnitude A_{iso}= +17 MHz, which is not resolved in the EPR spectrum.

In the [NiFe]-H_2ases, the photo-reduced Ni-L state corresponds to a formal Ni(I) species. The EPR spectrum (*g* = 2.30, 2.12, 2.05)[27] is considered to be indicative of a Ni(I) species with a $3d_{x2-y2}$ ground state.[27,28] The bonding in Ni-L was recently reinterpreted in terms of the symmetry-adapted $3d_{x2}$ and $3d_{z2-y2}$ orbitals[29] in which the $3d_{x2}$ orbitals of the Ni and the Fe formed bent sigma bonding and antibonding interactions, and the electron spin resides in a Ni-based $3d_{z2-y2}$ orbital. Depending on the cluster model, calculations on Ni-L indicate that the majority of unpaired spin resides on the Ni atom, between 0.63 and 0.71, and *one* of the four cysteinyl sulfur atoms (0.17-0.22), a very analogous situation to [**1**]$^+$.

2.8 Electron Self-Exchange of the 1/[1]$^+$ System

Due to the similar structures crystallographically observed for **1** and [**1**]$^+$, it was anticipated that the reorganization energy for this process was low. If true, the electron self-exchange between **1** and [**1**]$^+$ should be fast.

^{1}H-NMR spectra were recorded for solutions of **1** treated with varying equivalents of $FcBAr_4^F$ to generate mixtures of **1** and [**1**]$^+$ (Figure 2.18). At room temperature, only one set of signals was observed at chemical shifts corresponding to the average of the signals **1** and [**1**]$^+$, weighted according to their mole fractions. The observation of only one set of signals indicates that electron transfer is fast on the NMR time scale. Analysis of the line widths for the averaged signals allowed the determination of the electron self-exchange rate, which was (1.0 ± 0.1) × 10^7 $M^{-1}s^{-1}$. The derivation and tabulated data for this determination can be found in the supporting information. The electron self-exchange for the $Fc^{+/0}$ couple is similarly fast,[30] and such fast rates are in agreement with the minimal structural rearrangement crystallographically observed and theoretically predicted for this redox couple.

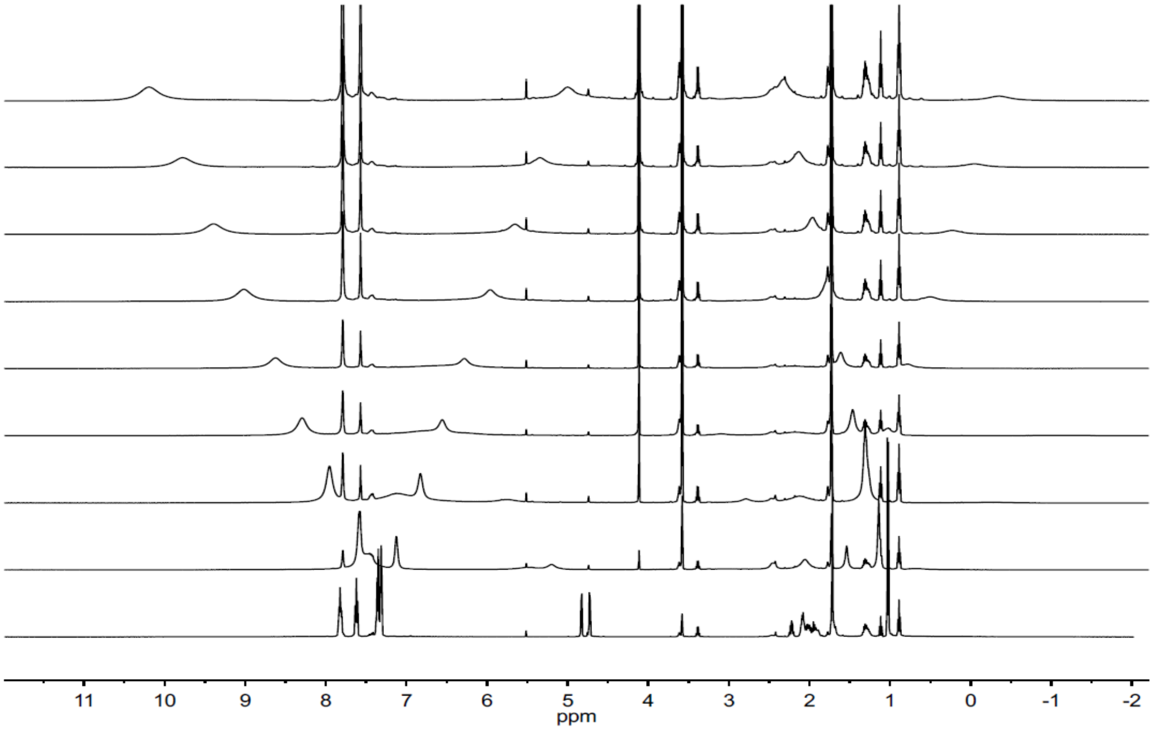

Figure 2.18. ^{1}H-NMR spectra of **1** (bottom) treated with various equivalents of $FcBAr_4^F$ (ascending). Diamagnetic (unshifted) resonances correspond to BAr_4^F, ferrocene, THF, *n*-pentane, and Et_2O.

2.9 Hydrogen Atom Abstraction of [1]$^+$

Freshly prepared samples of the mixed-valence complex [**1**]BAr_4^F were analyzed by high-resolution electrospray ionization mass spectrometry (ESI-MS) and consistently yielded a dominant ion at one mass unit less than expected (m/Z_{obs} = 797.0679 and m/Z_{calc} = 798.0756, see supporting information section). This difference indicated loss of a H radical to give a new compound, [**1**−H]$^+$. Solutions of the red-violet mixed-valence complex [**1**]BAr_4^F were found to be unstable over the course of several days, affording green-brown solutions. ^{1}H and ^{31}P NMR spectroscopic analysis revealed that two predominant complexes are produced, the hydride [**1**H]$^+$ and the new complex [**1**−H]$^+$ (Scheme 2.6)

Scheme 2.6. Hydrogen Atom Abstraction Reaction of [**1**]$^+$

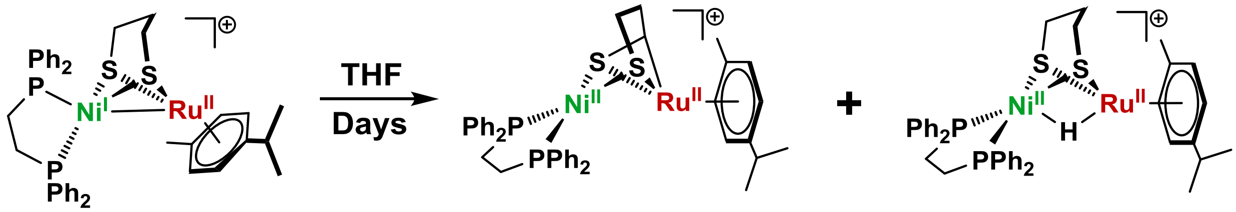

Crystallographic analysis showed that [**1**−H]$^+$ is a Ru-Ni complex of the ligand $SCHCH_2CH_2S^{x-}$, formally a thiolato-thioaldehyde derived by partial dehydrogenation of propanedithiolate. Complexes of this entity are known[31,32] and have been generated by radical reactions.[33] Treatment of [**1**]BAr^F_4 with 2,2,6,6-tetramethylpiperidine-1-oxy (TEMPO), an H-atom abstracting agent, afforded [**1**−H]BAr^F_4 in good yield.

The product of the dehydrogenation was characterized crystallographically (Figure 2.19). The μ-thioaldehyde group binds in an η^2-manner to Ru. The Ru adopts a pseudo-octahedral geometry and the Ni center is square planar, suggesting that the thioaldehyde ligand be viewed as the trianion $SCHCH_2CH_2S^{3-}$. The room temperature ^{31}P NMR spectrum of [**1**−H]$^+$ exhibits only a single resonance, indicating a dynamic exchange process between the two phosphorus centers, which should be inequivalent by symmetry. Upon cooling the sample, the resonance broadens and gradually develops into a pair of doubles at −70°C, supporting this dynamic exchange process.

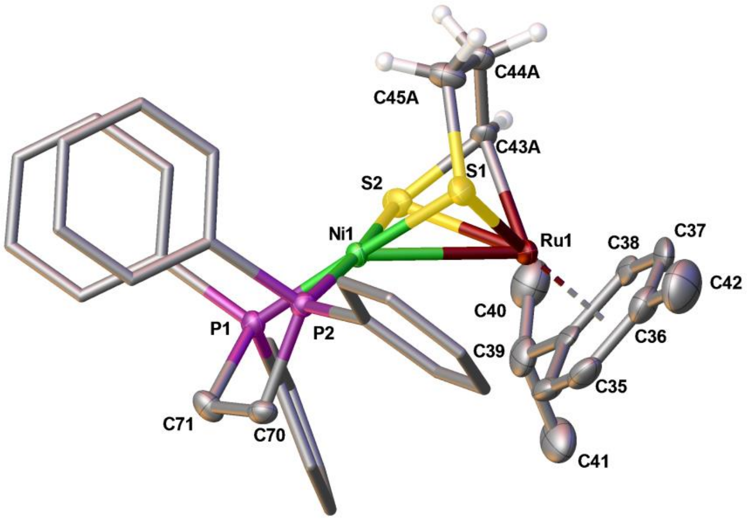

Figure 2.19. Structure of the cation [(cymene)Ru($S_2CHCH_2CH_2S$)Ni(dppe)]$^+$ ([**1**−H]$^+$). H atoms, except those in the bridging ligand, have been omitted for clarity. Selected distances (Å) and angles (deg): Ru1−Ni1, 2.7940(5); Ru−centroid, 1.691(3); Ru−C_{av}, 2.203(7); Ru−C43A, 2.143(6); Ru−S_{av}, 2.388(1); S1−Ru−S2, 82.4(1); Ni− S_{av}, 2.1909(9); S1−Ni−S2, 91.94(4); Ni−P_{av}, 2.1653(9); P1−Ni−P2, 84.76(3); S1−C45A, 1.897(5); S2−C43A, 1.716(5).

2.10 Reactivity of [1H]$^+$ with Hydrogen

Although other ruthenium-nickel thiolates have been reported to activate H_2 in the presence of base,[11] **1** is not reactive to H_2 under basic conditions. However, solutions of [**1**]$^+$ were found to react with H_2 over the course of several hours to form the bridging hydride complex [**1**H]$^+$ in quantitative yield. Because the reduced complex **1** can be regenerated by deprotonation of [**1**H]$^+$ with strong base, the cation [**1**]$^+$ is a formal H_2 oxidation catalyst, albeit a slow one. The exact mechanism for this process is not known definitively but is proposed to proceed through an H_2-adduct followed by deprotonation, perhaps facilitated by solvent (Scheme 2.7).

Scheme 2.7. Proposed Mechanism for Formation of [1H]$^+$ from [1]$^+$ and H_2

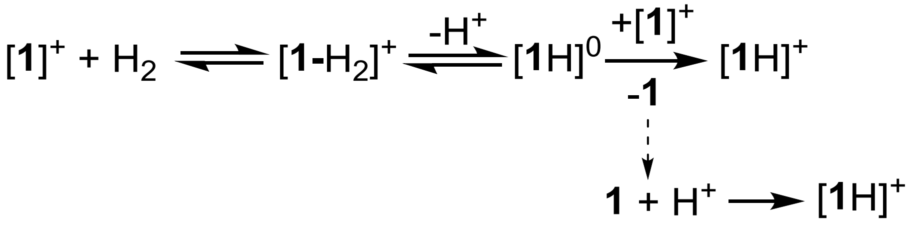

It was found that solutions of [**1**]BAr$_4^F$ in THF-d_8 catalyze the scrambling of H_2 and D_2, a property also observed in the hydrogenases. Due to the solution instability of [**1**]$^+$, the decomposition products $[\mathbf{1}{-}\mathrm{H}]^+$ and $[\mathbf{1}\mathrm{H}]^+$ were tested under identical conditions and were found not to catalyze this process. The mechanism proposed in Scheme 2.7 could additionally account for the observed H_2/D_2 scrambling where H_2 binding and deprotonation are reversible events. In order to detect the presence of a dihydrogen adduct, the EPR spectrum of [**1**]BAr_4^F was recorded under 1 atm of H_2, but was identical to the spectrum obtained under N_2.

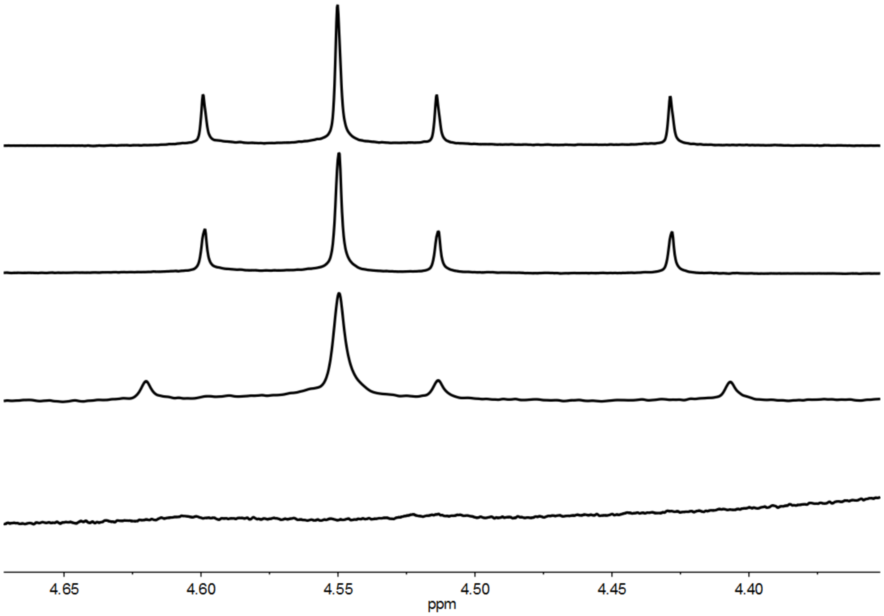

Figure 2.20. ^{1}H-NMR spectra of a THF-d_8 solution of [**1**]BAr_4^F under N_2 (bottom, 500 MHz), and (ascending) 15 min after exposure to 2 atm of a 1:1 H_2/D_2 mixture (400 MHz), 12h (500 MHz), and 36h (500 MHz) after the addition.

2.11 Conclusions

This chapter describes the first Ni(I)-containing bimetallic model for the H_2ases. The initial hypothesis that substituting the $Fe(CO)_3$ fragment with Ru(arene) would stabilize a Ni(I)Ru(II) mixed-valence state proved to be true.

The distorted tetrahedral coordination environment of Ni in the mixed-valence cation is unique in RuNi complexes. In the [NiFe]-hydrogenases, the dihedral angle between Ni(μ-*S*cys)$_2$ and Ni(*term*-*S*cys)$_2$ angle is 69.19° compared to a SNiS-PNiP dihedral angle of 71.78° in the Ni(I)Ru(II) model. Tetradentate dithiolate ligands, which are traditionally employed in modeling the [NiFe] hydrogenases, do not accommodate nickel in a biomimetic geometry.

Both theory and experiment suggest that the reduced model **1** is best described as a two-electron mixed-valence Ni(0)Ru(II) system. The alternative representation of Ni(I)Ru(I) is not consistent with the structural changes observed upon oxidation and the effect of ligand substitution on the oxidation couple.

Since both 1e^{-} redox changes of the NiRu complexes are Ni-localized, it is tempting to conclude that the ruthenium center is merely a spectator. However, ruthenium carries the hydride ligand as evidenced by the structure of [**1**H]$^{+}$. The oxidation state assignments point to Ni(0) as the initial site of protonation, as seen for many Ni^0L_4 complexes.[34] As originally proposed by Nicolet et al.,[35] the Ni center in the [NiFe]-hydrogenases may function as a relay center, conveying hydrogenic ligands to the redox-inactive d^6 center.

2.12 Experimental

Unless otherwise noted, reactions and manipulations were generally performed using standard Schlenk techniques at room temperature. Solvents were HPLC-grade and dried by filtration through activated alumina or distilled under nitrogen over an appropriate drying agent. $[(cymene)RuCl_2]_2$, Ni(dithiolate)(diphosphine) and $H(Et_2O)_2BAr_4^F$ were prepared according to established literature procedures.[36,6,37] Bu_4NPF_6 was purchased from GFS chemicals and was recrystallized multiple times from CH_2Cl_2 solution by the addition of hexane. $Bu_4NBAr_4^F$ was prepared according to Barrière and Geiger.[38] Chromatography was performed using Siliaflash P60 from Silicycle (230-400 mesh). ESI-MS data for compounds were acquired using a Waters Micromass Quattro II spectrometer. ^{1}H NMR spectra (500 MHz) were referenced to residual solvent relative to TMS. $^{31}P\{^1H\}$ NMR spectra (202 MHz) were referenced to an external 85% H_3PO_4. FT-IR spectra were recorded on a Perkin-Elmer 100 FT-IR spectrometer. Crystallographic data were collected using a Siemens SMART diffractometer equipped with a Mo K_α source (λ = 0.71073 Å) and an Apex II detector.

[(cymene)RuCl(pdt)Ni(dppe)]Cl, [1Cl]Cl. To a solution of $[(cymene)RuCl_2]_2$ (0.453 g, 0.74 mmol) in CH_2Cl_2 (50 mL) was added Ni(pdt)(dppe) (0.834 g, 1.48 mmol) in CH_2Cl_2 (50 mL). The resultant solution was stirred for 4 h under argon, during which the color of the solution deepened. The solvent was then removed under reduced pressure, and the red residue extracted into minimal MeCN and purified by flash chromatography in air. Byproducts eluted with MeCN. With MeCN/MeOH (90:10), [**1**Cl]Cl eluted as a dark red band. Solvent was removed under reduced pressure, yielding a red powder. Yield: 0.79 g (61%). ^{1}H-NMR ($CDCl_3$): δ 7.80 (t, J = 9.1 Hz, 4H), 7.50 (m, 16H), 7.16 (t, J = 7.5 Hz, 4H), 5.41 (d, J = 5.8 Hz, 2H), 5.42 (d, J = 5.8 Hz, 2H), 2.79 (sept, J = 7.0 Hz, 1H), 2.31 (m, 8H), 2.21 (d, J = 24.3 Hz, 4H), 1.98 (m, 2H), 1.20 (d, J = 7.0 Hz, 6H). $^{31}P\{^1H\}$-NMR ($CDCl_3$): δ 55.30. ESI-MS: m/*Z* 835 ([**1**Cl]+). Single crystals were obtained from slow diffusion of pentane into a concentrated acetone solution. Anal. Calcd for $C_{39}H_{44}Cl_2NiRuP_2S_2\cdot 1.5H_2O\cdot 0.5C_3H_6O$ (found): C 52.55 (52.46); H 5.44 (5.20). The solvation values agree with the 1H-NMR spectrum of the bulk mixture; however, the crystallographic analysis revealed solvation values of 2 H2O and 0.5 acetone.

[(cymene)RuCl(pdt)Ni(dcpe)]Cl. To a solution of [(cymene)RuCl$_2$]$_2$ (0.058 g, 0.059 mmol) in CH$_2$Cl$_2$ (10 mL) was added Ni(pdt)(dcpe) (0.111 g, 0.119 mmol) in CH$_2$Cl$_2$ (10 mL). The resultant solution was stirred for 2 h under argon. The solvent was removed under reduced pressure, and the red-orange residue extracted into minimal MeCN and purified by flash chromatography under nitrogen. The product eluted with 90:10 MeCN/MeOH as a red-orange band. Removal of the solvent gave a red-orange powder. The powder was recrystallized from CH$_2$Cl$_2$ and Et$_2$O. Yield: 98 mg (59%). ^{1}H-NMR (CD$_2$Cl$_2$): δ 5.43 (d, J = 5.9 Hz, 2H), 5.11 (d, J = 5.9 Hz, 2H), 2.91 (sept, J = 7.0 Hz, 1H), 2.62 (m, 5H), 2.34 (m, 3H), 2.31 (s, 3H), 2.11 (m, 4H), 1.71 (m, 26), 1.33 (d, J = 7.0 Hz, 6H), 1.28 (m, 16H). ^{31}P{^{1}H}-NMR (CD$_2$Cl$_2$): δ 71.56. ESI-MS: m/*Z* 859 ([M]+). Anal. Calcd for $C_{39}H_{68}Cl_2NiRuP_2S_2·CH_2Cl_2$ (found): C 49.09 (49.46); H 7.21 (7.08).

[(C$_6$Me$_6$)RuCl(pdt)Ni(dppe)]PF$_6$. To a solution of [(C$_6$Me$_6$)RuCl$_2$]$_2$ (0.061 g, 0.09 mmol) in CH$_2$Cl$_2$ (10 mL) was added Ni(pdt) (dppe) (0.103 g, 0.183 mmol). After stirring for 10 min, the solution was treated with NH$_4$PF$_6$ (0.026 g, 0.16 mmol). After stirring for an additional 30 min, the solution was filtered through Celite, and the filtrate evaporated. The residue was extracted into a minimum volume of CH$_2$Cl$_2$ and purified by flash chromatography in air. By-products eluted with 100% CH$_2$Cl$_2$. The product eluted with 90:10 CH2Cl2/MeCN as a red band. The solvent was removed under reduced pressure to yield a red powder. Yield: 0.015 g (15%). ^{31}P{1H} NMR (CD$_3$CN): δ 50.50 (s), −148.0 (sept). ESI-MS: m/*Z* 863 ([M]$^+$).

(cymene)Ru(pdt)Ni(dppe), 1. To a mixture of [**1**Cl]Cl (0.112 g, 0.129 mmol, 1.0 equiv.) and cobaltocene (0.068 g, 0.360 mmol, 1.4 equiv.) was added 10 mL of acetone. The solution immediately darkened with a gradual formation of a yellow precipitate of [Cp$_2$Co]Cl. After stirring the mixture for 30 min, solvent was removed under reduced pressure. The residue was extracted with toluene, which was filtered through a pad of Celite. The dark brown filtrate was evaporated, and this residue was washed several times with pentane to remove unreacted cobaltocene. The resulting black solid **1** was dried under vacuum. Yield: 0.099 g (96%). ^{1}H-NMR (C$_6$D$_6$): δ 7.92 (t, J = 8.5 Hz, 4H), 7.71 (t, J = 8.5 Hz, 4H), 7.16 (t, J = 7.5 Hz, 4H), 7.07 (t, J = 7.5 Hz, 6H), 7.01 (m, 2H), 4.93 (t, J = 5.3 Hz, 2H), 4.82 (t, J = 5.3 Hz, 2H), 2.50 (br, 2H), 2.43 (sept, J = 7.0 Hz, 1H), 2.03 (m, 5H), 1.88 (s, 3H), 1.87 (m, 2H), 1.54 (br, 1H), 1.11 (d, J = 7.0 Hz, 6H). ^{31}P{^{1}H}-NMR (C$_6$D$_6$): δ 57.18 (d, 2J = 16 Hz), 39.2 (br). Anal. Calcd for $C_{39}H_{44}NiRuP_2S_2$ (found): C 58.65 (58.75); H 5.55 (5.62). Single crystals were obtained by slow diffusion of hexane into a concentrated THF solution.

(cymene)Ru(pdt)Ni(dcpe). To a stirred suspension of [**2**Cl]Cl·CH_2Cl_2 (0.0328 g, 0.035 mmol) in THF (4 mL) was added decamethylcobaltocene (0.0255 g, 0.078 mmol) in THF (1 mL). The solution changed from red-orange to dark green concomitant with precipitation of a yellow solid. The mixture was allowed to stand for 15 min. The mixture was filtered through a pad of Celite, and solids were washed with Et_2O. The extracts were combined, and the solvent was removed under reduced pressure. The residue was washed twice with pentane (0.2 mL). The solvent was removed under reduced pressure to yield a black-green powder. Yield: 0.0162 g (56%). $^{31}P\{^1H\}$-NMR (THF-d8): δ 66.65 (d, 2J = 16 Hz), 60.66 (br). Anal. Calcd for $C_{39}H_{68}NiRuP_2S_2$ (found): C 56.93 (57.54); H 8.33 (8.43). Single crystals were obtained by layering of concentrated THF solutions with pentane.

(C_6Me_6)Ru(pdt)Ni(dppe). To a solution of cobaltocene (0.0128 g, 0.068 mmol) dissolved in THF (1.5-mL) was added a solution of [**3**Cl]Cl (0.0262 g, 0.029 mmol) in THF (1.5 mL). Solution became green concomitant with the formation of yellow precipitate. The solvent was removed under reduced pressure and the residue was extracted with toluene. The mixture was filtered through a pad of Celite, and solvent evaporated. Excess cobaltocene was removed by multiple extractions with pentane until the extract was colorless yielding a green-black powder. Yield: 0.022 g (92 %). ^1H NMR-(C_6D_6): δ 7.99 (t, *J* = 8.5 Hz, 4H), 7.83 (t, *J* = 8.5 Hz, 4H), 7.23 (t, *J* = 7.1 Hz, 4H), 7.10 (m, 6H), 7.04 (t, *J* = 7.1 Hz, 2H), 2.04 (br, 2H), 1.99 (m, 8H), 1.88 (s, 18H). $^{31}P\{^1H\}$-NMR (C_6D_6): δ 52.21 (*d*, 2*J* = 26 Hz), 38.7 (br).

[(cymene)Ru(μ-H)(pdt)Ni(dppe)]BAr$_4^F$, [1H]BAr$_4^F$. To a solution of **1** (0.048 g, 0.060 mmol) in THF (5 mL) was added a solution of $H(Et_2O)_2BAr_4^F$ (0.061g, 0.060 mmol) in THF (5 mL). The resulting solution became red immediately upon the addition. The solvent was removed under reduced pressure to yield a red residue, which was recrystallized by extraction into THF followed by the addition of hexane. Yield: 0.071 g (72%). ^1H-NMR (C_3D_6O): δ 7.85 (m, 8H), 7.79 (s, 8H), 7.67 (s, 4H), 7.62 (t, J = 7.2 Hz, 6H), 7.56 (t, J = 7.2 Hz, 6H), 5.60 (d, J = 5.8 Hz, 2H), 5.46 (d, J = 5.8 Hz, 2H), 2.72 (d, J = 19.3 Hz, 4H), 2.55 (m, 1H), 2.24 (sept, J = 7.0 Hz, 1H), 2.19 (m, 2H), 1.99 (t, J = 11.9, 2H), 1.73 (s, 3H), 1.65 (m, 1H), 0.97 (d, J = 7.0 Hz, 6H), −5.12 (br t, J = 3.9 Hz, 1H, hydride). $^{31}P\{^1H\}$-NMR (CD_2Cl_2): δ 67.3. ESI-MS: m/*Z* 799 ($[M]^+$). Anal. Calcd for $C_{71}H_{57}BF_{24}NiRuP_2S_2$ (found): C 51.28 (51.6); H 3.46 (3.52). Single crystals were obtained by slow diffusion of hexane into a concentrated THF solution.

[(cymene)Ru(μ-H)(pdt)Ni(dcpe)]BAr$_4^F$, [2H]BAr$_4^F$. To a solution of **2** (0.0082 g, 0.010 mmol) in THF (0.5 mL) was added a solution of $H(Et_2O)BAr_4^F$ (0.0103 g, 0.010 mmol) in THF (0.5 mL). The resulting solution immediately turned dark red. The solvent was removed under reduced pressure to yield a red residue. The residue was extracted into ether (0.5 mL), and the bridging hydride complex was precipitated upon addition of pentane. Yield: 0.0134 g (79%). ^{1}H NMR (THF-d_8): −5.16 (br t, J ≤ 2.6 Hz, 1H, hydride). ^{31}P{^{1}H}-NMR (THF-d_8): δ 89.97. ESI-MS: m/*Z* 823 ([M]$^+$).

[(cymene)Ru(μ-pdt)Ni(dppe)]BAr$_4^F$ ([1]BAr$_4^F$). A solution of FcBAr$_4^F$ (0.0142 g, 0.0135 mmol) in THF (0.5 mL) was added dropwise to a stirred solution of [1]0 (0.0108 g, 0.0135 mmol) in THF (0.5 mL). The resultant solution gradually became dark red-violet. The product precipitated upon the slow addition of 3 mL of pentane. A dark-red solid was collected by filtration and washed several times with pentane until the filtrate was colorless. Yield: 0.022 g (98%). Anal. Calcd for $C_{71}H_{56}BF_{24}NiP_2RuS_2$ (found): C, 51.31 (50.96); H, 3.40 (3.19). Single crystals were grown by slow diffusion of pentane into a concentrated THF solution.

[(cymene)Ru(μ-pdt)Ni(dcpe)]BAr$_4^F$. This compound was generated in solution for EPR characterization in a manner similar to that for [**1**]BAr$_4^F$.

Conversion of [1]$^+$ to [1H]$^+$. The hydride [**1**H]BAr$_4^F$ was prepared in good yield by treating a CD_2Cl_2 solution of [**1**]BAr$_4^F$ with an atmosphere of H_2 for 12 h.

[(cymene)Ru(μ-SCHCH$_2$CH$_2$S)Ni(dppe)]BAr$_4^F$ ([1-H]BAr$_4^F$). A solution of TEMPO (0.0026 g, 0.0166 mmol) in THF (1.0 mL) was added to a solution of [**1**]BAr$_4^F$ (0.0302 g, 0.0168 mmol) in THF (1 mL). The solution was stirred for 24 h, during which time the solution became dark green. The solvent was removed under reduced pressure to yield a green residue, which was extracted into THF and recrystallized by vapor diffusion of pentane. The solids were collected by filtration and washed with pentane. Yield: 0.024 g (80%). ^{31}P{^{1}H}-NMR (THF): δ 61.7. Anal. Calcd for $C_{71}H_{55}BF_{24}NiP_2RuS_2$ (found): C, 51.35 (51.98); H, 3.34 (3.57).

2.13 Supporting Information

Routine characterization NMR data not found in the main text or this supporting information can be found in published works.[39,40]

Determination of ΔG‡ for the Propanedithiolate Flipping Process in compounds 1 and 2.

The free energy of activation was determined using the Eyring equation (eq. 1).

$$\Delta G^{\ddagger} = RT\left(23.76 + \log\frac{T}{k}\right)\frac{J}{mol} \qquad (1)$$

The rate constant *k* for the isomerization process was extracted via dynamic NMR simulation. NMR spectra of **1** and **2** were simulated using the SpinWorks software package.

The frequency difference (Δv) between the resonances of a phosphorus center with its opposing conformer was approximated to be constant with temperature.

The ΔG between flippamers was determined using eq. 2 by integration of the ^{31}P-NMR resonances at 213 K. The change in entropy (ΔS) between flippamers was assumed to be negligible and thus the ΔG between flippamers was assumed to be constant with temperature. Equilibrium population distributions at varying temperatures were calculated using eq. 2.

$$e^{-\Delta G/RT} = K \qquad (2)$$

Error propagation was accounted for using eq. 3.[41]

$$(\sigma \Delta G^{\ddagger})^2 = R^2T^2\left[\left(\frac{\sigma T}{T}\right)^2 1 + ln\left(\frac{k_bT}{kh}\right) + \left(\frac{\sigma k}{k}\right)^2\right]\frac{J}{mol} \qquad (3)$$

Table 2.3. Experimental temperature and simulated rate constant data used in the determination of $\Delta G^{\ddagger}$ for the propanedithiolate flipping process in **1** (gray) and **2** (light red).

Temperature (K)	Error (K)	k (s^{-1})	Error (s^{-1})	$\Delta G^{\ddagger}$ (kcal/mol)	Error (kcal/mol)	Isomer Ratio
243	3	250	50	11.45	0.18	81.0 : 19.0
233	3	85	5	11.46	0.16	81.9 : 18.1
223	3	27	3	11.46	0.17	82.9 : 17.1
			Average	11.46	0.17	
233	3	275	25	10.92	0.15	65.2 : 34.8
223	3	90	10	10.93	0.16	65.9 : 34.1
213	3	23	2	10.99	0.17	66.6 : 34.4
			Average	10.95	0.16	

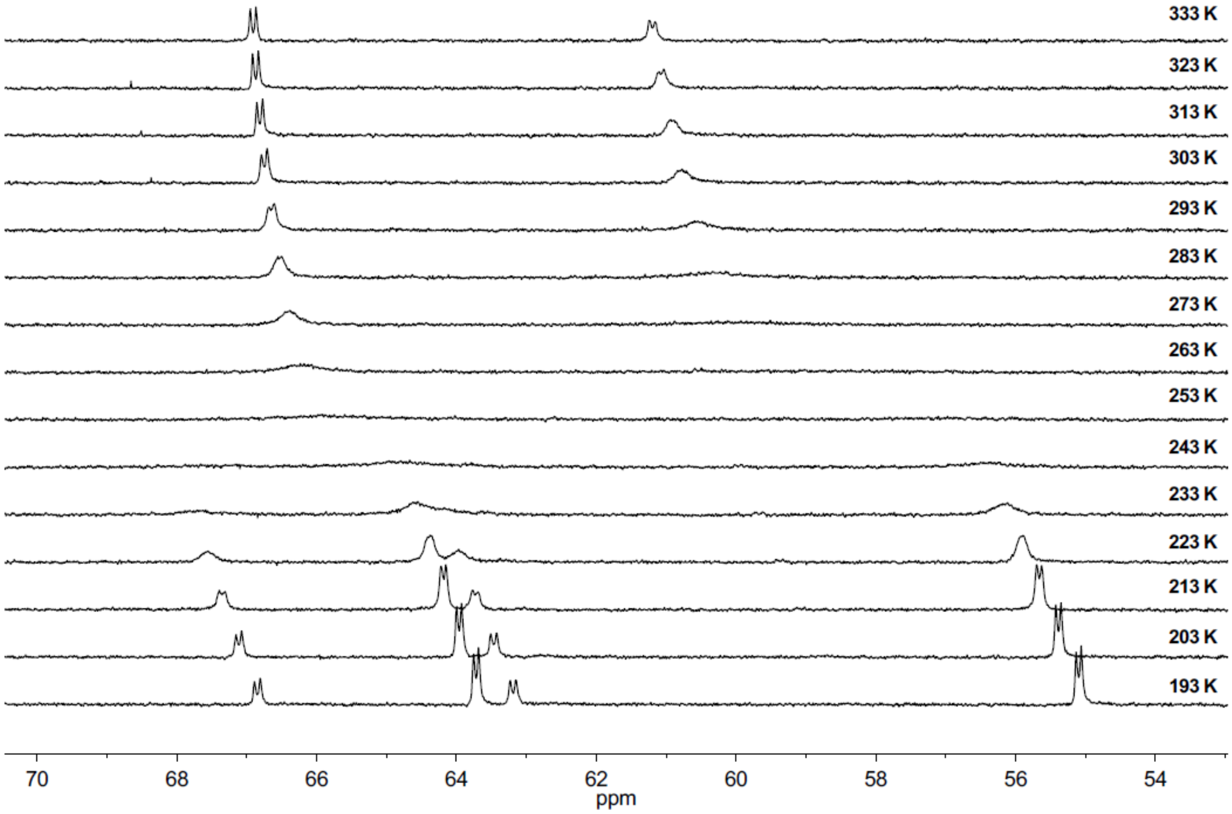

Figure 2.21. Variable temperature ^{31}P-NMR spectra of **2** in THF solution.

pK_a Determination of Complexes [1H]$^+$ and [2H]$^+$

The acid dissociation constants of the hydride complexes [**1**H]$^+$ and [**2**H]$^+$ were determined by partial protonation utilizing acids of known strength. Proportions of the metal complex (M) and its protonated product (MH$^+$) were determined using ^{31}P{^{1}H} NMR spectroscopy. Using the tabulated values for the pK_a of the chosen acid as well as the experimentally determined equilibrium concentrations of M, MH$^+$, AH, and A$^-$, the pK_a of MH$^+$ can be determined through the Henderson-Hasselbalch equation represented and rearranged below.

$$\mathrm{pH} = \mathrm{p}K_a + \log\left(\frac{[\mathrm{A}^-]}{[\mathrm{AH}]}\right)$$

$$\mathrm{pH} = \mathrm{p}K_{MH+} + \log\left(\frac{[\mathrm{M}]}{[\mathrm{MH}^+]}\right)$$

$$\mathrm{p}K_a - \mathrm{p}K_{MH+} = \Delta\mathrm{pH} = \log\left(\frac{[\mathrm{M}][\mathrm{AH}]}{[\mathrm{MH}^+][\mathrm{A}^-]}\right)$$

These studies were conducted in PhCN due to the poor solubility of complexes **1** and **2** in MeCN. The pK_a^{MeCN} of the acids used in these measurements is estimated to be the pK_a^{PhCN}, an approximation that was made in similar work.[18]

In both studies, the metal complex was dissolved in 0.5 mL of PhCN. A 10 μL aliquot of acid solution was injected into a solution of the metal complex. 30 minutes after the addition of acid, the ratio M/MH$^+$ was recorded. The ratio was calculated using the singlet of the MH$^+$ species relative to the relatively well resolved doublet of the M species. The MH$^+$ singlet corresponds to two equivalent phosphorus centers in MH$^+$ while the doublet in M corresponds to a single phosphorus center. The ratio was rechecked after 24 hours to confirm the solution had reached equilibrium concentrations. This procedure was repeated with a second aliquot of acid.

Pyrrolidinium tetrafluoroborate (pK_a^{MeCN}=19.51) and benzoic acid (pK_a^{MeCN}=21.51) were chosen as the acids in the case of **1** and **2** respectively (see citation 16 in main text). Homoassociation was taken into consideration for the chosen acids (pyrrolidinium (p$K_{HB_2^+}$ = 1.5), benzoic acid (p$K_{HA_2^-}$ = 3.9)). In both cases the free base is approximated to completely bind to free acid in the following scheme: $A^- + HA \rightarrow HA_2^-$. In the case of benzoic acid, this assumption is especially valid due to the high homoassociation constant, but is a slightly weaker assumption in the case of pyrrolidinium (c.a. 98% homoassociation under the experimental conditions). Incorporating these assumptions yields the equation shown below.

$$\Delta\mathrm{pH} = \log\left(\frac{[\mathrm{M}][\mathrm{AH}]}{[\mathrm{MH}^+][\mathrm{HA}_2^-]}\right)$$

$$\text{where } [\mathrm{AH}] = [\mathrm{AH}]_{\mathrm{init.}} - 2[\mathrm{MH}]_{\mathrm{obs}}$$

$$[\mathrm{HA}_2^-] = [\mathrm{MH}]_{\mathrm{obs}}$$

The concentrations used for the determination of pK_a^{MeCN} for **1** and **2** are shown in Table 2.4.

Table 2.4. Experimentally determined quantities of M and MH^+ for [**1**] (gray) and [**2**] (pink), values of HA and A^- at equilibrium, and calculated values for pK_a.

1_{obs} (μmol)	**$[1H]^+_{obs}$ (μmol)**	**BH^+_{added} (μmol)**	**$BH^+_{equil.}$ (μmol)**	**$B_2H^+_{equil.}$ (μmol)**	**pK_a**
6.35	3.11	11.46	5.24	3.11	18.97
4.68	4.78	28.65	19.09	4.78	18.92
				Average	18.94
2_{obs} (μmol)	**$[2H]^+_{obs}$ (μmol)**	**HA_{added} (μmol)**	**$HA_{equil.}$ (μmol)**	**$HA_2^-{}_{equil.}$ (μmol)**	**pK_a**
7.157	3.173	7.295	0.949	3.173	21.68
5.242	5.008	14.007	3.991	5.008	21.62
				Average	21.65

Experimental Details for the Determination of the Rate of Electron Self-Exchange.

The determination of the rate of electron self-exchange was determined using the procedure described by Jameson and Anand.

In a nitrogen filled glove-box, 11.1 mg (13.9 μmol) of **1** was dissolved in 0.6 mL of THF-d_8 and dispensed into a Wilmad® low vacuum/pressure (LVP) gas tight NMR tube. 13.5 mg (12.9 μmol) of $FcBAr_4^F$ was dissolved in 0.2 mL of THF-d_8. Aliquots of the $FcBAr^F{}_4$ solution were added in 20 μL increments and the combined solution was mixed thoroughly. All additions were performed in a nitrogen-filled glove-box. ^{1}H-NMR spectra were recorded after each addition. The generated ferrocene was assumed to have negligible effect on the rate of electron self-exchange. The rate constant for electron self-exchange was determined using equation (4)

$$k_{ex} = \frac{4\pi\chi_p\chi_d(\Delta\nu)^2}{C_{tot}(w_{pd} - \chi_p w_p - \chi_d w_d)} \qquad (4)$$

where χ_p is the mole fraction of $[\mathbf{1}]^+$, χ_d is the mole fraction of **1**, $\Delta\nu$ is the frequency difference (*Hz*) of the measured resonances of pure diamagnetic and paramagnetic species C_{tot} is the total concentration of **1** and $[\mathbf{1}]^+$, w_{pd} is the line width at half-height of the observed resonance in a mixture of **1** and $[\mathbf{1}]^+$, w_p is the line width at half-height of pure $[\mathbf{1}]^+$, and w_d is the line width at half-height of pure **1**. Mole fractions for each species were calculated using the equation (5)

$$\chi_d = \frac{|\nu_{dp} - \nu_p|}{\Delta\nu} \qquad (5)$$

where ν_{dp} is the observed frequency (*Hz*) of the resonance in a mixture and ν_p is the observed frequency of the pure paramagnetic complex. $\chi_p + \chi_d = 1$ is assumed to be true. Chemical shifts were assumed to vary linearly with mole fraction. Line widths were measured manually. Line widths were only measured in spectra in which the resonance was unobscured. The resonances used for the determination of electron self-exchange were one of the dppe phenyl and the *p*-cymene methyl proton resonances. Other resonances could be distinguished, but accurate line widths were unobtainable due to overlap of other resonances.

Table 2.5. Frequencies and line widths of the *p*-cymene methyl proton resonance obtained from spectra of [**1**]^0, [**1**]$^+$, and mixtures of [**1**]^0 and [**1**]$^+$. Rates of electron self-exchange were calculated using eq. (1).

Entry	**Frequency (*Hz*)**	**Line Width (*Hz*)**	χ_d	χ_p	C_{tot} **(*mM*)**	$k_{ex} * 10^{-7}$
Pure [1]^0	858	2.3	1	0	---	---
1	393	92.7	0.676	0.324	20.3	0.976
2	249	113.6	0.575	0.425	19.7	1.057
3	114	138.3	0.481	0.519	19.1	0.910
4	−25	152.8	0.384	0.616	18.6	0.994
5	−175	164.0	0.280	0.720	18.0	1.182
Pure [1]$^+$	−576	192.9	0	1	---	---
				Average		1.0 ± 0.1

Table 2.6. Frequencies and line widths of the dppe phenyl A proton resonance obtained from spectra of [**1**]^0, [**1**]$^+$, and mixtures of [**1**]^0 and [**1**]$^+$. Rates of electron self-exchange were calculated using eq. (1).

Entry	**Frequency (*Hz*)**	**Line Width (*Hz*)**	χ_d	χ_p	C_{tot} **(*mM*)**	$k_{ex} * 10^{-7}$
Pure [1]^0	3676	2.3	1	0	---	---
1	4144	69.4	0.762	0.238	20.9	1.149
2	4309	93.0	0.678	0.322	20.3	1.056
3	4505	110.0	0.578	0.422	19.7	1.121
4	4691	126.8	0.483	0.517	19.1	1.087
5	4884	139.5	0.385	0.615	18.6	1.059
6	5092	146.8	0.279	0.721	18.0	1.037
Pure [1]$^+$	5640	130.1	0	1	---	---
				Average		1.09 ± 0.04

The assumption that the chemical shifts vary linearly with mole fraction was supported by plotting the frequency observed of multiple resonances and the calculated mole fraction; different resonances yielded the same mole fraction.

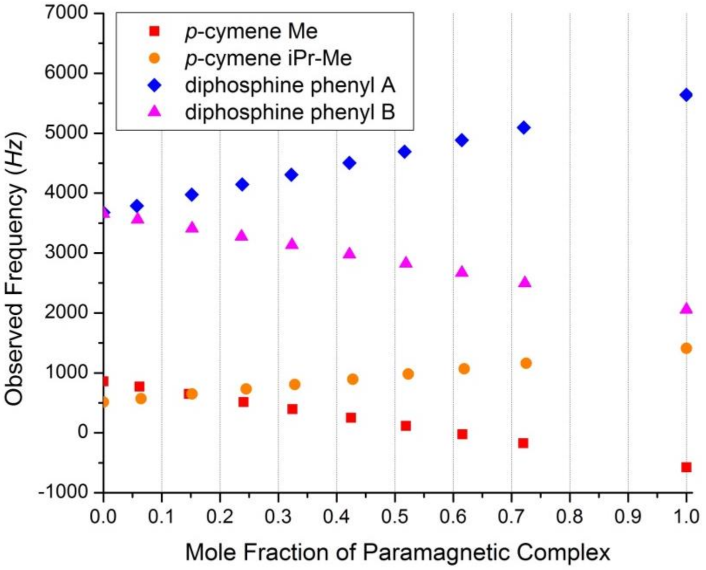

Figure 2.22. Plot of the observed frequencies of various resonances versus the mole fraction of [**1**]$^+$ in solution.

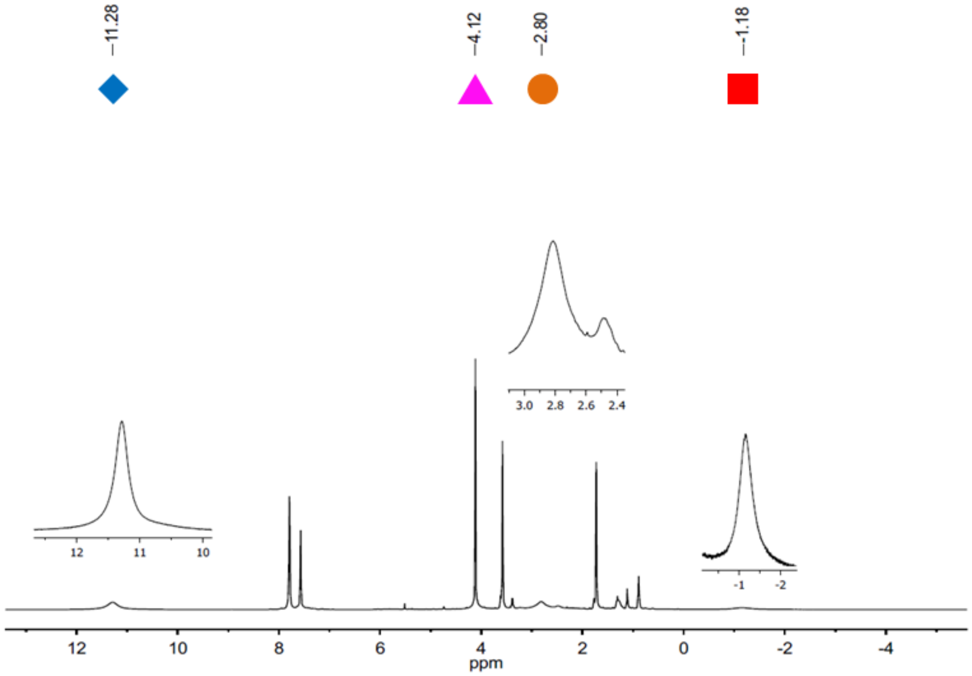

Figure 2.23. ^{1}H-NMR Spectrum of [**1**]$^+$. The labeled resonances correspond to those monitored in the generation of the plot shown in Fig. 2.22.

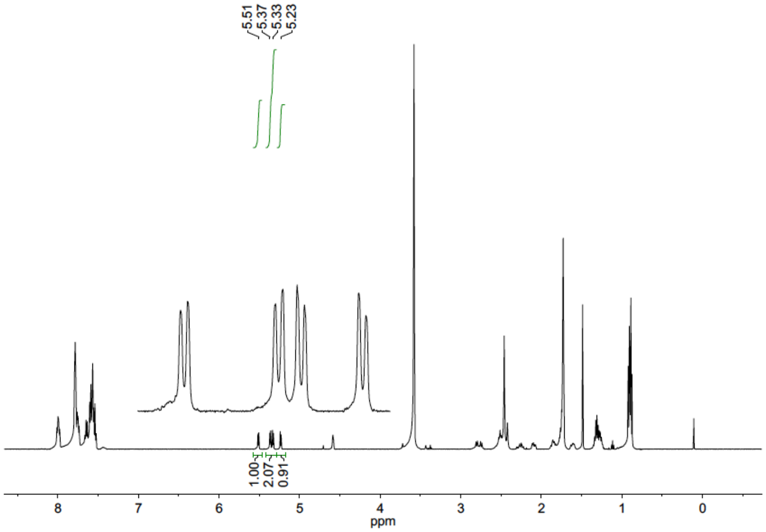

Figure 2.24. ^{1}H NMR spectrum of [**1**−H]BAr$^{F}{}_{4}$ in THF-d_8 at room temperature.

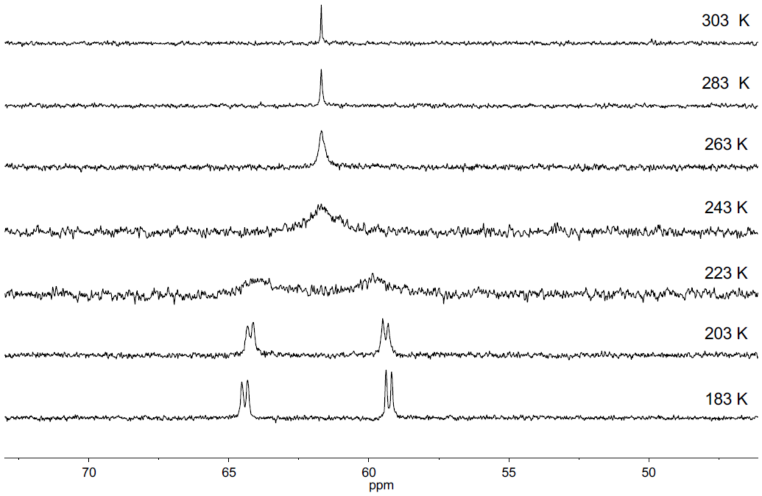

Figure 2.25. ^{1}H NMR spectrum of [**1**-H]BAr$^{F}{}_{4}$ in THF-d_8 at various temperatures.

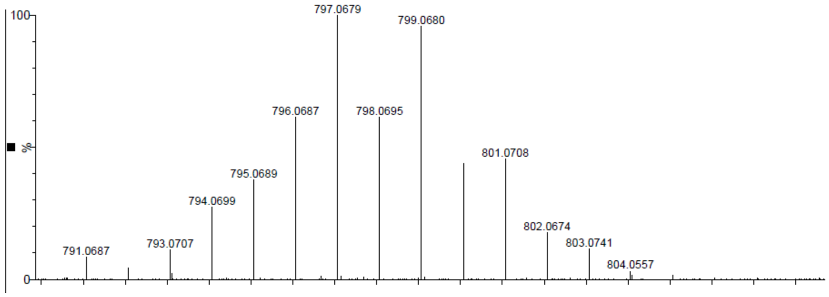

Figure 2.26. High resolution ESI mass spectrum of [**1**]BAr$^{F}{}_{4}$. m/Z_{obs} = 797.0679 and m/Z_{calc} = 798.0756.

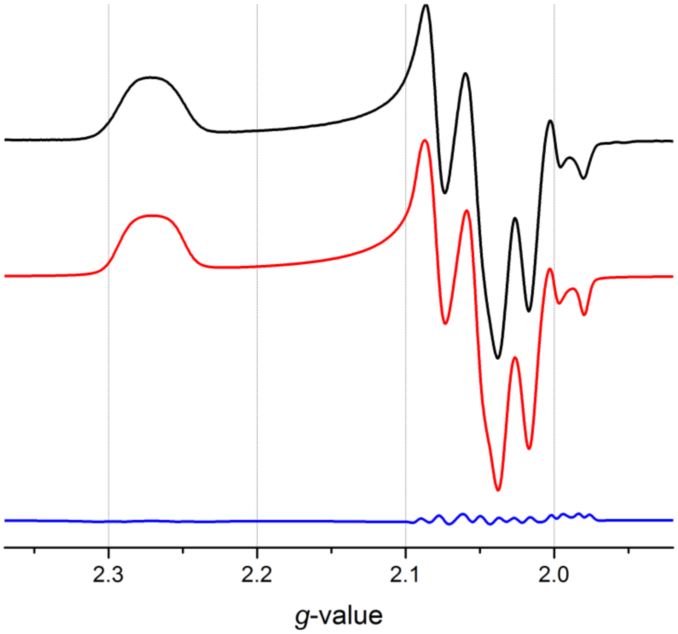

Figure 2.27. Experimental (black) and simulated (red) X-Band EPR spectra of [**2**]BAr$^F_4$ in frozen PhCl/PhMe solution at 110K. The spectrum was simulated as a two component system: the major component ([**2**]BAr$^F_4$) being present in 96.6% and an unknown impurity at 3.4%. Simulation parameters for major component: $g_x = 2.027$, $g_y = 2.066$, and $g_z = 2.271$; $A_{x1} = 93.12$, $A_{y1} = 120.40$, and $A_{z1} = 89.89$ MHz; $A_{x2} = 12.08$, $A_{y2} = 11.32$, and $A_{z2} = 45.24$ MHz. Simulation parameters for minor component: $g_x = 2.090$, $g_y = 2.001$, and $g_z = 1.980$.

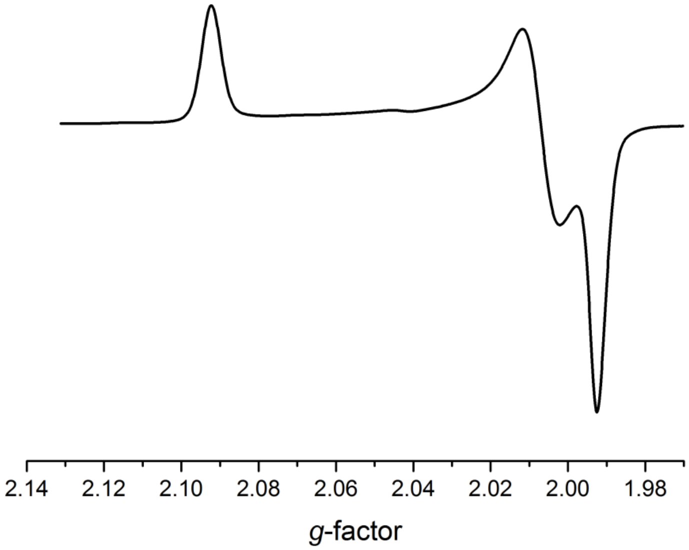

Figure 2.28. X-Band EPR spectrum of a frozen PhCl/PhMe solution (110 K) of [**2**]BAr$^F_4$ after sitting at room temperature for 48h showing the minor component present in a freshly prepared sample.

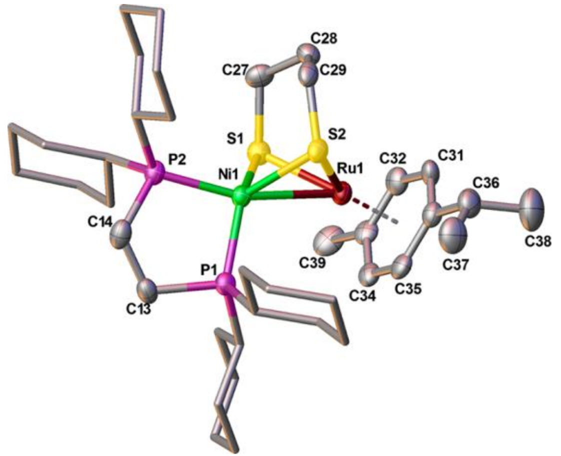

Figure 2.29. Structure of (cymene)Ru(pdt)Ni(dcpe) ([**2**]^0). Hydrogen atoms have been omitted for clarity. Selected distances (Å) and angles (deg): Ru−Ni, 2.6003(9); Ru-(cent), 1.718(8); Ru−C$_{av}$, 2.223(10); Ru−S$_{av}$, 2.335(2); S1−Ru−S2, 86.5(21); Ni−S$_{av}$, 2.256(2); S1−Ni−S2, 90.39(6); Ni−P2, 2.162(2); Ni−P1, 2.162(2); P1−Ni−P2 90.93(7).

2.14 References

(1) Lubitz, W.; Ogata, H.; Rüdiger, O.; Reijerse, E. *Chem. Rev.* **2014**, *114*, 4081.

(2) Li, Z.; Ohki, Y.; Tatsumi, K. *J. Am. Chem. Soc.* **2005**, *127*, 8950.

(3) Zhu, W. F.; Marr, A. C.; Wang, Q.; Neese, F.; Spencer, D. J. E.; Blake, A. J.; Cooke, P. A.; Wilson, C.; Schroder, M. *Proc. Natl. Acad. Sci. U. S. A.* **2005**, *102*, 18280.

(4) Barton, B. E.; Whaley, C. M.; Rauchfuss, T. B.; Gray, D. L. *J. Am. Chem. Soc.* **2009**, *131*, 6942.

(5) Barton, B. E.; Rauchfuss, T. B. *J. Am. Chem. Soc.* **2010**, *132*, 14877.

(6) Carroll, M. E.; Barton, B. E.; Gray, D. L.; Mack, A. E.; Rauchfuss, T. B. *Inorg. Chem.* **2011**, *50*, 9554.

(7) Schilter, D.; Nilges, M. J.; Chakrabarti, M.; Lindahl, P. A.; Rauchfuss, T. B.; Stein, M. *Inorg. Chem.* **2012**, *51*, 2338−2348.

(8) Schilter, D.; Rauchfuss, T. B.; Stein, M. *Inorg. Chem.* **2012**, *51*, 8931.

(9) Oudart, Y.; Artero, V.; Pecaut, J.; Fontecave, M. *Inorg. Chem.* **2006**, *45*, 4334.

(10) Ichikawa, K.; Nonaka, K.; Matsumoto, T.; Kure, B.; Yoon, K. S.; Higuchi, Y.; Yagi, T.; Ogo, S. *Dalton Trans.* **2010**, *39*, 2993.

(11) Ogo, S.; Kabe, R.; Uehara, K.; Kure, B.; Nishimura, T.; Menon, S. C.; Harada, R.; Fukuzumi, S.; Higuchi, Y.; Ohhara, T.; Tamada, T.; Kuroki, R. *Science* **2007**, *316*, 585.

(12) Matsumoto, T.; Kabe, R.; Nonaka, K.; Ando, T.; Yoon, K. S.; Nakai, H.; Ogo, S. *Inorg. Chem.* **2011**, *50*, 8902.

(13) Reynolds, M. A.; Rauchfuss, T. B.; Wilson, S. R. *Organometallics* **2003**, *22*, 1619.

(14) Kim, K.; Matsumoto, T.; Robertson, A.; Nakai, H.; Ogo, S. *Chemistry – An Asian Journal* **2012**, *7*, 1394.

(15) Connelly, N. G.; Geiger, W. E. *Chem. Rev.* **1996**, *96*, 877.

(16) Kütt, A.; Leito, I.; Kaljurand, I.; Sooväli, L.; Vlasov, V. M.; Yagupolskii, L. M.; Koppel, I. A. *J. Org. Chem.* **2006**, *71*, 2829.

(17) Kütt, A.; Leito, I.; Kaljurand, I.; Soovali, L.; Vlasov, V. M.; Yagupolskii, L. M.; Koppel, I. A. *J. Org. Chem.* **2006**, *71*, 2829.

(18) Carroll, M. E.; Barton, B. E.; Gray, D. L.; Mack, A. E.; Rauchfuss, T. B. *Inorg. Chem.* **2011**, *50*, 9554.

(19) Matsumoto, T.; Nagahama, T.; Cho, J.; Hizume, T.; Suzuki, M.; Ogo, S. *Angew. Chem. Int. Ed.* **2011**, *50*, 10578.

(20) Pfirrmann, S.; Limberg, C.; Ziemer, B. *Dalton Trans.* **2008**, *0*, 6689.

(21) Dong, Q.; Zhao, Y.; Su, Y.; Su, J.-H.; Wu, B.; Yang, X.-J. *Inorg. Chem.* **2012**, *51*, 13162.

(22) Crestani, M. G.; Muñoz-Hernández, M.; Arévalo, A.; Acosta-Ramírez, A.; García, J. J. *J. Am. Chem. Soc.* **2005**, *127*, 18066.

(23) Nilges, M. J.; Matteson, K.; Belford, R. L. In *ESR Spectroscopy in Membrane Biophysics, Biological Magnetic Resonance*; Hemminga, M. A., Berliner, L., Eds.; Springer: New York, 2007; Vol. 27.

(24) Wiedner, E. S.; Yang, J. Y.; Chen, S.; Raugei, S.; Dougherty, W. G.; Kassel, W. S.; Helm, M. L.; Bullock, R. M.; Rakowski DuBois, M.; DuBois, D. L. *Organometallics* **2011**, *31*, 144.

(25) Swart, M.; van Duijnen, P. T.; Snijders, J. G. *J. Comput. Chem.* **2001**, *22*, 79.

(26) Zhu, W.; Marr, A. C.; Wang, Q.; Neese, F.; Spencer, D. J. E.; Blake, A. J.; Cooke, P. A.; Wilson, C.; Schröder, M. *Proc. Natl. Acad. Sci.* **2005**, *102*, 18280.

(27) Foerster, S.; Stein, M.; Brecht, M.; Ogata, H.; Higuchi, Y.; Lubitz, W. *J. Am. Chem. Soc.* **2003**, *125*, 83.

(28) Stein, M.; van Lenthe, E.; Baerends, E. J.; Lubitz, W. *J. Am. Chem. Soc.* **2001**, *123*, 5839.

(29) Kampa, M.; Pandelia, M.-E.; Lubitz, W.; van Gastel, M.; Neese, F. *J. Am. Chem. Soc.* **2013**, *135*, 3915.
(30) McManis, G. E.; Nielson, R. M.; Gochev, A.; Weaver, M. J. *J. Am. Chem. Soc.* **1989**, *111*, 5533.
(31) Seyferth, D.; Womack, G. B.; Song, L. C.; Cowie, M.; Hames, B. W. *Organometallics* **1983**, *2*, 928.
(32) Huang, Y.; Etkin, N.; Heyn, R. R.; Nadasdi, T. T.; Stephan, D. W. *Organometallics* **1996**, *15*, 2320.
(33) Schenk, W. A. *Dalton Trans.* **2011**, *40*, 1209.
(34) Pool, D. H.; DuBois, D. L. *J. Organomet. Chem.* **2009**, *694*, 2858.
(35) Nicolet, Y.; de Lacey, A. L.; Vernede, X.; Fernandez, V. M.; Hatchikian, E. C.; Fontecilla-Camps, J. C. *J. Am. Chem. Soc.* **2001**, *123*, 1596.
(36) Bennett, M. A.; Huang, T. N.; Matheson, T. W.; Smith, A. K. *Inorganic Syntheses* **1982**, *21*, 74.
(37) Brookhart, M.; Grant, B.; Volpe, A. F. *Organometallics* **1992**, *11*, 3920.
(38) Barrière, F.; Geiger, W. E. *J. Am. Chem. Soc.* **2006**, *128*, 3980.
(39) Chambers, G. M.; Angamuthu, R.; Gray, D. L.; Rauchfuss, T. B. *Organometallics* **2013**, *32*, 6324.
(40) Chambers, G. M.; Mitra, J.; Rauchfuss, T. B.; Stein, M. *Inorg. Chem.* **2014**, *53*, 4243.
(41) Shelby, Q. D.; Lin, W.; Girolami, G. S. *Organometallics* **1999**, *18*, 1904.

Chapter 3:
Models of the Ni-L and Ni-SI$_a$ States of the Hydrogenase Active Site[†]

3.1 Introduction

The two most prominent paramagnetic states of the [NiFe]-H$_2$ase are the Ni(III)Fe(II) bridging hydride state Ni-C and Ni(I)Fe(II) state Ni-L; other paramagnetic states are generally inhibited or inactive. The Ni-C state has the distinction of being proposed in all catalytic mechanisms.[1-5] Despite the importance of this state, no synthetic analogues have been prepared with the characteristic Ni(III) hydride. The Ni-L state is the deprotonated version of Ni-C and was first generated by low temperature irradiation of the Ni-C state. Although first thought of as an artificial state, it has been shown to be stable at high pH's and is proposed to play a role in catalysis.[6]

The first reported S = ½ NiFe complex was [(diphos)Ni(pdt)Fe(CO)$_2$L]$^+$ (**R1**). Spectroscopic, crystallographic, and computational analyses show, however, that these cations are Ni(II)Fe(I) derivatives,[7,8] not Ni(I)Fe(II) as assigned to the Ni-L state of the enzyme.[9] This reversal is attributed to the Fe(CO)$_2$L center, which stabilizes Fe(I).

There are no known stable or transient Ni(III) species reported for NiFe model complexes, with or without hydrides. The cyanide containing model anion [(dppe)Ni(pdt)(μ-H)Fe(CN(BCF))$_2$(CO)]$^-$ (BCF = tris(pentafluorophenylborane)) was reported to have an irreversible oxidation that is iron-centered, generating an unstable Ni(II)Fe(III)H species (Scheme 3.1).[10] In chapter 2, the ruthenium based systems (dxpe)Ni(pdt)(μ-H)Ru(*p*-cymene)$^+$ (dxpe = dppe, dcpe) were found to have irreversible ruthenium centered oxidations, generating an unstable Ni(II)Ru(III)H^{2+} species. In order to stabilize trivalent nickel centers, stronger donor ligands are required at the nickel center.

Scheme 3.1. Iron Centered Oxidation of a Cyanide Containing NiFe Model

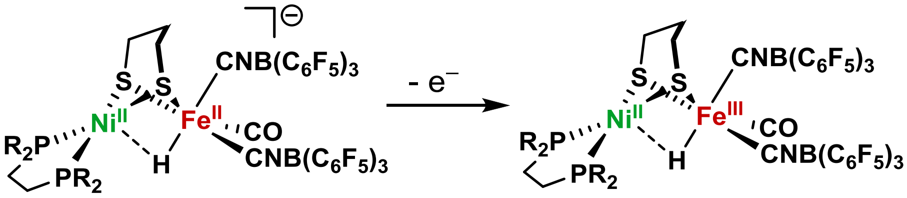

[†] Portions of this chapter are reproduced from the following publications with permission from the authors: Chambers, G. M.; Huynh, M. T.; Li, Y.; Hammes-Schiffer, S.; Rauchfuss, T. B.; Reijerse, E.; Lubitz, W. *Inorg. Chem.* **2015**.

As mentioned in the previous chapter, four-coordinate nickel complexes with strong field ligands are often tetrahedral in the zero and monovalent states while square-planar in the divalent state. In contrast, the NiFe active site changes only subtly as it converts between catalytic states.[9,11] Changing geometries following proton and electron transfer consequentially is a high reorganization energy process, such as the case in the transition between tetrahedral and square-planar nickel. Recent work on $(CO)_2LFe(xdt)Ni(dppe)$ (**R1**) and the palladium and platinum congeners shows that the coordination geometry at the group 10 metal has a drastic effects on the acid-base chemistry, and consequentially electrocatalysis.[12] This chapter addresses this weakness in the first generation of active site models to a degree.

The work presented in this chapter replaces the stereodynamic Ni(diphos) center with CpNi. This substitution addresses the two principal weaknesses addressed; the Cp ligand is well-known to form stable Ni(III) complexes,[13,14] and the Cp ligand minimizes reorganizational barriers. This substitution comes with the tradeoff of increasing the coordination number at nickel, which may have drastic influences on the reactivity.

The nickel center in CpNi complexes is relatively insensitive to redox in contrast to Ni(diphos)-based models (Figure 3.1). Not only does the hapticity of Cp not change, crystallographic studies show that the Ni-(C_5H_5) distances are relatively invariant (<0.12 Å) for Ni(I)-, Ni(II)-, and Ni(III)-(C_5H_5) compounds.[15-17]

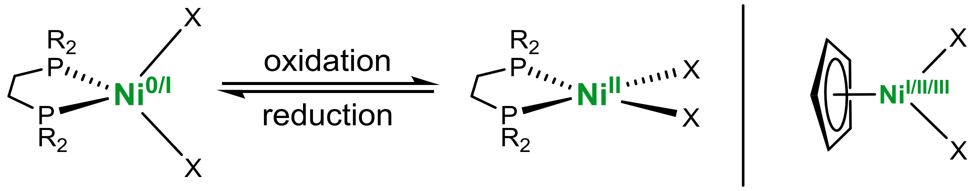

Figure 3.1. Ni-diphosphine-complexes change geometry upon reduction of tetrahedral $Ni^{0/I}$. The $Ni(C_5H_5)$ center is structurally invariant over three oxidation states.

3.2. Cyclopentadienylnickel Model Complexes: Models for Ni-SI_a

The reaction of $Fe(pdt)(CO)_2(dppe)$ and $[(C_5H_5)_3Ni_2]BF_4$ in nitromethane affords the salt $[(C_5H_5)Ni(pdt)Fe(dppe)(CO)]BF_4$, [**1a**]$BF_4$ (Scheme 3.2.) as a dark red powder. The derivatives $[(C_5H_5)Ni(pdt)Fe(dppv)(CO)]BF_4$ ([**1b**]BF_4), $[(C_5H_5)Ni(Me_2pdt)Fe(dppe)(CO)]BF_4$ ([**1c**]BF_4), and $[(CH_3C_5H_4)Ni(pdt)Fe(dppe)(CO)]BF_4$ ([**1d**]BF_4), (dppv = *cis*-1,2-$C_2H_2(PPh_2)_2$, Me_2pdt^{2-} = $Me_2C(CH_2S^-)_2$) were also prepared using the appropriate Ni and Fe precursors (Scheme 3.2). These salts are similar to [**1a**]BF_4 in terms of their reactivity and spectroscopic properties.

Scheme 3.2. Synthesis of the model complexes [**1a-d**]BF_4.

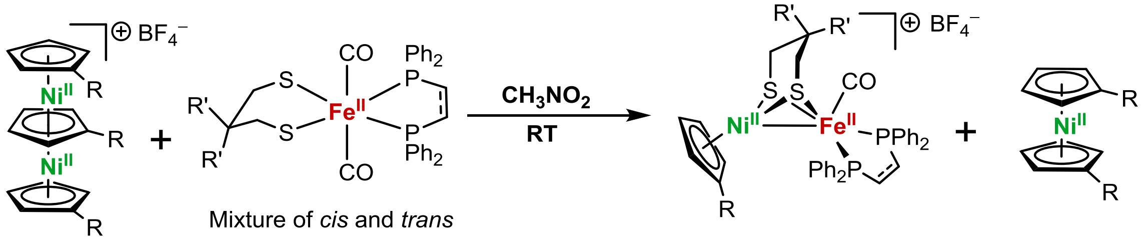

R = H, Me

R' = H, Me

[**1a**]BF_4 : R = H, R'= H, diphos = dppe
[**1b**]BF_4 : R = H, R' = H, diphos = dppv
[**1c**]BF_4 : R = H, R'= Me, diphos = dppe
[**1d**]BF_4 : R = Me, R'= H, diphos = dppe

The reaction of $Fe(pdt)(CO)_2(dppe)$ and $[(C_5H_5)_3Ni_2]BF_4$ proceeds via an intermediate with $\tilde{\nu}_{CO}$= 2050 cm^{-1} that converts to [**1a**]$^+$ (Figure 3.2, left) This intermediate band is assigned to the dicarbonyl complex *trans*-$[(C_5H_5)Ni(pdt)Fe(dppe)(CO)_2]BF_4$. The disappearance of the intermediate band follows first order decay (Figure 3.2, right). These data allow an estimated barrier for CO loss of 21 kcal/mol.

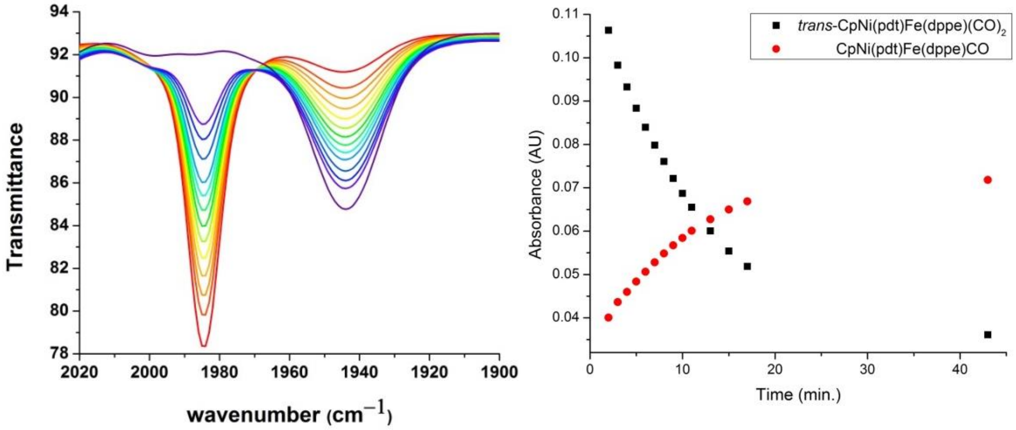

Figure 3.2. (Left) IR spectra from c.a. 5 minutes (red) to c.a. 50 minutes (purple) of the reaction of $[Cp_3Ni_2]BF_4$ and $Fe(pdt)(dppe)(CO)_2$. The product band ([**1a**]BF_4) occurs at 1943 cm^{-1}. Intervals for timepoint 1 to 10 are 1 minute, intervals for timepoints 11 to 13 are 2 minutes, and the final time point is after 50 minutes. (Right) IR absorbance versus time plot of the CO bands observed during the reaction of $[Cp_3Ni_2]BF_4$ and $Fe(pdt)(dppe)(CO)_2$. The half-life of the *trans*-$[CpNi(pdt)Fe(dppe)(CO)_2]$ product is ca. 480 sec., equating to an activation barrier of 21 kcal/mol under the experimental conditions.

When the reaction progress is monitored by ^{31}P-NMR spectroscopy, the iron precursor is consumed within c.a. 5 min and two new singlet resonances are observed, one of which corresponds to the product [**1a**]$^+$ (Figure 3.3). Additionally, ESI-MS of the reaction mixture indicates the presence of the molecular cation $[CpNi(pdt)Fe(dppe)(CO)_2]^+$. These observations are consistent with rapid attachment of "CpNi$^+$" to the two isomers of the iron(dithiolate). The *cis*-carbonyl derivative appears to release CO rapidly, whereas the isomer with *trans* CO ligands is somewhat persistent.

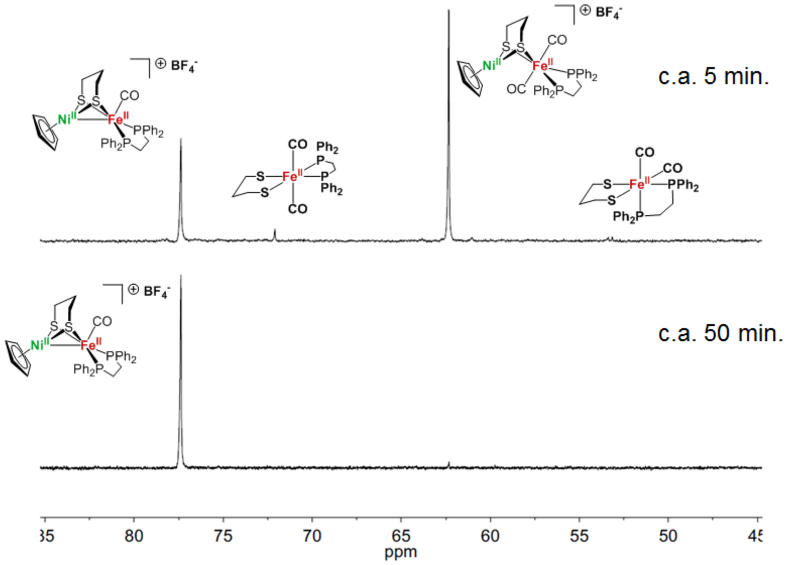

Figure 3.3. ^{31}P-NMR spectra of the reaction between $[Cp_3Ni_2]BF_4$ with $Fe(pdt)(CO)_2(dppe)$.

The purified compounds [**1a-d**]BF$_4$ display a single $\tilde{\nu}_{CO}$ band in the range 1940 - 1951 cm^{-1}, which is consistent with the presence of one isomer. These values are similar to those observed in Ni-SI$_a$, which range from 1927 to 1947 cm^{-1} (Table 3.1).[1]

Table 3.1. IR Data for Compounds [**1a-d**]BF$_4$ and [**2b**]BF$_4$ in CH_2Cl_2 Solution and the Ni-SI$_a$ State

Compound	Exp	Calc[a]
	$\tilde{\nu}_{CO}$ (cm^{-1})	
$[(C_5H_5)Ni(pdt)Fe(dppe)(CO)]BF_4$, ([**1a**]BF$_4$)	1943	1948/1946
$[(C_5H_5)Ni(pdt)Fe(dppv)(CO)]BF_4$, ([**1b**]BF$_4$)	1951	1951/1949
$[(C_5H_5)Ni(Me_2pdt)Fe(dppe)(CO)]BF_4$, ([**1c**]BF$_4$)	1940	1937/1935
$[(CH_3C_5H_4)Ni(pdt)Fe(dppe)(CO)]BF_4$, ([**1d**]BF$_4$)	1943	1947/1945
$[(C_5H_5)Ni(SPh)_2Fe(dppv)(CO)]BF_4$ ([**2b**]BF$_4$)	1956	1959
Ni-SI$_a$ (*D. vulgaris* Miyazaki F)[18]	1943	n/a
Ni-SI$_a$ (*A. vinlandii*)[18]	1931	n/a
Ni-SI$_a$ (*D. gigas*)[18]	1934	n/a

[a] The first value corresponds to the conformer in which the central CH_2 of the Fe(pdt)Ni core is oriented toward Fe, and the second value corresponds to the conformer in which the same CH_2 is oriented toward Ni. The calculations were performed in the absence of BF_4^-.

The structure of the cation [**1a**]$^+$ was determined by X-ray crystallography. The Ni-Fe distance is 2.5145(4) Å (Figure 3.4). This short distance is consistent with the presence of metal-metal bonding. Although the enzyme in the SI$_a$ state has not been characterized crystallographically, it is generally assumed that the Ni-Fe distance is ~2.6 Å in all active states.[1]

The stereochemistry of the $FeL_2(CO)$ site is biomimetic in the sense that CO occupies an apical site, and the two Lewis basic phosphine ligands are approximately trans to the sulfur centers of the thiolates.

The ^{31}P-NMR spectra of complexes [**1a-d**]BF_4 are simple, exhibiting only a single resonance, indicating either chemically equivalent phosphorus centers or a dynamic process. The diphosphine in complexes [**1a-d**]BF_4 is only observed in the dibasal arrangement, whereas other Fe(dithiolate)(diphosphine)CO compounds have been shown to adopt both a dibasal and an apical-basal arrangement.[19] The phosphorus centers remain NMR-equivalent at −90 ºC, suggesting either an exceptionally low barrier for isomerization or the presence of a single isomer. The possibility of apical-basal to dibasal isomerization is explored using DFT in a later section. In the IR spectra, only a single isomer is observed which has both donor ligands in basal positions, similar to the enzyme's active site.

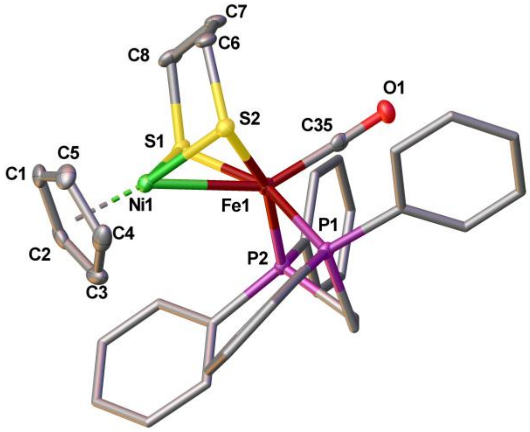

Figure 3.4. Solid state structure of [**1a**]BF_4 shown at the 50% probability level. Hydrogen atoms, counterions, and solvent have been omitted for clarity. Selected bond distances (Å): Ni1-Fe1, 2.5145(4); Ni1-Cent, 1.722(3); Ni1-S_{avg}, 2.1645(7); Fe1-S_{avg}, 2.2208(7); Fe1-C35, 1.757(2); C35-O1, 1.147(2).

The reaction of *cis,cis*-$Fe(SPh)_2(CO)_2$(dppv) and $[(C_5H_5)_3Ni_2]BF_4$ gave the dicarbonyl $[(C_5H_5)Ni(SPh)_2Fe(dppv)(CO)_2]BF_4$ ([**2b**CO]BF_4), isolated as dark, almost black microcrystals. The ^{1}H NMR spectrum of [**2b**CO]BF_4 exhibits only one Cp signal, and an AB quartet pattern in the ^{31}P NMR spectrum, indicating low symmetry. The structure was determined crystallographically (Figure 3.5). In contrast to [**1a-d**]BF_4, The Ni---Fe distance in [**2b**CO]BF_4 is quite long and is 3.308(1) Å. The stereochemistry at Fe is identical to the precursor, wherein all ligands are *cis*.

The dicarbonyl complex [**2b**CO]BF_4 is readily decarbonylated upon treatment with Me_3NO, to give [**2b**]BF_4 which is isolated as a black solid. The IR spectrum of [**2b**]BF_4 in CH_2Cl_2

solution displays a single $\tilde{\nu}_{CO}$ band at 1956 cm^{-1}, vs 2042, 2002 cm^{-1} observed for the precursor. The monocarbonyl cation [**2b**]$^+$ decomposes gradually in CH_2Cl_2 solutions; however, the complex is stable in MeCN and the $\tilde{\nu}_{CO}$ band shifts 22 cm^{-1} to higher energies, suggesting the formation of an adduct. The ^{31}P NMR spectrum of [**2b**]$^+$ exhibits a singlet at δ78.8 in CH_2Cl_2. Under 1 atm of CO, MeCN solutions of [**2b**]$^+$ partially convert back to [**2b**CO]$^+$. In contrast, [**1a**]$^+$ is not reactive towards CO.

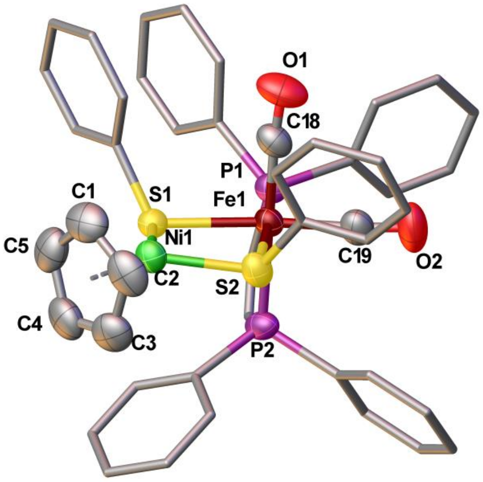

Figure 3.5. Solid-state structure of [**2b**CO]BF_4 shown at the 35% probability level with hydrogen atoms, counterion, and dichloromethane solvate omitted for clarity. The diffraction data were collected at room temperature. Selected bond distances (Å): Ni1-Fe1, 3.308(1); Ni1-cent, 1.754(9); Ni1-S_{avg}, 2.180(1); Fe1-S_{avg}, 2.353(1); Fe1-C18, 1.795(4); Fe1-C19, 1.796(4); C18-O1, 1.133(5); C19-O2, 1.129(5). Fe1-P1, 2.252(1); Fe1-P2, 2.291(1).

3.3. Electrochemistry of the Cyclopentadienylnickel Model Complexes

The cyclic voltammetry of [**1a**]BF_4 in dichloromethane is very rich (Figure 3.6). Compounds [**1b-d**]$^+$ produce similar voltammograms (Table 3.2). Compounds [**1a-d**]$^+$ exhibit an irreversible oxidation near +0.65 V vs Fc$^{0/+}$, a reversible one-electron reduction near −1.20 V. Additionally, a quasi-reversible reduction is observed near −2.15 V, which becomes fully reversible when in THF with $[Bu_4N]BAr_4^F$ as electrolyte. An irreversible reduction wave is generated at ca. 0.0 V vs Fc$^{0/+}$ following the irreversible oxidation.

The redox couples in the different derivatives are relatively similar. The reversible couple is most affected by substitution of pdt with Me_2pdt. The donor properties of pdt^{2-} and Me_2pdt^{2-} are similar in this system, as indicated by the observed $\tilde{\nu}_{CO}$ difference of 3 cm^{-1} (Table 3.1). Thus, the difference of 70 mV in the potential of the Ni^{II}Fe^{II}/Ni^{I}Fe^{II} redox couple observed between the Me_2pdt derivative [**1c**]BF_4 and [**1a**]BF_4 may be due to the steric effects of the methyl groups.

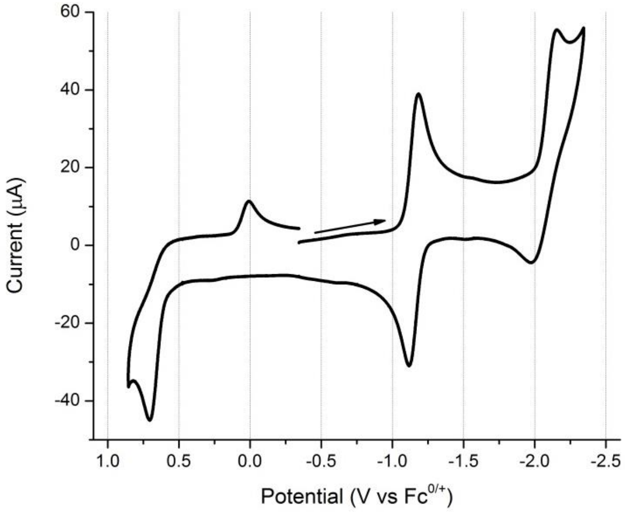

Figure 3.6. Cyclic voltammogram of [**1a**]BF_4 at 500 mVs^{-1}. Conditions: ~1 mM in CH_2Cl_2, 100 mM $[NBu_4]PF_6$, glassy carbon electrode (d = 3 mm); Ag wire as pseudoreference with internal Fc standard at 0 V; Pt counter electrode.

Table 3.2. Electrochemical Properties of Compounds [**1a-d**]$^+$ (V vs Fc$^{+/0}$ in CH_2Cl_2).[a]

Compound	$E_{p, ox}$ ($Ni^{II}Fe^{II}/Ni^{III}Fe^{II}$)	Calc[b,c]	$E_{½}$ ($Ni^{II}Fe^{II}/Ni^{I}Fe^{II}$)	Calc[b,c]	$E_{p, red}$[d] ($Ni^{I}Fe^{II}/Ni^{I}Fe^{I}$)	Calc[b,c,d]
[**1a**]BF_4	0.70	0.70	−1.16	−1.16	−2.15	−2.15
[**1b**]BF_4	0.72	0.73	−1.15	−1.12	−2.18	−2.05
[**1c**]BF_4	0.67	0.76	−1.09	−1.16	−2.15	−2.12
[**1d**]BF_4	0.62	0.66	−1.21	−1.23	−2.17	−2.18

[a] For the calculated values, the central CH_2 of the Fe(pdt)Ni core is oriented toward Fe and assumed to remain in this orientation upon reduction or oxidation. Additional calculated values corresponding to the same CH_2 being oriented toward Ni, or flipping from Fe to Ni, are available in the Supporting Information (Tables S1-S2). In all cases, the conformation of the Fe(pdt)Ni core does not affect the potential. [b] [**1a**]BF_4 was used as the reference so the experimental and calculated values agree by construction. [c] The calculations were performed on the positively charged species in the absence of BF_4^-. [d] This wave is assigned to a Ni^IFe^{II}/Ni^IFe^I couple, where the Ni^IFe^I state is an open-shell singlet.

The reversible reduction of the MeCp derivative [**1d**]BF_4 is shifted to more positive potentials by 50 mV compared to [**1a**]BF_4, indicating that this couple is likely nickel centered. This effect suggests that the reduction is nickel centered, generating a Ni^IFe^{II} species. MeCp substitution most affected the oxidation observed at ≈0.75 V, shifting this couple by −80 mV, whereas other substitutions only generate a 20-30 mV effect. This observation suggests that oxidation is Ni-centered, generating a formally Ni(III)Fe(II) species. The reduction near −2 V is negligibly affected by the Ni-based ligands, and is proposed to be an Fe-centered reduction, generating a Ni(I)Fe(I) species.

DFT was used to calculate the potentials associated with the couples [**1a-d**]$^{2+/+}$, [**1a-d**]$^{+/0}$, and [**1a-d**]$^{0/-}$. The potentials were calculated relative to [**1a**]BF_4 and are provided in Table 3.2. The experimental trends are reproduced well by the calculations. The BF_4^- ions were not included in the calculations, which may explain deviations between the calculated and experimental values.

3.4 Reduction of the Cyclopentadienylnickel Models: Models for Ni-L

The reduced species **1a**-**d** and **2b** were produced on a preparative scale by treatment with $(C_5H_5)_2Co$ ($E^0 = -1.23$ V, Scheme 3.3). Purified samples **1a-d** and **2b** were isolated as black, air-sensitive solids. Reduction of [**1a-d**]$^+$ and [**2b**]$^+$, a Ni^{II}Fe^{II}/Ni^{I}Fe^{II} couple, shifts $\tilde{\nu}_{CO}$ by ca. 40 cm^{-1} to around 1900 cm^{-1} (Table 3.3). A similar change is observed for reduction of $[(dppe)Ni(pdt)Fe(CO)_3]^+$, a Ni^{II}Fe^{I}/Ni^{I}Fe^{I} couple, ($\Delta\tilde{\nu}_{CO} \approx 35$ cm^{-1}).[7] Oxidation state changes centered at iron typically shift $\tilde{\nu}_{CO}$ by ca. 100 cm^{-1} as observed for in $[(dppe)Pt(pdt)Fe(CO)_3]^{+/0}$, a Pt^{II}Fe^{I}/Pt^{II}Fe^{0} couple.[20] For the Ni-L state of the [NiFe]-hydrogenases, values of $\tilde{\nu}_{CO}$ range from 1911 (*D. vulgaris* Miyazaki F)[21] to 1862 cm^{-1} (*A. aeolicus*).[22,23]

Scheme 3.3. Reduction of [1a-d]BF$_4$

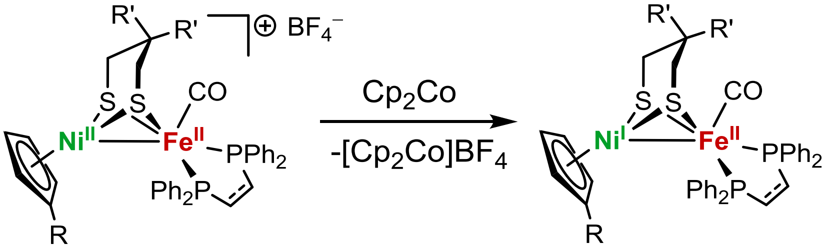

Table 3.3. IR Data for $\tilde{\nu}_{CO}$ in Compounds **1a-d** and **2b** in CH_2Cl_2 Solution.

Compound	**Expt** $\tilde{\nu}_{CO}$ (cm^{-1})	**Calc**^{a} $\tilde{\nu}_{CO}$ (cm^{-1})
1a	1901	1901/1901
1b	1903	1909/1906
1c	1897	1898/1899
1d	1898	1900/1900
2b	1915	1911

^{a}The first value corresponds to the isomer in which the central CH_2 of the Fe(pdt)Ni core is oriented toward Fe, and the second value corresponds to the isomer in which the same CH_2 is oriented toward Ni.

X-ray crystallographic analysis confirmed that the solid state structures of **1a** (Figure 3.7) and [**1a**]$^+$ (Figure 3.4) are very similar. The principal changes in these structures are in the coordination sphere of nickel, which further suggest that the couple [**1a**]$^{+/0}$ involves a Ni-centered reduction. The Ni-(C_5H_5) and Ni-S bonds elongate by about 5% while the Fe-ligand bond lengths remain virtually unchanged. The Ni-Fe distance shortens by ~0.1 Å to 2.4593(5) Å, which is well within the sum of the atomic radii (2.56(6) Å), indicating metal-metal bonding is still present. Although there are no crystallographic data on the metal-metal bonded Ni-L state of the enzyme, DFT calculations predict this distance to be 2.56 Å.[24] The observed structural changes are consistent with reduction at the nickel center in the transformation of [**1a**]$^+$ to **1a**. The DFT optimized structures of [**1a**]$^+$ and **1a** were in excellent agreement with the crystal structures (Table 3.4).

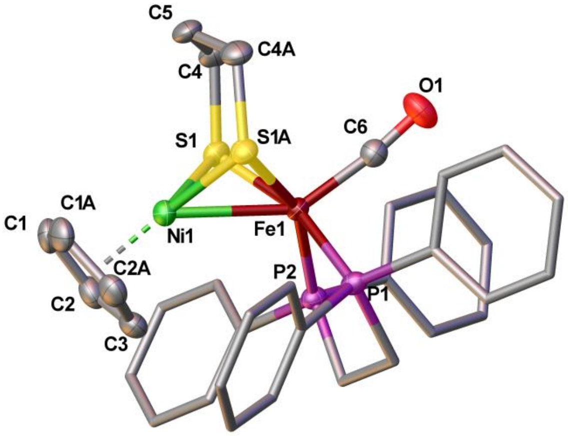

Figure 3.7. Solid state structure of **1a** shown at the 50% probability level. Hydrogen atoms and solvent have been omitted for clarity. Selected bond distances (Å): Ni1-Fe1, 2.4593(6); Ni1-Cent, 1.795(3); Ni1-S_{avg}, 2.2772(5); Fe1-S_{avg}, 2.2544(5); Fe1-C6, 1.745(3); C6-O1, 1.159(3).

Table 3.4. Key Bond Distances (Å) in [**1a**]BF_4, **1a,** and the Difference from Crystal Structures and DFT Calculations.

Bond	[1a]BF_4	Calc	1a	Calc	Experimental Difference	DFT Difference
Ni-Fe	2.5145(4)	2.566	2.4593(5)	2.508	−0.055	−0.058
Ni-centroid	1.722(3)	1.739	1.795(3)	1.814	+0.073	+0.075
Ni-S_{avg}	2.1645(7)	2.168	2.2772(5)	2.259	+0.113	+0.091
Fe-S_{avg}	2.2208(7)	2.236	2.2544(5)	2.252	+0.034	+0.016
Fe-P_{avg}	2.2256(7)	2.249	2.235(8)	2.236	+0.009	−0.013
Fe-C	1.757(2)	1.721	1.745(3)	1.727	−0.012	+0.006
C-O	1.147(2)	1.171	1.159(3)	1.174	+0.012	+0.003

DFT analysis of the spin density was used to determine the site of reduction of [**1a-d**]$^{+}$. The plot of the spin density for **1a** (Figure 3.8) reveals that the unpaired electron resides primarily on the Ni center, with some delocalization onto the pdt^{2-} and $(C_5H_5)^{-}$ ligands, but no significant delocalization onto the Fe. This result is consistent with the Ni(I)Fe(II) assignment and the experimentally observed elongation of the Ni-ligand bonds upon reduction of [**1a**]$^{+}$.

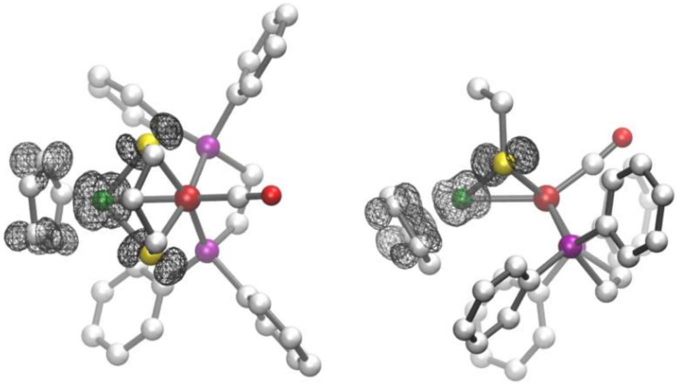

Figure 3.8. Views of the isocontour plot of the spin density for **1a**, looking down the Ni-Fe bond (left) and from the side of the Ni-Fe bond (right). The spin density is localized about the Ni coordination sphere. Color scheme: green, Ni; maroon, Fe; yellow, S; purple, P; red, oxygen; white, C. The hydrogens have been removed for clarity.

The spin densities for the reduced species **1a-d** and **2b** are given in Table 3.5 and consistently indicate a Ni-based reduction across all species. As observed for related NiFe dithiolate complexes,[7,20] the spin densities are not significantly affected by the conformation of the pdt ligand. Furthermore, the calculations also predict that an Fe-based reduction would require potentials 0.2–0.4 V more negative than the experimentally observed Ni-based reduction potentials.

Table 3.5. Calculated Spin Densities in Mixed-Valence Species **1a**-**d** and **2b**.[a]

Compound	Ni	Fe	2S	C_5H_5
1a	0.71	−0.17	0.24	0.24
	0.71	−0.19	0.23	0.25
1b	0.69	−0.16	0.22	0.25
	0.69	−0.17	0.22	0.25
1c	0.69	−0.15	0.22	0.24
	0.71	−0.20	0.24	0.25
1d	0.69	−0.17	0.23	0.25[b]
	0.70	−0.19	0.23	0.26[b]
2b	0.72	−0.20	0.20	0.26

[a] For each complex, the first entry corresponds to the isomer in which the central CH_2 of the Fe(pdt)Ni core is oriented toward the Fe center, and the second entry corresponds to the isomer in which the same CH_2 is oriented toward the Ni center. [b] For **1d**, this is the spin density over the $CH_3C_5H_4$ ligand.

Due to the minor structural differences between [**1a**]$^+$and **1a**, one might expect a fast electron self-exchange rate between these species. Indeed, ^{1}H-NMR mixtures of these two species exhibits one resonance that appears at a chemical shift that is the weighted average of the chemical shifts of the individual components (Figure 3.9). The Cp ligand, which is attached to the atom with the majority of the spin density, is not observed in the ^{1}H-NMR spectrum in a 13:87 **1a**:[**1a**]$^+$ mixture even at extreme high and low fields. The electron self-exchange rate from derived from these spectra are on the order of 10^6 s^{-1}, similar to that of ferrocene.[25]

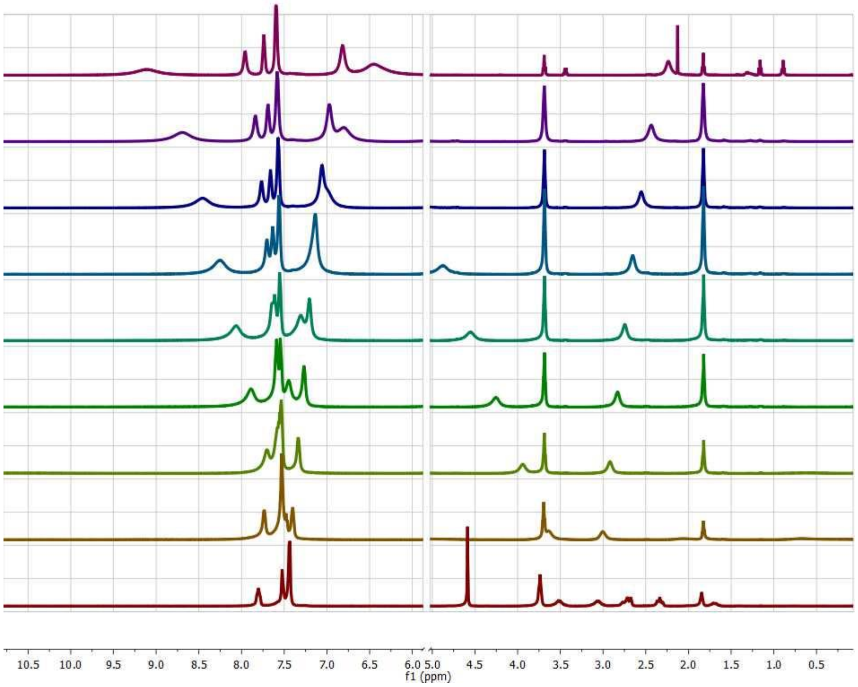

Figure 3.9 ^{1}H-NMR spectra of [**1a**]BF_4 (bottom, red) with increase amounts of Cp_2Co added (ascending). The final, top spectrum is of isolated **1a**.

Crystallographic analysis revealed that the structure of **2b** differs strongly from that of **1a** (Figure 3.10). Specifically the Fe center is inverted such that the CO ligand is poised between the Fe and Ni centers (Scheme 3.4).

Scheme 3.4. Rotation of the CO group upon reduction of [**2b**]$^+$

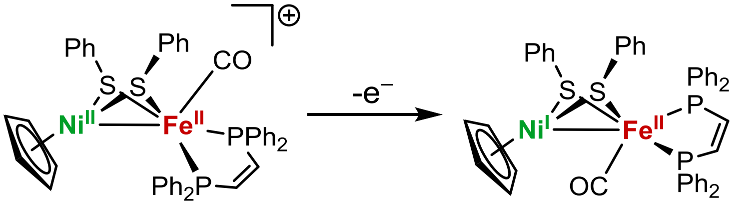

The CO ligand is not bridging as indicated by the long Ni---CO distance of 2.878 Å. The DFT optimized geometry of **2b** is in good agreement with the crystal structure and the Ni---CO distance is calculated to be 2.916 Å. Furthermore, the $\tilde{\nu}_{CO}$ for **2b** is calculated to be 1911 cm^{-1} for the rotated structure, close to the observed value of 1915 cm^{-1}. A small shoulder at approximately 1900 cm^{-1} is also observed in the spectrum that may result from the presence of a second rotamer. For **2b**, the isomer in which the CO is apical, as it is in the structure of [**2b**]$^{+}$, is calculated to be higher in free energy by 3.70 kcal/mol compared to the isomer in which the CO ligand is poised between the Fe and Ni centers. This free energy difference is consistent with the crystal structure of **2b** featuring an inverted Fe center.

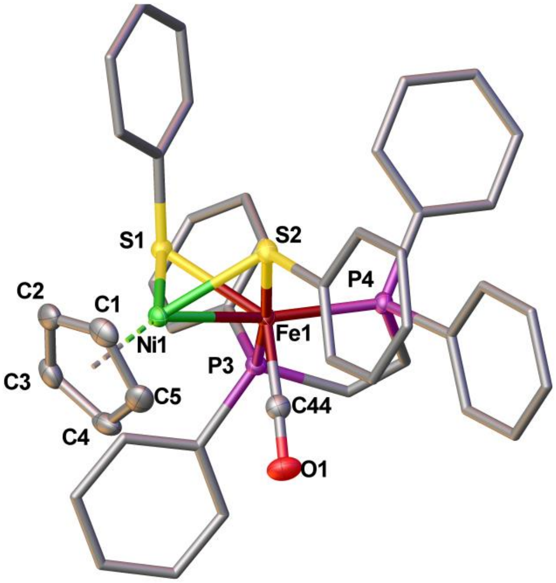

Figure 3.10. Solid state structure of **2b** shown at the 50% probability level. Hydrogen atoms and solvent have been omitted for clarity. Selected bond distances (Å): Ni1-Fe1, 2.4594(3); Ni1-cent, 1.817(2); Ni1-S$_{avg}$, 2.3067(5); Fe1-S$_{avg}$, 2.2868(5); Fe1-P$_{avg}$, 2.1934(5); Fe1-C44, 1.738(2); C44-O1, 1.162(2).

3.5 Models for Ni-L: EPR Spectroscopy

The X-band CW-EPR spectrum of **1a** is rhombic with *g*-values of 1.991, 2.031, and 2.138 with no hyperfine coupling observed (Figure 3.11). Spectra of **1b-d** are very similar to **1a** (Table 3.6). The absence of significant ^{31}P hyperfine coupling is consistent with a nickel centered radical, indicating that these compounds feature (C_5H_5)Ni(I) centers. In contrast, large ^{31}P hyperfine coupling was observed in related mixed-valence compounds containing Fe(I) phosphine centers, e.g., [(CO)$_2$(PR$_3$)Fe(pdt)Ni(diphosphine)]$^{+}$.[7,8]

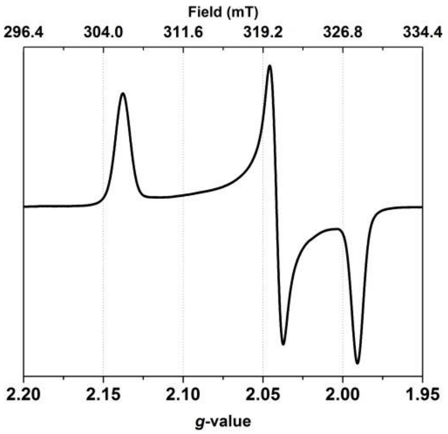

Figure 3.11. X-band CW-EPR spectrum of ~2 mM frozen solution of **1a** in 1:1 CH_2Cl_2/THF (110K).

Table 3.6. EPR Parameters for Compounds **1a-d** and **2b** (frozen CH_2Cl_2/toluene solution at 110 K) and the Ni-L State in *D. gigas*.[1]

Compounds	g_1, g_2, g_3
1a	1.991, 2.031, 2.138
1b	1.987, 2.031, 2.134
1c	1.997, 2.031, 2.134
1d	1.987, 2.039, 2.130
2b	1.984, 2.039, 2.143
Ni-L1 (*D. vulgaris*)	2.046, 2.118, 2.296

Q-band ENDOR experiments were conducted to probe the spin distribution in the mixed-valence state. Consistent with the absence of obvious hyperfine splitting in the CW-EPR spectrum, the ^{31}P hyperfine couplings were found to be very small (~11 MHz) (Table 3.7). Several proton hyperfine contributions were detected using ENDOR spectroscopy with hyperfine splittings ranging from 4 to 11 MHz. The variant of complex **1a** carrying C_5D_5 (**1a**-*d*$_5$) in place of C_5H_5 afforded a greatly simplified ^{1}H ENDOR pattern with the largest proton coupling (~11 MHz) being absent (Figure 3.12), indicating that the spin density is localized on the Ni and its immediate coordination sphere. The weaker ^{1}H couplings observed for **1a**-*d*$_5$ are assigned to the methylene protons of pdt^{2-}. These observations are consistent with the DFT analysis, which shows that the spin density in **1a** and **2b** is primarily localized on the (C_5H_5)Ni(pdt) center (Figure 3.8, Table 3.5). Despite the different stereochemistry at Fe, at least in the solid state, and the presence of SPh$^-$ vs R$_2$pdt^{2-}, the CW-EPR spectra of all mixed valence compounds are similar.

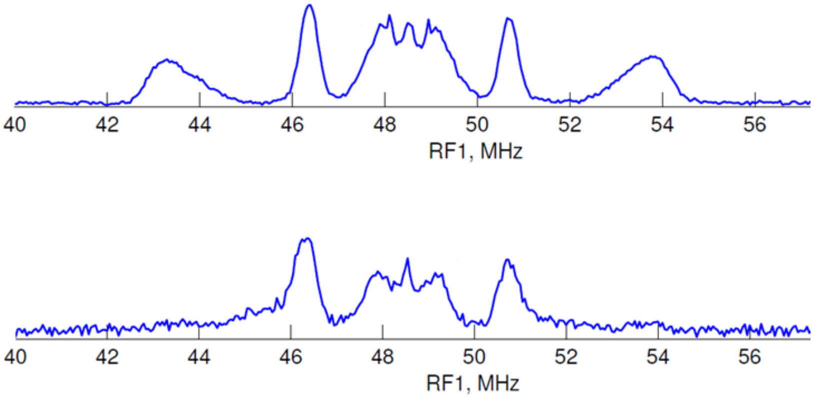

Figure 3.12. (Top) Q-band Davis ENDOR of **1a** in proton frequency range. (Bottom) Q-band Davis ENDOR of **1a-*d*₅** in proton frequency range.

The **1a**-d_5 orientation-selective ENDOR patterns could be simulated with one proton hyperfine interaction. Although, in principle, up to nine protons (Cp + $CH_2(C\mathit{H}_2S)_2$) could contribute to the ^1H ENDOR spectra of **1a**, only one additional contribution, assigned to the Cp ligand, could be distinguished and evaluated. The simulation parameters of the Cp and pdt contributions are given in Table 3.7.

Table 3.7. Hyperfine Couplings in **1a** from Q-band ENDOR and Applied Field Mössbauer Measurements.

Nucleus	**HFI Exp. (MHz)**		
	A_1	A_2	A_3
$C_5{}^1H_5$	−4.86	+3.25	−11.25
$CH_2(C^1H_2S)_2$ (pdt)	7.3	4.4	4.36
^{31}P	11.1	11.3	12.7
^{57}Fe	−3.8	−0.73	−0.9

3.6 Models for Ni-L: Mössbauer Spectroscopy

The measured Mössbauer spectra of **1a-c** and the corresponding cations are quite similar. All exhibit low isomer shifts of δ = 0.11 to 0.14 mm/s and small quadrupole splittings of ΔE_q = 0.72 to 1.15 mm/s (Table 3.8). The Mössbauer data are in agreement with a low-spin iron in all complexes. Consistent with other data in this paper, the spectra support the oxidation state assignments of Ni(II)Fe(II) for compounds [**1a-c**]BF_4 and Ni(I)Fe(II) for compounds **1a-c**. The isomer shifts observed in the Ni(I)Fe(II) compounds **1a-c** are larger than the shift observed for the Ni(II)Fe(I) compound [(dppe)Ni(pdt)Fe(CO)$_3$]BF_4 (δ = 0.04 mm/s), while the quadrupole splittings are comparable (ΔE_q = 0.57).[7] Mössbauer data for the [NiFe]-hydrogenases are sparse and suffer from difficulties in identifying and correcting for the dominating subspectra of the accessory FeS clusters.[26,27] Isomer shifts in the range of 0.05-0.15 mm/s have been assigned to the iron center of the [NiFe] center.[28]

Table 3.8. Mössbauer Parameters for Compounds [**1a-c**]BF_4, **1a-c**, and Ni-SI_a in Regulatory Hydrogenase (RH) from *Ralstonia eutropha.*

Compound	**δ** **mm/s**	**ΔE_q[a]** **mm/s**	**η**
[**1a**]BF_4	0.11	1.15	
[**1b**]BF_4	0.11	1.10	
[**1c**]BF_4	0.12	0.87	
1a	0.14	−0.73	0.13
1b	0.13	−0.72	
1c	0.13	−0.76	
Ni-SIa *RH* (*R. eutropha*)	0.10	1.60	

[a]ΔE_q Signs for **1a-c** are obtained from magnetic Mössbauer spectra.

The Mössbauer spectrum of **1a** was further examined at high magnetic fields. This spectrum shows a very weak internal field contribution with an isotropic ^{57}Fe hyperfine coupling of 2 MHz. For comparison, magnetic Mössbauer spectra of the Fe(I) center in the H_{ox} state of the [FeFe]-hydrogenase indicate ^{57}Fe hyperfine couplings in the range 10-20 MHz.[29,30] The weak coupling is consistent with the spin being localized on the nickel center.

3.7. Electronic Structure Analysis of the Metal-Metal Bonding in 1a-d and [1a-d]$^+$

The geometries of the various species were optimized using DFT/BP86 and compared to the available experimental data to further probe the electronic structure of [**1a-d**]$^+$ and **1a-d**. The optimized geometries are in good agreement with the X-ray crystal structures. Relevant bond lengths for [**1a**]$^+$ and **1a** are compared in Table 5. The BF_4^- counterions were not included in the geometry optimizations, which may introduce minor discrepancies between the X-ray crystal structure and the DFT optimized structure. Comparisons between the DFT and X-ray crystal structures for species [**1b-d**]$^+$ and **2b** as well as structural and energetic information for all systems studied. Moreover, the CO stretching frequencies ($\tilde{\nu}_{CO}$) calculated with DFT are also in good agreement with experimental data.

The short Ni–Fe distances in both [**1a**]$^+$ and **1a** suggest the presence of metal-metal bonding interactions. According to previous analyses, such Ni-Fe bonds typically arise from overlap of the d_{z^2} orbitals.[20,31,32] Interestingly, however, the nature of the Ni-Fe bonding is quite different between [**1a**]$^+$ and **1a**, as revealed by analysis of the bonding molecular orbitals localized using the Pipek-Mezey criteria.[33] For [**1a**]$^+$, the bonding orbital (Figure 3.13, left) reveals a dative Ni→Fe 2-center, 2-electron bond, which resembles a Lewis acid-base type interaction between the d^8 Ni(II) and d^6 Fe(II) centers. In contrast, for **1a**, a more covalent 2-center, 2-electron bond is present (Figure 3.13, right), in which the Ni and Fe d_{z^2} orbitals contribute equally to the bonding orbital. The formation of a stronger *σ*-bond in **1a** is consistent with the experimentally observed contraction of the Ni-Fe bond distance from 2.51 Å in [**1a**]$^+$ to 2.46 Å in **1a**. This Ni-Fe bond length contraction is also found in the DFT-optimized structures (Table 3.5). These chemical bonding patterns are similar for [**2b**]$^+$ and **2b**, indicating that the stereochemistry at Fe and the presence of SPh^- or R_2pdt^{2-} does not disrupt the Ni-Fe bond.

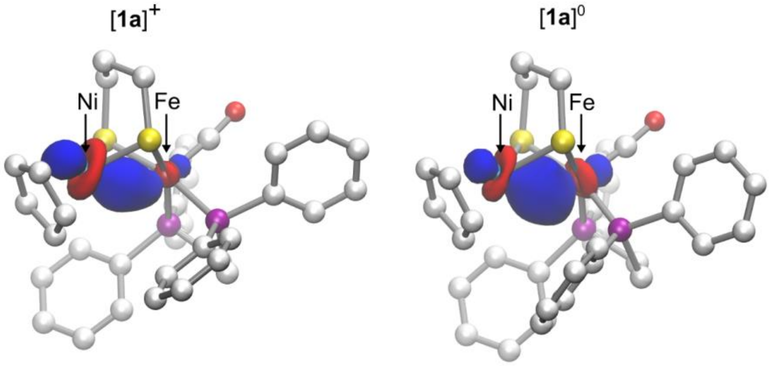

Figure 3.13. Pipek-Mezey localized molecular orbitals showing the Ni-Fe *σ*-bonds in [**1a**]$^+$ and **1a**. The composition of the MO in [**1a**]$^+$ is 85% Ni and 15% Fe, and the composition of the MO in 1a is 53% Ni and 47% Fe. Only the α orbital is shown for 1a; however, the β orbital is similar.

3.8 Protonation of Ni-L Model.

Upon treatment with ≥ 1 equiv. acid, solutions of **1a** liberate H_2 and generate [**1a**]$^+$ (Scheme 3.5).

Scheme 3.5. Reaction between **1a** and acids yielding [**1a**]$^+$ and 0.5 equiv. of H_2

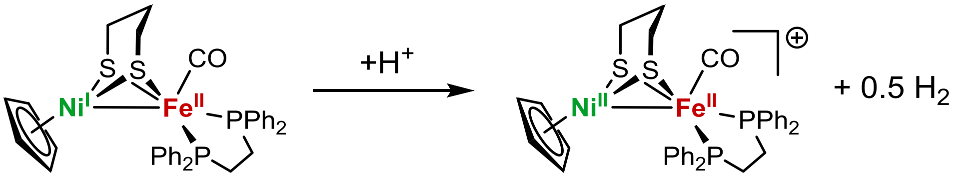

Hydrogen evolution was observed for HBF_4, *p*-toluenesulfonic acid (pK_a^{MeCN} = 8.01), and [pyridinium]BF_4 (pK_a^{MeCN} = 12.33), but not for $[NH_4]PF_6$ (pK_a^{MeCN} = 14.46). The yield of H_2 was determined to be 0.44 equiv. by gas chromatography, with 0.5 equiv. predicted with **1a** functioning as a $1e^-$ reductant.

The protonolysis of **1a** to give [**1a**]$^+$ entails the conversion of an *S* = 1/2 precursor to an *S* = 0 product, which implicates a multistep process involving electron transfer. We anticipated that protonation of **1a** would afford [(C_5H_5)Ni(pdt)HFe(CO)(dppe)]$^+$ ([H**1a**]$^+$), a Ni(III)-Fe(II) species . However, hydrides were not obtained experimentally; rather, only [**1a**]$^+$ was obtained. To explain this result, [H**1a**]$^+$ is proposed to undergo reduction by its conjugate base **1a**, giving H**1a**, which in turn undergoes protonolysis to give [**1a**]$^+$. Similarly, we found that protonation of **2b** afforded [**2b**]$^+$. The proposed sequence of reactions is summarized in Scheme 3.6.

Scheme 3.6. Proposed Reaction Sequence for H_2 Evolution

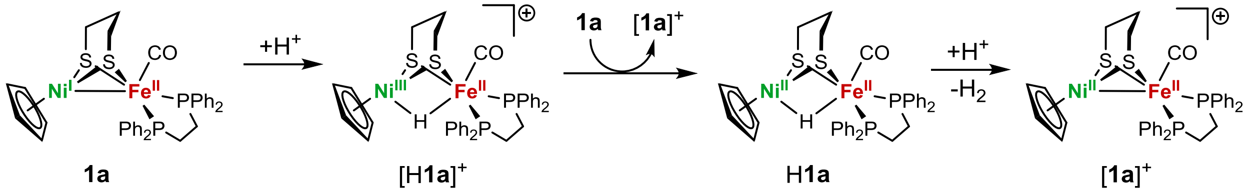

When **1a** was treated with substoichiometric amounts of acid and monitored using IR spectroscopy, an intermediate $\tilde{\nu}_{CO}$ band was observed (Figure 3.14, left). The spectrum with nearly equivalent intensity $\tilde{\nu}_{CO}$ bands could be simulated and the intermediate band was found to have $\tilde{\nu}_{CO}$ = 1927.6 cm^{-1} (Figure 3.14, right). This band is proposed to be the reduced hydride complex H**1a**, but the assignment is not definitive. The ^{1}H-NMR spectra of three-species mixture is complex and the presence of a transition metal hydride was inconclusive. These mixtures could not be separated.

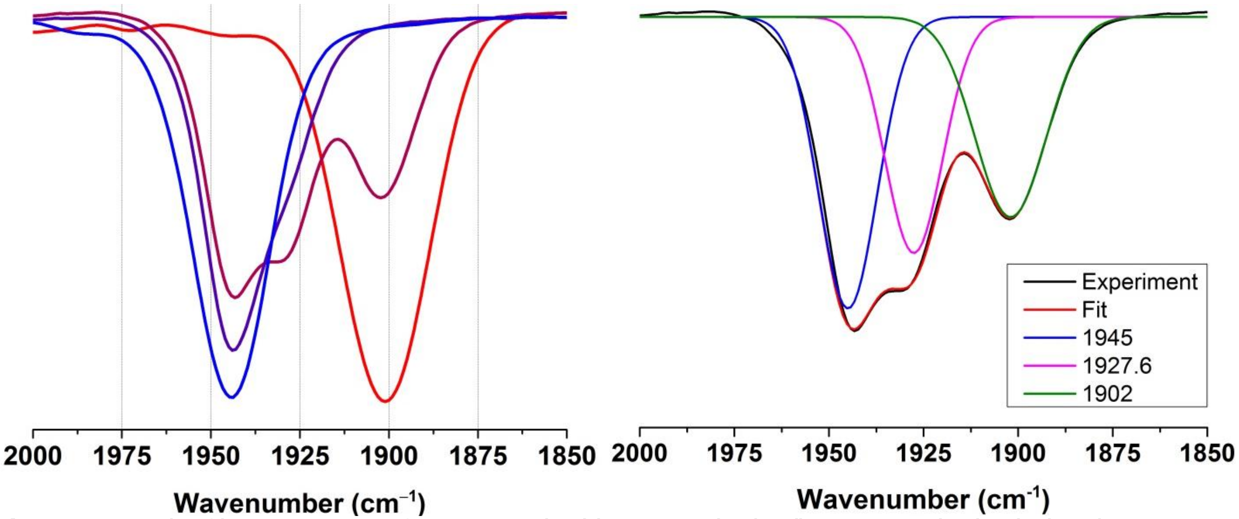

Figure 3.14. (Left) IR Spectra of **1a** treated with 0.0 equiv (red), 0.25 equiv (red-violet), 0.5 equiv (violet), and 1.0 equiv (blue) of acid. (Right) Simulated IR Spectrum of the mixture produced by treatment of **1a** with 0.25 equiv. of acid. The red trace is the simulation and the black trace is the experimental data. The blue magenta, and green traces are the components that sum to the red trace. Simulated wavenumber values for these species are indicated within the figure.

3.9 Proposed H_2 Evolution Mechanism

In the presence of excess acid, [**1a**]$^{+/0}$ is a formal, albeit slow electrocatalyst for hydrogen evolution. Using trifluoroacetic acid, catalytic current is observed at −1.16V, corresponding to the [**1a**]$^{+/0}$ couple, with an acid-independent rate[34] of ca. 4 s^{-1} (Figure 3.15).

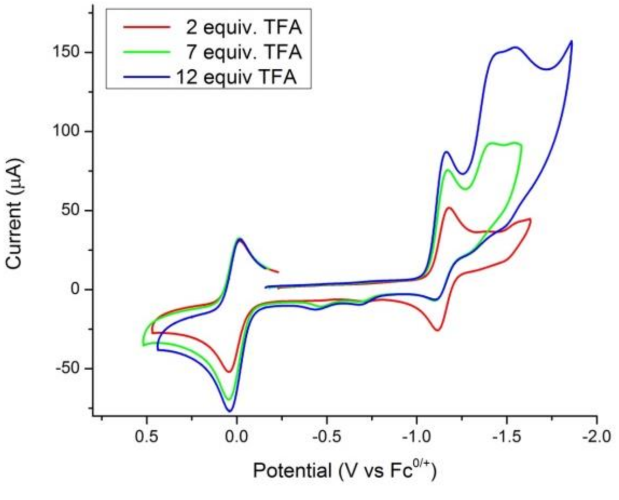

Figure 3.15. Cyclic voltammogram of [**1a**]BF_4 in CH_2Cl_2 at 500 mV s^{-1} with increasing amounts of trifluoroacetic acid showing a catalytic wave centered at the [**1a**]$^{+/0}$ couple. The maximum i_c/i_p observed in the acid independent region is approximately 2, yielding a rate of 3.88 s^{-1}.[34] Glassy carbon is known to catalyze proton reduction of trifluoroacetic acid at −1.81 V under these conditions.[35]

Since hydride intermediates could not be isolated, DFT was used to analyze the mechanism for hydrogen evolution. Additionally, the exclusive observation of the dibasal intermediate prompted theoretical investigation of an apical-basal isomer. These calculations provide insight into the structure and bonding of the hydride intermediates and also predict the occurrence of two parallel catalytic cycles involving isomers of **1a**. Similar bimetallic hydrides have been known to adopt different isomers.[36,37] Furthermore, recent work suggests that the protonation of (dppe)Ni(pdt)Fe(CO)$_3$ proceeds via an isomer that is not observed spectroscopically.[20]

According to the calculations, the dibasal and apical-basal isomers of **1a** are nearly isoergic ($\Delta G°$ = +0.48 kcal/mol) and interconvert via a relatively low free energy barrier, $\Delta G^{\ddagger}$ = 11.76 kcal/mol (Table 3.9); however, all other protonation and oxidation states have a much higher barrier for isomerization (ΔG > 20 kcal/mol). This result prompted the investigation of two parallel pathways for hydrogen evolution, labeled A and B in Figure 3.16.

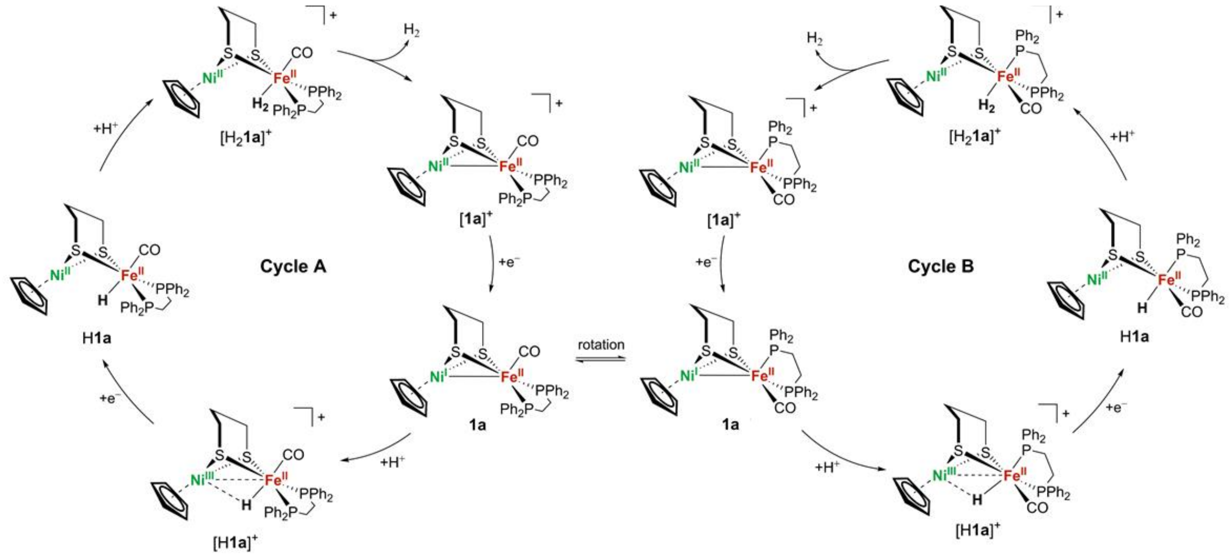

Figure 3.16. Proposed mechanism for H$_2$ production proceeding through two isomers. Cycle A, on the left, proceeds through structures in which the dppe ligand is in the dibasal position. Cycle B, on the right, proceeds through structures in which the dppe ligand spans apical-basal positions. Isomerization of **1a**, which has the lowest free energy barrier, could lead to a transition between Cycle A and Cycle B.

These pathways are initiated by protonation of isomers of **1a** that differ in terms of the stereochemistry of the (pdt)Fe(dppe)(CO) site. The adoption of the apical-basal isomer does not disrupt the Ni-Fe σ-bond or the localization of the unpaired spin density (Table 3.10). The isomerization from the dibasal to the apical-basal configuration is expected to occur only for the

1a species because the calculated Δ$G^‡$ values for the analogous isomerization for all other intermediates in the catalytic cycle shown in Figure 3.16 are more than 20 kcal/mol (Table 3.9). DFT analysis revealed that the transition state for this isomerization disrupts the metal-metal bonding (Figure 3.17). For **1a**, the transition state is best described as Ni(II)Fe(I), while the transition state is Ni(II)Fe(II) in [**1a**]$^+$. The lower isomerization barrier for **1a** is attributed to the greater stability of 5-coordinate iron(I) compared to 5-coordinate iron(II).

Table 3.9. Calculated Reaction Free Energies and Free Energy Barriers (kcal/mol) for Isomerization of Dibasal to Apical-Basal Isomers for **1a** and its Derivatives in the Proposed Catalytic Cycle.^{a,b}

Compound	**Δ*G*°**	**Δ*G*‡**
1a	0.48	11.76
[H**1a**]$^+$	2.21	20.84
H**1a**	5.18	25.64
[H_2**1a**]$^+$	9.86	30.03
[**1a**]$^+$	2.03	21.54

[a]See Figure 9 for structures of all species. [b]For the isomerization considered here, the central CH_2 of the Fe(pdt)Ni core is oriented toward the Ni. [c]The potential energy surface was found to be relatively flat along the isomerization pathway, leading to relatively small imaginary frequencies for the transition states (TS's).

Table 3.10. Spin Densities and Bond Lengths (Å) of **1a**, [H**1a**]$^+$, and H**1a**.^{a}

	1a		[H**1a**]$^+$		H**1a**	
	Isomer A	**Isomer B**	**Isomer A**	**Isomer B**	**Isomer A**	**Isomer B**
ρ(Ni)	0.71	0.70	0.45	0.42	0.00	0.00
ρ(Fe)	–0.19	–0.16	0.24	0.29	0.00	0.00
ρ(2S)	0.23	0.23	0.12	0.09	0.00	0.00
ρ(C_5H_5)	0.25	0.23	0.18	0.16	0.00	0.00
d(Ni-Fe)	2.53	2.47	2.60	2.59	3.01	2.85
d(Ni-H)	n/a	n/a	1.80	1.79	2.44	2.05
d(Fe-H)	n/a	n/a	1.61	1.58	1.54	1.53

[a]For these calculations, the central CH_2 of the Fe(pdt)Ni core is oriented toward the Ni center.

The first step in the catalytic cycle produces isomers of [H**1a**]$^+$. In both isomers, the unpaired electron is localized mainly in the Ni coordination sphere (Table 3.10), indicating that these species are best described as Ni(III)HFe(II), analogous to the Ni-C state in the enzyme. Moreover, the DFT-optimized structure of [H**1a**]$^+$ reveals that the hydride is more closely bound to Fe than to Ni.

Subsequent to its formation, [H**1a**]$^+$ is reduced by a second equiv. of **1a** to form [**1a**]$^+$ and the Ni(II)Fe(II) hydride H**1a**. This electron transfer is proposed to occur spontaneously on the basis of the calculated reduction potential of [H**1a**]$^+$, which is less negative than the calculated reduction potential of [**1a**]$^{+}$ by 0.16 (Cycle A) and 0.03 V (Cycle B) vs Fc$^{+/0}$ in CH_2Cl_2. Reduction to form H**1a** mainly affects the Ni center and results in significant elongation of the Ni-H distance by 0.64 and 0.26 Å for the A and B isomers, respectively. Thus, H**1a**, which would be analogous to the Ni-R state of the enzyme, which features an Ni(II)Fe(II) core with a bridging hydrido ligand. The difference in M-H bond length suggests that H**1a** is more accurately described as a semi-terminal Fe(II)-hydride than a bridging hydride.

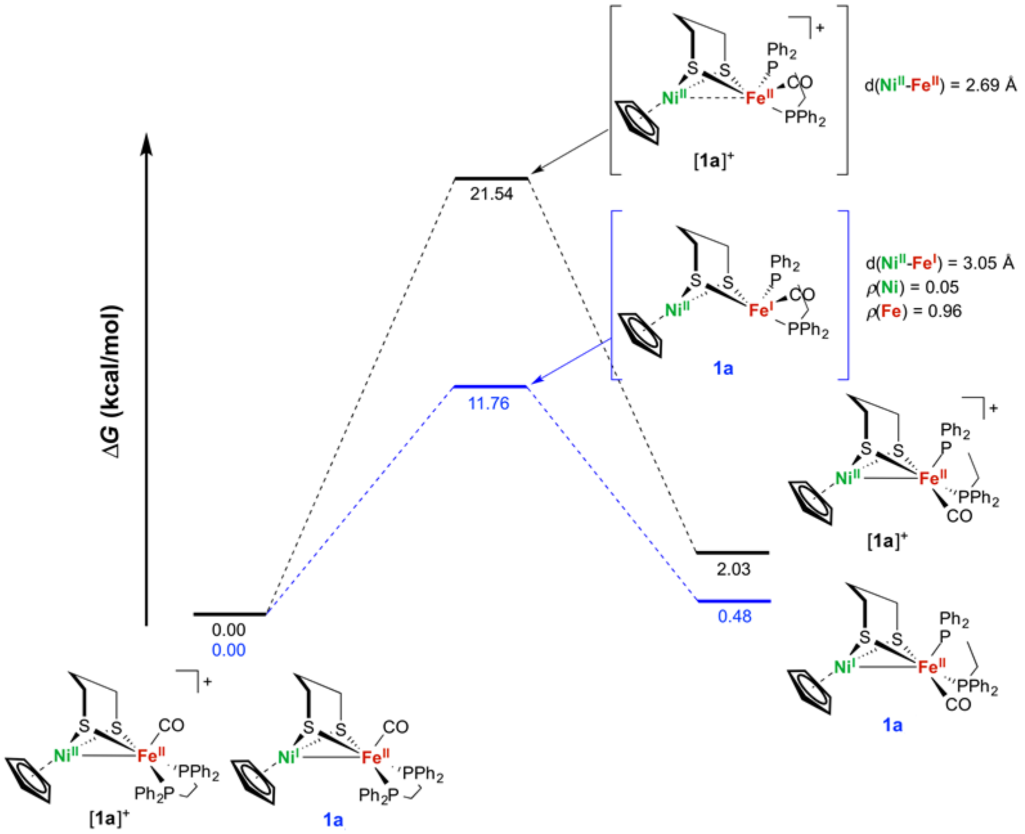

Figure 3.17. Free energy diagram for the isomerization of the Fe(CO)(dppe) subunit from dibasal (Cycle A) to apical-basal (Cycle B) for [**1a**]$^{+}$ (black numbers) and **1a** (blue numbers).

The catalytic cycle closes with the protonation of H**1a** to produce the H_2-adduct intermediate, [H_2**1a**]$^{+}$, followed by the release of H_2 from [H_2**1a**]$^{+}$ to generate [**1a**]$^{+}$. Although the two cycles are very similar energetically, the calculations predict that this protonation is thermodynamically less favorable for the apical-basal isomer H**1a**^{B} than for the dibasal isomer H**1a**^{A} by ~5 kcal/mol.

In light of these computational results, additional experiments were performed to probe the presence of two isomers in the catalytic cycle. The calculated $\tilde{\nu}_{CO}$ values for **1a**^{A} and **1a**^{B}

are 1901 and 1904 cm^{-1}, respectively, and the calculated $\tilde{\nu}_{CO}$ values for [**1a**^{A}]$^{+}$ and [**1a**^{B}]$^{+}$ are 1946 and 1949 cm^{-1}, respectively. These small calculated $\tilde{\nu}_{CO}$differences between the isomers are within the numerical accuracy of DFT. As previously mentioned, solutions of [**1a**]$^{+}$, which were synthesized directly, were confirmed crystallographically and spectroscopically to exist only in the dibasal geometry. However, preparation of [**1a**]$^{+}$ by the addition of excess acid to **1a**, presumably going through the catalytic cycle(s) to generate H_2, produced a solution containing both isomers of [**1a**]$^{+}$. The ^{31}P NMR spectrum of the [**1a**]$^{+}$ or [**1b**]$^{+}$ solution obtained after presumably proceeding through the catalytic cycle(s) displayed two ^{31}P NMR signals (Figures 3.18 and 3.19), one assigned to the dibasal isomer (Cycle A), in which the two ^{31}P centers are equivalent, and the other assigned to the apical-basal isomer (Cycle B), in which the two ^{31}P centers are equilibrated by the rocking motion shown in Scheme 3.7.

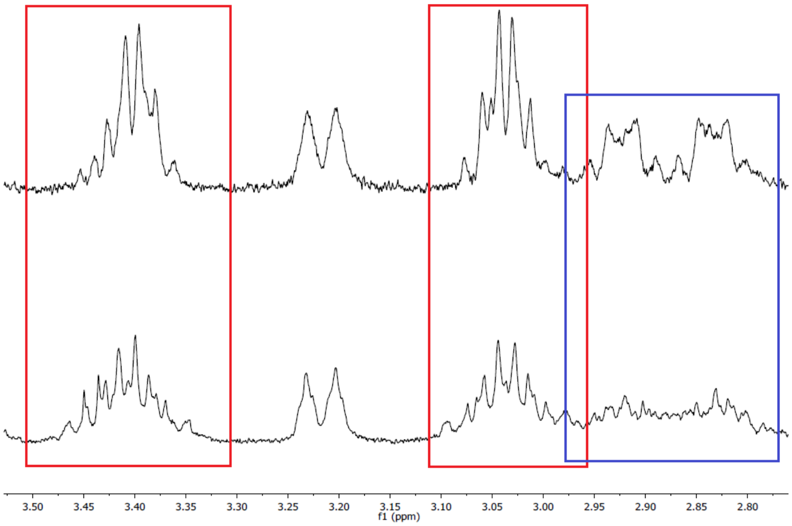

Figure 3.18. ^{1}H NMR spectrum of **1a** after treatment with excess acid, focusing on the ethylene protons of the diphosphine (bottom). ^{1}H{^{31}P}-NMR spectrum focusing on the ethylene protons of the diphosphine (top). The red box highlights the resonances assigned to the dibasal isomer and the blue box highlights the resonances assigned to the proposed apical-basal isomer.

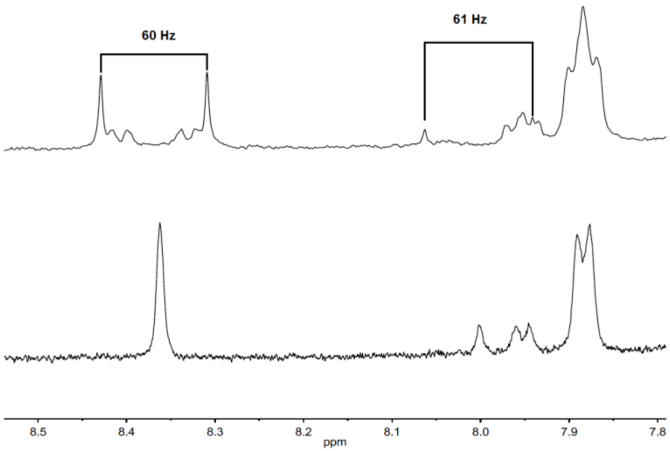

Figure 3.19. ^{1}H NMR Spectrum of **1b** after treatment with excess acid, highlighting the vinylidene protons of the diphosphine (top). The ^{1}H{^{31}P} NMR spectrum highlighting the vinylidene protons of the diphosphine (bottom). The dibasal isomer is assigned to the resonance at c.a. 8.35 ppm and the proposed apical-basal isomer is assigned to the resonance at c.a. 8.00 ppm.

The free energy barrier to this rocking motion is calculated to be relatively low, $\Delta G^{\ddagger} = 9.5$ kcal/mol, and the ^{31}P-NMR spectrum of the isomer mixture was unchanged when recorded at −100 °C, consistent with a relatively low free energy barrier. These analyses support the proposal that H_2 evolution can proceed via either Cycle A or Cycle B shown in Figure 3.16, thereby producing both isomers of [**1a**]$^{+}$.

Scheme 3.7. Representation of the Fe-centered rocking motion in [**1a**^{B}]$^{+}$.

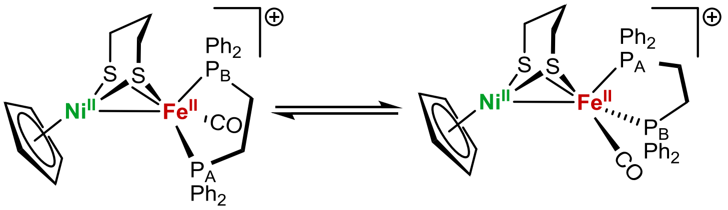

3.10 Conclusions

Experiment and theory indicate that the new complexes reported in this paper replicate aspects of the following enzyme states: Ni-SI$_a$, Ni-L, Ni-C, and Ni-R. Two of these species, the Ni(II)Fe(II) and Ni(I)Fe(II) derivatives, were crystallized and fully characterized. The other two species are implicated in a hydrogen evolution experiment and characterized computationally.

The Ni-SI$_a$ state is distinguished by the Ni(II)Fe(II) bimetallic core and the absence of a third bridging ligand, features that are replicated in compounds [**1a-d**]BF_4. The Ni-L state is distinguished by the formal Ni(I)Fe(II) oxidation states, a feature that is replicated in **1a-d**. The oxidation state assignments are supported by EPR and Mössbauer spectroscopic data, crystallographic results, voltammetric measurements, and DFT calculations.

The previous attempts to model states with Ni(II)Fe(II) cores suffered from the presence of hexacoordinate Fe centers.[38,39] The Ni(II)Fe(II) models reported in this paper in fact arise via such $FeL_4(SR)_2$-containing intermediates, followed by rapid decarbonylation. DFT analysis of the bonding suggests that decarbonylation is driven by formation of the Ni-Fe bond. Although [**1a-d**]$^+$ and [**2b**]$^+$ are reasonable spectroscopic models for the Ni-SI_a state of the enzyme, challenges remain. In the Ni-SI_a state the Ni center binds carbon monoxide to give Ni-SI_a^{CO}.[1,40] In contrast, [**1a-d**]$^+$ exhibit no detectable affinity for CO. Substitution of the dithiolate bridge with bridging monothiolates, as in [**2b**]$^+$, facilitates the binding of carbon monoxide at iron. In contrast, the enzyme binds carbon monoxide at nickel. This difference is understandable because the $(C_5H_5)Ni(SR)_2$ site has a higher electron count than the $(RS)_2Ni(SR)_2$ site found in the enzyme. Replicating terminal thiolate ligation at nickel remains one of the central challenges in this area.[41]

The first attempts to model the mixed valence active site of the Ni-L state focused on the $[(CO)_2LFe(pdt)Ni(diphosphine)]^+$.[7,8] These cations are described as Ni(II)Fe(I), which is reversed from the Ni(I)Fe(II) states assigned in Ni-L. More recently, we have characterized complexes with the configuration Ni(I)Ru(II), wherein the Ru(II) replaces the redox-inactive ferrous site in active site.[42] In this work, the $Fe(CO)_2(PR_3)$ center in previous Fe-Ni models was replaced by a $Fe(CO)(PR_3)_2$ center, which stabilizes the Fe(II) state, as illustrated by **1a-d** and **2b**.

Hydrogenic ligands are a major focus in research concerning the hydrogenases and their models because they are substrates.[43,44] The DFT-optimized analysis of the Ni(III)Fe(II) hydride [H**1a**]$^+$ reveals that the unpaired electron is localized mainly in the Ni coordination sphere, as seen in Ni-C. In the model, the hydride ligand is more closely bound to Fe than to Ni (M-H ~ 0.2 Å). This report is the first suggestion of the accessibility of such a state in [NiFe]-hydrogenase model complexes. In the enzyme, proton transfer reactions are coupled to electron transfer reactions,[9] and a similar effect is seen in the reduction of [H**1a**]$^+$ by **1a**. The resulting Ni(II)Fe(II) hydride H**1a**, analogous to the Ni-R state of the enzyme, reacts with proton sources to liberate H_2. Although thwarting efforts to isolate this hydride, this facile protonolysis is analogous to the behavior of the Ni-R/Ni-SI pair.[9] According to our calculations, the Ni(II)Fe(II) hydride is more accurately described as a terminal Fe(II)-hydride than a bridging hydride. In contrast, high resolution X-ray crystallographic analysis of Ni-R from *D. vulgaris* reveals Ni-H and Fe-H distances of 1.58 and 1.78 Å (error 0.08 Å), respectively, i.e., the hydride is more closely associated with nickel.[9] The structural difference between the model complex and the protein may reflect the influence of terminal thiolate ligands on nickel.[41]

3.11 Experimental

Reactions and manipulations were performed using standard Schlenk techniques at room temperature or in a nitrogen atmosphere glove box. Solvents were HPLC-grade and dried by filtration through activated alumina or distilled under nitrogen over an appropriate drying agent. Bu_4NPF_6 (GFS Chemicals) was recrystallized multiple times from CH_2Cl_2 solution by the addition of hexane. Chromatography was performed using Siliflash P60 from Silicycle (230−400 mesh). ESI-MS data for compounds were acquired using a Waters Micromass Quattro II spectrometer. ^1H NMR spectra (500 MHz) were referenced to residual solvent relative to TMS. $^{31}P\{^1H\}$ NMR spectra (202 MHz) were referenced to an external 85% H_3PO_4. FT-IR spectra were recorded on a Perkin-Elmer 100 FT-IR spectrometer. Crystallographic data for compounds **1a**, **1c, 2b,** and [**2b**]BF_4 were collected using a Siemens SMART diffractometer equipped with a Mo-K_α source (λ = 0.71073 Å), and crystallographic data for compounds [**1a**]BF_4 and [**1d**]BF_4 were collected using a Bruker D8 Venture diffractometer equipped with a Mo-K_α microfocus-source and a Photon 100 detector. X-band EPR Spectra were recorded on a Varian E-line 12" Century Series X-band continuous-wave spectrometer. Q-Band ENDOR spectra were recorded on a Bruker Elexsys E580 Q-band pulse EPR spectrometer using a homebuilt pulse Q-band ENDOR resonator[45] and an ENI 300L RF amplifier. Cryogenic temperatures were achieved using a Cryogenic Ltd closed cycle cryostat. ENDOR simulations and spectral fits were performed using EasySpin ("salt")[46] and homewritten scripts in Matlab. Mössbauer spectra were recorded on an alternating constant-acceleration spectrometer. The minimum experimental line width was 0.24 mm/s (full width at half-maximum). The sample temperature was maintained constant in either an Oxford Variox or an Oxford Mössbauer-Spectromag cryostat. The latter is a split-pair conducting magnet system for applying fields of up to 8 T to the samples that can be kept at temperatures in the range 1.5−250 K. The field at the sample is perpendicular to the γ-ray beam. Isomer shifts are quoted relative to metallic iron at 300 K. Mössbauer spectra were simulated with a home-written spin-Hamiltonian program based on the usual nuclear Hamiltonian formalism.[26]

$[(C_5H_5)_3Ni_2]BF_4$, $[(MeC_5H_4)_3Ni_2]BF_4$, and $[(C_5D_5)_3Ni_2]BF_4$. In a modification of Werner's procedure,[47] a solution of nickelocene (2.08 g, 11.0 mmol) in Et_2O (150 mL) was treated dropwise with an excess of $HBF_4 \cdot Et_2O$ (2 mL, 13.8 mol). Over the course of several minutes, a purple solid precipitated from a pale yellow. The solid was collected by filtration and washed thoroughly with ether. Yield: 2.07 g (95%). ^{1}H NMR (nitromethane-d_3): δ 5.48 (10H, s), 4.80 (5H, s). $^{13}C\{^1H\}$ NMR (nitromethane-d_3): δ 87.8, 56.6.

$[(C_5H_5)Ni(pdt)Fe(dppe)(CO)]BF_4$ ([1a]BF_4). To a solution of $[(C_5H_5)_3Ni_2]BF_4$ (498 mg, 1.24 mmol) in CH_3NO_2 (50 mL) was added a solution of $Fe(pdt)(dppe)(CO)_2$[37] (771 mg, 1.25 mmol) in CH_3NO_2 (25 mL). After 30 min., the slurry converted to a dark-red solution. Solvent was removed under reduced pressure, and the residue was washed several times with pentane until the filtrate was colorless. The residue was extracted into minimal volume of CH_2Cl_2 and subjected to column chromatography. Byproducts elute with 100% CH_2Cl_2. The product eluted with 90:10 CH_2Cl_2/THF as a dark-red band. The solvent was removed under reduced pressure to yield a dark-red solid. Yield: 841 mg (85%). ^{1}H NMR (acetone-d_6): 8.01 (m, 4H), 7.5 (m, 16H), 4.75 (s, 5H, $C_5\boldsymbol{H_5}$), 3.83 (m, 2H, $PC\boldsymbol{H_2}C\boldsymbol{H_2}P$), 3.62 (m, 2H, PCH_2CH_2P), 2.83 (m, 3H), 2.43 (m, 2H), 1.66 (m, 1H, $S_2CH_2C\boldsymbol{H_2}CH_2S_2$). $^{31}P\{^1H\}$ NMR (acetone-d_6): δ 77.1. ESI-MS: *m*/Z 711 ($[M]^+$), 683 ($[M{-}CO]^+$). IR (CH_2Cl_2): ν_{CO} = 1943 cm^{-1} (THF). Anal. Calcd for $C_{35}H_{35}FeNiOP_2S_2$ (found): C, 52.61 (52.67); H 4.42 (4.70). Single crystals of [**1**]BF_4 were obtained by vapor diffusion of pentane into THF solutions.

$[(C_5H_5)Ni(pdt)Fe(dppv)(CO)]BF_4$ ([1b]BF_4). Compound [**1b**]BF_4 was prepared in a similar fashion to [**1**]BF_4 using $Fe(pdt)(dppv)(CO)_2$[37] as the iron reagent. Yield: 66%, dark-red powder. ^{1}H NMR (CH_2Cl_2): 8.44 (m, 2H, $PC\boldsymbol{H}C\boldsymbol{H}P$), 7.91 (br, 4H), 7.54 (s, br, 4H), 7.45 (s, br 12H), 4.31 (s, 5H, $C_5\boldsymbol{H_5}$), 2.77 (m, 3H) 2.36 (m, 2H), 1.69 (m, 1H, $S_2CH_2C\boldsymbol{H_2}CH_2S_2$). $^{31}P\{^1H\}$ NMR (CH_2Cl_2): δ 83.8. ESI-MS: *m*/Z 709 ($[M]^+$), 681 ($[M{-}CO]^+$). IR (CH_2Cl_2): $\tilde{\nu}_{CO}$= 1951 cm^{-1}.

$[(C_5H_5)Ni(Me_2pdt)Fe(dppe)(CO)]BF_4$ ([1c]BF_4). Compound [**1c**]BF_4 was prepared in a similar fashion to [**1**]BF_4 using $Fe(Me_2pdt)(dppe)(CO)_2$[37] as the iron source. Yield: 77%, dark-red powder. . ^{1}H NMR (CH_2Cl_2): 7.77 (m, 4H), 7.46 (m, 16), 4.46 (s, 5H, $C_5\boldsymbol{H_5}$), 3.65 (m, 2H, $PC\boldsymbol{H_2}C\boldsymbol{H_2}P$), 3.11 (m, 2H $PC\boldsymbol{H_2}C\boldsymbol{H_2}P$), 2.71 (m, 2H, $S_2C\boldsymbol{H_2}CMe_2C\boldsymbol{H_2}S_2$), 2.17 (m, 2H, $S_2C\boldsymbol{H_2}CMe_2C\boldsymbol{H_2}S_2$), 1.50 (s, 3H, $S_2CH_2C\boldsymbol{Me_2}CH_2S_2$), 1.19 (s, $S_2CH_2C\boldsymbol{Me_2}CH_2S_2$). $^{31}P\{^1H\}$ NMR (CD_2Cl_2): δ 75.1. ESI-MS: *m*/Z 739 ($[M]^+$), 711 ($[M{-}CO]^+$). IR (CH_2Cl_2): $\tilde{\nu}_{CO}$= 1940 cm^{-1}. Single crystals of [**1c**]BF_4 were obtained by evaporation of concentrated THF solutions.

$[(CH_3C_5H_4)Ni(pdt)Fe(dppe)(CO)]BF_4$ ([1d]BF_4). Compound [**1d**]BF_4 was prepared in a similar fashion to [**1a**]BF_4 using the $[(CH_3C_5H_4)_3Ni_2]BF_4$ as the nickel source and $Fe(pdt)(dppe)(CO)_2$ as the iron source. Yield: 81%, dark-red powder. ^{1}H NMR (CH_2Cl_2): 7.80 (br, 4H) 7.52 (br, 4H) 7.43(br, 12H), 4.67 (br, 1H) 3.91 (br, 1H), 3.82 (s, 3H), 3.43 (m, 2H, PC***H*₂**C***H*₂**P), 3.05 (m, 2H, PC***H*₂**C***H*₂**P), 3.05 (m, 3H), 2.31 (m, 2H), 1.89 (br, 2H), 1.75 (m, 1H, $S_2CH_2C\boldsymbol{H_2}CH_2S_2$). $^{31}P\{^1H\}$ NMR (CD_2Cl_2): δ 79.2. ESI-MS: *m*/Z 725 ($[M]^+$), 697 ($[M{-}CO]^+$). IR (CH_2Cl_2): $\tilde{\nu}_{CO}$= 1943 cm^{-1}.

$[(C_5D_5)Ni(pdt)Fe(dppe)(CO)]BF_4$ ([1a]BF_4-*d*$_5$). Compound [**1a**]BF_4-*d*$_5$ was prepared in a similar fashion to [**1a**]BF_4 using $[(C_5D_5)_3Ni_2]BF_4$ as the nickel source. The product was characterized by ESI-MS, which indicated >95% deuteration (see SI).

$Fe(SPh)_2(CO)_2(dppv)$. This compound was synthesized similarly to the published procedure.[48] To a mixture of $FeSO_4·7H_2O$ (1.112g, 4.0 mmol) and dppv (1.584 g, 4.0 mmol) in MeOH (80 mL), a solution of PhSNa (1.056 g, 8.0 mmol) in MeOH (20 mL) was added dropwise with stirring under the presence of CO. After stirring for 6 h at room temperature, solvent was removed under reduced pressure. The residue was extracted with CH_2Cl_2 (40 mL). After filtration to remove Na_2SO_4, the extract was concentrated (15 mL), diluted with hexane (50 mL). Cooled this mixture at -20 ℃ for 12h gave a red solid. Yield: 2.23 g (77%). ^1H NMR (CD_2Cl_2): δ 6.85–8.03 (32H, m). $^{31}P\{^1H\}$ NMR (CD_2Cl_2): δ 81.9 (d, *J* = 55 Hz), 61.1 (d, *J* = 55 Hz). IR (CH_2Cl_2): $\tilde{\nu}_{CO}$= 2023, 1978 cm^{-1}.

$[(C_5H_5)Ni(SPh)_2Fe(dppv)(CO)_2]BF_4$ ([2bCO]BF_4). To a solution of $[(C_5H_5)_3Ni_2]BF_4$ (200 mg, 0.5 mmol) in CH_3NO_2 (15 mL) was added a solution of $Fe(SPh)_2(dppv)(CO)_2$ (364 mg, 0.5 mmol) in CH_3NO_2 (10 mL). After 30 min, the slurry converted to a dark-red solution. Solvent was removed under reduced pressure, and the residue was washed with pentane until the filtrate was colorless. The residue was extracted into minimal volume of CH_2Cl_2 and subjected to column chromatography. After eluting impurities with 100% CH_2Cl_2, the product eluted with 90:10 CH_2Cl_2/THF as a dark-red band. The solvent was removed under reduced pressure to yield a dark-red solid. Yield: 380 mg (81%). ^1H NMR (CD_2Cl_2): δ 6.85–8.57 (32H, m), δ 4.46 (5H, s). $^{31}P\{^1H\}$ NMR (CD_2Cl_2): δ 75.9 (d, *J* = 45 Hz), 64.2 (d, *J* = 45 Hz). ESI-MS: *m*/Z 849 ($[M]^+$), 821 ($[M{-}CO]^+$), 793 ($[M{-}2CO]^+$). IR (CH_2Cl_2): $\tilde{\nu}_{CO}$= 2042, 2002 cm^{-1}. Anal. Calcd for $C_{45}H_{37}BF_4FeNiO_2P_2S_2·CH_2Cl_2$ (found): C, 54.05 (53.69); H 3.85 (3.72). Single crystals of [**2b**CO]BF_4 were obtained by solvent diffusion of pentane into CH_2Cl_2 solutions.

$[(C_5H_5)Ni(SPh)_2Fe(dppv)(CO)]BF_4$ ([2b]BF_4). To a solution of [**2b**CO]BF_4 (280 mg, 0.3 mmol) in CH_2Cl_2 (30 mL) was added $Me_3NO·2H_2O$ (34 mg, 0.3 mmol). After 1h, the solvent was removed under reduced pressure, and the residue was washed several times with pentane. The residue was extracted into minimal volume of CH_2Cl_2 (5 mL), pentane (30 mL) was added and the mixture was cooled to -20℃. The product was collected as a black powder. Yield: 200 mg (74%). $^{31}P\{^1H\}$ NMR (CD_2Cl_2): δ 78.8. ESI-MS: *m*/Z 821 ($[M]^+$), 793 ($[M{-}CO]^+$). IR

(CH_2Cl_2): $\tilde{\nu}_{CO}$= 1956 cm^{-1}. Anal. Calcd for $C_{44}H_{37}BF_4FeNiOP_2S_2{\cdot}0.5CH_2Cl_2$ (found): C, 56.16 (56.08); H 4.02 (4.19).

(C_5H_5)Ni(pdt)Fe(dppe)(CO) (1a). To a stirred solution of [**1a**]BF_4 (21.2 mg, 26.5 μmol) in THF (3 mL) was added cobaltocene (5.8 mg, 30.7 μmol) in THF (3 mL). The solution immediately darkened. and solid [$(C_5H_5)_2$Co]BF_4 precipitated. The solvent is removed under reduced pressure and redissolved in toluene (2 mL). The slurry was filtered through diatomaceous earth to yield a homogeneous, brown-black solution. The product is crystallized upon addition of pentane (15 mL). Yield: 17.0 mg (90%), black powder. Single crystals were obtained by vapor diffusion of pentane into concentrated toluene solutions. IR (CH_2Cl_2): $\tilde{\nu}_{CO}$= 1901 cm^{-1}. Anal. Calcd. for $C_{35}H_{35}FeNiOP_2S_2$ (found): C, 59.02 (58.72); H 4.95 (4.65).

(C_5H_5)Ni(pdt)Fe(dppv)(CO) (1b). Compound **1b** was prepared in a similar fashion to **1a**. Yield: 86%, black powder. IR (CH_2Cl_2): $\tilde{\nu}_{CO}$= 1903 cm^{-1}.

(C_5H_5)Ni(Me_2pdt)Fe(dppe)(CO) (1c). Compound **1c** was prepared in a similar fashion to **1a**. Yield: 87%, black powder. IR (CH_2Cl_2): $\tilde{\nu}_{CO}$= 1897 cm^{-1}.

($CH_3C_5H_4$)Ni(pdt)Fe(dppe)(CO) (1d). Compound **1d** was prepared in a similar fashion to [**1a]^{0}**. Yield: 80%, black powder. IR (CH_2Cl_2): $\tilde{\nu}_{CO}$= 1898 cm^{-1}.

(C_5D_5)Ni(pdt)Fe(dppe)(CO) (1a-*d*$_5$). Compound **1a-***d*$_5$ was prepared in a similar fashion to **1a**.

(C_5H_5)Ni$(SPh)_2$Fe(dppv)(CO) (2b). Compound **2b** was prepared in a similar fashion to **1a**. Yield: 61%, black powder. IR (CH_2Cl_2): $\tilde{\nu}_{CO}$= 1915 cm^{-1}. Single crystals of **2b** were obtained by vapor diffusion of pentane into concentrated toluene solutions.

Computational Methods. DFT results reported herein were performed using the BP86 density functional.[49,50] Additional benchmarking was performed using the B3P86,[49,51] BP86-D2,[49,50,52] M06-L,[53] and ωB97XD[52,54-56] functionals. The DFT calculations were performed with the Stuttgart pseudopotential and associated basis set of Preuss and co-workers (SDD)[57] for the Ni and Fe centers, the 6-31G** basis set[58] for the μ-H ligand, and the 6-31G* basis set[59,60] for all other atoms. The starting geometries for [**1a-d**]$^{+}$, **1a**, and **2b** were obtained from their respective crystal structures. The starting coordinates for species without crystal structures were obtained by manually altering the most closely related crystal structure. Solvation free energies were calculated in dichloromethane (CH_2Cl_2) using the conductor-like polarizable continuum model (C-PCM)[61,62] with the Bondi atomic radii[63] and including the nonelectrostatic contributions of dispersion,[64,65] repulsion,[64,65] and cavitation energies.[66]

For the results presented in the main paper, the geometry optimizations were performed in the gas phase. However, geometry optimizations were also performed in solution and were found to be consistent with the gas phase optimizations. A comparison of the structures optimized in the gas phase and solution phase is provided in the Supporting Information (Tables S4-S7). In all cases, the minimum-energy structures were confirmed to have no imaginary frequencies. The v_{CO} frequencies were calculated within the harmonic model. Typically, DFT is more reliable for calculating changes in frequencies than absolute frequencies, and often scaling factors dependent on the functional are used.[67] Herein, however, the absolute $\tilde{\nu}_{CO}$ values are reported because the BP86 functional gives excellent agreement with the experimental values without the application of scaling factors. The transition states (TSs) for isomerization of the Fe(dppe)(CO) subunit were identified using the synchronous transit-guided quasi-Newton method,[68,69] and the TSs were confirmed to have only one imaginary frequency. Each TS was verified to lead to the relevant dibasal or apical-basal isomers by following the intrinsic reaction coordinate (IRC) using the local quadratic approximation[70,71] for steps in the forward and reverse directions and subsequently optimizing the geometries.

Thermochemical data were calculated at T = 298.15 K. All calculated free energies included zero-point energy, entropic contributions, and solvation effects. The reaction free energies ($\Delta G°$) and free energy barriers ($\Delta G^{\ddagger}$) associated with the isomerization of the Fe(dppe)(CO) subunit in solution were calculated from the optimized geometries and TSs. The relative reduction potentials were calculated from the corresponding reaction free energies using methodology described elsewhere.[72-75] Chemical bonding analysis was performed using the Pipek-Mezey localization criteria[33], using keyword IOp(4/9=20212), and Natural Bond Orbitals (NBO).[76] All calculations were performed using the *Gaussian 09* electronic structure program.[77]

3.12 References

(1) Lubitz, W.; Ogata, H.; Rüdiger, O.; Reijerse, E. *Chem. Rev.* **2014**, *114*, 4081.
(2) Tard, C.; Pickett, C. J. *Chem. Rev.* **2009**, *109*, 2245.
(3) De Lacey, A. L.; Fernández, V. M.; Rousset, M.; Cammack, R. *Chem. Rev.* **2007**, *107*, 4304.
(4) Siegbahn, P. E. M.; Tye, J. W.; Hall, M. B. *Chem. Rev.* **2007**, *107*, 4414.
(5) Wu, H.; Hall, M. B. *C. R. Chim.* **2008**, *11*, 790.
(6) Murphy, B. J.; Hidalgo, R.; Roessler, M. M.; Evans, R. M.; Ash, P. A.; Myers, W. K.; Vincent, K. A.; Armstrong, F. A. *J. Am. Chem. Soc.* **2015**, *137*, 8484.
(7) Schilter, D.; Nilges, M. J.; Chakrabarti, M.; Lindahl, P. A.; Rauchfuss, T. B.; Stein, M. *Inorg. Chem.* **2012**, *51*, 2338−2348.
(8) Schilter, D.; Rauchfuss, T. B.; Stein, M. *Inorg. Chem.* **2012**, *51*, 8931.
(9) Ogata, H.; Nishikawa, K.; Lubitz, W. *Nature* **2015**, *520*, 571.
(10) Manor, B. C.; Rauchfuss, T. B. *J. Am. Chem. Soc.* **2013**, *135*, 11895.
(11) Greene, B. L.; Wu, C.-H.; McTernan, P. M.; Adams, M. W. W.; Dyer, R. B. *J. Am. Chem. Soc.* **2015**, *137*, 4558.
(12) Huynh, M. T.; Schilter, D.; Hammes-Schiffer, S.; Rauchfuss, T. B. *Journal of the American Chemical Society* **2014**, *136*, 12385.
(13) Nomura, M.; Okuyama, R.; Fujita-Takayama, C.; Kajitani, M. *Organometallics* **2005**, *24*, 5110.
(14) Gribble, J. D.; Wherland, S. *Inorg. Chem.* **1990**, *29*, 1130.
(15) Priego, J. L.; Doerrer, L. H.; Rees, L. H.; Green, M. L. H. *Chem. Commun.* **2000**, 779.
(16) Seiler, P.; Dunitz, J. D. *Acta Cryst. B* **1980**, *36*, 2255.
(17) Byers, L. R.; Dahl, L. F. *Inorg. Chem.* **1980**, *19*, 680.
(18) Lubitz, W.; van Gastel, M.; Gärtner, W. In *Nickel and Its Surprising Impact in Nature*; Sigel, A., Sigel, H., Sigel, R. K. O., Eds.; Wiley-VCH: Weinheim, 2007, p 279.
(19) Carroll, M. E.; Chen, J. Z.; Gray, D. E.; Lansing, J. C.; Rauchfuss, T. B.; Schilter, D.; Volkers, P. I.; Wilson, S. R. *Organometallics* **2014**, *33*, 858.
(20) Huynh, M. T.; Schilter, D.; Hammes-Schiffer, S.; Rauchfuss, T. B. *J. Am. Chem. Soc.* **2014**, *136*, 12385.
(21) Kellers, P.; Pandelia, M.-E.; Currell, L. J.; Görner, H.; Lubitz, W. *Phys. Chem. Chem. Phys.* **2009**, *11*, 8680.
(22) Pandelia, M.-E.; Infossi, P.; Stein, M.; Giudici-Orticoni, M.-T.; Lubitz, W. *Chem. Commun.* **2012**, *48*, 823.
(23) Hidalgo, R.; Ash, P. A.; Healy, A. J.; Vincent, K. A. *Angew. Chem., Int. Ed.* **2015**, n/a.
(24) Kampa, M.; Pandelia, M.-E.; Lubitz, W.; van Gastel, M.; Neese, F. *J. Am. Chem. Soc.* **2013**, *135*, 3915.
(25) McManis, G. E.; Nielson, R. M.; Gochev, A.; Weaver, M. J. *J. Am. Chem. Soc.* **1989**, *111*, 5533.
(26) Gütlich, P.; Bill, E.; Trautwein, A. X. *Mössbauer Spectroscopy and Transition Metal Chemistry. Fundamentals and Applications*; Springer: Berlin, 2011.
(27) Pandelia, M.-E.; Bykov, D.; Izsak, R.; Infossi, P.; Giudici-Orticoni, M.-T.; Bill, E.; Neese, F.; Lubitz, W. *Proc. Natl. Acad. Sci. U.S.A.* **2013**, *110*, 483.
(28) Surerus, K. K.; Chen, M.; van der Zwaan, J. W.; Rusnak, F. M.; Kolk, M.; Duin, E. C.; Albracht, S. P. J.; Muenck, E. *Biochemistry* **1994**, *33*, 4980.
(29) Pereira, A. S.; Tavares, P.; Moura, I.; Moura, J. J. G.; Huynh, B. H. *J. Am. Chem. Soc.* **2001**, *123*, 2771
(30) Popescu, C. V.; Münck, E. *J. Am. Chem. Soc.* **1999**, *121*, 7877.

(31) Zhu, W.; Marr, A. C.; Wang, Q.; Neese, F.; Spencer, D. J. E.; Blake, A. J.; Cooke, P. A.; Wilson, C.; Schröder, M. *Proc. Natl. Acad. Sci. U.S.A.* **2005**, *102*, 18280.
(32) Schilter, D.; Pelmenschikov, V.; Wang, H.; Meier, F.; Gee, L. B.; Yoda, Y.; Kaupp, M.; Rauchfuss, T. B.; Cramer, S. P. *Chem. Commun.* **2014**, *50*, 13469.
(33) Pipek, J.; Mezey, P. G. *J. Chem. Phys.* **1989**, *90*, 4916.
(34) Pool, D. H.; DuBois, D. L. *J. Organomet. Chem.* **2009**, *694*, 2858.
(35) McCarthy, B. D.; Martin, D. J.; Rountree, E. S.; Ullman, A. C.; Dempsey, J. L. *Inorg. Chem.* **2014**, *53*, 8350.
(36) Wang, W.; Rauchfuss, T. B.; Moore, C. E.; Rheingold, A. L.; De Gioia, L.; Zampella, G. *Chem. Eur. J.* **2013**, *19*, 15476.
(37) Carroll, M. E.; Chen, J.; Gray, D. E.; Lansing, J. C.; Rauchfuss, T. B.; Schilter, D.; Volkers, P. I.; Wilson, S. R. *Organometallics* **2014**, *33*, 858.
(38) Li, Z.; Ohki, Y.; Tatsumi, K. *J. Am. Chem. Soc.* **2005**, *127*, 8950.
(39) Jiang, J.; Maruani, M.; Solaimanzadeh, J.; Lo, W.; Koch, S. A.; Millar, M. *Inorg. Chem.* **2009**, *48*, 6359.
(40) Pandelia, M.-E.; Ogata, H.; Currell, L. J.; Flores, M.; Lubitz, W. *Biochim. Biophys. Acta - Bioenerg.* **2010**, *1797*, 304.
(41) Weber, K.; Krämer, T.; Shafaat, H. S.; Weyhermüller, T.; Bill, E.; van Gastel, M.; Neese, F.; Lubitz, W. *J. Am. Chem. Soc.* **2012**, *134*, 20745.
(42) Chambers, G. M.; Mitra, J.; Rauchfuss, T. B.; Stein, M. *Inorg. Chem.* **2014**, *53*, 4243.
(43) Tschierlei, S.; Ott, S.; Lomoth, R. *Energy Environ. Sci.* **2011**, *4*, 2340.
(44) Gloaguen, F.; Rauchfuss, T. B. *Chem. Soc. Rev.* **2009**, *38*, 100.
(45) Reijerse, E.; Lendzian, F.; Isaacson, R.; Lubitz, W. *J. Magn. Reson., Ser A* **2012**, *214*, 237.
(46) Stoll, S.; Schweiger, A. *J. Magn. Reson., Ser A* **2006**, *178*, 42.
(47) Salzer, A.; Werner, H. *Angew. Chem. Int. Ed.* **1972**, *11*, 930.
(48) de Beer, J. A.; Haines, R. J. *J. Organomet. Chem.* **1972**, *36*, 297.
(49) Perdew, J. P. *Phys. Rev. B* **1986**, *33*, 8822.
(50) Becke, A. D. *Phys. Rev. A* **1988**, *38*, 3098.
(51) Becke, A. D. *J. Chem. Phys.* **1993**, *98*, 5648.
(52) Grimme, S. *J. Comput. Chem.* **2006**, *27*, 1787.
(53) Zhao, Y.; Truhlar, D. G. *J. Chem. Phys.* **2006**, *125*, 194101.
(54) Becke, A. D. *J. Chem. Phys.* **1997**, *107*, 8554.
(55) Kamiya, M.; Tsuneda, T.; Hirao, K. *J. Chem. Phys.* **2002**, *117*, 6010.
(56) Chai, J.-D.; Head-Gordon, M. *Phys. Chem. Chem. Phys.* **2008**, *10*, 6615.
(57) Dolg, M.; Wedig, U.; Stoll, H.; Preuss, H. *J. Chem. Phys.* **1987**, *86*, 866.
(58) Hariharan, P. C.; Pople, J. A. *Theoret. Chim. Acta* **1973**, *28*, 213.
(59) Hehre, W. J.; Ditchfield, R.; Pople, J. A. *J. Chem. Phys.* **1972**, *56*, 2257.
(60) Francl, M. M.; Pietro, W. J.; Hehre, W. J.; Binkley, J. S.; Gordon, M. S.; DeFrees, D. J.; Pople, J. A. *J. Chem. Phys.* **1982**, *77*, 3654.
(61) Barone, V.; Cossi, M. *J. Phys. Chem. A* **1998**, *102*, 1995.
(62) Cossi, M.; Rega, N.; Scalmani, G.; Barone, V. *J. Comput. Chem.* **2003**, *24*, 669.
(63) Bondi, A. *J. Phys. Chem.* **1964**, *68*, 441.
(64) Floris, F.; Tomasi, J. *J. Comput. Chem.* **1989**, *10*, 616.
(65) Floris, F. M.; Tomasi, J.; Ahuir, J. L. P. *J. Comput. Chem.* **1991**, *12*, 784.
(66) Pierotti, R. A. *Chem. Rev.* **1976**, *76*, 717.
(67) Alecu, I. M.; Zheng, J.; Zhao, Y.; Truhlar, D. G. *J. Chem. Theory Comput.* **2010**, *6*, 2872.
(68) Peng, C.; Bernhard Schlegel, H. *Isr. J. Chem.* **1993**, *33*, 449.
(69) Peng, C.; Ayala, P. Y.; Schlegel, H. B.; Frisch, M. J. *J. Comput. Chem.* **1996**, *17*, 49.
(70) Page, M.; McIver, J. W. *J. Chem. Phys.* **1988**, *88*, 922.

(71) Koseki, S.; Gordon, M. S. *J. Phys. Chem.* **1989**, *93*, 118.
(72) Solis, B. H.; Hammes-Schiffer, S. *Inorg. Chem.* **2011**, *50*, 11252.
(73) Fernandez, L. E.; Horvath, S.; Hammes-Schiffer, S. *J. Phys. Chem. C* **2012**, *116*, 3171.
(74) Solis, B. H.; Hammes-Schiffer, S. *Inorg. Chem.* **2014**, *53*, 6427.
(75) Qi, X.-J.; Fu, Y.; Liu, L.; Guo, Q.-X. *Organometallics* **2007**, *26*, 4197.
(76) Glendening, E. D.; Reed, A. E.; Carpenter, J. E.; Weinhold, F. *NBO Version 3.1*; University of Wisconsin System: Madison, WI, 1996.
(77) Frisch, M. J.; Trucks, G. W.; Schlegel, H. B.; Scuseria, G. E.; Robb, M. A.; Cheeseman, J. R.; Scalmani, G.; Barone, V.; Mennucci, B.; Petersson, G. A.; Nakatsuji, H.; Caricato, M.; Li, X.; Hratchian, H. P.; Izmaylov, A. F.; Bloino, J.; Zheng, G.; Sonnenberg, J. L.; Hada, M.; Ehara, M.; Toyota, K.; Fukuda, R.; Hasegawa, J.; Ishida, M.; Nakajima, T.; Honda, Y.; Kitao, O.; Nakai, H.; Vreven, T.; Montgomery, J. A.; Peralta, J. E.; Ogliaro, F.; Bearpark, M.; Heyd, J. J.; Brothers, E.; Kudin, K. N.; Staroverov, V. N.; Kobayashi, R.; Normand, J.; Raghavachari, K.; Rendell, A.; Burant, J. C.; Iyengar, S. S.; Tomasi, J.; Cossi, M.; Rega, N.; Millam, J. M.; Klene, M.; Knox, J. E.; Cross, J. B.; Bakken, V.; Adamo, C.; Jaramillo, J.; Gomperts, R.; Stratmann, R. E.; Yazyev, O.; Austin, A. J.; Cammi, R.; Pomelli, C.; Ochterski, J. W.; Martin, R. L.; Morokuma, K.; Zakrzewski, V. G.; Voth, G. A.; Salvador, P.; Dannenberg, J. J.; Dapprich, S.; Daniels, A. D.; Farkas; Foresman, J. B.; Ortiz, J. V.; Cioslowski, J.; Fox, D. J. *Gaussian 09, Revision D.01*; Gaussian, Inc.: Wallingford CT, 2010.

Chapter 4:
Cyclopentadienyl Nickel Thiolates Derived from Nickelocene and Dithiols

4.1 Introduction

Bimetallic dithiolates with $M_2(SR)_2$ cores are common throughout coordination chemistry. This motif is present at the active sites of the [NiFe]- and [FeFe]-hydrogenase (H_2ase) enzymes. One commonality of these active sites is the pyramidalization of the M_2S_2 core. While this distortion from planarity is enforced by the protein in biological systems, pyramidalization of the M_2S_2 core can be enforced in small molecules by the use of chelating dithiolates. Pyramidalization of the M_2S_2 core inherently decreases the metal-metal distance which has two consequences in regard to the reactivity of the dimetallic unit. First, a non-bridging ligand L would have a weakened M-L bond, as it would compete with M-M bonding (Figure 4.1, top). Second, the decreased metal-metal distance should enhance redox activity through charge delocalization, M-M bonding, and pre-organization (Figure 4.1, bottom).

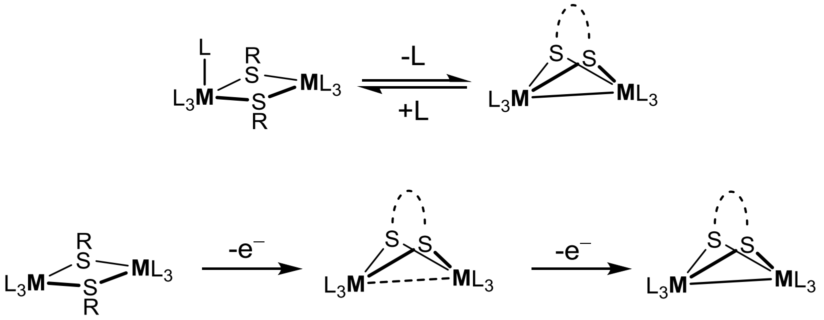

Figure 4.1. Reversible ligand binding and metal-metal bond formation of a $[L_3MSR]_2$ dimer (top). Oxidation and subsequent pyramidalization of a $[L_3MSR]_2$ dimer (bottom).

As discussed in chapter 1, synthetic routes to heterobimetallic models of the [NiFe]-H_2ase involve either the nucleophilic attack of a nickel(thiolate) on an iron center or the nucleophilic attack of an iron(thiolate) on a nickel center. Chapter 3 discussed CpNi(thiolate) based NiFe models for [NiFe]-H_2ase which were synthesized using the triple-decker sandwich compound $[Cp_3Ni_2]BF_4$ and $Fe(pdt)(dppe)(CO)_2$. Initial strategies sought CpNi(thiolate) precursors to generate the CpNiFe models (Scheme 4.1). However, methods of synthesizing cyclopentadienyl nickel thiolates with alkylthiolates necessary for this approach have not been reported.

Scheme 4.1. Proposed synthesis of a [NiFe]-H_2ase Model Complex using "CpNi(thiolate)"

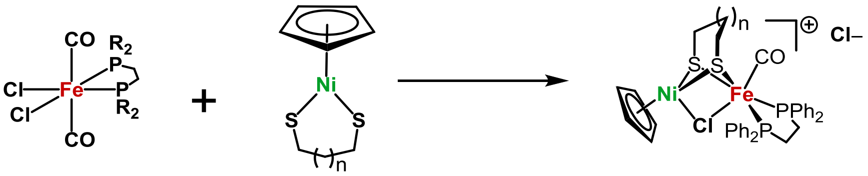

It has long been known that nickelocene (Cp_2Ni) reacts efficiently with thiols to give dimers of the form $[CpNi(SR)]_2$ (eq. 1). In this conversion, the $20e^-$ species Cp_2Ni undergoes protonolysis to yield an $18e^-$ product with loss of cyclopentadiene. A range of thiols undergo this reaction, as summarized in many reports.[1-6] These reactions reliably produce dinickel-dithiolate compounds, all of which are intensely colored, diamagnetic, and thermally robust. Structurally, these compounds feature a planar Ni_2S_2 core with long Ni---Ni distances of ~3.0 Å, typically too long to form meaningful metal-metal interactions. In fact planar, diamagnetic Ni_2S_2 cores are characteristic of all organo-$Ni^{II}_2(SR)_2$ systems.

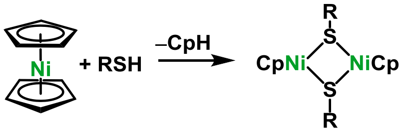

(1)

It was anticipated that the reaction between nickelocene and *di*thiols would produce similar a structure or perhaps a mononuclear species (eq. 2). In contrast to the monothiolate complexes, the dinickel complex bridged by a dithiolate would not possess a planar Ni_2S_2 core by virtue of the geometric constraints imposed by the carbon backbone. The one reported CpNi(dithiolate) complex thus far, Cp_2Ni_2(μ-α,α'-xylenedithiolate), the Ni_2S_2 dihedral angle is 30.92(5)º. For dithiolates with smaller bite angles, such as 1,2-ethane- and 1,3-propanedithiolate, the M_2S_2 core distortion is expected to be more prominent.

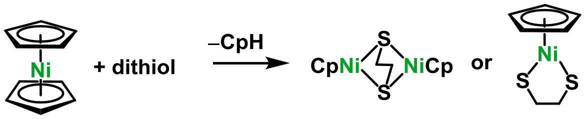

(2)

This chapter discusses the reactivity and characterization of nickelocene with various dithiols. These reactions was found to be quite complex and the resulting compounds have unusual properties.

4.2 Reaction of Nickelocene with Dithiols

4.2.1 Overview

Pentane solutions of nickelocene react with organic dithiols over the course of hours to yield di- and multi-metallic compounds. Generally, compounds of the formula $Cp_2Ni_2(xdt)$ ($\mathbf{1}^{\mathbf{xdt}}$) (where xdt is a dithiol) remain soluble in pentane whereas higher nuclearity compounds precipitate as crystalline solids. The nuclearity of the major species depends on the dithiol. Propanedithiol ($pdtH_2$) forms a mixture of both dinickel ($\mathbf{1}^{\mathbf{pdt}}$) and trinickel ($\mathbf{2}^{\mathbf{pdt}}$) products. Benzenedithiol ($bdtH_2$) and ethanedithiol ($edtH_2$) favor trinickel products ($\mathbf{2}^{\mathbf{bdt}}$, $\mathbf{2}^{\mathbf{edt}}$). Compounds with higher nuclearities are insoluble. Most of these complexes and their derivatives were characterized crystallographically and the various bond-length parameters are tabulated in Table 4.1.

4.2.2 Reaction of Nickelocene with 1,3-propanedithiol

A solution of 1,3-propanedithiol ($pdtH_2$) and 2 equiv. of nickelocene in pentane remains green and homogeneous for several minutes at room temperature but gradually becomes yellow-brown. Over the course of several hours, the solution becomes dark and red-black crystals of a trinickel species precipitates (Scheme 4.2).

Scheme 4.2. Synthesis of $\mathbf{1}^{\mathbf{pdt}}$ and $\mathbf{2}^{\mathbf{pdt}}$

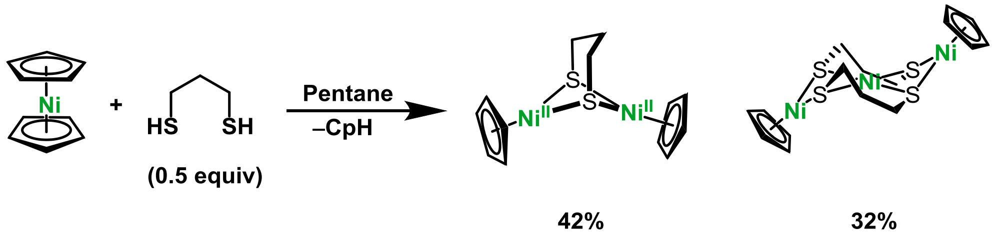

Evaporation of the filtrate gave red-black microcrystals of $Cp_2Ni_2(pdt)$ ($\mathbf{1}^{\mathbf{pdt}}$). X-ray crystallographic analysis confirmed the expected distorted M_2S_2 structure (Figure 4.2). The Ni-Ni separation is 2.863(1) Å, which is c.a. 0.2 Å shorter than that observed in $[CpNi(SEt)]_2$ ($\mathbf{1}^{\mathbf{SEt}}$), but similar to the 2.918(1) Å distance for the α,α'-xylenedithiolate $Cp_2Ni_2(SCH_2)_2C_6H_4$.[7] In $Cp_2Ni_2(SPh)_2$, the Ni---Ni separation is 3.097(1) Å.[7] The variability in the Ni---Ni distances is consistent with a flexible nonbonding interaction.

Table 4.1. Selected Bond Distances (Å) for Thiolate Derivatives of CpNi(II) and CpNi(III).

Complex	**Ni---Ni**	**Cp_{cent}-Ni**	**CpNi-S**	**Ni-S (non CpNi)**
$Cp_2Ni_2(SEt)_2$ (**1**^{SEt})	3.145(1)[a]	1.75(3)[a]	2.182(5)[b]	
$Cp_2Ni_2(SPh)_2$	3.097(1)	1.753(7)	2.190(1)[b]	
$Cp_2Ni_2(SCH_2)_2C_6H_4$	2.918(1)	1.755(8)	2.181(2)[b]	
$Cp_2Ni_2(pdt)$ (**1**^{pdt})	2.916[a]	1.76(3)[a]	2.181(5)[b]	
$[Cp_2Ni_2(thiolate)_2]^+$ and $[Cp_2Ni_2(dithiolate)]^+$ Salts				
$[Cp_2Ni_2(SEt)_2]BF_4$[e]	2.4727(6)	1.739(5)	2.1924(8)	
$[Cp_2Ni_2(edt)]BF_4$ ([**1**^{edt}]BF_4)	2.4442(8)	1.726(5)	2.191(1)[b]	
$[Cp_2Ni_2(pdt)]BF_4$ ([**1**^{pdt}]BF_4)	2.4537(3)	1.725(4)	2.1823(7)[b]	
$Cp_2Ni_3(dithiolate)_2$				
$Cp_2Ni_3(edt)_2$[e] (**2**^{edt})	2.6774(5) 2.9327(5)	1.749(4)	2.196(1)[c] 2.179(1)[c]	2.167(2)[d]
trans-$Cp_2Ni_3(pdt)_2$ (**2**^{pdt})	2.8267(7)[f]	1.761(4)[f]	2.1867(9)[b,f]	2.1399(8)[d]
cis-$Cp_2Ni_3(pdt)_2$ (**2**^{pdt})	2.8630(6)[f]	1.761(6)[f]	2.173(1)[c,f]	2.1902(9)[d]
$Cp_2Ni_3(bdt)_2$ (**2**^{bdt})	2.8082(8) 2.7592(8)	1.74(1)	2.192(1)[c]	2.168(1)[d]
$[Cp_2Ni_3(dithiolate)_2]^+$ Salt				
$[Cp_2Ni_3(pdt)_2]BF_4$ ([**2**^{pdt}]BF_4)	2.763(1) 2.649(1)	1.736(9)	2.168(2)[c] 2.176(2)[c]	2.199(2)[d]
$Cp_2Ni_5(dithiolate)_4$				
$Cp_2Ni_5(edt)_4$ (**3**^{edt})	2.6257(8)[f] 2.9603(6)[f]	1.747(6)[f]	2.210(2)[c,f]	2.172(3)[d] 2.211(1)[d,f]

[a] Average of two molecules in the asymmetric unit. [b] Average value of all CpNi-S bonds in the asymmetric unit. [c] Average value of CpNi-S bonds to that particular nickel atom. [d] Average value of all (non Cp)Ni-S bonds in the asymmetric unit. [e] Values for this complex come from one molecule in the asymmetric unit. The other molecule has an identical skewed conformation and very similar bond distances. [f] Molecule lies on a special position and the other corresponding distance is enforced to be the same.

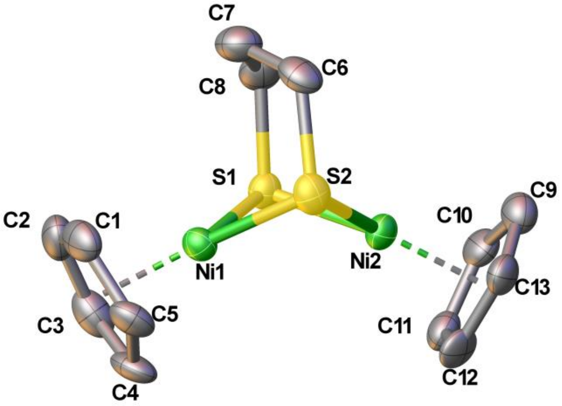

Figure 4.2. Solid state structure of $\mathbf{1^{pdt}}$**.** Hydrogen atoms have been omitted for clarity. Selected distances and angles are collected in Table 4.1.

The pentane-insoluble red-black precipitate from the H_2pdt + Cp_2Ni reaction was determined to have the formula $Cp_2Ni_3(pdt)_2$ ($\mathbf{2^{pdt}}$) by X-ray crystallography (Figure 4.3). Single crystals of the trinickel species $\mathbf{2^{pdt}}$ were obtained as a THF solvate and a solvent-free form. Both structures exhibited similar bonding distance between atoms. In the THF solvate the trinickel center adopts a cisoid geometry, whereas the transoid nickel geometry is observed for the solvent-free form. Isomerism arising from crystal habit of metal clusters and multimetallic complexes is rare, one example being $Ir_6(CO)_{12}(\mu_3\text{-}CO)_4$ vs $Ir_6(CO)_{12}(\mu_2\text{-}CO)_4$.[8] The Ni1-Ni2 distance in both isomers is similar with a distance of 2.8630(6) Å for the cisoid structure and a distance of 2.8267(7) Å for the transoid structure.

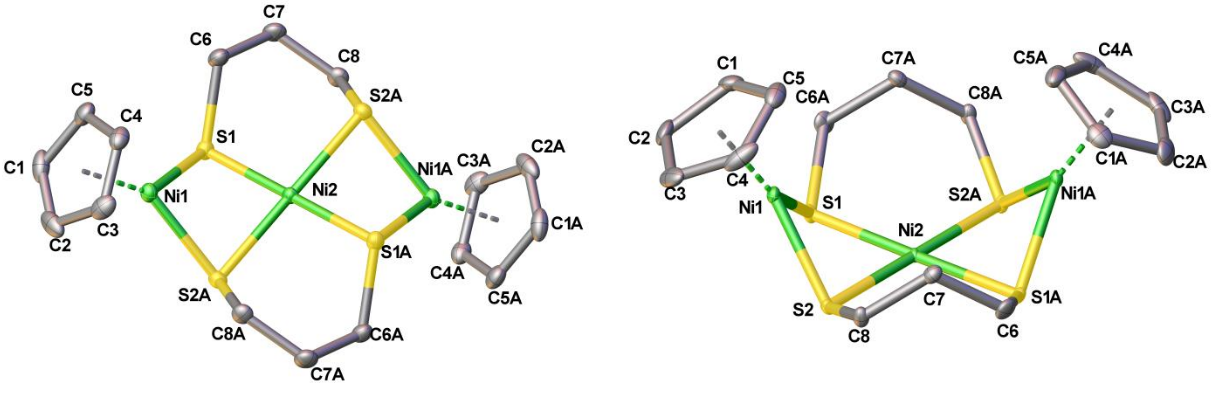

Figure 4.3. Solid state structures of *trans*- and *cis*-$Cp_2Ni_3(pdt)_2$ ($\mathbf{2^{pdt}}$). The cations have crystallographically imposed symmetry: inversion for the trans isomer and reflection for cis isomer. Hydrogen atoms have been omitted for clarity. Selected distances and angles are collected in Table 4.1.

4.2.3 Reaction of Nickelocene with 1,2-ethanedithiol

The reaction of nickelocene and ethanedithiol in pentane afforded $Cp_2Ni_3(edt)_2$ (**2^{edt}**) together with small amounts of insoluble material, some of which is a Ni_5 complex (**3^{edt}**) , based on crystallographic analysis (Scheme 4.3).

Scheme 4.3. Synthesis of **2^{edt}** and **3^{edt}**

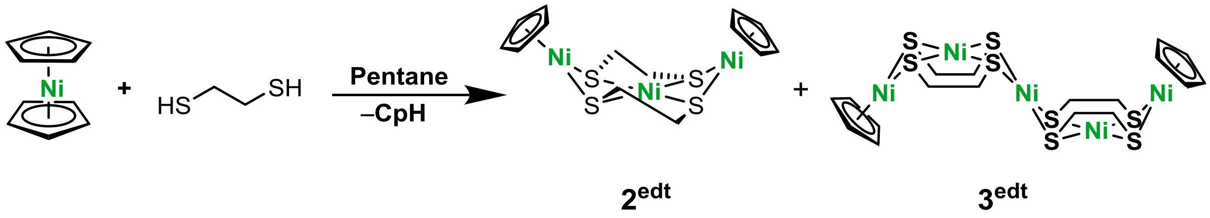

The trinickel complex **2^{edt}** was isolated as dark-purple CH_2Cl_2 soluble microcrystals in ~80% yield. Crystallographic analysis revealed that **2^{edt}** to be a C_s-symmetric species (Figure 4.4), similar to that of *cis*-**2^{pdt}**. In $(PPh_4)_2[Ni(edt)_2]$, the $[Ni(edt)_2]^{2-}$ center is centrosymmetric.[9] In **2^{edt}**, the 5-membered Ni(edt) rings adopt mirror-image skew conformations. The nonequivalence of the CpNi centers is reflected in the differing Ni1-Ni2 and Ni2-Ni3 separations of 2.677 and 2.933 Å. This large difference indicates the pliability of the weak Ni---Ni interactions. Indeed only one Cp resonance was observed in the ^1H NMR spectrum at -95 ºC, consistent with a highly flexible molecule.

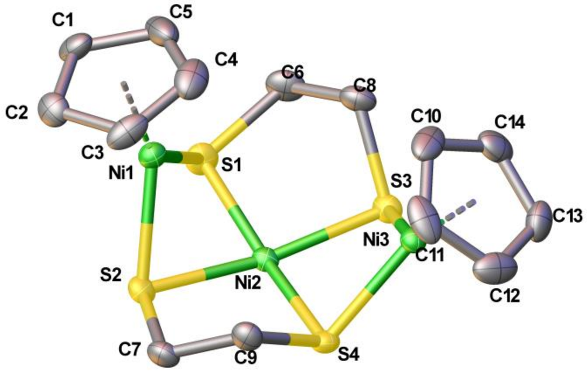

Figure 4.4. Solid state structure of one molecule of $Cp_2Ni_3(edt)_2$ (**2^{edt}**) of two in the asymmetric unit (see SI for selected parameters for the second molecule). Hydrogen atoms have been omitted for clarity. Selected distances and angles are collected in Table 4.1.

The poorly soluble derivative was identified crystallographically as the pentanickel complex $Cp_2Ni_5(edt)_4$ (**3^{edt}**) (Figure 4.4). These crystals were not soluble in dichloromethane, carbon disulfide, methanol, DMSO, or DMF. This pentanickel molecule is centrosymmetric, the core of which consists of a pair of planar $[Ni(edt)_2]^{2-}$ subunits conjoined by a Ni^{2+} center. The resulting $[(Ni(edt)_2)]_2Ni^{2-}$ core is end-capped with two $CpNi^+$ centers (Figure 4.5). The Ni---Ni interactions indicate nonbonding interactions 2.6257(8) and 2.9603(6) Å.

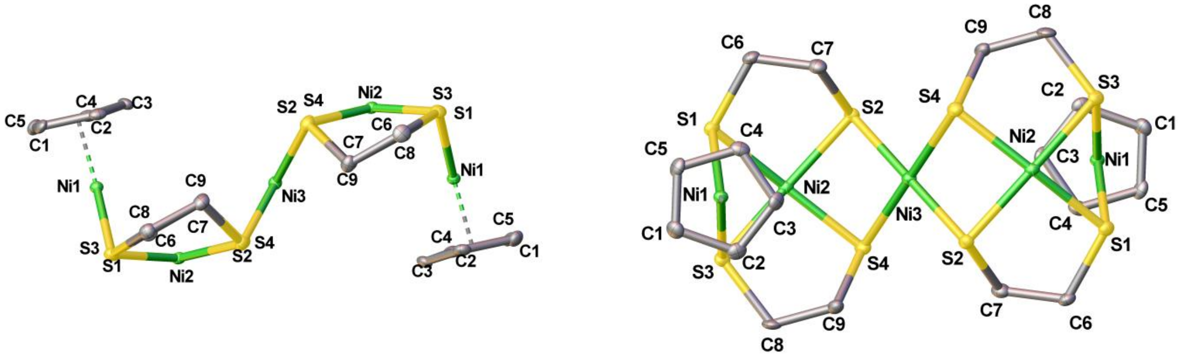

Figure 4.5. Solid state structure of $Cp_2Ni_5(edt)_4$ (**3^{edt}**) viewed from the side (left, note: edt backbones are eclipsed), and viewed from above (right). Hydrogen atoms have been omitted for clarity. Selected distances and angles are collected in Table 4.1.

4.2.4 Reaction of Nickelocene with 1,2-benzenedithiol

The reaction of nickelocene with 1,2-benzenedithiol (H_2bdt) gave results similar to those for 1,2-ethanedithiol. Formed in high yield is the dark violet trinickel complex $Cp_2Ni_3(bdt)_2$ (**2^{bdt}**). As in the edt case, no dinickel product was observed. X-ray crystallography established the compound adopts a bowl-like shape similar to that in **2^{edt}**, but with symmetrical Ni1-Ni2 distances (Figure 4.6).

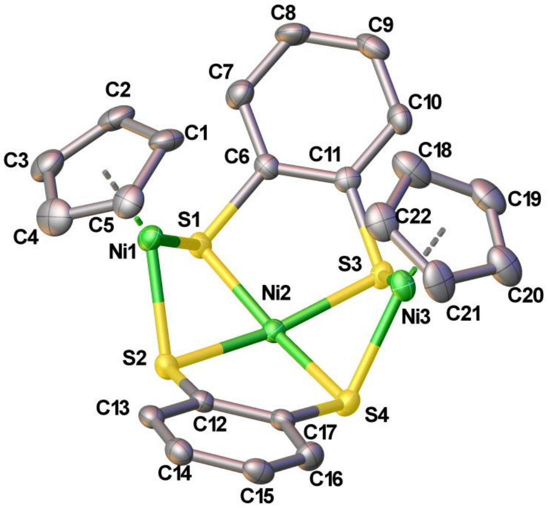

Figure 4.6. Solid state structure of $Cp_2Ni_3(bdt)_2$ (**2^{bdt}**). Hydrogen atoms have been omitted for clarity. Selected distances and angles are collected in Table 4.1.

4.3 Solution Instability of $Cp_2Ni_n(xdt)_m$ Compounds

The dinickel and trinickel compounds are not stable in solution and have the propensity to eliminate Cp ligands and form insoluble, longer chain nickel thiolates deposited mostly as red, amorphous precipitates. In the case of $\mathbf{2}^{\mathbf{pdt}}$, $Ni_6(pdt)_6$ was mechanically isolated as a minor component of the precipitate deposited from dichloromethane solution. These red crystals were identified crystallographically as the known[10] hexanuclear cyclic complex. The remaining majority of red solid precipitates showed no X-ray diffraction as a powder, indicating the material was amorphous and likely polymeric.

Mirroring the instability of $\mathbf{2}^{\mathbf{pdt}}$, Et_2O/CH_2Cl_2 solutions of $\mathbf{2}^{\mathbf{edt}}$ deposit red crystals upon standing for days which were identified crystallographically as $\mathbf{3}^{\mathbf{edt}}$.

The occurrence of two nuclearities of CpNi-pdt complexes, i.e., $\mathbf{1}^{\mathbf{pdt}}$ and $\mathbf{2}^{\mathbf{pdt}}$, raises questions about their interconvertability. Treatment of $\mathbf{1}^{\mathbf{pdt}}$ with 1 equiv. $pdtH_2$ at room temperature gave $\mathbf{2}^{\mathbf{pdt}}$ and insoluble material over the course of 24h. The yield of $\mathbf{2}^{\mathbf{pdt}}$ was only 22%, and full conversion is not observed. These results suggest that $\mathbf{2}^{\mathbf{pdt}}$ is more reactive towards $pdtH_2$ than is $\mathbf{1}^{\mathbf{pdt}}$.

4.4 Singlet-Triplet Equilibrium of $\mathbf{1}^{\mathbf{pdt}}$

The room temperature ^{1}H-NMR spectrum of $\mathbf{1}^{\mathbf{pdt}}$ is unusual with the $C_5\mathit{H}_5$ signal at δ2.90, and the CH_2 signals observed at δ4.60 and δ2.76. Resonances for $C_5\mathit{H}_5$ are typically observed near δ5 and propanedithiolate resonances are typically observed in the δ2-3 region. These unusual chemical shifts prompted a variable temperature NMR study (Figure 4.7). The ^{1}H-NMR spectrum at −65 °C exhibits chemical shifts closer to typical values: $C_5\mathit{H}_5$ at δ4.87 and $C\mathit{H}_2(C\mathit{H}_2S)$ signals δ2.21 and 3.11, respectively. These chemical shifts varied nonlinearly with $1/T$, suggesting a thermally accessible paramagnetic state (Figure 4.8).

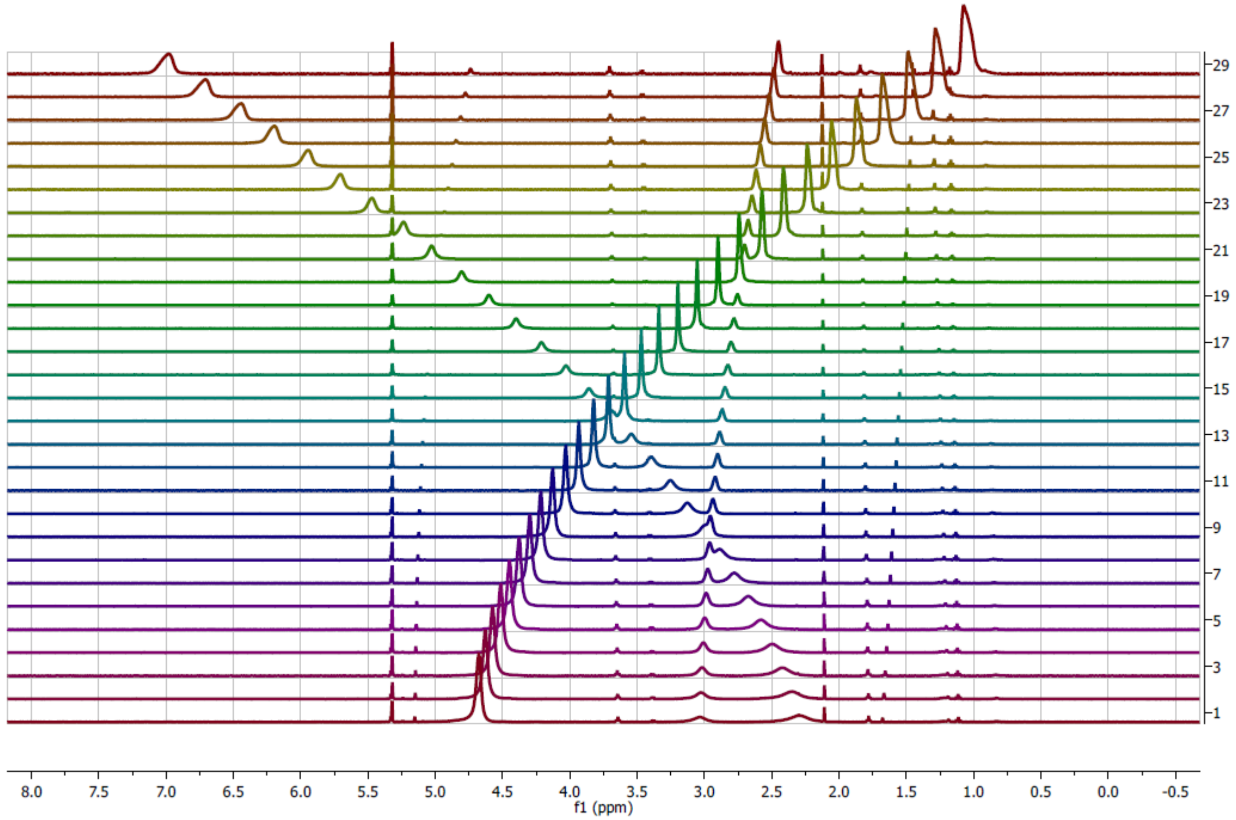

Figure 4.7. Variable temperature ^{1}H-NMR spectra of a CD_2Cl_2 solution of Cp_2Ni_2(pdt) in a sealed tube under solvent vapor pressure. Temperature increases from bottom to top ranging from 208 K to 348 K. The resonances at the diamagnetic limit are observed at δ4.68 ($C_5\boldsymbol{H}_5$), δ3.04 ($S_2CH_2C\boldsymbol{H}_2CH_2$), and δ2.29 ($S_2C\boldsymbol{H}_2CH_2C\boldsymbol{H}_2$). The resonances at the 348 K are observed at δ1.10 ($C_5\boldsymbol{H}_5$), δ2.71 ($S_2CH_2C\boldsymbol{H}_2CH_2$), and δ7.00 ($S_2C\boldsymbol{H}_2CH_2C\boldsymbol{H}_2$). Principal impurities: Et_2O, THF, and *n*-pentane.

The data obtained from variable temperature ^{1}H-NMR spectra were fit to eq. 3 (see the supporting information section for derivation) to obtain the free energy difference between the diamagnetic ground state and a paramagnetic excited state. ΔG was determined to be 2.65±0.05 kcal/mol in $CDCl_3$ and 3.2±0.05 kcal/mol in toluene-d_8, which, at 298 K, equates to a 1.1% and 0.5% population of the paramagnetic state, respectively. No EPR signal in parallel or perpendicular mode was observed for solution or solid samples of $\mathbf{1}^{pdt}$ at room temperature.

$$\delta_{obs} = \frac{(\delta_d - \delta_p)}{e^{\frac{-\Delta G}{RT}} + 1} + \delta_p \quad \text{(eq. 3)}$$

where
δ_{obs} = observed ^{1}H NMR chemical shift
δ_d = chemical shift of diamagnetic component
δ_p = chemical shift of paramagnetic component
ΔG = free energy difference between the paramagnetic and diamagnetic state
R = universal gas constant
T = temperature (K)

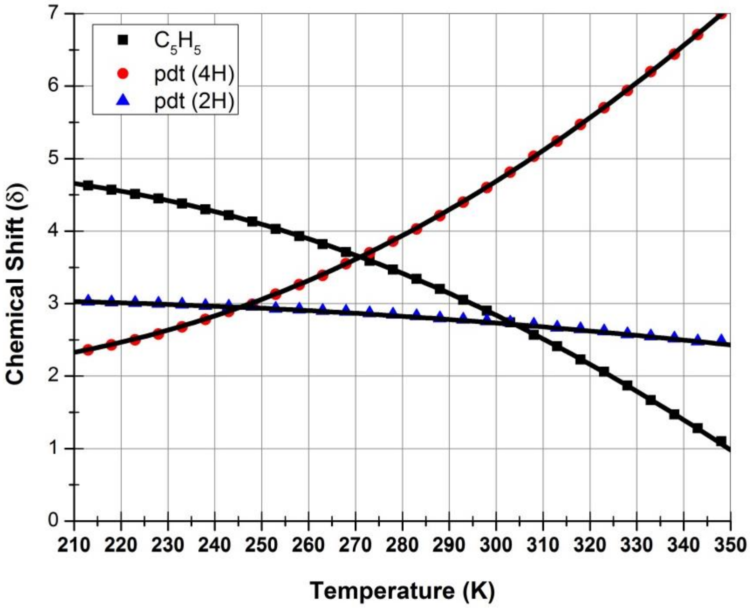

Figure 4.8. Plot of ^{1}H-NMR chemical shift versus temperature of the resonances observed in $\mathbf{1}^{\mathbf{pdt}}$ in $CDCl_3$ and fitted curves. Extrapolated chemical shifts $\delta_{\text{diamagnetic}}$ ($\delta_{\text{paramagnetic}}$): 5.02±0.03 (−180±10), 3.08±0.01 (−27±2), 1.91±0.05 (242±15).

In CD_2Cl_2 solution at room temperature, $\mathbf{2}^{\mathbf{pdt}}$ exhibits a complex ^{1}H NMR spectrum in the CH_2 region, but only one C_5H_5 resonance. Unlike the dinickel compound, the trinickel complex is fully diamagnetic. Similarly diamagnetic ^{1}H-NMR spectra are obtained from complexes $\mathbf{2}^{\mathbf{edt}}$ and $\mathbf{2}^{\mathbf{bdt}}$.

4.5 DFT Analysis of the Singlet-Triplet Splitting.

In contrast to $\mathbf{1}^{\mathbf{pdt}}$, previous examples of thiolates $Cp_2Ni_2(SR)_2$ and related phosphides $Cp_2Ni_2(PR_2)_2$ do not exhibit paramagnetism or a small singlet-triplet (S-T) splitting. To probe this difference, the effect of folding the Ni_2S_2 core was investigated computationally. The calculations included conformational optimizations of singlet vs triplet structures and the computation of S-T free energy difference, leading to the construction of a Walsh diagram. The solid state structure of **1**^{SEt} was the starting point for the DFT modeling. After testing a series of density functionals, the BP86-D3/def-TZVP level was adopted. The inclusion of D3 dispersion corrections is mandatory to treat the effect of the thiolate substituents more accurately.

The optimized geometry for the ground state of **1**^{SEt} agreed with the structure observed crystallographically: a flat, square Ni_2S_2 core with Ni-S distances very similar to those observed in the solid state. When the structure was optimized with an unrestricted $S = 1$ spin state, a Ni_2S_2 distorts from planarity and resembles the bent structure of dithiolate derivatives. In the triplet state, approximately half of the spin density is on the dinickel core, the remainder delocalized on the ligands, especially sulfur (Figure 4.9).

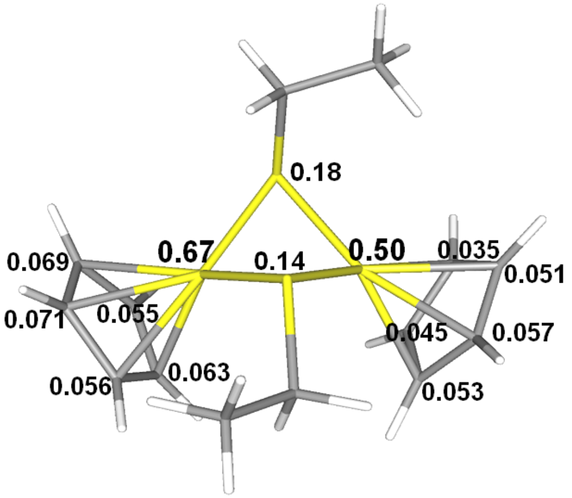

Figure 4.9. Spin density distribution of the optimized triplet state of *trans*-**1**^{SEt}.

The dependence of the S-T splitting on the *non*-planarity of the Ni_2S_2 core was investigated (Figure 4.10). Although only the *trans* ethyl isomer is observed crystallographically, two additional isomers, the *cis*-down and *cis*-up, were also investigated. For low bending angles ($\alpha < 40°$, see Figure 4.10 for a depiction of α) the S-T splitting remains large, but greater distortions strongly stabilize the triplet state. For the *trans* isomer, the triplet has a minimum energy at $\alpha \approx 60^o$. For the *cis*-up isomer (akin to **1**^{pdt}) the minimum is at $\alpha \approx 50^o$, which is similar to the 51.3^o observed in **1**^{pdt}**.**

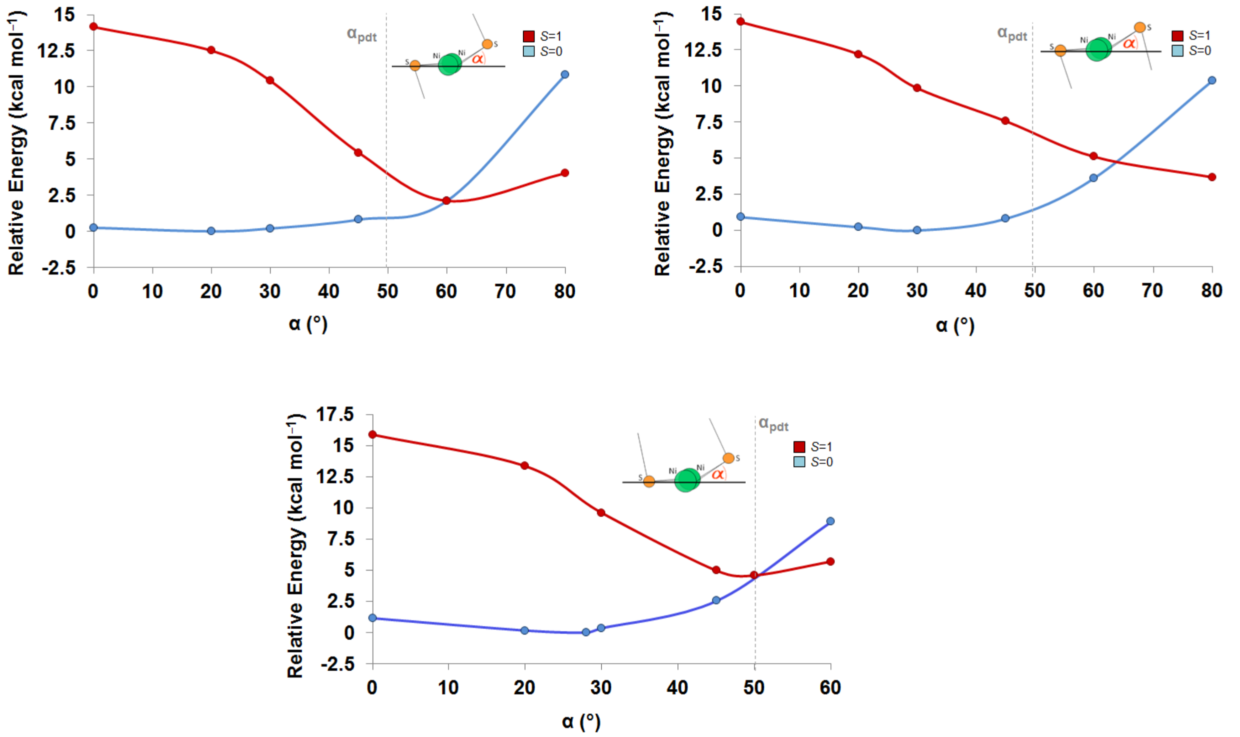

Figure 4.10. The free energy plots of the singlet and triplet states of **1**^{SEt} while varying the angle between the S1-Ni$_2$ and S2-Ni$_2$ planes. The dashed lined indicates the angle observed in **1**^{pdt}. The energy *cis*-up isomer (bottom middle), was only calculated to an alpha of 60 degrees because of drastically increased energies from ethyl-ethyl steric hindrances. The energies for each state varied by up to 2 kcal/mol depending on the free-rotation orientation of the ethyl group.

The Ni-S-Ni angle in the solid state structures of **1**^{pdt} and **1**^{SEt} are 83° and 92° respectively, where the idealized bond angle would be slightly greater than 90 degrees. Distortion from 90º would diminish overlap of the S *p*-orbitals with the Ni orbitals, weakening the Ni-S interaction. The decreased Ni-S overlap elevates the singlet state, but is offset by a Ni-Ni bonding interaction in the triplet state, although not significantly enough to favor a triplet ground state. Consistent with less electron donation from ligand-to-Ni is the increased negative charge on sulfur (Table 4.2).

Table 4.2. Calculated Atomic/Ligand Charge and Distances in Singlet and Triplet **1**^{SEt}.

	S = 0	*S* = 1	Difference (Average)
S Partial Charge (*q*)	**−0.20**	**−0.25, −0.28**	**−0.06**
Cp Partial Charge (*q*)	**−0.44**	**−0.44, −0.45**	**−0.05**
Ni-S Distance (Å)	**2.202**	**2.244**	**+0.042**
Ni-Cp Distance (Å)	**2.155**	**2.182**	**+0.028**

The frontier and adjacent molecular orbitals calculated for the optimized structure of $\mathbf{1}^{\mathrm{SEt}}$ in the singlet and triplet states differ substantially (Figure 4.11). For the *S* = 0 state, the HOMO and HOMO-1 are principally Cp-Ni antibonding. The LUMO also exhibits Cp-Ni antibonding, but is predominantly sulfur *p*-orbital in character. In contrast, the frontier orbitals for the *S* = 1 state are more delocalized. The α-SOMO is essentially a metal-ligand antibonding orbital, while the α-SOMO-1 is metal-metal antibonding.

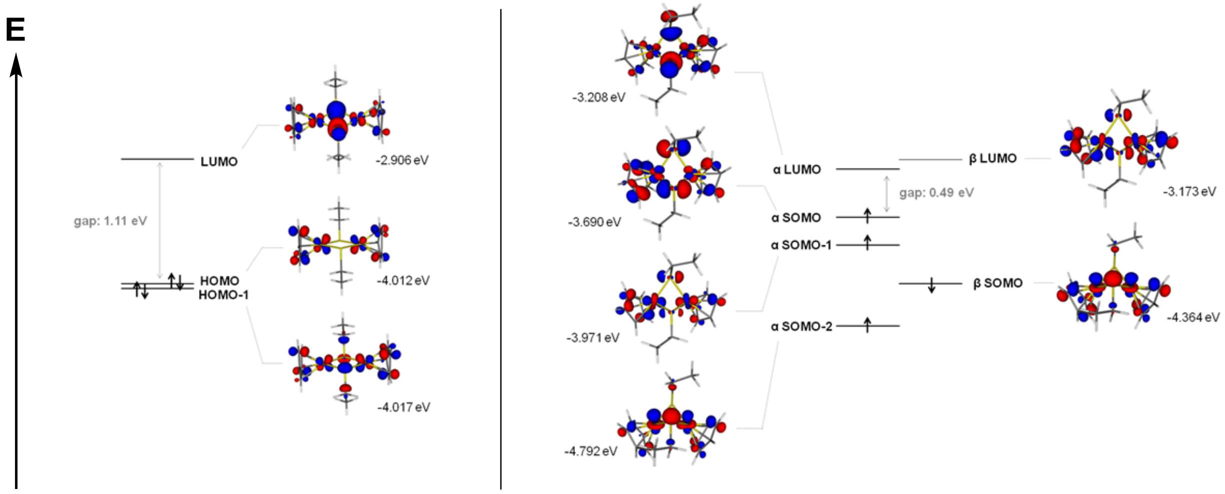

Figure 4.11. Frontier and adjacent molecular orbital diagram of $\mathbf{1}^{\mathrm{SEt}}$ for the *trans* isomer in the S=0 state (left) and the S=1 state (right).

To illustrate the trend shown in Figure 4.11, a Walsh diagram was constructed examining the energies of the HOMO, HOMO-1, LUMO, and LUMO+1 of the SEt system in the singlet state with respect to the singlet optimized geometry and the triplet optimized geometry (Figure 4.12). The energies of LUMO+1 and the HOMO decrease slightly upon distortion of the core, while the energy of the LUMO is raised in energy. The energy of HOMO-1 is raised significantly.

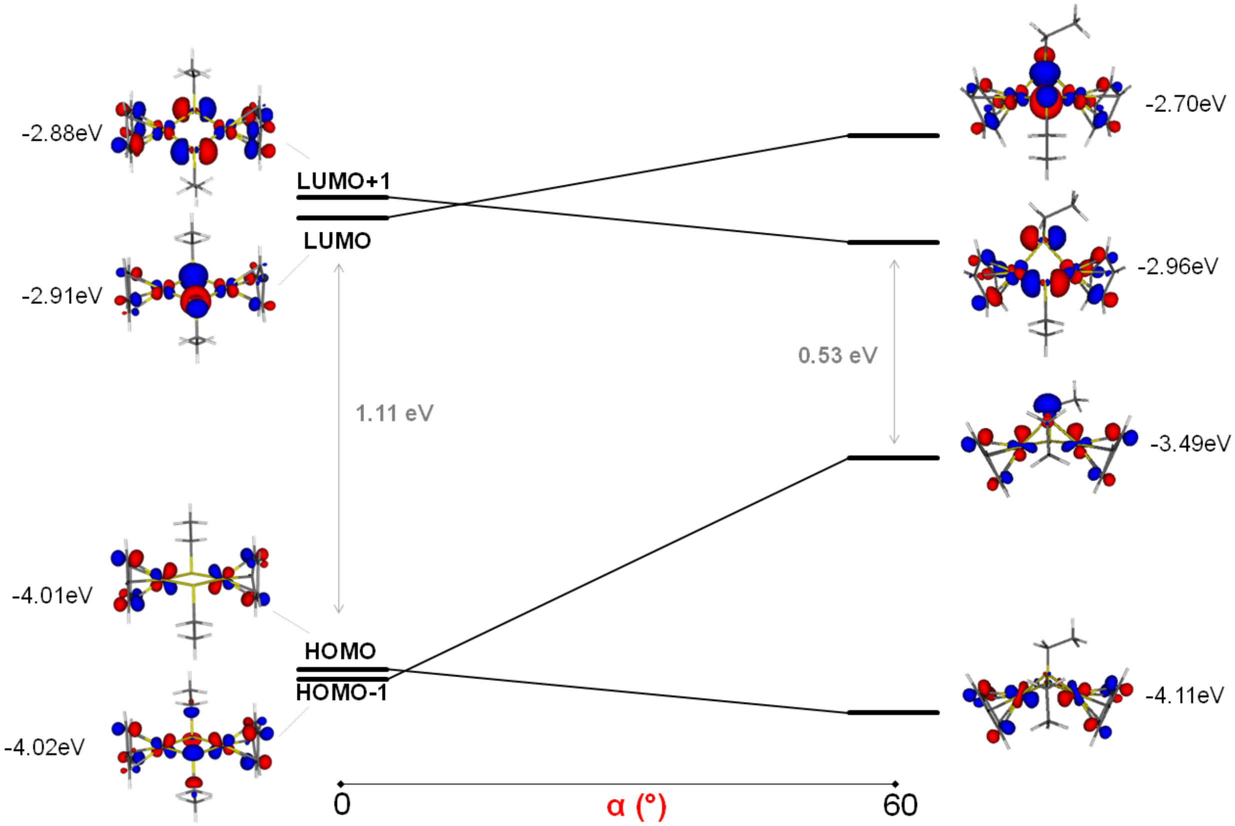

Figure 4.12. Walsh diagram for $\mathbf{1}^{\mathrm{SEt}}$ showing the effect of distorting the singlet Ni_2S_2 core from planarity.

4.6 Redox Chemistry of $Cp_2Ni_n(xdt)_m$

The dinickel complexes display reversible redox couples while the trinickel species exhibit quasi-reversible redox couples (Table 4.3). The trinickel complex $\mathbf{2}^{\mathrm{pdt}}$ reversibly oxidizes at −0.25 and 0.10 V at 100 mVs^{-1} (Figure 4.14, left), although these couples are less reversible at slower scan rates.

Chemical oxidation using $FcBF_4$ gave the dinickel salt $[\mathbf{1}^{\mathrm{pdt}}]BF_4$ concomitant with the formation of insoluble red precipitates, proposed to be Ni(thiolate) oligomers and polymers. An unstable intermediate in this oxidation, $[\mathbf{2}^{\mathrm{pdt}}]BF_4$, was crystallized somewhat fortuitously from a vapor diffusion of pentane to a solution of the mixture of $FcBF_4$ and $\mathbf{2}^{\mathrm{pdt}}$ at −35 °C. Characterization of $[\mathbf{2}^{\mathrm{pdt}}]BF_4$ by X-ray diffraction revealed that the cation resembles the cisoid isomer of $\mathbf{2}^{\mathrm{pdt}}$ with idealized C_{2v} symmetry (Figure 4.13). The (Ni---Ni) distances in $[\mathbf{2}^{\mathrm{pdt}}]BF_4$ are shorter than in $\mathbf{2}^{\mathrm{pdt}}$ by ~0.2 Å, though not contracted sufficiently to enable metal-metal bonding. The other bonding parameters remain relatively unchanged; the Ni-C-and all Ni-S distances contracted by only <0.02 Å.

Table 4.3. Electrochemical Parameters for Selected Compounds

Complex	Potential (vs $Fc^{0/+}$)	i_{pa}/i_{pc}
$Cp_2Ni_2(SEt)_2$ (**1**^{SEt})	−0.420	0.943
$Cp_2Ni_2(pdt)$ (**1**^{pdt})	−0.516	0.962
$[Cp_2Ni_2(edt)]BF_4$ ([**1**^{edt}]BF_4)	−0.534	0.975
$Cp_2Ni_3(edt)_2$ (**2**^{edt})	+0.649, −0.012, −0.118	0.925, n.d.[a], n.d.[a]
$Cp_2Ni_3(pdt)_2$ (**2**^{pdt})	+0.124, −0.276	0.910[a], 1.064[b]
$Cp_2Ni_3(bdt)_2$ (**2**^{bdt})	−0.015, −0.949[c]	1.291, irr.

n.d. = not determined. irr. = irreversible. [a] These waves become irreversible in the same scan window at 10 mVs^{-1}. [b] This wave has an i_{pa}/i_{pc} ratio of 0.913 at 10 mVs^{-1} [c] This wave occurs at the potential for the reduction of CpNi(bdt). Conditions: ~1 mM in CH_2Cl_2, 100 mM $[NBu_4]PF_6$, glassy carbon electrode (d = 3 mm); Ag wire as pseudoreference with internal Fc standard at 0 V; Pt counter electrode.

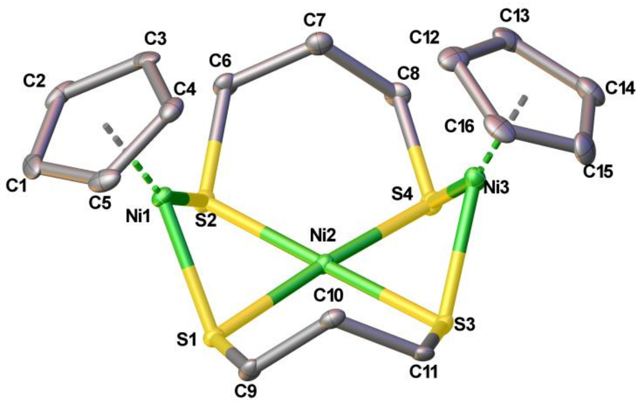

Figure 4.13. Solid state structure of the cation in $[Cp_2Ni_3(pdt)_2]BF_4$. Selected distances and angles are collected in Table 4.1.

The CV of **2**^{edt} is more complicated than that of **2**^{pdt} (Figure 4.14, right). Compound **2**^{edt} first oxidizes at −0.1 V, about 150 mV more positive than the [**2**^{pdt}]$^{0/+}$ couple. Similar to **2**^{pdt}, preparative scale oxidation of **2**^{edt} with $FcBF_4$ gave [**1**^{edt}]BF_4, although in poor yield.

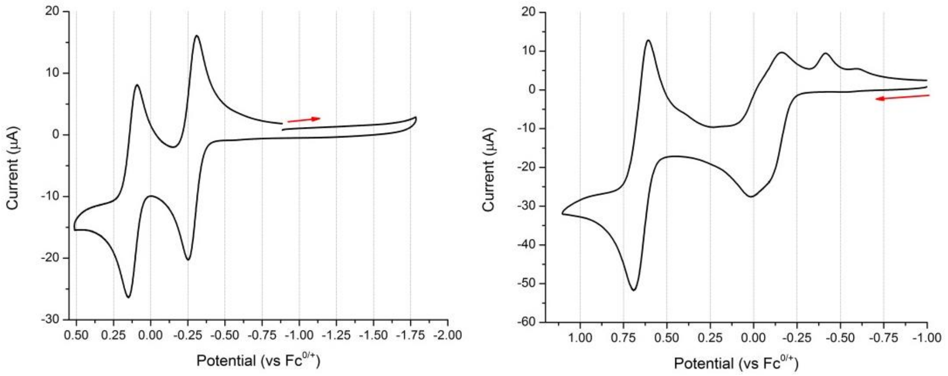

Figure 4.14. CV of $\mathbf{2}^{\mathbf{pdt}}$ (left). CV of $\mathbf{2}^{\mathbf{edt}}$ right). Conditions: CH_2Cl_2 solution, ~1 mM analyte, 100 mM $[Bu_4N][PF_6]$, 100 mVs^{-1}. Starting point and initial direction is indicated using a red arrow.

The cyclic voltammogram of $\mathbf{2}^{\mathbf{bdt}}$ exhibits a quasi-reversible oxidation (i_{pa}/i_{pc} = 1.291) at −0.02 V vs Fc$^{0/+}$ which generates two reductions on the return scan at −0.33 V and −0.95 V. The second reduction observed on the return scan corresponds to the redox couple observed for the known complex CpNi(bdt).[11,12] The EPR spectrum of the a mixture of $\mathbf{2}^{\mathbf{bdt}}$ and one equivalent of $FcBF_4$ at 77K exhibited a rhombic signal with g-tensors g_1 = 2.123, $g_2 \approx g_3$ = 2.02, consistent with previously reported spectra.[13] Upon standing in air, solutions of $\mathbf{2}^{\mathbf{bdt}}$ slowly oxidize to the green complex CpNi(bdt), as determined by cyclic voltammetry. Preparative scale oxidation of $\mathbf{2}^{\mathbf{bdt}}$ with 1 equiv. of $FcBF_4$ produced ~50% yield of the Ni(III) complex CpNi(bdt)[11].

The redox properties of $[\mathbf{1}^{\mathbf{edt}}]BF_4$ and $\mathbf{1}^{\mathbf{pdt}}$ were also examined by cyclic voltammetry exhibited similar redox couples. In CH_2Cl_2, $\mathbf{1}^{\mathbf{pdt}}$ undergoes a one-electron reduction at $E_{1/2}$ = −0.520 V vs Fc$^{0/+}$. This highly reversible couple (i_{pc}/i_{pa} = 0.967) is assigned to the $[\mathbf{1}^{\mathbf{pdt}}]^{+/0}$ redox couple. Under similar conditions, the $[\mathbf{1}^{\mathbf{edt}}]^{+/0}$ redox couple was observed at almost the identical potential (−0.534 V) and is also reversible (i_{pc}/i_{pa} = 0.975). The difference in the oxidation potential for the $\mathbf{1}^{\mathbf{edt}}$ and $\mathbf{1}^{\mathbf{pdt}}$ complexes is minor. This similarity is not unprecedented; for the heterobimetallic system $[(dppe)Ni(xdt)Fe(CO)_3]^{+/0}$ (xdt = edt, pdt) the potentials for the redox couple differ by only 40 mV.[14] It is known that $[CpNi(SEt)]_2$ can be oxidized at mild potentials.[15] This oxidation occurs at −0.423 V vs Fc$^{0/+}$ in CH_2Cl_2 solution. In THF solution, $\mathbf{1}^{\mathbf{pdt}}$ reversibly reduces at $E_{1/2}$ = −1.91 V (i_{pc}/i_{pa} = 0.99, ΔE_p ~ 91 mV), assigned to the $[\mathbf{1}^{\mathbf{pdt}}]^{0/-}$ couple.

Crystallographic characterization of $[\mathbf{1}^{\mathbf{pdt}}]BF_4$ and $[\mathbf{1}^{\mathbf{edt}}]BF_4$ revealed a similar "butterfly" Ni_2S_2 core as in $\mathbf{1}^{\mathbf{pdt}}$ (Figure 4.15). Oxidation causes contraction of the Ni---Ni from 2.890(2) Å (avg.) to 2.4537 (3) Å. Similar short contacts have been observed in other mixed-valent Ni(II)Ni(III) systems of the type $[Ni_2(\mu\text{-}SR)_2(PR_3)_2(SR)_4]^-$, which was found to be 2.501(2) Å.[16] Also relevant is the square pyramidal mixed valence cluster $[Cp_3Ni_3S_2]^+$. This cluster features two bonding and one nonbonding Ni---Ni contacts of 2.536(2) and 3.145(2) Å. The bonding contacts are assigned to a pair of Ni(III)-Ni(II) interactions (vs a single Ni(III)-Ni(III) interaction).[17]

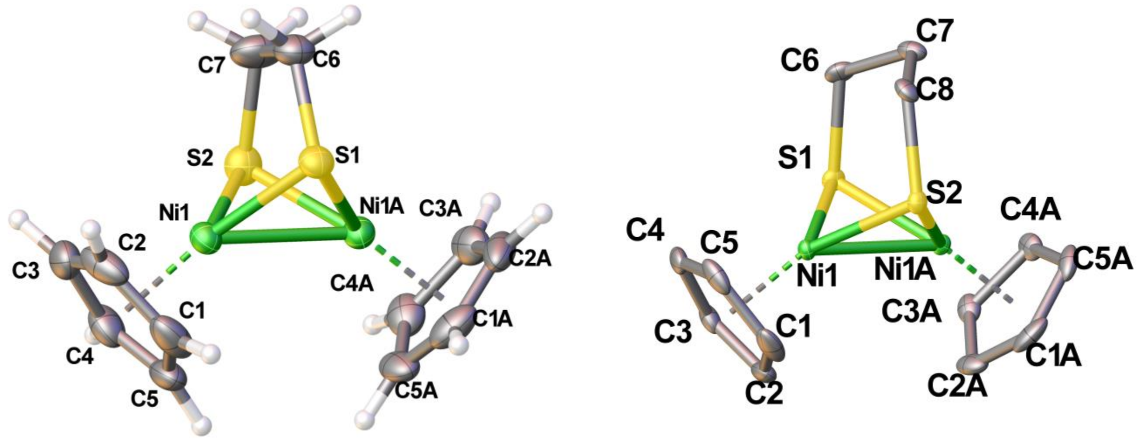

Figure 4.15. Solid state structure of $[\mathbf{1}^{\mathrm{edt}}]\mathrm{BF}_4$ and $[\mathbf{1}^{\mathrm{pdt}}]\mathrm{BF}_4$. The BF_4^- anions have been omitted for clarity. Hydrogen atoms have been omitted for clarity in $[\mathbf{1}^{\mathrm{pdt}}]\mathrm{BF}_4$ Selected distances and angles are collected in Table 4.1.

Due to the rather negative potentials for the redox couples, the dinickel complexes were investigated for their ability to produce hydrogen by treatment with strong acids. Evans estimates that reduction of $\mathrm{CF_3SO_3H}$ in MeCN solution to give $\mathrm{H_2}$ will occur near −300 mV.[18-20] Thus, with the $[\mathbf{1}^{\mathrm{pdt}}]^{+/0}$ couple at −550 mV vs $\mathrm{Fc}^{+/0}$, has the reducing power to convert strong acids into $\mathrm{H_2}$. When treated with excess $\mathrm{HBF_4}$, however, $\mathbf{1}^{\mathrm{pdt}}$ converted to $[\mathbf{1}^{\mathrm{pdt}}]^+$ in poor yield (<5%) and amorphous precipitate with formation of only traces of $\mathrm{H_2}$ (<1% equiv.) observed by gas chromatography. No bridging hydride complexes were observed.

The mixed-valence cations $[\mathbf{1}^{\mathrm{pdt}}]^+$ and $[\mathbf{1}^{\mathrm{edt}}]^+$ were investigated by EPR spectroscopy at 77K and produced similar spectra (Figure 4.16). The *g*-tensors were g_1= 2.092, g_2 = 2.007, g_3 = 1.992 and g_1= 2.083, g_2 = 1.993, g_3 = 1.983 for $[\mathbf{1}^{\mathrm{pdt}}]^+$ and $[\mathbf{1}^{\mathrm{edt}}]^+$ respectively. As expected, no significant hyperfine coupling is observed in the CW-EPR spectrum. In contrast to the neutral CpNi(thiolate) complexes, these cations are stable in solution.

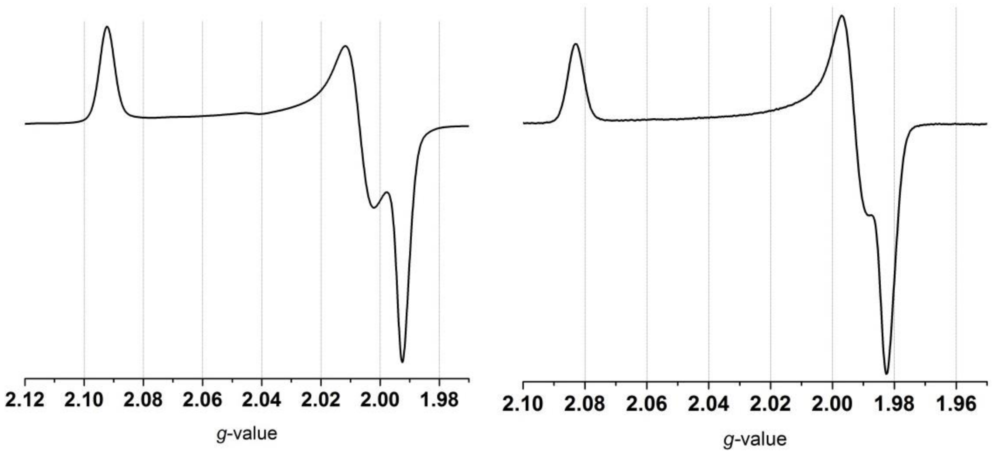

Figure 4.16. X-Band EPR spectrum of $[\mathbf{1}^{\text{edt}}]\text{BF}_4$ (left) and $[\mathbf{1}^{\text{edt}}]\text{BF}_4$ (right) at 77K as a CH_2Cl_2 glass.

The known black complex $\mathbf{1}^{\text{SEt}}$ and its one-electron oxidation product were characterized crystallographically. Treatment of the black neutral precursor with one equiv. of FcBF_4 gave $[\text{Cp}_2\text{Ni}_2(\text{SEt})_2]\text{BF}_4$ ($[\mathbf{1}^{\text{SEt}}]\text{BF}_4$) as a dark red powder. The solid state structure crystallographically revealed a butterfly Ni_2S_2 core, in contrast to the flat Ni_2S_2 core observed in $\mathbf{1}^{\text{SEt}}$. Similar to the dithiolate system, the Ni---Ni distance contracts significantly (~3.15 to 2.47 Å), indicating the presence of metal-metal bonding (Figure 4.17).

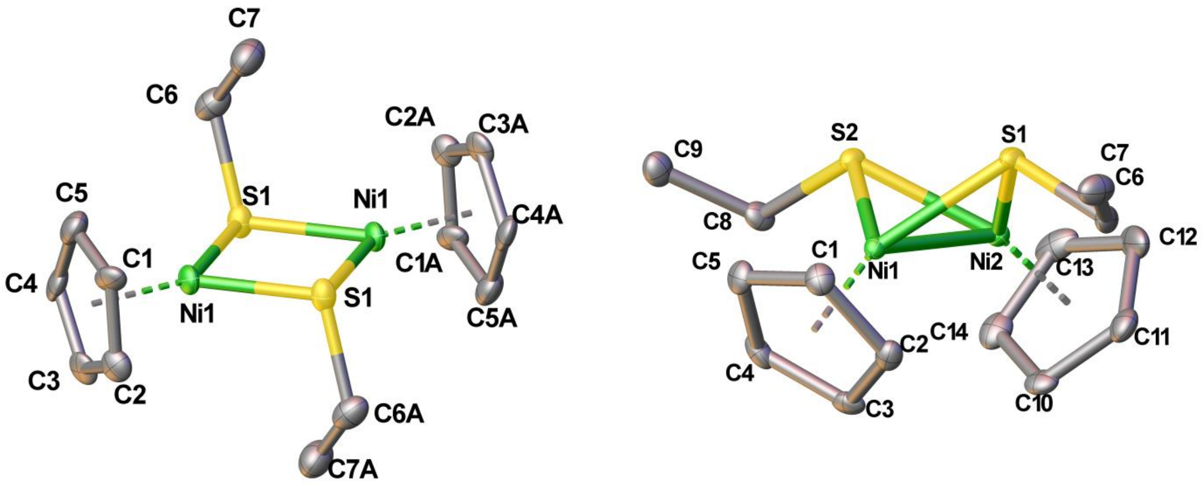

Figure 4.17. Solid state structure of $\mathbf{1}^{\text{SEt}}$ (left) and $[\mathbf{1}^{\text{SEt}}]\text{BF}_4$ (right). The BF_4^- anions and hydrogen atoms have been omitted for clarity. Selected distances and angles are collected in Table 4.1.

4.7 Reduction of [$\mathbf{1}^{\mathbf{edt}}$]$^+$

The neutral dinickel complex $\mathbf{1}^{\mathbf{edt}}$ does not arise from the reaction of edtH_2 and nickelocene ($\mathbf{2}^{\mathbf{edt}}$ is obtained in high yield). However, $\mathbf{1}^{\mathbf{edt}}$ could be prepared by reduction of [$\mathbf{1}^{\mathbf{edt}}$]$BF_4$, which in turn was obtained by oxidation of $\mathbf{2}^{\mathbf{edt}}$, though is poor yield (Scheme 4.4). The reduction was effected with Cp_2Co to give the pentane-soluble complex in high yield. Although its solutions decompose over the course of a couple hours at room temperature, the stability is sufficient to characterize its NMR properties.

Scheme 4.4. Synthesis of $\mathbf{1}^{\mathbf{edt}}$

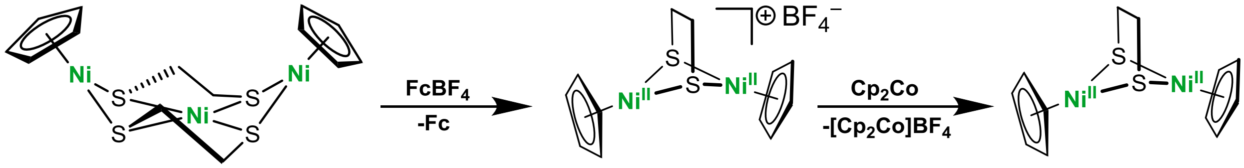

The ^{1}H NMR behavior of $\mathbf{1}^{\mathbf{edt}}$ is diagnostic of a very small S-T splitting (Figure 4.17). Specifically, the spectrum consists of singlets at δ+66.6 and −34.3 in a 4:10 ratio at room temperature. The spectrum is relatively insensitive to temperature down to −60 ºC. Over the interval +60 to −60 ºC, the signals shift ~15 ppm towards diamagnetic shifts. Using the Evans method, the complex has a magnetic moment of 1.09, which corresponds to approximately half of the ideal spin only contribution magnetic moment of the triplet (2.82). DFT analysis reproduced the observed lower free energy difference of the singlet and triplet states in $\mathbf{1}^{\mathbf{edt}}$ compared to that in $\mathbf{1}^{\mathbf{pdt}}$.

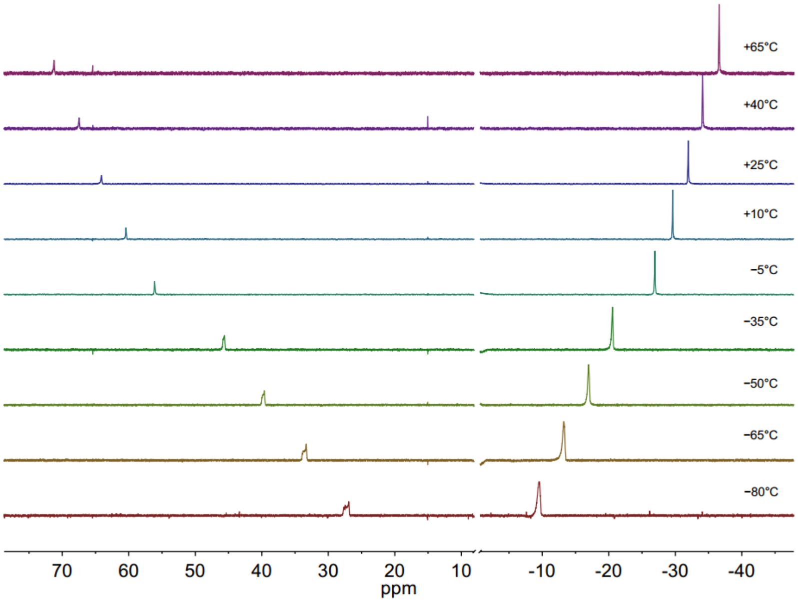

Figure 4.18. Variable temperature ^{1}H-NMR spectra of a CD_2Cl_2 solution of Cp_2Ni_2(edt) in a sealed tube under solvent vapor pressure. Temperatures are indicated in line. The down field resonance is assigned to the methylene protons on the thiolate ligand and the high field resonance is assigned to the cyclopentadienide ligand.

4.8 Concluding Remarks – Broader Implications

Synthetic Chemistry. The reaction of thiols with nickelocene has been long known, but studies of dithiols have revealed unexpected structural and electronic diversity. Whereas Fe_2(dithiolate)$(CO)_{6-x}L_x$ and Cp_2Co_2(dithiolate) are $34e^-$ species with M-M bonding, the electron count of Cp_2Ni_2(dithiolate) is $36e^-$. Indeed structural studies show that simple the $Ni_2(SR)_2$ complexes lack metal-metal bonding, reliably exist as diamagnetic, thermally rugged dimers.

The thiol-nickelocene reaction proceeds via an associative kinetics and is characterized by a k_H/k_D of 2.8.[21] Loss of CpH is proposed to give the $16e^-$ complex CpNiSR, which dimerizes. With *di*thiols, this reaction is likely to result in chelation of the second sulfur group. The Ni_2 derivatives could then be envisioned to form via the reaction of this intermediate with nickelocene. Proposed steps are shown for the propanedithiol case in Scheme 4.5.

Scheme 4.5. Proposed Mechanism for the formation of Cp_2Ni_2(pdt) ($\mathbf{1}^{\mathbf{pdt}}$)

$$Cp_2Ni + pdtH_2 \longrightarrow CpNi(\kappa^2\text{-}S(CH_2)_3SH) + CpH$$

$$Cp_2Ni + CpNi(\kappa^2\text{-}S(CH_2)_3SH) \longrightarrow Cp_2Ni_2(pdt) + CpH$$

Such dinickel species are only observed for the $pdtH_2$ reaction. With $edtH_2$ and $bdtH_2$, the reaction between the dinickel thiolate species with additional thiol must be relatively fast.

Oligomerization would require Ni-S bond scission and displacement of the cyclopentadienyl ligand. The triplet state, which possesses weakened metal-ligand bonds, is expected to be more labile and the oligomerization process might proceed through the triplet state. This may account for the lower solution stability of the neutral edt complex $\mathbf{1}^{\mathbf{edt}}$ compared to the pdt complex $\mathbf{1}^{\mathbf{pdt}}$, which has a higher singlet-triplet free energy gap.

Structural Chemistry. The dithiol-nickelocene system gives rise to di-, tri-, and pentanickel dithiolates, end-capped with $CpNi^+$ centers. The structural trends reflect (i) the preference of $[Ni(SR)_4]^{2-}$ sites for square planarity and (ii) the tendency of Ni-S-Ni angles to approach 90º. The absence of Ni---Ni bonding confers flexibility, allowing the formation of μ-thiolate-bridged oligomers. Oxidation of these oligomers turns on Ni---Ni bonding, as manifested in the short Ni---Ni distances for the mixed valence Ni(III)-Ni(II) species . The results highlight the robustness of $Cp_2Ni^{2.5}{}_2(SR)_2$ core. These findings suggest a revised description of $Cp_4Ni_5(\mu^3\text{-}S)_4$. This diamagnetic cluster features two pairs of $Cp_2Ni_2(\mu\text{-}SR)_2$-like subunits attached to a central planar nickel center (Figure 4.18).[22] The CpNi---NiCp distances of 2.495(3) Å in the cluster match the 2.4442(8) Å Ni-Ni bond in $[\mathbf{1}^{\mathbf{edt}}]^+$. In view of the new results, the cluster could be described as $(CpNi^{2.5})_4(\mu^3\text{-}S)_4Ni^{II}$, with antiferromagnetic coupling between the two $[Cp_2Ni_2S_2]^-$ centers, mediated by the square planar Ni(II) center. This perspective avoids the previous description that invokes square planar Ni(0).

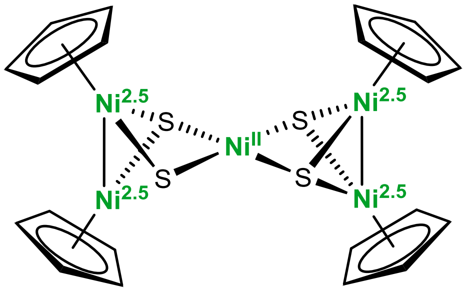

Figure 4.19. The pentanickel cluster$(CpNi^{2.5})_4(\mu^3\text{-}S)_4Ni^{II}$.

Metal-Metal Bonding Between 18e⁻ Metal Centers. A singlet-triplet equilibrium also been proposed for the Ni center in the [NiFe]-hydrogenases,[23-25] but models for such spin equilibria are lacking. The results show that $Cp_2Ni_2(pdt)$ and $Cp_2Ni_2(edt)$ exist in equilibrium with a low-lying paramagnetic states.[26] In contrast, $Cp_2Ni_2(SEt)_2$ is completely diamagnetic.

A singlet-triplet spin equilibrium in 18e⁻ cyclopentadienyl nickel(II) complexes was originally observed for $(C_5Me_5)Ni(acac)$.[27] A related singlet-triplet spin equilibrium is observed for $(C_5R_5)_2Ni_2Br_2$ ($R_5 = H^iPr_4$, $H_2{}^tBu_3$, $H_2{}^iPr_3$), wherein a pair of *S* = 1 centers are antiferromagnetically coupled.[28] These systems feature bulky Cp ligands, which exert weakened ligand fields, which do not sufficiently stabilize the singlet state. These complexes are related to simple complexes such as $[Ni_2(\mu\text{-}Cl)_2Cl_6]^{4-}$.[29] The bonding in $(C_5R_5)_2Ni_2Br_2$, with $r_{Ni\cdots Ni}$ = 3.445(3) Å, differs from the high spin form of $\mathbf{1}^{\mathbf{pdt}}$ wherein the Ni(II) centers are engaged in Ni-Ni bonding, enforced by the propanedithiolate. This high spin state is even more accessible in the unstable complex $\mathbf{1}^{\mathbf{edt}}$. These results highlight the intriguing possibility of high-spin bimetallic complexes with M-M bonding.

4.9 Experimental

Unless otherwise noted, reactions and manipulations were generally performed using standard Schlenk techniques at room temperature or in a nitrogen atmosphere glove box. Solvents were HPLC-grade and dried by filtration through activated alumina or distilled under nitrogen over an appropriate drying agent. Bu_4NPF_6 was purchased from GFS Chemicals and was recrystallized multiple times from CH_2Cl_2 solution by the addition of hexane. ESI-MS data for compounds were acquired using a Waters Micromass Quattro II spectrometer. ^{1}H NMR spectra (500 MHz) were referenced to residual solvent relative to TMS. Crystallographic data were collected using a Siemens SMART diffractometer equipped with a Mo-K_α source (λ = 0.71073Å) and an Apex II detector or using a Bruker D8 Venture diffractometer equipped with a Mo-K_α microfocus source and a photon 100 detector (see CIF file for specific instrument). X-band EPR Spectra were recorded on a Varian E-line 12” Century Series X-band continuous-wave spectrometer.

Nickelocene and 1,2-Ethanedithiol. A solution of nickelocene (1.027 g, 5.4 mmol) in pentane (100 mL) was treated with 1,2-ethanedithiol (3.8 mmol, 0.7 equiv). The reaction mixture slowly becomes dark brown and eventually dark violet. After stirring overnight, the reaction mixture consists of faintly violet solution with a dark-violet microcrystalline solid. The mixture was filtered, and the solid washed several times with pentane until the filtrates is colorless. The solid was extracted into CH_2Cl_2, and this extract was filtered to remove some solids. The dark violet filtrate was concentrated, and diluted with Et_2O to give dark violet crystals. Yield: 0.673 g (76 %). The preparation was conducted on 5x scale with similar yields. ^{1}H-NMR ($CDCl_3$): δ 5.29 (s, 10H), 2.00 (m, 4H), 1.87 (m, 4H). Anal. Calcd for $C_{14}H_{18}S_4Ni_3$ (found): C, 34.27 (34.09); H, 3.70 (33.34); Ni 35.89 (35.72); S 26.14 (26.29). Single crystals were grown by vapor diffusion of pentane into dichloromethane solutions. A CH_2Cl_2/Et_2O (10 mL) solution of $\mathbf{2}^{\mathbf{edt}}$ (10.3 mg) was allowed to stand at room temperature for 3 days, single crystals of $Cp_2Ni_5(edt)_4$ ($\mathbf{3}^{\mathbf{edt}}$), identified crystallographically, were deposited (3 mg).

Nickelocene and 1,3-Propanedithiol. A solution of nickelocene (1.250 g, 6.62 mmol) in pentane (100 mL) was treated with 1,3-propanedithiol (3.38 mmol, 0.51 equiv). The reaction mixture was stirred overnight to yield a dark-red solution with black, microcrystalline precipitate. The mixture was filtered and washed several times with pentane until the filtrate was colorless. The solid was collected and dissolved in CH_2Cl_2; this extract was filtered and the solvent was removed under reduced pressure to yield $Cp_2Ni_3(pdt)_2$ as a red solid. Yield: 0.558 g (32 %). ^{1}H-NMR (CH_2Cl_2, 298K): δ 4.60 (br, 4H), 2.90 (br, 10H), 2.76 (br, 2H). Anal. Calcd for $C_{16}H_{22}Ni_3S_4$ (found): C, 37.05 (37.07); H 4.28 (4.28); Ni 32.85 (32.92); S 24.73 (25.9). Single crystals were grown by vapor diffusion of pentane into CH_2Cl_2 solutions. Solvent was removed from the combined dark-red pentane filtrates to yield $Cp_2Ni_2(\mu\text{-pdt})$ as a black solid. Yield: 0.503 g (43%). ^{1}H-NMR (CD_2Cl_2, -78 ºC): δ 4.87 (5H), 2.21 (2H, $CH_2CH_2CH_2$), and 3.11 (4H, CH_2S). Anal. Calcd for $C_{13}H_{16}Ni_2S_2$ (found): C, 44.13 (44.43); H 4.56 (4.63); Ni 33.18 (32.85); S 18.13 (17.83). Single crystals were obtained by evaporation of pentane solutions.

Nickelocene and 1,2-Benzenedithiol. A solution of nickelocene (0.163 g, 0.86 mmol) in pentane (50 mL) was treated with 1,2-benzenedithiol (bdtH_2, 0.082 g, 0.58 mmol, 0.67 equiv). The reaction mixture changes from dark brown and to dark violet over the course of several hours. After stirring overnight, the reaction mixture consisted of a faintly violet solution and a dark-violet microcrystalline solid. The solid was collected by filtration and washed with pentane until the filtrate is colorless. A CH_2Cl_2 extract of the solid was filtered through Celite. The solution was evaporated, leaving $Cp_2Ni_3(bdt)_2$ as a dark violet crystals. Yield: 0.132 g (78%). ^{1}H-NMR (CD_2Cl_2): δ 7.12 (m, 2H), 6.96 (m, 2H), 4.60 (s, 5H). Anal. Calcd for $C_{22}H_{18}Ni_3S_4$ (found): C, 45.04 (44.65); H, 3.09 (3.03); S 21.86 (22.57); Ni 30.01 (29.66). Single crystals were grown by vapor diffusion of pentane into a solution of the complex in CH_2Cl_2.

Oxidation of $Cp_2Ni_3(bdt)_2$. A solution of $\mathbf{2}^{bdt}$ (5.6 mg, 9.5 μmol) in dichloromethane (3 mL) was treated with $FcBF_4$ (2.6 mg, 9.5 μmol) in CH_2Cl_2 (3 mL). The reaction mixture darkened and was allowed to stand for 30 min. The mixture was filtered and the solvent was removed under reduced pressure. The residue was washed several times with pentane until the washings were colorless. The resultant solid was then extracted with ether, yielding a green solution of CpNi(bdt). The solution was evaporated, yielding green microcrystals (1.2 mg, 4.5 μmol, 0.47 equiv).

$[Cp_2Ni_2(pdt)]BF_4$, $[1^{pdt}]BF_4$. *From 1^{pdt}:* A solution of $\mathbf{1}^{pdt}$ (0.031 g, 0.087 mmol) in CH_2Cl_2 (2 mL) was treated with $FcBF_4$ (0.023 g, 0.084 mmol) in CH_2Cl_2 (2 mL). The reaction mixture remains dark red. The solvent was removed under reduced pressure and the resultant solid was washed several times with pentane until the washings were colorless. The dark red residue was purified by crystallization from CH_2Cl_2 and pentane (0.034g, 89%) ESI-MS: *m/Z* 352 ($[M]^+$). Anal. Calcd for $C_{13}H_{16}BF_4Ni_2S_2$ (found): C, 31.86 (31.74); H, 3.27(3.66); S, 14.56 (16.77); Ni, 26.64 (25.73). Single crystals were grown by vapor diffusion of pentane into a solution of the complex in CH_2Cl_2.

From $\mathbf{2}^{pdt}$*:* A solution of $\mathbf{2}^{\mathbf{pdt}}$ (0.012 g, 0.023 mmol) in CH_2Cl_2 (1 mL) was treated with $FcBF_4$ (0.0061 g, 0.022 mmol) in CH_2Cl_2 (1 mL). The reaction mixture was cooled to −35°C and crystals of $[\mathbf{2}^{\mathbf{pdt}}]BF_4$ suitable for crystallographic analysis were obtained by vapor diffusion of pentane into the reaction mixture.

$[Cp_2Ni_2(edt)]BF_4$, $[\mathbf{1}^{edt}]BF_4$. A solution of $\mathbf{2}^{\mathbf{edt}}$ (0.055g, 0.106 mmol) in CH_2Cl_2 (2 mL) was treated with $FcBF_4$ (0.015g 0.054 mmol) in CH_2Cl_2 (2 mL). The reaction mixture immediately changed from a deep purple to a dark red-brown color. The solvent was reduced under reduced pressure followed by dilution with ca. 5 mL of pentane. The mixture was filtered and washed several times with pentane until the washings were colorless. The solid residue was extracted with CH_2Cl_2; evaporation of the extract gave $[Cp_2Ni_2(edt)]BF_4$ as a dark red powder. Yield: 0.004 g (18% yield). ESI-MS: *m/Z* 338 ($[M]^+$). Single crystals were grown by vapor diffusion of pentane into a solution of the complex in CH_2Cl_2. The product was identified by X-ray crystallography.

[**$Cp_2Ni_2(SEt)_2]BF_4$.** A solution of $Cp_2Ni_2(SEt)_2$ (0.0503 g, 0.137 mmol) in CH_2Cl_2 (10 mL) was treated with $FcBF_4$ (0.0354 g, 0.130 mmol) in CH_2Cl_2 (10 mL). The black solution of the neutral nickel thiolate instantly became dark red. Solvent was removed under reduced pressure, and the residue was washed multiple times with pentane until the washings were colorless. Yield: 0.0569 g (96%). Single crystals were grown from vapor diffusion of pentane into concentrated CH_2Cl_2 solutions.

$Cp_2Ni_2(edt)$, $\mathbf{1}^{edt}$. A solution of $[\mathbf{1}^{\mathbf{edt}}]BF_4$ (0.037 g, 0.0087 mmol) in CH_2Cl_2 (1 mL) was treated with Cp_2Co (0.0016 g, 0.0085 mmol). The solution immediately changed from brown to dark red. Solvent was removed under reduced pressure, and the residue was extracted into Et_2O. This extract was filtered through Celite and evaporated to leave a black residue. Mass yield was nearly quantitative; however NMR spectra indicated formation of $Cp_2Ni_2(edt)$ and solutions produced insoluble solids upon standing for several minutes. ^1H-NMR ($CDCl_3$): δ 68.5 (s, 4H), −34.8 (m, 10H). The magnetic moment of this complex was determined using Evan's method. The fluorocarbon trifluoromethylbenzene (TFT) was used for this determination as well as the $CHCl_3$ solvent residual. The solution not containing the analyte was prepared in a seal glass capillary with 0.1 mL of a solution of 99.6% $CDCl_3$ and TFT in a 1:50 mixture. A freshly prepared solution of **1^{edt}** in 0.38 mL of $CDCl_3$ was spiked with 0.01 mL of TFT and the capillary was inserted. Because solutions of **1^{edt}** are unstable, the quantity of the analyte was determined using TFT as an internal standard. The magnetic moment (μ_{eff}) was determined to be 1.09 and 1.32 B.M. using ^{1}H-NMR spectroscopy and ^{19}F-NMR spectroscopy respectively.

DFT Calculations. Calculations were implemented in the TURBOMOLE package.[30] Among the tested functionals, BP86,[31,322,3] TPSS,[33] and B3LYP[34,35] overestimated the Ni-Ni distance (Table S1). A good match DFT vs XRD parameters is obtained by the TPSSH[36] and BP86-D3[37] functionals. BP86-D3/def-TZVP level was adopted since TPSSH functional failed to reproduce the ground state spin multiplicity experimentally observed (singlet), thus overestimating the triplet state stability. The inclusion of D3 dispersion corrections is mandatory to treat more accurately the effect of the thiolate pendants on the intermetallic interaction.

Determination of ΔG for Diamagnetic → Paramagnetic States in 1^{pdt}. It was assumed that species **1^{pdt}** is in equilibrium with exactly one diamagnetic state and one paramagnetic state. The observed ^{1}H-NMR chemical shift can be determined using eq. 4, which is the weighted average of the chemical shifts of the diamagnetic species and the paramagnetic species.

$$\delta_{obs} = \delta_d x_d + \delta_p x_p \quad \text{(eq. 4)}$$

where

δ_{obs} = observed chemical shift

δ_d = “pure diamagnetic” chemical shift

δ_p = “pure paramagnetic” chemical shift

x_d = diamagnetic mole fraction

x_p = paramagnetic mole fraction

This expression can be rearranged to yield eq. 5 using the definition that $x_p = 1 - x_d$.

$$\delta_{obs} = \delta_d x_d + \delta_p(1 - x_d)$$
$$\delta_{obs} = \delta_d x_d + \delta_p - \delta_p x_d$$
$$\delta_{obs} = x_d(\delta_d - \delta_p) + \delta_p \quad \text{(eq. 5)}$$

The free energy difference between two species at equilibrium is given in eq. 6.

$$\Delta G = -RT \ln K \quad \text{(eq. 6)}$$

where

ΔG = free energy difference

R = universal gas constant

T = temperature

K = equilibrium constant

Taking the diamagnetic state as the ground state, using the substitution $K = \frac{x_p}{x_d}$, and the definition that $x_p = 1 - x_d$ an expression can derived in terms of x_d.

$$\Delta G = -RT \ln \frac{x_p}{x_d}$$

$$\ln\left(\frac{x_p}{x_d}\right) = \frac{-\Delta G}{RT}$$

$$\frac{x_p}{x_d} = e^{\frac{-\Delta G}{RT}}$$

$$\frac{1 - x_d}{x_d} = e^{\frac{-\Delta G}{RT}}$$

$$1 - x_d = x_d * e^{\frac{-\Delta G}{RT}}$$

$$1 = x_d * e^{\frac{-\Delta G}{RT}} + x_d$$

$$1 = x_d(e^{\frac{-\Delta G}{RT}} + 1)$$

$$x_d = \frac{1}{e^{\frac{-\Delta G}{RT}} + 1}$$

Substituting this expression into eq. 5 yields equation 7, which is independent of mole fraction.

$$\delta_{obs} = \frac{(\delta_d - \delta_p)}{e^{\frac{-\Delta G}{RT}} + 1} + \delta_p \text{ (eq. 7)}$$

4.10 Characterization Data

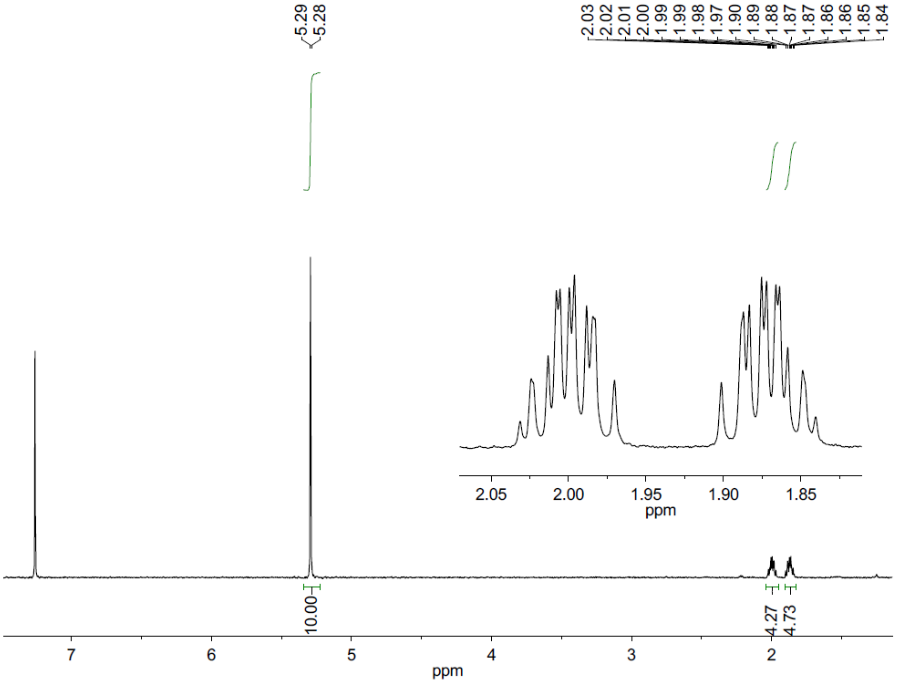

Figure 4.20. ^{1}H-NMR Spectrum of $Cp_2Ni_3(edt)_2$ in $CDCl_3$.

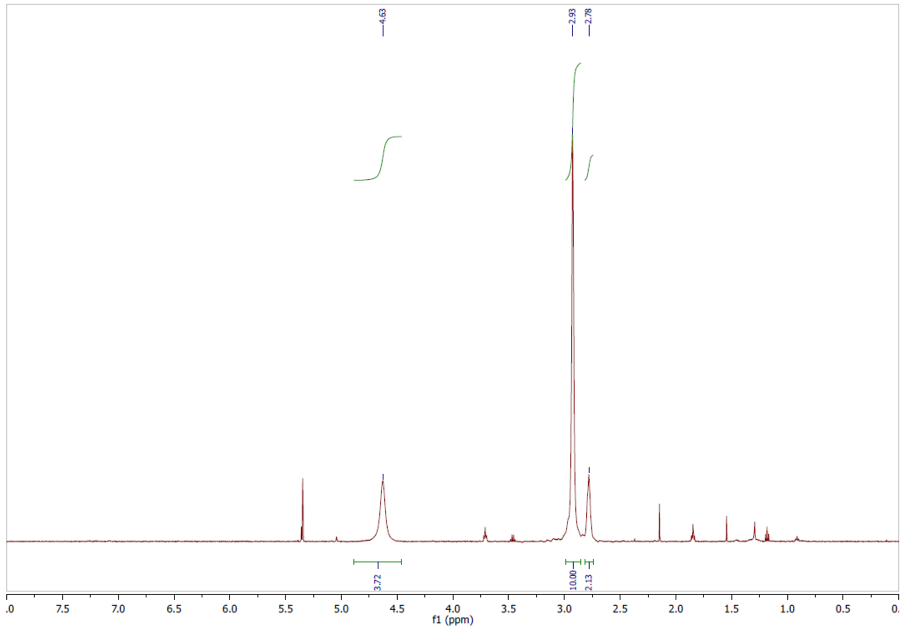

Figure 4.21. ^{1}H-NMR spectrum of Cp_2Ni_2(pdt) in CD_2Cl_2. Principal impurities are: Et_2O, CH_2Cl_2, THF, and *n*-pentane.

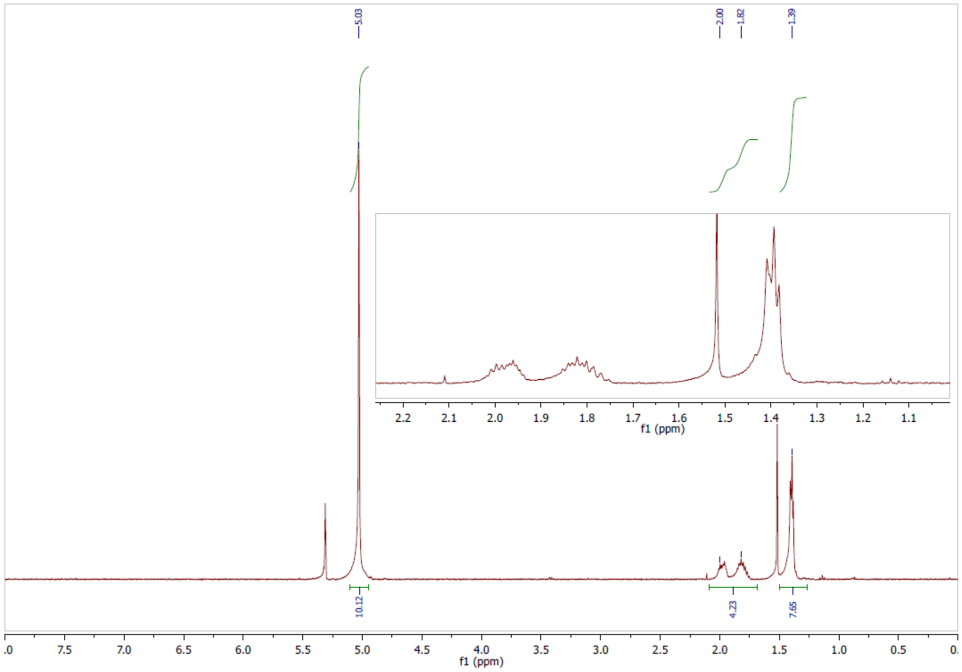

Figure 4.22. ^{1}H-NMR spectrum of $Cp_2Ni_3(pdt)_2$ in CD_2Cl_2.

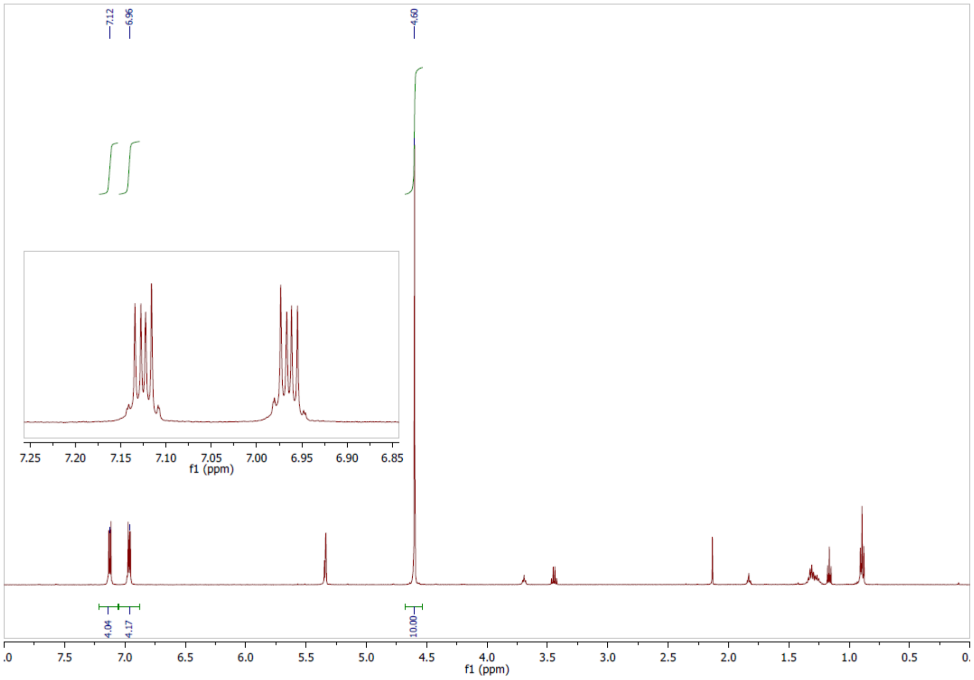

Figure 4.23. ^{1}H-NMR spectrum of Cp_2Ni_2(bdt) in CD_2Cl_2. Principal impurities are: Et_2O, CH_2Cl_2, THF, and *n*-pentane.

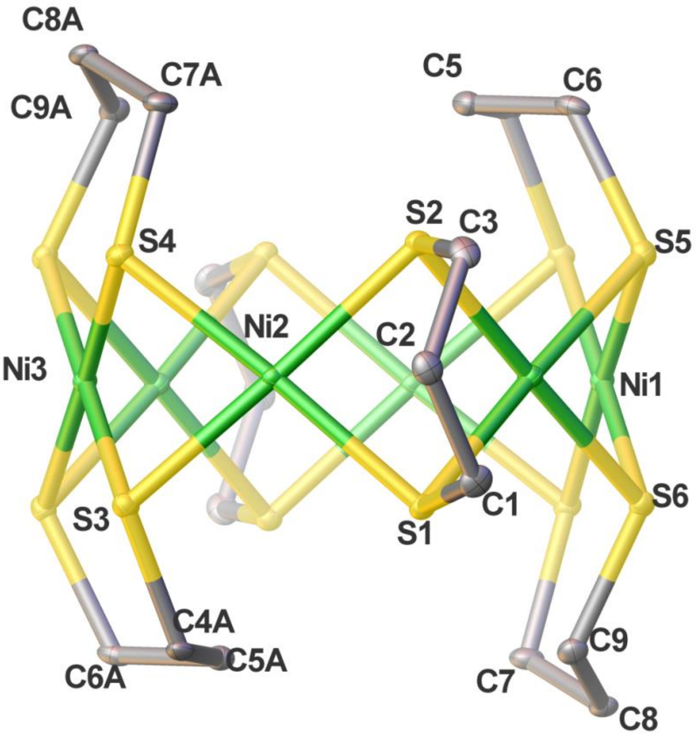

Figure 4.24. Solid state structure of one $Ni_6(pdt)_6$ unit of two in the grown asymmetric unit (hydrogen atoms and chloroform solvate omitted for clarity). Selected distances (Å) and angles (deg): Ni-Ni$_{avg}$: 2.881(2); Ni-S$_{avg}$: 2.184(2); S-Ni-S$_{avg}$ (obtuse): 99.26(5); S-Ni-S$_{avg}$ (acute): 80.75(5).

Cyclic Voltammetry

Unless stated otherwise, cyclic voltammograms were obtained under the following conditions: CH_2Cl_2 solution, ~1 mM analyte, 100 mM $[Bu_4N][PF_6]$, 100 mVs^{-1}. Starting point and initial direction is indicated using a red arrow.

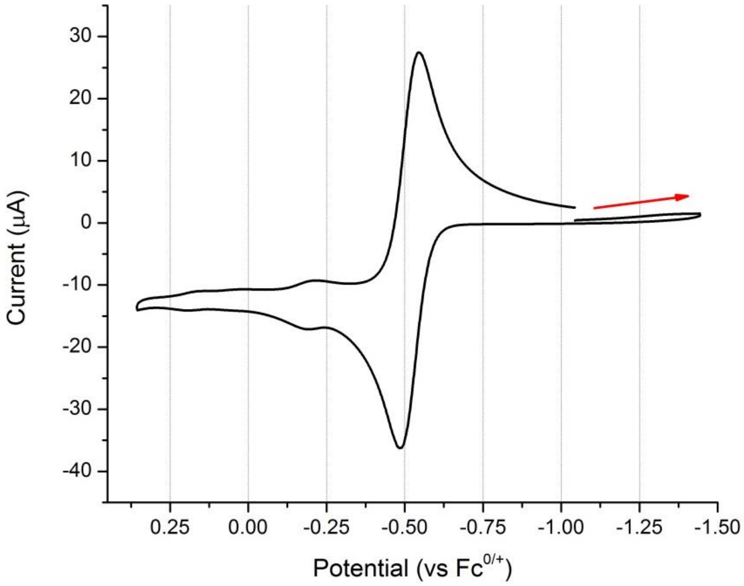

Figure 4.25. CV of $Cp_2Ni_2(pdt)$.

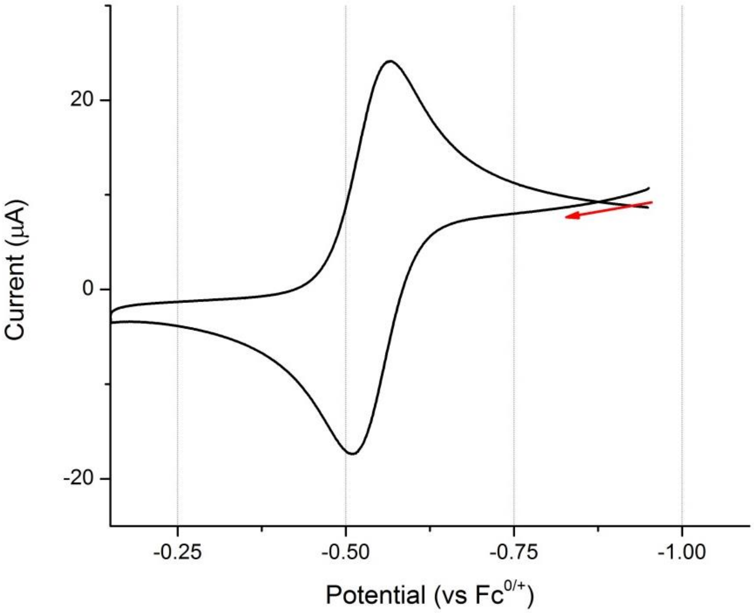

Figure 4.26. CV of $Cp_2Ni_2(edt)BF_4$.

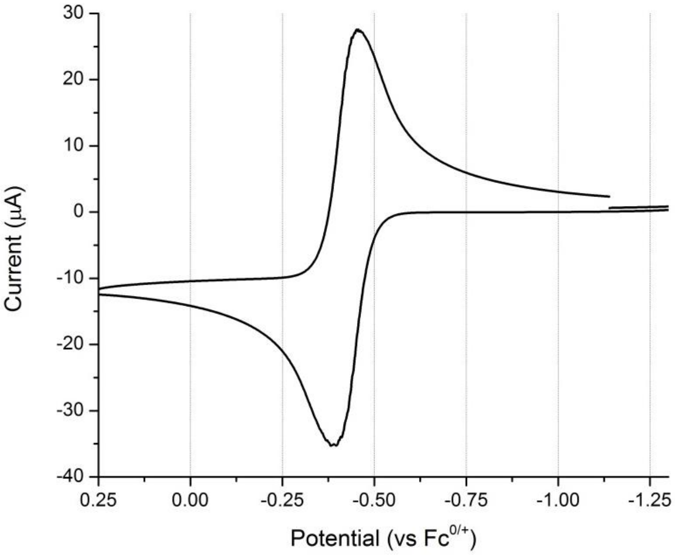

Figure 4.27. CV of $Cp_2Ni_2(SEt)_2$.

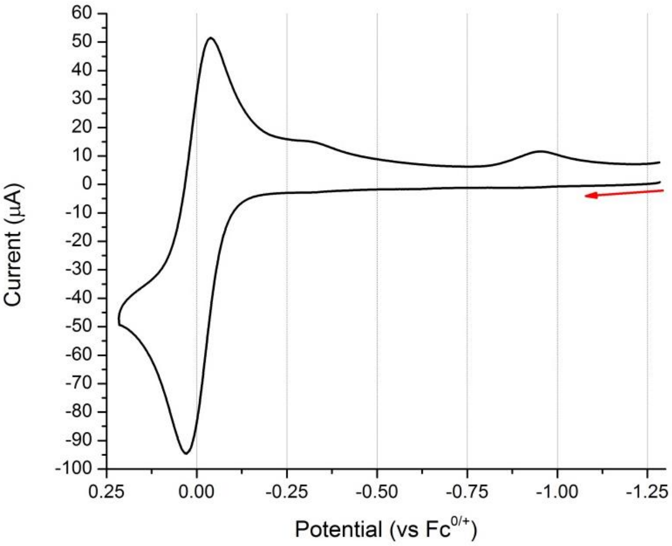

Figure 4.28. CV of $Cp_2Ni_3(bdt)_2$. Scan Rate: 500 mVs^{-1}.

4.11 References

(1) Ellgen, P. C.; Gregory, C. D. *Inorg. Chem.* **1971**, *10*, 980.
(2) Schropp, W. K. *J. Inorg. Nucl. Chem.* **1962**, *24*, 1688.
(3) Bladon, P.; Bruce, R.; Knox, G. R. *Chem. Commun. (London)* **1965**, 557.
(4) Davidson, J. L.; Sharp, D. W. A. *J. Chem. Soc., Dalton Trans.* **1972**, 107.
(5) Teo, B. K.; Bakirtzis, V.; Snyder-Robinson, P. A. *J. Am. Chem. Soc.* **1983**, *105*, 6330.
(6) Darkwa, J.; Bothata, F.; Koczon, L. M. *J. Organomet. Chem.* **1993**, *455*, 235.
(7) Ho, N.-F.; Mak, T. C. W.; Luh, T.-Y. *J. Chem. Soc. Dalton Trans.* **1990**, 3591.
(8) Braga, D.; Grepioni, F. *Adv. Mol. Struct. Res.* **1996**, *2*, 25.
(9) Baidya, N.; Mascharak, P. K.; Stephan, D. W.; Campagna, C. F. *Inorg. Chim. Acta* **1990**, *177*, 233.
(10) Sletten, J.; Kovacs, J. A. *Acta Chem. Scand.* **1994**, *48*, 929.
(11) Nomura, M.; Cauchy, T.; Geoffroy, M.; Adkine, P.; Fourmigué, M. *Inorg. Chem.* **2006**, *45*, 8194.
(12) Nomura, M.; Cauchy, T.; Fourmigué, M. *Coord. Chem. Rev.* **2010**, *254*, 1406.
(13) Grosshans, P.; Adkine, P.; Sidorenkova, H.; Nomura, M.; Fourmigué, M.; Geoffroy, M. *J. Chem. Phys. A* **2008**, *112*, 4067.
(14) Carroll, M. E.; Barton, B. E.; Gray, D. L.; Mack, A. E.; Rauchfuss, T. B. *Inorg. Chem.* **2011**, *50*, 9554.
(15) Frisch, P. D.; Lloyd, M. K.; McCleverty, J. A.; Seddon, D. *J. Chem. Soc., Dalton Trans.* **1973**, 2268.
(16) Franolic, J. D.; Wang, W. Y.; Millar, M. *J. Am. Chem. Soc.* **1992**, *114*, 6587.
(17) North, T. E.; Thoden, J. B.; Spencer, B.; Dahl, L. F. *Organometallics* **1993**, *12*, 1299.
(18) Felton, G. A. N.; Glass, R. S.; Lichtenberger, D. L.; Evans, D. H. *Inorg. Chem.* **2006**, *45*, 9181.
(19) Fourmond, V.; Jacques, P.-A.; Fontecave, M.; Artero, V. *Inorg. Chem.* **2010**, *49*, 10338.
(20) Roberts, J. A. S.; Bullock, R. M. *Inorg. Chem.* **2013**, *52*, 3823.
(21) Ellgen, P. C.; Gregory, C. D. *Inorg. Chem.* **1971**, *10*, 980.
(22) Vahrenkamp, H.; Dahl, L. F. *Angew. Chem., Int. Ed. Engl.* **1969**, *8*, 144.
(23) Kaliakin, D. S.; Zaari, R. R.; Varganov, S. A. *J. Phys. Chem. A* **2015**, *119*, 1066.
(24) Keith, J. M.; Hall, M. B. *Inorg. Chem.* **2010**, *49*, 6378.
(25) Siegbahn, P. E. M.; Tye, J. W.; Hall, M. B. *Chem. Rev.* **2007**, *107*, 4414.
(26) Köhler, F. H. In *eMagRes*; John Wiley & Sons, Ltd: New York, 2007.
(27) Smith, M. E.; Andersen, R. A. *J. Am. Chem. Soc.* **1996**, *118*, 11119.
(28) Schär, M.; Saurenz, D.; Zimmer, F.; Schädlich, I.; Wolmershäuser, G.; Demeshko, S.; Meyer, F.; Sitzmann, H.; Heigl, O. M.; Köhler, F. H. *Organometallics* **2013**, *32*, 6298.
(29) Laskowski, E. J.; Felthouse, T. R.; Hendrickson, D. N.; Long, G. J. *Inorg. Chem.* **1976**, *15*, 2908.
(30) Furche, F.; Ahlrichs, R.; Hättig, C.; Klopper, W.; Sierka, M.; Weigend, F. *Wiley Interdisc. Rev.: Comput. Mol. Sci.* **2014**, *4*, 91.
(31) Becke, A. D. *Phys. Rev. A* **1988**, *38*, 3098.
(32) Perdew, J. P. *Phys. Rev. B* **1986**, *33*, 8822.
(33) Tao, J.; Perdew, J. P.; Staroverov, V. N.; Scuseria, G. E. *Phys Rev Lett.* **2003**, *91*, 146401.
(34) Becke, A. D. *J. Chem. Phys.* **1993**, *98*, 5648.
(35) Lee, C.; Yang, W.; Parr, R. G. *Phys. Rev. B* **1988**, *37*, 785.
(36) Staroverov, V. N.; Scuseria, G. E.; Tao, J.; Perdew, J. P. *J. Chem. Phys.* **2003**, *119*, 12129.
(37) Grimme, S. *J. Chem. Phys.* **2006**, *124*, 034108.

Chapter 5:

Mixed-Valent Cyclopentadienyl Cobalt Dithiolates

5.1 Introduction

Mixed-valent metal clusters are a common theme in many biological systems.[1] The hydrogenases are one such example. Models of these enzymes with mixed-valent states are immensely underrepresented outside of the work discussed in this thesis. Chapter 4 discussed cyclopentadienyl nickel dithiolate complexes, of which were the stable mixed-valent compounds $[Cp_2Ni_2(pdt)]BF_4$, $[Cp_2Ni_2(edt)]BF_4$, and $[Cp_2Ni_2(SEt)_2]BF_4$. Though not direct models of [NiFe]- or [FeFe]-H_2ase *per se*, these compounds demonstrated the capability of the Cp-metal-dithiolate motif to stabilize mixed-valence states. This chapter discusses the cobalt derivatives of these systems.

A large number of model compounds of the [FeFe]-H_2ase and [NiFe]-H_2ase active sites are of the form $Fe_2(pdt)(CO)_6$ or $(CO)_3Fe(S)_2Ni(L_2)$ respectively. This framework ignores the fact that the active sites of both of these enzymes do not contain $Fe(CO)_3$ subunits, but $Fe(CO)_2(CN)$ and $Fe(CN)_2(CO)$ subunits, which are more electron-rich than $Fe(CO)_3$ centers. As discussed in chapter 1, initial attempts to incorporate cyanide ligated Fe centers suffered from oligiomerization via Fe-CN-Fe linkages, particularly following oxidation.[2,3] Due to this self-destructive reactivity, phosphines are often used as a surrogate for cyanide.[4]

Models of enzyme active sites can benefit from the use of isoelectronic relationships between different metals and synthetic fragments. This chapter focuses on the CpCo unit. This unit has relevance to models of both the [FeFe]- and [NiFe]-H_2ase active sites due to the chemical similarities between CpCo and $Fe(CO)_3$ (Scheme 5.1). This similarity is well established and many pairs of compounds are known wherein "$Fe(CO)_3$" with 'CpCo' centers are interchangeable of which $(B_4H_8)Fe(CO)_3$ to $(B_4H_8)CoCp$[5] and the series $S_2[Fe(CO)_3]_{3-n}[CpCo]_n$ are examples.[6] In relation of hydrogenase models, mixed-valent heterobimetallic CoFe compounds and their acid-base and redox chemistry have been reported.[7]

Scheme 5.1. Generic Model Compounds using CpCo in place of $Fe(CO)_3$

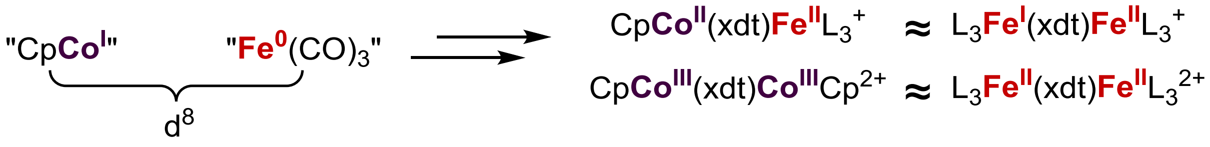

In addition to the interchangeability of $Fe(CO)_3$ with CpCo, iron carbonyl compounds have similar reactivity to cyclopentadienyl cobalt compounds. Two examples of this are: the reaction of $CpCo(CO)_2$ and $Fe(CO)_5$ with dienes and the reaction of $CpCo(CO)_2$ and $Cp_2Fe_2(\mu\text{-}CO)_2(CO)_2$ with disulfides (Scheme 5.1).[8,9]

Scheme 5.2. Examples where CpCo and $Fe(CO)_n$ Compounds Exhibit Similar Reactivity.

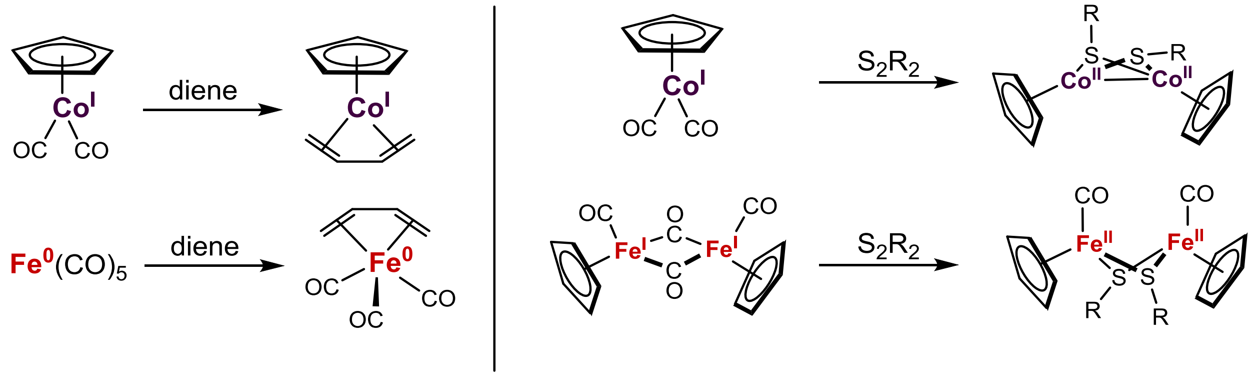

There are some differences worth noting between Cp^- and CO ligands. Most obviously these two ligands differ by charge. The charge difference can have a substantial effect on the redox properties of the corresponding complexes; however, this effect is mostly mitigated by interchanging two neutral fragments such as $Fe(CO)_3$ with CpCo. Secondly, the carbon monoxide ligand is a much stronger π-acceptor. Substitution of cyclopentadienide for carbon monoxide should result in a more electron rich metal center, allowing for the stabilization of higher oxidation states.

Compared to the complexes based on the CpNi fragment discussed in chapter 4, complexes with the CpCo fragment have found many more useful applications, particularly in organic synthesis. Such examples include hydroacylation of alkenes, epoxide ring opening, cyclotrimerization of alkynes, [2+2+2] cyclizations, [2+2] cyclizations, and the synthesis of quinones.[10]

This chapter will address improved synthetic procedures for cyclopentadienyl cobalt dithiolates and the properties of these compounds, particularly in regard to the acid-base and redox chemistry.

5.2 Synthesis and Characterization of Cp_2Co_2(xdt) Complexes

The synthesis of CpCo compounds bridged by thiolates is well developed. The first reported example of this type is the methylthiolate complex $Cp_2Co_2(SMe)_2$.[11] For dithiolates, the ethanedithiolate compound $(CpCo)_2$(edt) was reported to form in low yield from the reaction of

$CpCo(CO)_2$ with thiirane; the specific product is sensitive to the equivalent of thiirane used (Scheme 5.2).[12]

Scheme 5.3. Synthesis of Cp_2Co_2(edt) from Thiirane

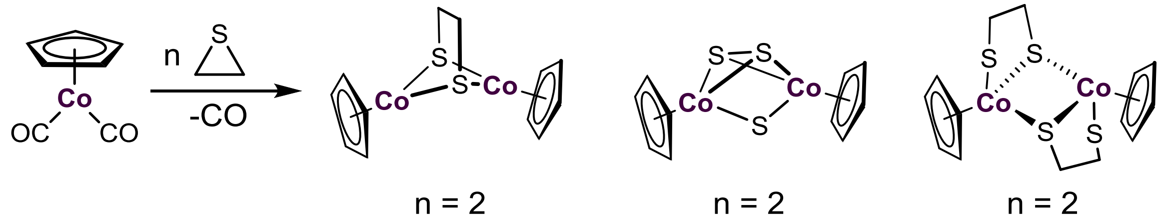

An improved synthesis of Cp_2Co_2(xdt) compounds entails heating toluene solutions of cobaltocene or $CpCo(CO)_2$ with the appropriate dithiol to reflux (Scheme 5.3). Derivatives of edt, pdt, and 3,4-toluenedithiol (tdt) have been prepared using this methodology.[13] Additionally, the MeC_5H_4 (Cp') analogue Cp'_2Co_2(pdt) were prepared through this method.[14] These CpCo thiolates are typically green to greenish brown. In contrast to the synthesis of cyclopentadienyl nickel thiolates, these syntheses do not produce appreciable amounts of soluble compounds of higher nuclearity.

Scheme 5.4. Synthesis of Cp_2Co_2(xdt) Compounds

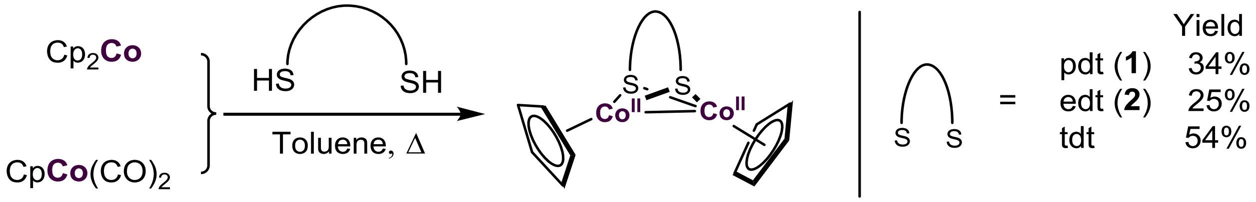

These neutral, bimetallic compounds are diamagnetic and produce predictable NMR spectra. For the pdt derivatives, the flipping of the propanedithiolate ring was found to be slow on the NMR timescale at −70°C, displaying a ^{1}H-NMR spectrum with inequivalent Cp ligands.[13] In contrast, this behavior was not observed for the corresponding nickel derivatives. This difference could be due to the metal-metal bonding present in the cobalt derivatives that is absent in the nickel derivatives. The metal-metal bond present in the cobalt system brings the metals closer together and consequently increases the cobalt distance to the central pdt methylene, decreasing the steric hindrance between these fragments.

The redox properties of the dicobalt(II) complexes were examined by cyclic voltammetry. Complexes **1**-**2** and the tdt derivative oxidize at mild potentials. The $Co^{III}Co^{II}$ products are d^7d^6

metal centers and are in some ways isoelectronic with the H_{ox} state of the [FeFe]-H_2ase.[15] The pdt derivatives oxidize at ≈120 mV more negative potentials than the edt compounds, a trend also observed in the Fe_2(xdt)$(CO)_4$(dppv) system.[3] The Cp' complexes are oxidized at more positive potentials by 90 mV compared to the Cp derivatives, reflecting the electron donating property of the methyl substituent (Table 5.1). A similar shift of 100 mV is observed for the $Cp_2Fe^{+/0}$ vs $Cp'_2Fe^{+/0}$ couples.[16] While the redox events of the aliphatic thiolate compounds are reversible, oxidation of the arylthiolate tdt is irreversible. Multiple redox events were present following the irreversible oxidation, one of which was a couple at ≈−1.1 mV, which corresponds to the known $Co^{III/II}$ couple for $[Co(tdt)_2]^-$.[17] This instability of the arene-dithiolate derivative is reflected in the $Cp_2Ni_3(bdt)_2$ system reported in the previous chapter which forms CpNi(tdt) upon oxidation.

Table 5.1. Redox Couples of $(Cp^RCo)_2$(xdt) Complexes and Related Species.

Compound	**$E_{1/2}$ (mV vs $Fc^{0/+}$)**
$(CpCo)_2$(edt) (1)	-153
$(CpCo)_2$(pdt) (2)	-275
$(CpCo)_2$(tdt) (3)	-199
$Fe_2(pdt)(CO)_4(PMe_3)_2$	-200
$(Cp'Co)_2$(pdt) (2a)	-365

In MeCN solution compound **1** has an additional oxidation close to 0.0 V vs $Fc^{0/+}$ that is not observed in CH_2Cl_2 solutions (Figure 5.1). This second oxidation, which is only observed in MeCN, could indicate the formation of an adduct ([**1(**MeCN$)_n]^+$) , which in turn, oxidizes more easily than $[\mathbf{1}]^+$ (Scheme 5.4).

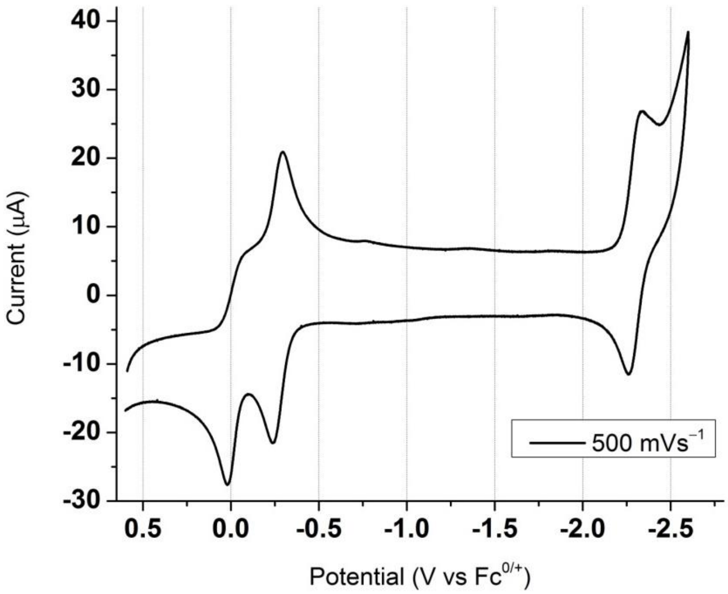

Figure 5.1. CV of Cp_2Co_2(pdt) (**1**). Conditions: MeCN solution, ~1 mM analyte, 100 mM $[Bu_4N][PF_6]$, 500 mVs^{-1}.

Scheme 5.5. Proposed Adduct Formation Facilitating the Double Oxidation of **1**

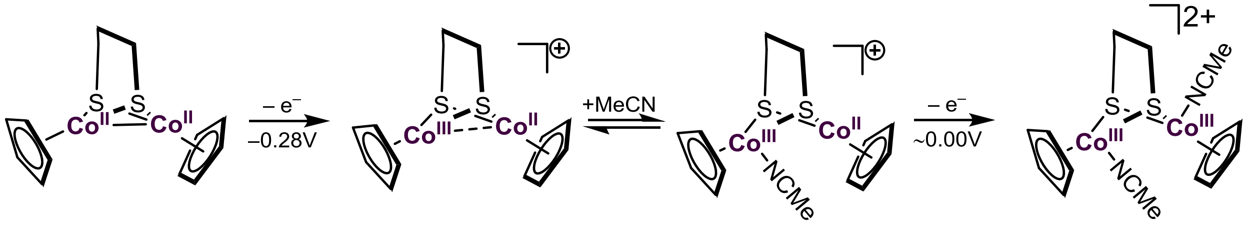

The neutral compounds **2** and Cp_2Co_2(tdt) have been characterized crystallographically and selected bond lengths and angles have been tabulated, along with other compounds discussed in this chapter, in Table 5.2.

Table 5.2. Selected Bond Distances (Å) and Angles (°) for Derivatives of CpCo(II) and CpCo(III)

Compound	Co-Co	Cp_{cent}-Co[a]	∡Cp_{cent}-Co-Co[a]	Co-S_{avg}[b]	Co-X[a]	Co-L[a]
Cp'_2Co_2(pdt)	2.4112(5)	1.684(2) 1.685(2)	N.R.	2.1927(8)	n/a	n/a
Cp_2Co_2(tdt)	2.392(1)	1.68(4) 1.68(2)	N.R.	2.211	n/a	n/a
[**1**]BF_4[c]	2.439(1)	1.73(2)	141.6(6)	2.176(4)	n/a	n/a
[**1**]BAr_4^F	2.458(1)	1.70(4) 1.70(4)	138.7(6) 142.3(6)	2.184(4)	n/a	n/a
[**1**H]BF_4	2.4201(6)	1.65(1) 1.65(1)	157.3(2) 131.1(2)	2.1934(9)	1.58(3) 1.52(3)	n/a
[**2**H]BF_4	2.418	N.R.	N.R.	2.193(2)	1.51(1)	n/a
[**1**OH]BF_4	2.7808(9)	1.669 1.669	173.6(4) 176.1(4)	2.2415(4)	1.944(4) 1.945(4)	n/a
[**1**OH]$BF_4 \cdot 3H_2O$	2.7927(5)	1.672 1.677	175.4(3) 176.1(3)	2.2685(6)	1.955(2) 1.960(2)	n/a
[**1**SPh]BAr_4^F	2.9223(7)	1.69(2) 1.69(2)	178.0(6) 177.9(6)	2.236(3)	2.258(1) 2.241(1)	n/a
[**3**][BAr_4^F]$_2$	2.901(1)	1.63(4) 1.68(4)	177.2(6) 177.1(6)	2.231(4)	2.235(2) 2.224(1)	n/a
[**4**]BF_4	2.4976(4) 2.4869(4) 2.5170(4)	n/a	n/a	2.241(2)	n/a	1.907(1) 1.889(2) 1.896(2)

N.R. = not reported. [a] In the case where the multiple values are given because the cobalt environments are unique, the specific cobalt is matched with the one in the same line in the next column (e.g. the "Cp1-Co1" distance would be in the same line as the "Co1-X" distance. For the angles, "Cp1-Co1" would be in the same line as "∡Cp1-Co1-Co2" and "Cp2-Co2" would be in the same line as "∡Cp2-Co2-Co1"). [b] The Co-S distances did not differ appreciably between the two metal centers. [c] The asymmetric unit contained only half of the cation. The rest of the cation was generated by symmetry.

5.3 The Hydride Complexes of Cp_2Co_2(xdt)

Treatment of the dicobalt(II) dithiolates with $HBF_4 \cdot Et_2O$ or $[H(Et_2O)_2]BAr_4^F$ produced the corresponding hydride salts and were characterized using NMR spectroscopy. Annoyingly, there is no color change observed in this reaction; both the starting materials and products produce dark green solutions, offering no immediate visual indication that a reaction has occurred. The hydride salts produced in this reaction are soluble in CH_2Cl_2, and the BAr_4^{F-} salts are also soluble in THF and Et_2O. Protonation of these compounds is reversible, which allowed the pK_a's of these salts to be determined.[14] Additionally, the activity of compounds **1** and **2** as proton reduction catalysts was investigated.[13]

The hydride compounds $[Cp_2Co_2(pdt)H]BF_4$ ([**1**H]BF_4) (Figure 5.2) and $[Cp_2Co_2(edt)H]BF_4$ ([**2**H]BF_4) were characterized crystallographically. The structural features of these cations are very similar. Both have short Co-Co contacts of ≈2.4 Å, which are strikingly similar to the distances observed in the neutral compounds Cp_2Co_2(tdt) and Cp'_2Co_2(pdt) (Table 5.2). The neutral compounds **1** and **2** were not structurally characterized so direct comparisons cannot be made. The bridging hydride ligand, which was located in the difference map, has a symmetrical interaction between both centers and a relatively short M-H distance of ≈1.5 Å. Both structures show a relatively bent Cp-Co-Co angle between 130° and 160°, with the edt derivative being more symmetrically bent in contrast to the the pdt derivative which has a difference in this angle between the two CpCo environments (Table 5.2).

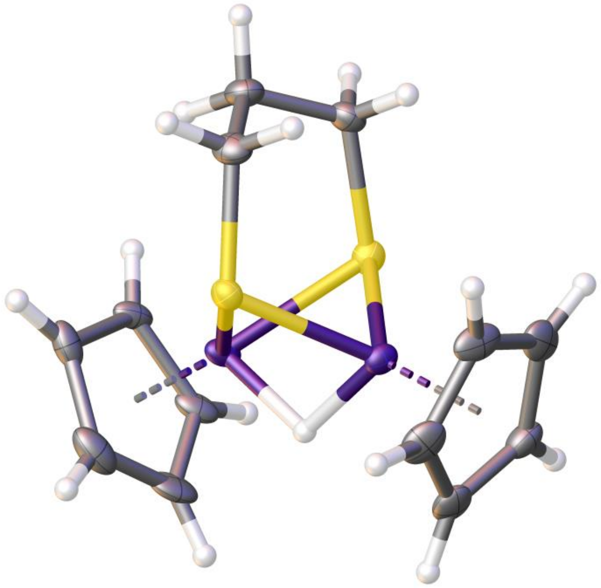

Figure 5.2. Solid state structure of [**1**]BF_4. The BF_4^- counterion has been omitted for clarity. Bridging hydride ligand was located in the difference map. Selected bond distances can be found in Table 5.2.

The cation [**1**H]$^+$ exhibits Lewis acidity similar to that observed for the related phosphide cations of the form $[Cp_2Co_2(PR_2)_2H]^+$.[18] Under an atmosphere of carbon monoxide, [**1**H]$^+$ generates a new metallic carbonyl species displaying two bands at 1959 cm^{-1} and 2024 cm^{-1} in the IR spectrum.[14] The carbonyl adduct of [**1H**]$^+$ forms over the course of several hours and retains the bridging hydride ligand, as determined by ^{1}H-NMR Spectroscopy. The presence of two IR bands may suggest the presence of two isomers, which are proposed in Scheme 5.5.

Scheme 5.6. CO Binding and Subsequent Isomerization of [1H]$^+$

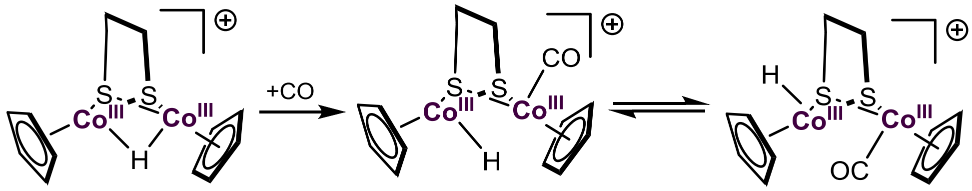

Solutions of the bridging hydride complexes are not stable in coordinating solvents. In MeCN solution, initially green solutions of [**1**H]BF_4 gradually become red with concomitant formation of insoluble precipitates. From the degraded solutions, the tricobalt complex cation $Co_3(pdt)_3(MeCN)_3^+$ ([**4**]$^+$) could be crystallized as the tetrafluoroborate salt and was characterized using X-ray crystallography (Figure 5.3). The isolation of this compound indicates that coordination of Lewis base can facilitate the scission of the Cp-Co bond. This loss of the cyclopentadienide ligand is paralleled in the nickel thiolate compounds discussed in chapter 4.

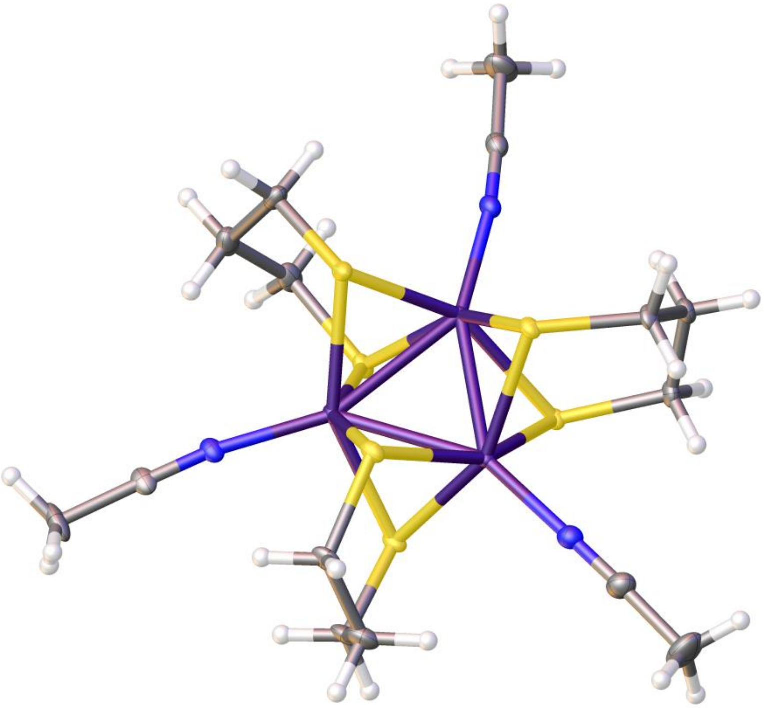

Figure 5.3. Solid state structure of [**4**]BF_4. The BF_4^- counterion has been omitted for clarity. Bridging hydride ligand was located in the difference map. Selected bond distances can be found in Table 5.2.

The tricobalt [**4**]$^+$ cluster is roughly D_{3h} symmetric and features short Co---Co contacts on the order of 2.5 Å. By charge balance, the cation [**4**]$^+$ must be a Co(II)$_2$Co(III), though the highly symmetrical environment suggests that a more delocalized description of Co(2.33)$_3$ is more accurate.

When investigated by ^{1}H-NMR spectroscopy, MeCN-*d*$_3$ solutions of [**1**H]BF$_4$ showed gradual decay of the hydride resonance concomitant with the formation of numerous, complex resonances in the δ2-3 range (Figure 5.4). Resonances in this range could suggest the formation of oligomers in which the propanedithiolate backbones would have very similar, but different chemical environments.

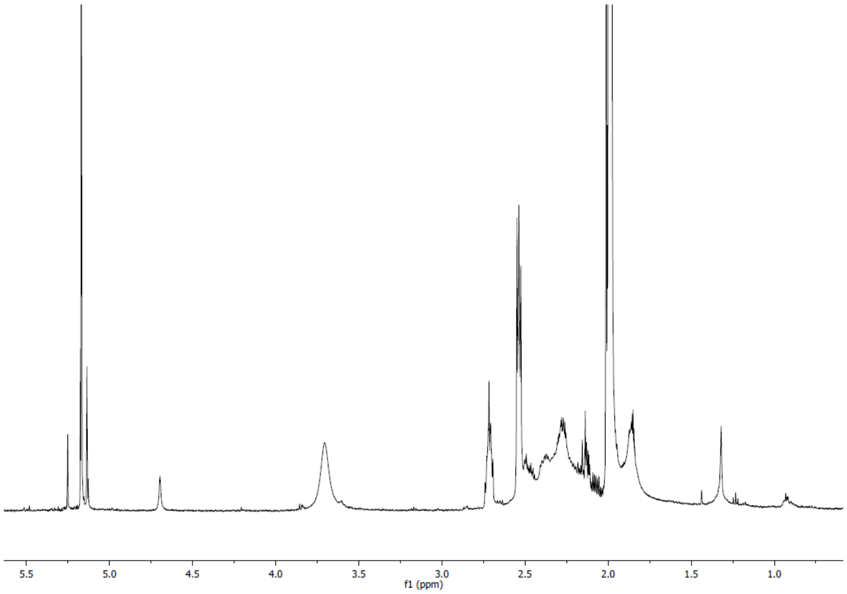

Figure 5.4. ^{1}H-NMR spectrum of [**1**H]BF$_4$ in MeCN-*d*$_3$.

Solutions of [**1**H]BF$_4$ in acetone were also found to be unstable. The ^{1}H-NMR spectrum of [**1**H]BF$_4$ indicates some degradation immediately in acetone degrades over the course of minutes producing numerous resonances, many of which appeared to be paramagnetic with chemical shifts above δ10 and below δ0 (Figure 5.5). The reaction mixture was investigated using ESI-MS, which indicated the presence of higher nuclearity species, specifically $Cp_2Co_3(pdt)_3^+$ which has an *m/Z* of 625 (Figure 5.6). The structure of this Co(III)$_3$ cation is proposed to be an octahedral Co(III) core ligated by three pdt ligands capped with CpCo (Figure 5.7).

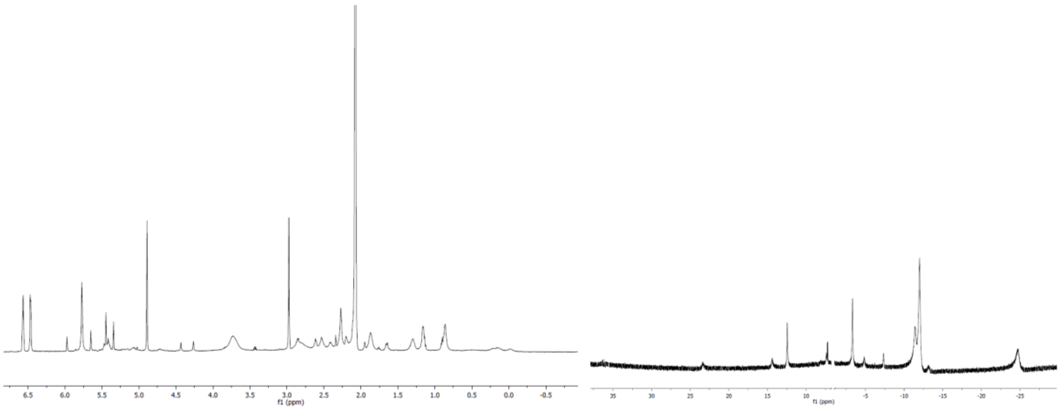

Figure 5.5. ^{1}H-NMR spectrum of [**1**H]BF$_4$ dissolved in acetone showing immediate decomposition. (Left) Region of -1 to 7 ppm. (Right) Region of −30 to 40 ppm with −1 to 7 ppm excluded.

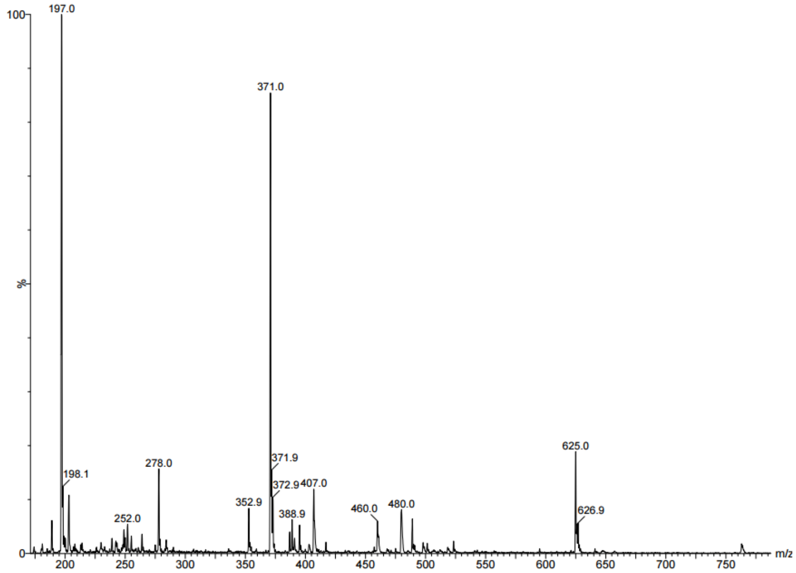

Figure 5.6. ESI-MS of [**1**H]BF$_4$ treated with aqueous acetone.

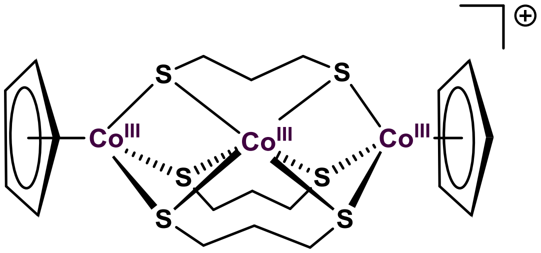

Figure 5.7. Proposed structure of the cation Cp$_2$Co$_3$(pdt)$_3$$^+$.

The retained Lewis acidity of the hydride complex prompted the investigation of the protonation of **1** using acids with coordinating counterions. In a mixture of acetone and hydrochloric acid solution, the hydride complex [**1**H]BF_4 is not long lived. Instead, the blue chloride compound [Cp_2Co_2pdtCl]Cl ([**1**Cl]Cl) is generated in solution after mixing, as indicated by ESI-MS by the molecular ion $[Cp_2Co_2pdtCl]^+$ with *m/Z* of 389 (Figure 5.8). The chloride compound is not stable in solution and attempts to isolate it for further characterization were not successful. Some of the decomposition products could be identified as hydrated cobalt chloride salts.

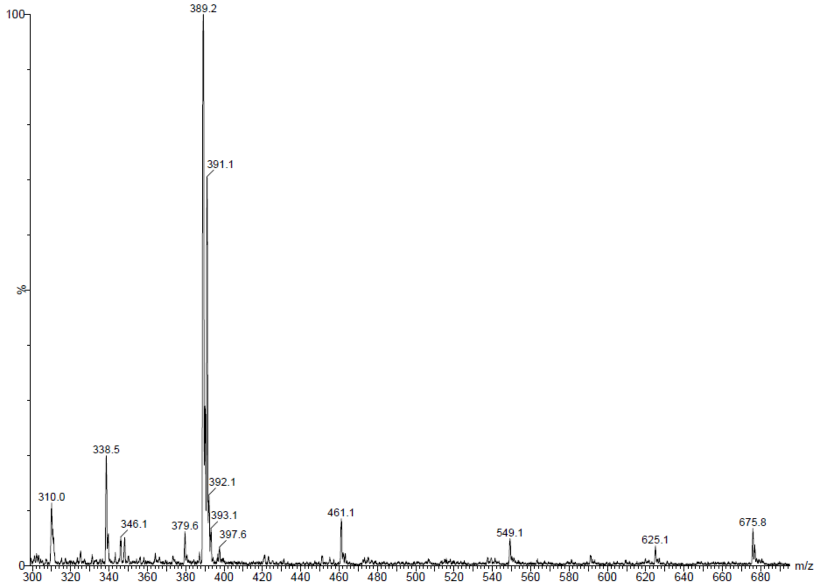

Figure 5.8. ESI-MS of **1** treated with a mixture of acetone and aqueous HCl.

In view of the Lewis acidity of the hydride complex, the reactivity of Et_2O solutions of [**1**H]BAr_4^F with H_2 was investigated. Although the hydride complex binds substrates such as MeCN, acetone, and carbon monoxide, the complex does not exchange with D_2. Additionally, no hydride complexes were detected in mixtures of Cp_2Co_2(xdt) and base under an atmosphere of H_2.

5.4 Redox Chemistry

Compounds **1** (Figure 5.1) and **2**[13] exhibit reversible one electron oxidation couples as determined by cyclic voltammetry. This observation prompted the preparative scale oxidation of these compounds to generate the corresponding mixed-valence cations. Treatment of **1** and **2** with $FcBF_4$ or $FcBAr_4^F$ afforded the corresponding salt in high yield. Similar to the protonation chemistry, solutions of **1** and **2** and the corresponding salts of [**1**]$^+$ and [**2**]$^+$ are similarly green, providing no immediate visual indication that a reaction has taken place. The cation [**1**]$^+$ was crystallographically characterized as both the BF_4^- (Figure 5.9) and BAr_4^{F-} salts (Table 5.2). These mixed-valence cations retain the metal-metal bond, as indicated by the short contacts of ≈2.4 Å. Similarly short distances are present in the parent neutral compounds and the cationic hydrides. The Cp-Co-Co angles are noticeably bent at ≈140°, also similar to the parent neutral compounds and cationic hydrides.

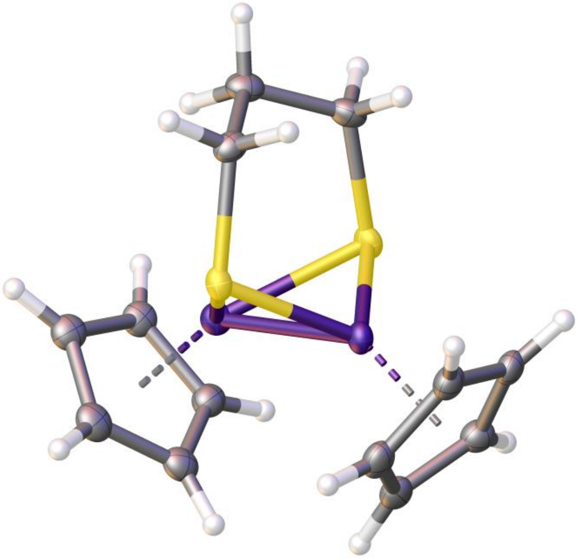

Figure 5.9. Solid state structure of [**1**]BF_4. The BF_4^- counterion has been omitted for clarity. Selected bond distances can be found in Table 5.2.

The EPR spectrum of [**1**]BAr_4^F in Et_2O solution exhibits equivalent hyperfine coupling to two cobalt centers ($I(^{57}Co)=7/2$, 100% abundant) of 55 MHz and an isotropic *g*-value of 1.966 (Figure 5.10). The EPR spectrum at 77K as a frozen glass is axial and exhibits surprisingly different coupling features (Figure 5.11). The *g*-values for the frozen spectrum are $g_1 = 2.225$ and $g_2 = 1.984$ which have an isotropic *g*-value of $g_{iso} = 2.145$, which is *not* equal to the g_{iso} observed at room temperature. Additionally, coupling is observed to only *one* cobalt center in the frozen spectrum (A_{Co} = 173 MHz). The predicted isotropic hyperfine coupling from the frozen EPR data is 58 MHz, which is close to the value observed at room temperature. Warming the solution back to room temperature generates the same previously observed spectrum. These data suggest that the ground state for the $[\mathbf{1}]^+$ cation is a discrete Co(III)Co(II) system and at room temperature, the spin appears to be delocalized, but advanced interpretation may be required.

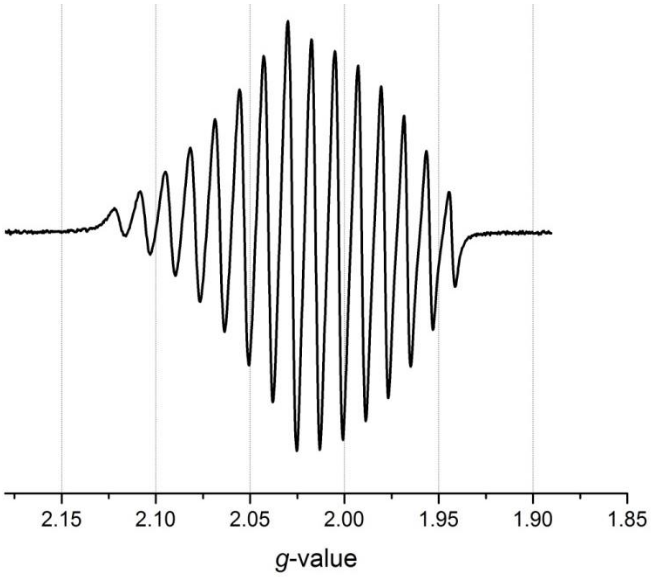

Figure 5.10. X-Band CW-EPR spectrum of [**1**]BAr_4^F in Et_2O solution at room temperature.

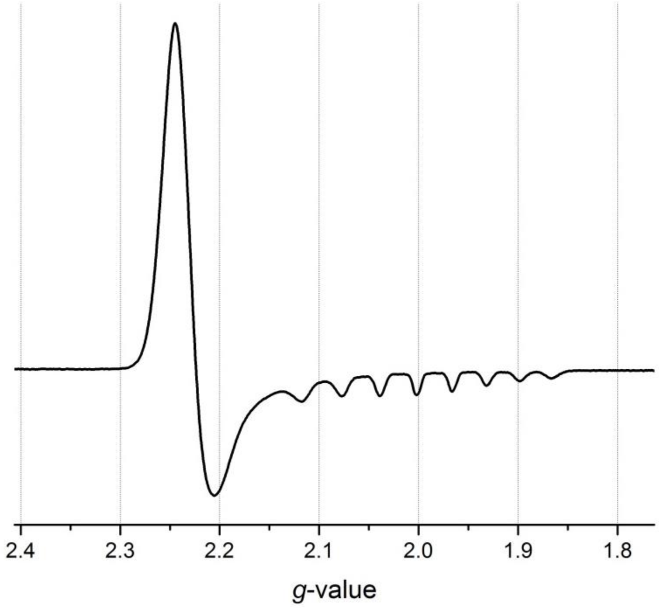

Figure 5.11. X-Band CW-EPR spectrum of [**1**]BAr_4^F as at 77K in an Et_2O glass.

The curious features of the EPR spectra of [**1**]BAr_4^F at room temperature and 77K prompted an investigation of this cation with DFT analysis using the BP86 functional and 6-311+G** basis set. These calculations indicate that the ground state for this complex is indeed a discrete, localized Co(III)Co(II) system (Figure 5.12), in agreement with the EPR spectrum observed at 77K. The spin density is heavily biased to one CpCo side. The electronic asymmetry apparently results from to the orientation of the pdt ring; orientation of the pdt ring over the cobalt center with the greatest spin density caused the spin to shift to the cobalt not under the pdt ligand.

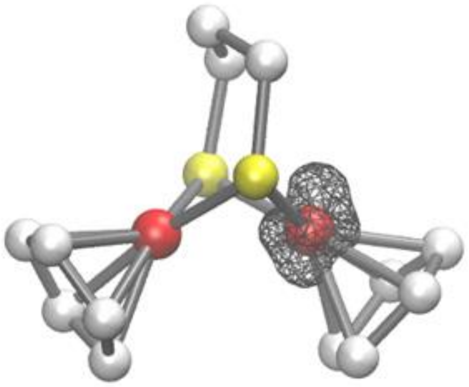

Figure 5.12. Spin density plot of the mixed-valence cation [**1**]$^+$ showing localization to one cobalt center.

Table 5.3. Spin density distribution in [**1**]$^+$.

Atom*	Spin Density*
Co	0.0477
Co	0.7293
C_5H_5	0.0273
C_5H_5	0.1521
S_2	0.0197

*Black Co corresponds to the black C_5H_5 and Red Co corresponds to the red C_5H_5.

5.5 Reaction of the Mixed-Valence Cation [1]$^+$ with H_2O

The mixed-valence complexes, similar to the bridging hydride compounds, were found to be unstable in coordinating solvents such as MeCN and acetone, generating red solutions with concomitant formation of precipitates. No effort was made to identify the red species in solution. These cations were found to be air-sensitive and tested for reactivity with O_2 and H_2O. Solutions of the cation [**1**]$^+$ degraded over the course of c.a. 30 minutes under 1 atm of O_2 to yield brown precipitates that were not soluble in organic solvents. In contrast, treatment of [**1**]$^+$ in THF solution with degassed H_2O produced deeply violet solutions, with no visual indication of precipitation.

The ESI-MS spectrum depicted in Figure 5.7 displays a strong signal with an *m/Z* of 371. This signal corresponds to the bridging hydroxide cation [Cp_2Co_2pdtOH]$^+$ ([**1**OH]$^+$). This species can be effectively prepared from the mixed-valence cation [**1**]$^+$ by treatment with aqueous THF. The reaction mixture showed no indication of other cationic species such as [**1**H]$^+$ or higher nuclearity products by ESI-MS (Figure 5.13).

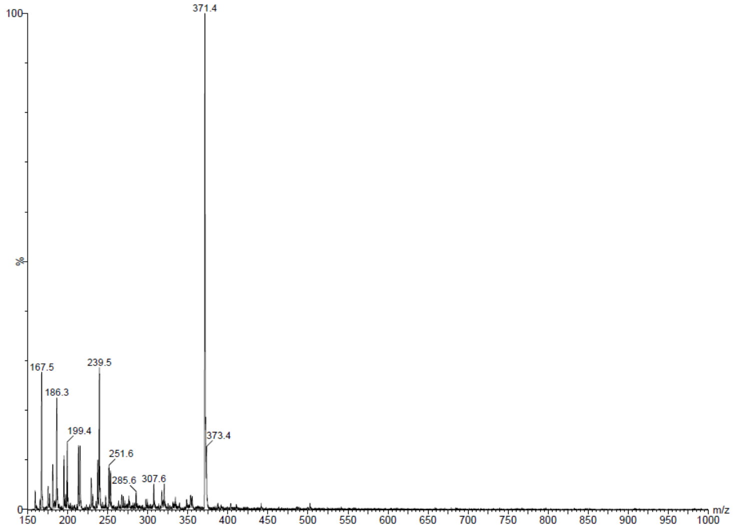

Figure 5.13. ESI-MS of the reaction mixture of [**1**]BAr_4^F with aqueous THF. The signal with *m*/*Z* 371 corresponds to the cation $[Cp_2Co_2pdtOH]^+$.

The bridging hydroxide cation $[\mathbf{1}OH]^+$ was structurally characterized as the tetrafluoroborate salt, as both the anhydrous form (Figure 5.14) and the trihydrate (Figure 5.15). The anhydrous form was obtained via vapor diffusion of anhydrous ether into concentrated dichloromethane solutions of [**1**OH]BF_4 while the trihydrate was crystallized by vapor diffusion of ether into hydrous acetone solutions of [**1**OH]BF_4.

The structures of [**1**OH]BF_4 as the anhydrous and hydrous salts are overall very similar. In contrast to the neutral compounds, the mixed-valence compounds, and the bridging hydride compounds, the bridging hydroxide cation $[\mathbf{1}OH]^+$ features a long Co---Co distance of ≈2.8 Å and a fairly linear Cp-Co-Co angle of ≈170° (Table 5.2). For the structure of the anhydrous hydroxide salt, a O-H---F distance of 1.94(1) Å between the hydroxide hydrogen and the tetrafluoroborate fluorine indicates a hydrogen bond that is primarily electrostatic in nature.[19] The Co_2OH---OH_2 distance in the trihydrate structure are slightly longer (2.10(3) Å) and the Co_2O---H_2O distance is 1.97(1); both distance are in the regime of moderate strength hydrogen bonding.

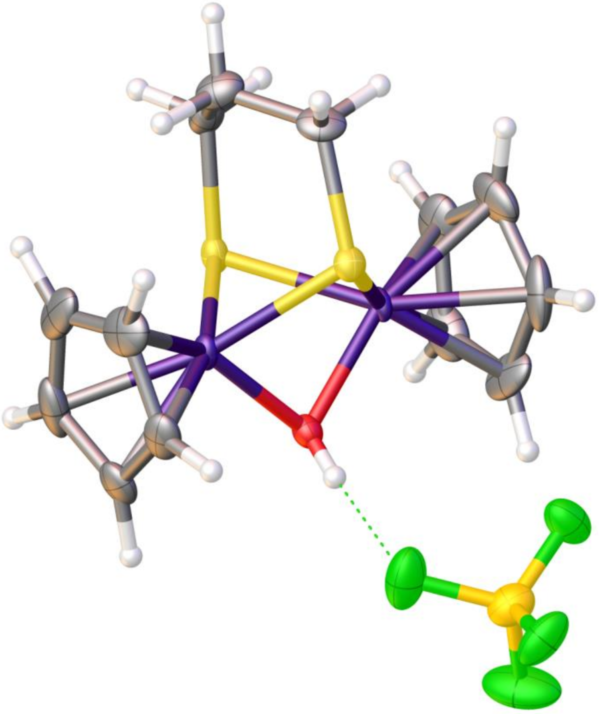

Figure 5.14. Solid state structure of [**1**OH]BF_4 depicting a hydrogen bonding interaction between the bridging hydroxide and the BF_4^- counterion. The hydroxide hydrogen atom was located in the difference map. Selected bond distances can be found in Table 5.2.

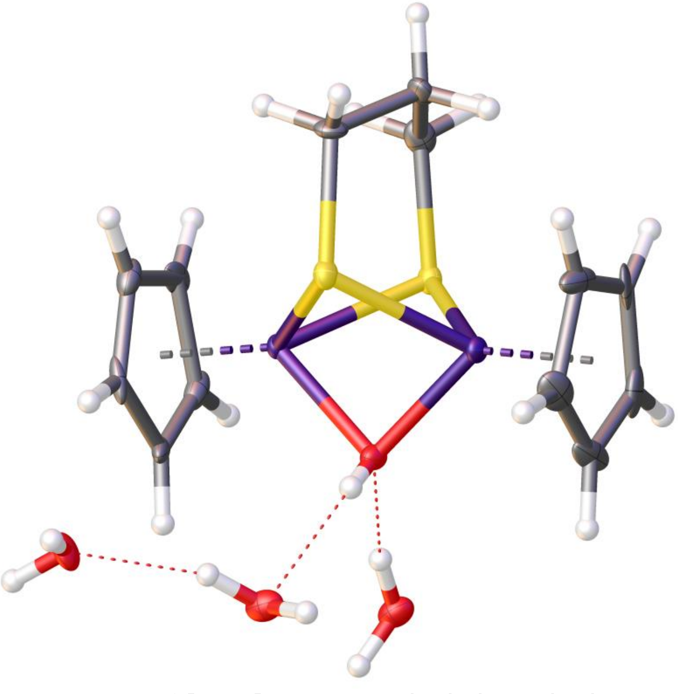

Figure 5.15. Solid state structure of [**1**OH]$BF_4 \cdot 3H_2O$ depicting a hydrogen bonding interactions between the bridging hydroxide and solvates. The BF_4^- counterion has been omitted for clarity. The hydroxide hydrogen atom and the water hydrogen atoms were located in the difference map. Selected bond distances can be found in Table 5.2

The ^{1}H-NMR spectrum of the bridging hydroxide [**1**OH]$^+$ is relatively simple (Figure 5.16). The C_5H_5 resonance is observed at δ5.09 and the pdt resonances appear at δ2.36 and δ2.03. The O*H* signal is shifted rather upfield at δ−3.04. The hydroxide OH resonance immediately vanishes when THF solutions of [**1**OH]BAr$_4^F$ are treated with CD_3OD, (Figure 5.17).

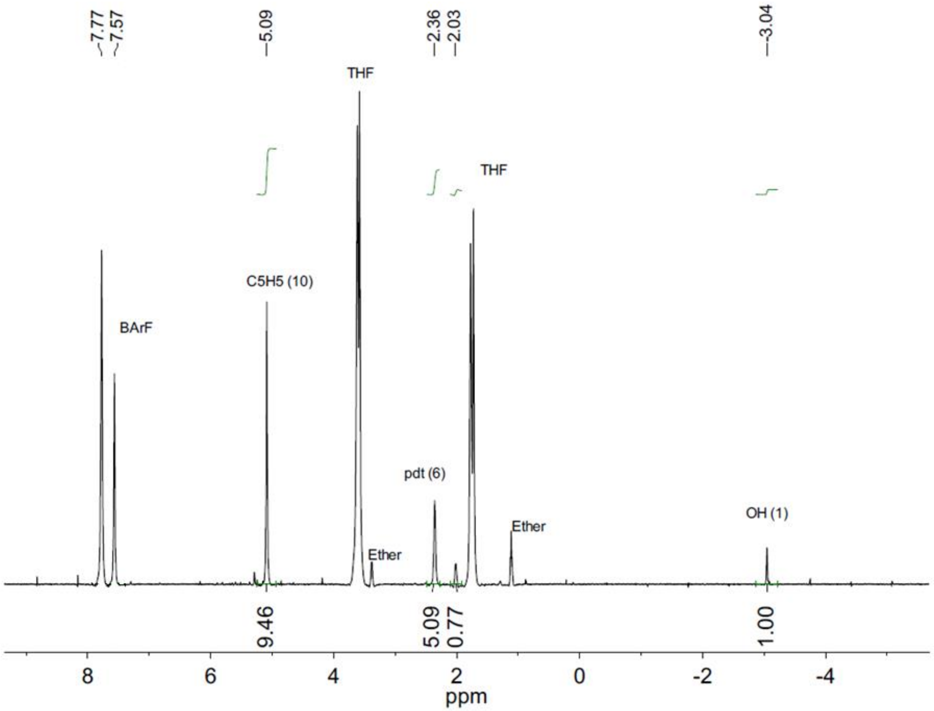

Figure 5.16. ^{1}H-NMR spectrum of [**1**OH]BAr$_4^F$ in THF-d_8.

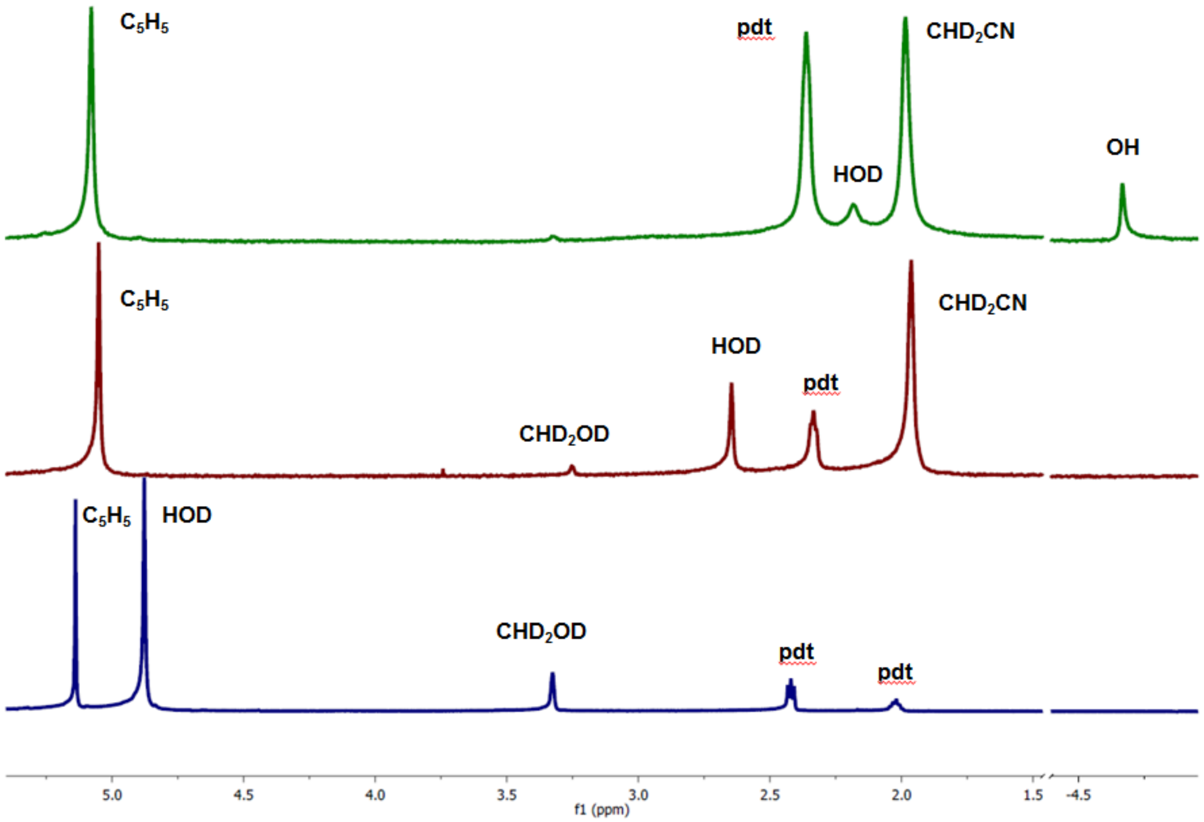

Figure 5.17. (Top) ^{1}H-NMR spectrum of $[Cp_2Co_2(pdt)OH]BF_4$ in MeCN-d_3. (Middle) ^{1}H-NMR spectrum of $[Cp_2Co_2(pdt)OH]BF_4$ in MeCN-d_3/CD_3OD 95:5. (Bottom) ^{1}H-NMR spectrum of $[Cp_2Co_2(pdt)OH]BF_4$ in CD_3OD.

The mechanism for the formation of the bridging hydroxide [**1**OH]$^+$ is peculiar, as it entails the formation a diamagnetic Co(III)Co(III) species from a mixed-valent Co(II)Co(III) precursor. Because no hydridic species were observed, even when reaction mixtures of [**1**]$^+$ with aqueous THF were examined by ^{1}H-NMR spectroscopy, we initially proposed a balanced reaction that implicated the evolution of H_2 (Scheme 5.6). A possible mechanism was proposed for this process which involves hydroxo-hydrido species (Scheme 5.7). When, however, solutions of [**1**]$^+$ in THF were prepared in air-tight vessels and treated with H_2O by injection. The headspace was subsequently sampled and analyzed by gas chromatography. No hydrogen was detected.

Scheme 5.7. Reaction of $[\mathbf{1}]^+$ with H_2O

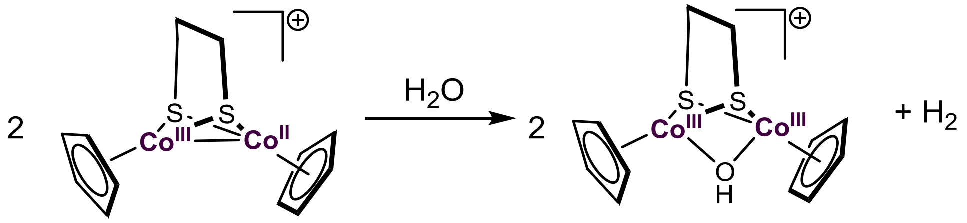

Scheme 5.8. Initially proposed mechanism for the formation $[\mathbf{1}OH]^+$ via H_2 evolution.

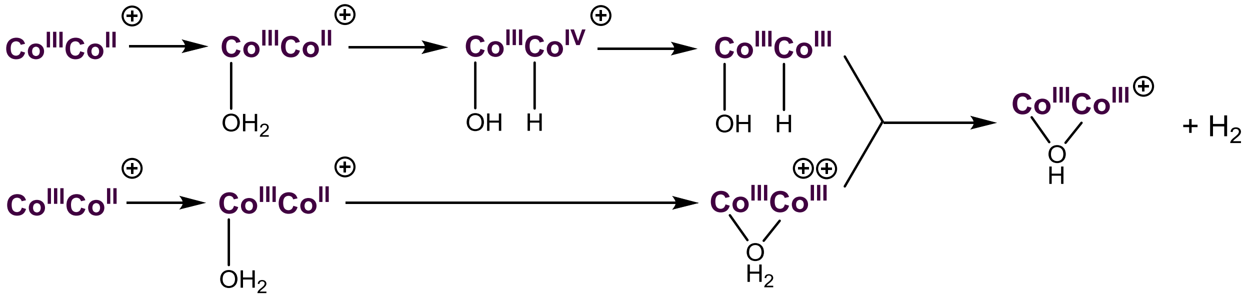

A new pathway was proposed in which the oxidized compound $[\mathbf{1}]^+$ first associates with H_2O and is subsequently deprotonated by free H_2O, generating the reduced hydroxo species **1**OH (Scheme 5.8). This species is in turn oxidized by $[\mathbf{1}]^+$ to generate $[\mathbf{1}OH]^+$ and **1**. In this mechanism, **1** is proposed to form $[\mathbf{1}H]^+$, but this species has not been detected (Figure 5.14). For the mechanism proposed in Scheme 5.8 to be consistent, $[\mathbf{1}H]^+$ must degrade quickly under these conditions or alternative mechanism is necessary. Scheme 5.8 would be consistent with the experimentally obtained yield of ~50% for $[\mathbf{1}OH]BF_4$.

Scheme 5.9. Proposed Mechanism for the Formation of $[\mathbf{1}OH]^+$

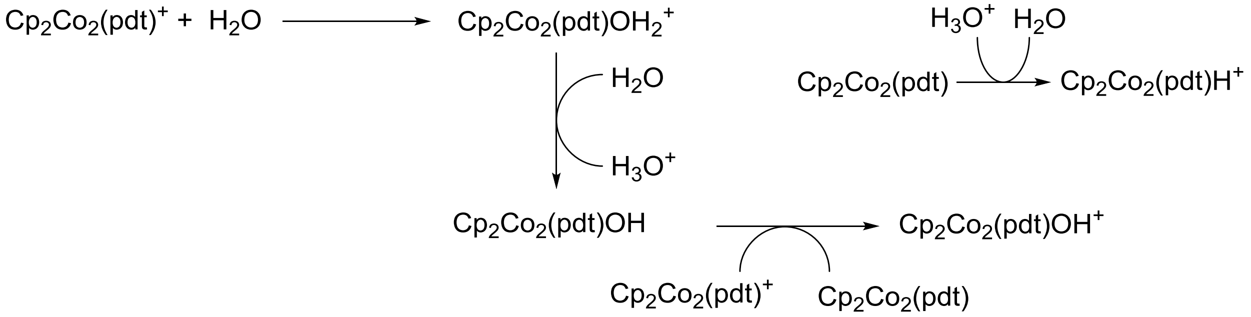

The electrochemistry of the bridging hydroxide cation [**1**OH]$^+$ is complex (Figure 5.18). In MeCN solution, compound [**1**OH]BF_4 exhibits an irreversible oxidation at ≈0.8 V vs $Fc^{0/+}$. This oxidation produces the dication Co(IV)Co(III)OH^{2+}, which is predicted to increase the acidity of the O-H bond significantly. The rapid deprotonation of $[Cp_2Co_2OH]^{2+}$ could explain the observed irreversibility of this oxidation. In addition to an irreversible oxidation, [**1**OH]BF_4 has several irreversible reductions that being at ≈−1.1 V vs $Fc^{0/+}$ that appear to be slightly affected by the scanning direction.

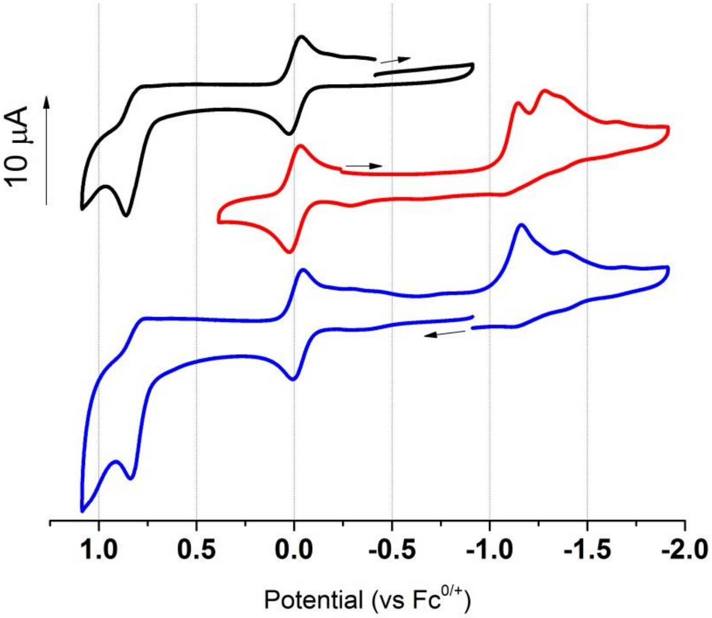

Figure 5.18. Cyclic voltammogram of [**1**OH]BF_4 from various starting positions with ferrocene as an internal standard. Conditions: MeCN solution, ~1 mM analyte, 100 mM $[Bu_4N][PF_6]$, 100 mVs^{-1} scan rate. Starting point and initial direction is indicated using a black arrow.

The reactivity of the bridging hydroxide complex was not been explored extensively, however, the hydroxide complex was found to be reactive with silanes. Upon treatment with excess Ph_2SiH_2, the bridging hydroxide [**1**OH]$^+$ is converted to the bridging hydride complex [**1**H]$^+$.

5.6 Reaction of [1]$^+$ with Thiols

The reactivity of [**1**]$^+$ with H_2O spurred interest in the reactivity between [**1**]$^+$ and other protic substrates, specifically thiols. Similar to the facile conversion of [**1**]$^+$ to [**1**OH]$^+$, upon treatment with excess PhSH, green solutions of [**1**]$^+$ became red upon mixing. The generated bridging thiophenolate cation $[Cp_2Co_2(pdt)SPh]^+$ was characterized as the BAr_4^F salt (Figure 5.19). The thiophenolate derivative, similar to the hydroxide, features a long Co---Co distance of

2.92 Å and a fairly linear Cp-Co-Co angle of 178°. The mechanism for this reaction may be similar to the formation of the bridging hydroxide proposed in scheme 5.8.

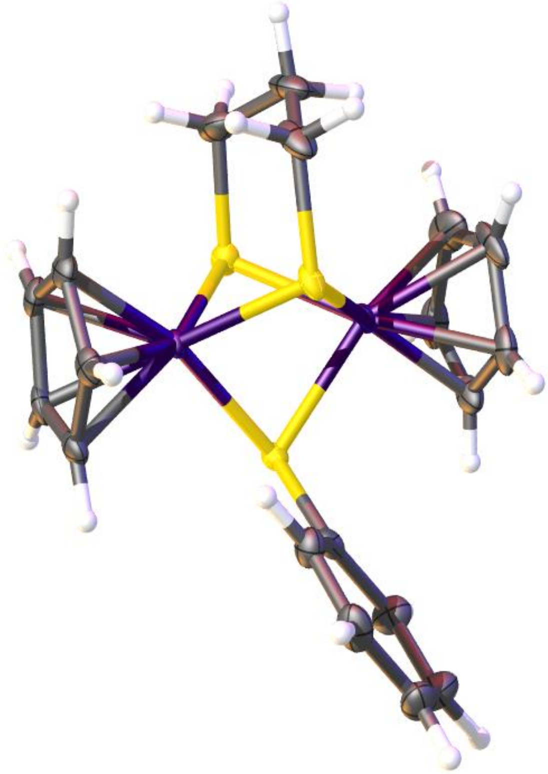

Figure 5.19. Solid state structure of [**1**SPh]BAr$_4^{F}$ depicting a hydrogen bonding interaction to the BF$_4^-$ counterion. Selected bond distances can be found in Table 5.2.

The ^{1}H-NMR spectrum of [**1**SPh] is as would be expected (Figure 5.20). The Cp resonances are observed at δ5.04 and the bridging thiophenolate protons are observed in the δ7.4 to δ8.00 range. The non-equivalent pdt methylene protons exhibit complex coupling.

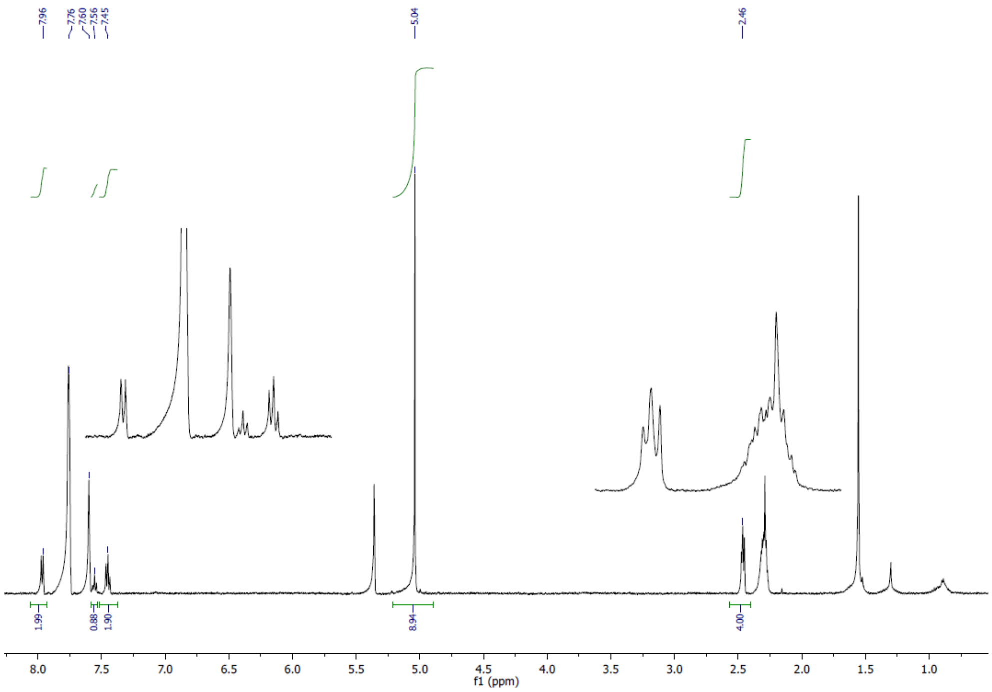

Figure 5.20. ^{1}H-NMR Spectrum of [**1**SPh]BAr$_4^F$ in CD_2Cl_2.

In addition to thiophenol, the reaction of [**1**]$^+$ with the dithiol pdtH$_2$ was investigated. A solution of [**1**]BAr$_4^F$ in THF was treated with a pdtH$_2$ in slight excess. The reaction mixture was probed by ESI-MS, which indicated the formation of the pdtH$^-$ adduct $Cp_2Co_2pdt(SCH_2CH_2CH_2SH)$ (*m/Z* = 461), which was not successfully isolated (Figure 5.21).

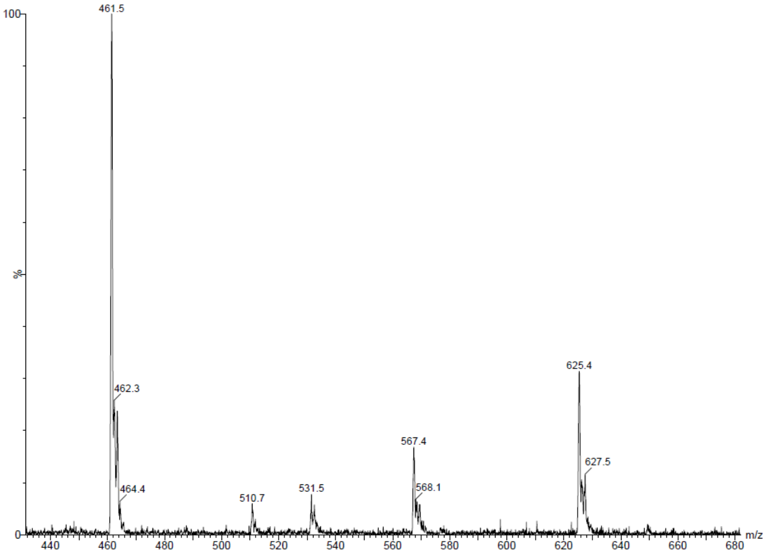

Figure 5.21. ESI-MS of the reaction mixture [**1**]BAr$_4^F$ and pdtH$_2$.

Upon standing for several days, dilute mixtures of the mixed-valence compound [**1**]$^+$ and pdtH$_2$ deposited single crystals suitable for X-ray crystallography. These crystals were found to contain the tetracobalt dication $[(Cp_2Co_2pdt)_2pdt]^{2+}$ (Figure 5.22). Overall, the structure of this dication are similar to the thiophenolate derivative. The Co---Co distance is long at 2.901(1) Å and the Cp-Co-Co angle is nearly linear at 177°.

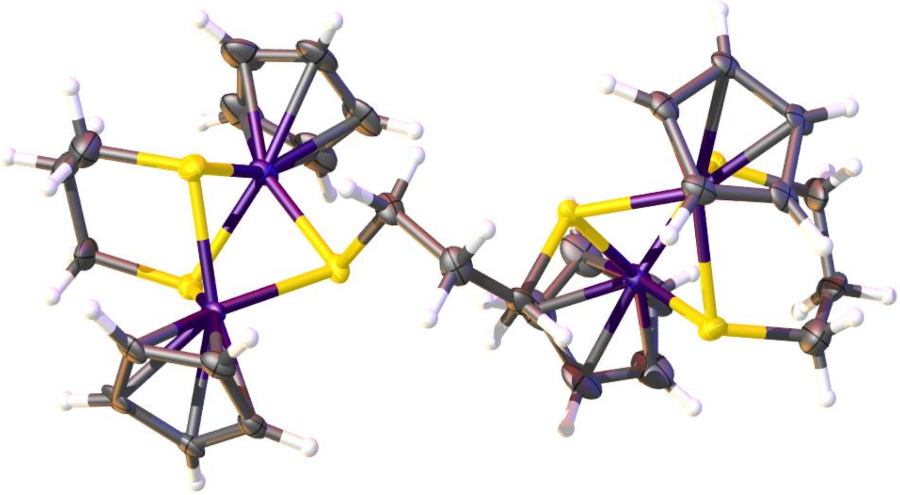

Figure 5.22. Solid state structure of [**3**]$[BAr_4^F]_2$ depicting a hydrogen bonding interaction to the BF_4^- counterion. Selected bond distances can be found in Table 5.2

5.7 The Reduced Bridging Hydride Complexes 1H and 2H

The bridging hydride compounds [**1**H]BF$_4$ and [**2**H]BF$_4$ exhibit reversible one electron reductions at −0.950 and −0.980 vs Fc$^{0/+}$ respectively. Additionally, these compounds produce catalytic waves at these potentials in the presence of acid, however the rates are slow tend to be on the order of 10^1 s^{-1}. We were interested in the nature of these reduced, mixed-valence hydride catalytic intermediates.

The reduced hydride compound Cp$_2$Co$_2$pdtH (**1**H) and Cp$_2$Co$_2$edtH (**2**H) are readily prepared in high yield by treatment of dichloromethane solutions of [**1**H]BF$_4$ and [**2**H]BF$_4$ 1 equiv. of Cp$_2$Co. The byproduct [Cp$_2$Co]BF$_4$ was removed by filtration through Celite in a suspension of Et$_2$O. The reduced hydride compounds **1**H and **2**H were isolated as brown powders.

The EPR spectrum of **1**H at room temperature is similar in appearance to that of the mixed-valence cation [**1**]$^+$, although the linewidth is somewhat broader (Figure 5.23). Hyperfine coupling to two inequivalent cobalt centers is observed. The two distinct cobalt couplings indicates that the reduced hydride is a discrete Co(III)Co(II) species.

The spectrum obtained at 77K as an Et_2O glass is significantly more complicated than $[\mathbf{1}]^+$ (Figure 5.24). Although $[\mathbf{1}]^+$ displays an axial spectrum at 77K with coupling to only one cobalt center and is also a discrete Co(III)Co(II) species, **1**H displays a rhombic spectrum with coupling to both cobalt centers at 77K. Multiple species appear to be present. We propose that the EPR spectrum of **1**H at 77K is possesses mixture of two isomers that differ by the orientation of the pdt ligand. These "flippamers" have been known to produce similar, though distinct, EPR spectra.[20]

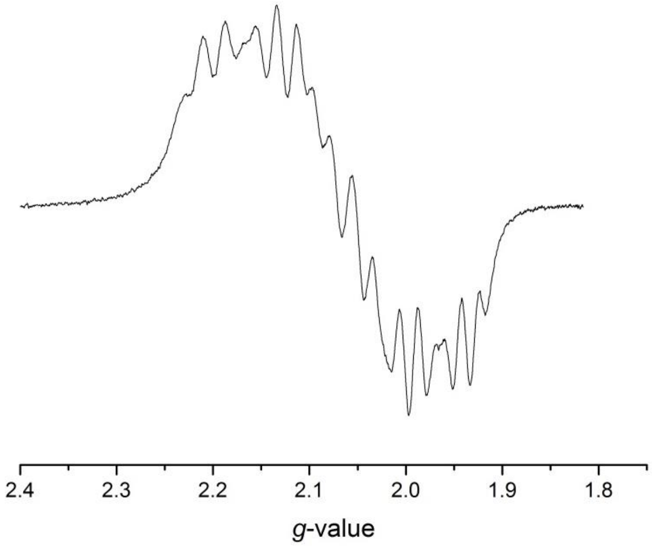

Figure 5.23. X-Band CW-EPR Spectrum of **1**H in Et_2O at room temperature.

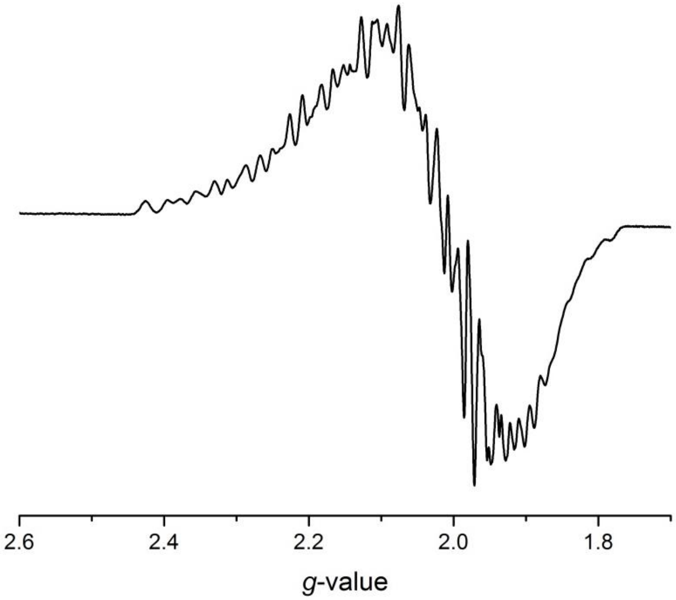

Figure 5.24. X-Band CW-EPR Spectrum of **1**H at 77K in an Et_2O Glass.

The EPR spectra of the edt derivative **2**H is greatly simplified compared to the pdt derivative, further suggesting that the additional complexity observed in the spectra of **1**H are due to “flippamers.” The EPR spectrum of **2**H at room temperature in Et_2O solution exhibits coupling two to cobalt centers that is equivalent or nearly equivalent (Figure 5.25). The EPR spectrum of **2**H at 77K as a glass in Et_2O has a somewhat similar visual appearance to the 77 EPR spectrum of **1**H, but is overall vastly simplified (Figure 5.26). This rhombic spectrum shows hyperfine coupling to two nearly equivalent cobalt centers and additional hyperfine coupling to an I = ½ nucleus. A similar coupling can be discerned in the spectrum of **1**H, but it is largely obscured.

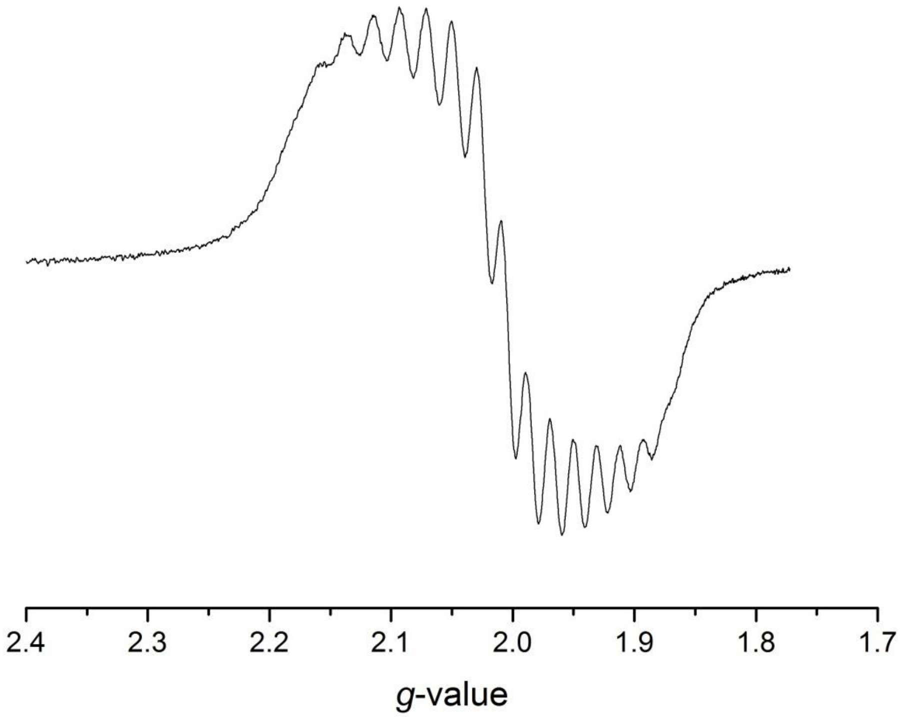

Figure 5.25. X-Band CW-EPR Spectrum of **2**H in Et_2O at room temperature.

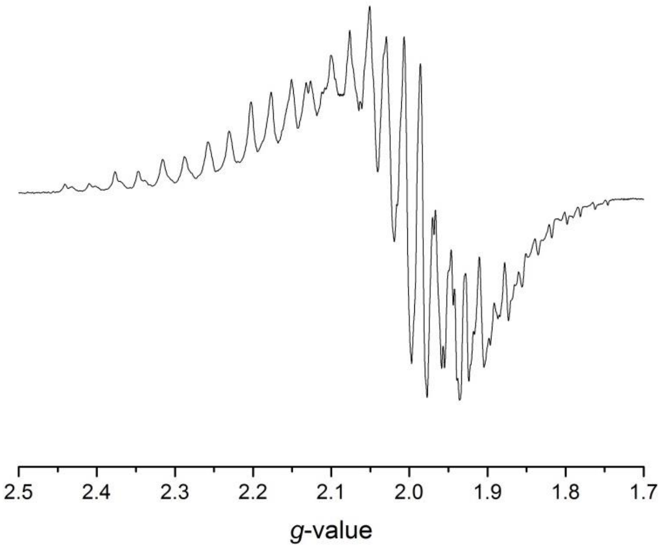

Figure 5.26. X-Band CW-EPR spectrum of **2**H in Et_2O at 77K in an Et_2O glass.

5.8 Concluding Remarks

This chapter primarily discussed the properties of the mixed-valence cation $[Cp_2Co_2pdt]^+$ ($[\mathbf{1}]^+$) and the bridging hydride cation $[Cp_2Co_2pdtH]^+$ ($[\mathbf{1}H]^+$). The mixed-valence species reacts with the protic substrates H_2O, PhSH, and $pdtH_2$ to give the corresponding hydroxide and thiolate complexes. The mixed-valence compounds $[\mathbf{1}]^+$ and **1**H are best described as Co(III)Co(II) compounds. This is in contrast to the mixed-valence cyclopentadienyl nickel thiolate compounds discussed in chapter 4, which are delocalized $Ni(2.5)_2$ centers. Compounds **1** and **2** are modest proton reduction catalysts.[13] The reduced hydrides **1**H and **2**H are proposed intermediates in the catalytic cycles for these catalysts and have been prepared and characterized by EPR Spectroscopy.In contrast to other Co(III) containing complexes discussed in this chapter, the bridging hydroxide cation $[\mathbf{1}OH]^+$ is robust and is stable in the presence of coordinating solvents such as acetone and MeCN. All cobalt(III) containing compounds discussed without hydroxo or thiolate ligands as the third bridging ligand are unstable in the presence of Lewis Bases. This instability could be due to the lability of CpCo(xdt)L and or $CpCoL_3$ fragments (Scheme 5.8).

Scheme 5.10. Possible Decomposition Pathway of Co(III) Containing Cp_2Co_2(xdt) Complexes

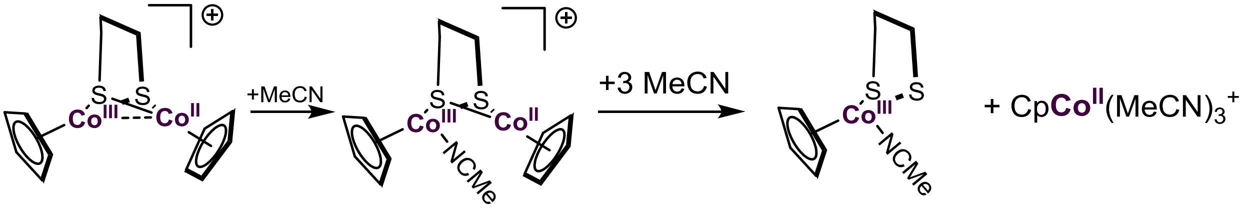

5.9 Experimental

In most cases, reactions were performed using standard Schlenk and glovebox techniques. Most reagents were purchased from either Strem or Sigma-Aldrich. Solvents were HPLC-grade or better and were further purified by filtration through activated alumina or distilled under nitrogen. The compounds $[H(OEt_2)_2]BAr_4^F$,[21] $[Bu_4N]BAr_4^F$,[22] and Cp'Co(CO)$_2$ were prepared according to literature procedures. $[Bu_4N]PF_6$ was recrystallized from ethanol. ^{1}H NMR spectra (500 MHz) are referenced to residual solvent referenced to TMS. $^{31}P\{^1H\}$ NMR spectra (202 MHz) are referenced to external 85% H_3PO_4. FT-IR spectra were recorded on a Perkin Elmer 100 FT-IR spectrometer, focusing primarily on the ν_{CO} region. ESI-MS data were recorded of dilute CH_2Cl_2 solutions on a Waters Micromass Quattro II spectrometer. CV data was recorded on a CHI model 630D instrument, using Pt working and counter electrodes. An Ag bar was used as a pseudo reference electrode. After each CV measurement, Fc was added as an internal standard. Chromatography was performed on basic alumina that was deactivated by the addition of 5% water by weight.

$(CpCo)_2$(pdt) (1). A solution of CpCo(CO)$_2$ (1.0 mL, 7.5 mmol) in 50 mL of toluene was treated with 1,3-propanedithiol (375 µL, 3.75 mmol). The red solution was heated to reflux in an oil bath, and the progress of the reaction was monitored by IR spectroscopy, for the loss of CpCo(CO)$_2$ bands at 2023 and 1960 cm^{-1}. After heating for 16 h, the solution had changed color from red to green. The solvent was removed from the cooled reaction mixture. The product was extracted into hexanes and filtered through a pad of Celite to yield a green solution. Removal of solvent yielded a green solid. Yield: 448 mg (34%). ^{1}H NMR (500 MHz, CD_2Cl_2, room temperature): δ 4.87 (*s*, C_5H_5), 1.29 (*s*, SCH_2CH_2), 1.17 (*s*, SCH_2). When the NMR sample is cooled to -70 °C, an additional signal is present at 0.524 ppm, and the signal corresponding to C_5H_5 is split. ^{1}H NMR (500 MHz, CD_2Cl_2) -70°C : δ 4.91, 4.78 (*d*, C5H5), 1.90 (*s*), 1.71 (*s*), 0.52(*s*). FD-MS m/z: 354. Anal Calcd for $C_{13}H_{16}Co_2S_2$ (found): C, 44.1 (44.02); H, 4.55 (4.48).

$(CpCo)_2(edt)$ (2). A solution of solution of $CpCo(CO)_2$ (1 mL,7.5 mmol) in 100 mL of toluene was treated with 1,2-ethanedithiol (315 μL, 3.75 mmol). The red solution was heated to reflux in a 120°C oil bath, and the progress of the reaction was monitored by IR spectroscopy, for the loss of $CpCo(CO)_2$ bands at 2023 and 1960 cm^{-1}. After 20 h, the solution had changed color from red to brown. The cooled solution was filtered, and the remaining brown residue was washed with toluene to remove any undissolved product. The brown product was concentrated to dryness under vacuum and extracted into pentane. The pentane solution was concentrated and cooled to -20 °C, resulting in crystallization of the product. ^1H NMR (500 MHz, CD_2Cl_2): δ 4.867 (s, 10H, C_5H_5), 1.285 (s, SCH_2CH_2S, extraneous hexane solvent throws off integration). FD-MS m/z: 340.0. Anal. Calcd for $C_{12}H_{14}Co_2S_2$ (found): C, 42.3 (42.14); H, 4.15 (4.45).

$[(CpCo)_2(pdt)(\mu\text{-}H)]BF_4$ ([1H]BF_4]). A solution of $(CpCo)_2(pdt)$ (100 mg, 0.28 mmol) in 10 mL of CH_2Cl_2 was treated with one equiv. of $HBF_4{\cdot}Et_2O$ (50 μL 54% wt/v, 0.28 mmol). The solution stirred for 20 min., and then it was concentrated to dryness under vacuum to yield a green solid. Yield: 111 mg (89%). ^1H NMR (CD_2Cl_2): δ 5.54 (s, 10 H, C_5H_5), 2.15 (s, 12.11 H, $SCH_2CH_2CH_2S$), -13.28 (s, 1.52 H, Co-H-Co). ESI-MS: m/z: 355.2. Anal Calcd for $Co_2S_2C_{13}H_{17}BF_4$ (found): C, 35.32 (34.76); H, 3.88 (4.07).

$[(CpCo)_2(pdt)(\mu\text{-}H)]$ BAr_4^F ([1H]BAr_4^F). [**1H**]BAr_4^F was prepared in a similar fashion as [**1H**]BF_4 using $[H(Et_2O)_2]BAr_4^F$ as the acid. Yield: 94%. ESI-MS: m/z: 355.2.

$[(CpCo)_2(edt)(\mu\text{-}H)]BF_4$ ([2H]BF_4]). A solution of $(CpCo)_2(edt)$ (101 mg, 0.3 mmol) in 20 mL of CH_2Cl_2 was treated with one equiv. of $HBF_4{\bullet}Et_2O$ (50 μL 54% wt/v, 0.3 mmol). The solution stirred for ten minutes, and then it was concentrated to dryness under vacuum. The resulting brown solid was recrystallized from dichloromethane and hexanes. ^1H NMR (CD_2Cl_2): 5.551 (*s*, C_5H_5), 2.621 (*s*, SCH_2CH_2S), -15.641 (*s*, Co-H-Co). ESI-MS: m/z: 341.2. Diffraction quality crystals of $[(CpCo)_2(edt)(\mu\text{-}H)]BF4$ were obtained by vapor diffusion of Et_2O into a solution of the compound in CH_2Cl_2.

$[(CpCo)_2(edt)(\mu\text{-}H)]BAr_4^F$ ([2H]BAr_4^F). [**2H**]BAr_4^F was prepared in a similar fashion as [**2H**]BF_4 using $[H(Et_2O)_2]BAr_4^F$ as the acid. Yield: 94%.

$[(CpCo)_2(pdt)]BF_4$ ([1]BF_4). A solution of 50 mg (0.141 mmol) of **1** in 2 mL of CH_2Cl_2 was treated with 38.5 mg of $[Fc]BF_4$ (0.141 mmol) in 10 mL of CH_2Cl_2. After stirring for 30 minutes, the solvent was reduced to 2 mL and 8 mL of Et_2O was added. The slurry was filtered through Celite and washed several times with Et_2O. The residue was extracted with CH_2Cl_2 and the solvent was removed from the subsequent filtrate. Yield: 56 mg (91 %). Crystals were grown at room temperature by the vapor diffusion of ether into concentrated CH_2Cl_2 solutions.

$[(CpCo)_2(pdt)]BAr_4^F$ ($[1]BAr_4^F$). [**1**]BAr_4^F was prepared in a similar fashion as [**1**]BF_4 using $FcBAr_4^F$ as the oxidant. Yield: 94%.

$[(CpCo)_2(edt)]BF_4$ and $[(CpCo)_2(edt)]BAr_4^F$ ($[2H]BF_4$ $[2H]BAr_4^F$). These compounds were prepared in a similar fashion a [**1**]BF_4 using the appropriate precursor and oxidant**.**

$[(CpCo)_2(pdt)(\mu\text{-}OH)]BF_4$ ($[1OH]BF_4$). A solution of 20 mg (0.045) of [**1**]BF_4 in 10 mL CH_2Cl_2 was agitated with 2 mL of degassed H_2O. The organic and aqueous layers become dark purple. All volatiles were moved under reduced pressure yielding a purple residue. The residue was extracted into CH_2Cl_2 and dried with $MgSO_4$. After filtration, the solvent was removed under reduced pressure to yield a purple powder. The crude product was recrystallized from CH_2Cl_2 and Ether. Yield: 8.7 mg (42%). Single crystals of the anhydrous salt were obtained by vapor diffusion of ether into concentrated dichloromethane solutions. Single crystals of the trihydrate were obtained by vapor diffusion of ether into concentrated aqueous acetone solutions.

$[(CpCo)_2(pdt)(\mu\text{-}OH)]BAr_4^F$ ($[1OH]BAr_4^F$). A solution of 12.1 mg (0.010 mmol) of [**1**]BAr_4^F in 1 mL THF was treated with 0.2 mL of degassed H_2O dissolved in 0.2 mL of THF. The mixture immediately became dark purple. All volatiles were moved under reduced pressure yielding a purple residue. The residue was extracted into Et_2O and dried with $MgSO_4$. After filtration, the solvent was removed under reduced pressure to yield a purple powder. The crude product was recrystallized from Et_2O and pentane. Yield: 10.2mg (83%).

$(CpCo)_2(pdt)(\mu\text{-}H)$ (1H). A solution of 8.0 (0.0181 mmol) mg of [**1**H]BF_4 in 2 mL of CH_2Cl_2 was treated with 3.4 mg (0.0180 mmol) of Cp_2Co. The solution immediately became brown and yellow $[Cp_2Co_2]BF_4$ precipitated. The solvent was removed under reduced pressure and the residue was slurried into Et_2O, and the supernatant was filtered through Celite. The solvent was removed from the filtrate to give **1**H as a brown powder. Yield: 5.9 mg (92%).

$(CpCo)_2(edt)(\mu\text{-}H)$ (2H). **2**H was prepared in a similar fashion to **1**H. Yield: 88%.

5.10 References

(1) Wieghardt, K. *Mixed-Valence Systems: Applications in Chemistry, Physics, and Biology* Amsterdam, 1990.

(2) Gloaguen, F.; Lawrence, J. D.; Schmidt, M.; Wilson, S. R.; Rauchfuss, T. B. *J. Am. Chem. Soc.* **2001**, *123*, 12518.

(3) Justice, A. K.; De Gioia, L.; Nilges, M. J.; Rauchfuss, T. B.; Wilson, S. R.; Zampella, G. *Inorg. Chem.* **2008**, *47*, 7405.

(4) van der Vlugt, J. I.; Rauchfuss, T. B.; Wilson, S. R. *Chem. Eur. J.* **2006**, *12*, 90.

(5) Brint, P.; Spalding, T. R. *J. Chem Soc. Dalt. Trans.* **1980**, 1236.

(6) Cowie, M.; DeKock, R. L.; Wagenmaker, T. R.; Seyferth, D.; Henderson, R. S.; Gallagher, M. K. *Organometallics* **1989**, *8*, 119.

(7) Carroll, M. E.; Chen, J. Z.; Gray, D. E.; Lansing, J. C.; Rauchfuss, T. B.; Schilter, D.; Volkers, P. I.; Wilson, S. R. *Organometallics* **2014**, *33*, 858.

(8) King, R. B.; Treichel, P. M.; Stone, F. G. A. *J. Am. Chem. Soc.* **1961**, *83*, 3593.

(9) King, R. B.; Treichel, P. M.; Stone, F. G. A. *J. Am. Chem. Soc.* **1961**, *83*, 3600.

(10) Malacria, M.; Aubert, C.; Renaud, J. L. *Science of Synthesis*; Thieme Chemistry, 2001; Vol. 1.

(11) King, R. B.; Treichel, P. M.; Stone, F. G. A. *J. Am. Chem. Soc.* **1961**, *83*, 3600.

(12) Drobnik, S.; Stoll, C.; Noeth, H.; Polborn, K.; Hiller, W.; Lorenz, I.-P. *Z. Naturforsch., B: Chem. Sci.* **2006**, *61*, 1365.

(13) Carroll, M. E., University of Illinois, Champaign-Urbana, 2013.

(14) Lansing, J. C., University of Illinois, Champaign-Urbana, 2015.

(15) Lubitz, W.; Ogata, H.; Rüdiger, O.; Reijerse, E. *Chem. Rev.* **2014**, *114*, 4081.

(16) Trojánek, A.; Langmaier, J.; Samec, Z. *Electrochim. Acta* **2012**, *82*, 457.

(17) McNamara, W. R.; Han, Z.; Yin, C.-J.; Brennessel, W. W.; Holland, P. L.; Eisenberg, R. *Proceedings of the National Academy of Sciences* **2012**, *109*, 15594.

(18) Werner, H.; Hofmann, W.; Zolk, R.; Dahl, L. F.; Kocal, J.; Kuehn, A. *J. Organomet. Chem.* **1985**, *289*, 173.

(19) Jeffrey, G. A. *An Introduction to Hydrogen Bonding*; Oxford University Press, 1997.

(20) Schilter, D.; Rauchfuss, T. B.; Stein, M. *Inorg. Chem.* **2012**, *51*, 8931.

(21) Brookhart, M.; Grant, B.; Volpe, A. F. *Organometallics* **1992**, *11*, 3920.

(22) LeSuer, R. J.; Buttolph, C.; Geiger, W. E. *Anal. Chem.* **2004**, *76*, 6395.